Technische Universität München
Institut für Energietechnik

Lehrstuhl für Thermodynamik

Modeling of auto-ignition and NOx formation in turbulent reacting flows

Frédéric Bernard Collonval

Vollständiger Abdruck der von der Fakultät für Maschinenwesen der Technischen Universität München zur Erlangung des akademischen Grades eines

Doktor – Ingenieurs

genehmigten Dissertation.

Vorsitzender:
Univ.-Prof. Dr.-Ing. Hans-Jakob Kaltenbach
Prüfer der Dissertation:
1. Univ.-Prof. Wolfgang Polifke, Ph.D.
2. Univ.-Prof. Patrick Jenny, Ph.D., ETH Zürich

Die Dissertation wurde am 29.09.2014 bei der Technischen Universität München eingereicht und durch die Fakultät für Maschinenwesen am 30.01.2015 angenommen.

I believe no matter how random something may appear, there's still a plan.

Col. John "Hannibal" Smith

Preface

Die vorliegende Arbeit entstand am Lehrstuhl für Thermodynamik der Technischen Universität München.

Meinem Herrn Professor W. Polifke, Ph. D., gilt mein ganz besonderer Dank für die Freiheit bei der wissenschaftlichen Arbeit und das mir entgegengebrachte Vertrauen.

Herrn Professor Dr. Patrick Jenny danke ich für die freundliche Übernahme des Koreferates und Herrn Professor Dr.–Ing. Hans-Jakob Kaltenbach für den Vorsitz bei der mündlichen Prüfung.

I want to thank Professor C. Jimenez and her team for hosting me at the CIEMAT during two weeks in May 2010. The discussions and simulations done there help me for understanding the limits and the strengths of the model.

I'm grateful to Dr. Ruedel, Dr. B. Bukunte and the combustion team of Alstom Power. The 10 weeks spent in your team were a great experience of research in industrial context.

During this work, I made intensive use of open-source and free softwares; especially Cantera, Matplotlib, Numpy, OpenFOAM®, ParaView, and Scipy. I'm deeply thankful to their authors and contributors. And my thoughts go in particular to Professor David Goodwin (author of Cantera) and John Hunter (author of Matplotlib) who passed away recently.

Je tiens également à remercier Piotr et Gary pour m'avoir supporté (ainsi que les étudiants du lab de CFD) durant de longs mois et pour m'avoir appris des rudiments de polonais et de français de France.

La vie dans le département n'aurait pas été aussi douce sans les découvertes culinaires avec Eva et Katrin.

Je remercie aussi Johannes, Alejandro, Mathieu et Rohit pour les échanges de connaissances et les débats d'idées.

Un tout grand merci à Anja, Ahtsham, Danilo, Jannis, Marek, Robert, Vanja et Volker pour les discussions des pause-midi, des pauses cafés, des pauses gâteaux; bref des pauses forcées ou voulues.

Je n'aurai pas pu terminer cette thèse de doctorat sans le soutien de mes parents et de mes soeurs. Spécial merci à vous.

Et puis comment ne pas mentionner les remises en condition belges par Arnaud, Benoit, Luc, Sven et Thibaut.

Un double remerciement à Eva, Johannes et Mathieu sans qui ce manuscript ne serait pas aussi poli et raffiné.

Ces trois années germaniques furent riches en découverte, en expérience et en émotions. Je tiens donc à remercier tous ceux que j'ai certainement oublié (je m'en excuse) et qui m'ont permis d'adoucir les aigreurs et de sublimer les euphories.

This work has been made possible thanks to the financial support of the European Union's Seventh Framework Programme FP7/2007-2013 under grant agreement n° PITN-GA-2008-210781 (MyPlanet).

Munich, in May 2013 Frédéric Collonval

Teile dieser Dissertation wurden vom Autor bereits standardmäßig vorab als Konferenz- und Zeitschriftenbeiträge veröffentlicht [15, 17, 18]. Alle Vorveröffentlichungen sind entsprechend der gültigen Promotionsordnung ordnungsgemäß gemeldet. Sie sind deshalb nicht zwangsläufig im Detail einzeln referenziert. Vielmehr wurde bei der Referenzierung eigener Vorveröffentlichungen Wert auf Verständlichkeit und inhaltlichen Bezug gelegt.

Significant parts of this Ph.D. thesis were published by the author beforehand in conference proceedings, journal papers, and reports [15, 17, 18]. All of these prior printed publications are registered according to the valid doctoral regulations. However, not all of them are quoted explicitly everywhere as they are part of this present work being official documents. Whether these personal prior printed publications were referenced, depended on maintaining comprehensibility and providing all necessary context.

Kurzfassung

Der weltweite Energiebedarf steigt aufgrund des anhaltenden wirtschaftlichen Wachstums dramatisch an. Trotz der zunehmenden Bedeutung von erneuerbaren Energieträgern wird die Vorherrschaft fossiler Energieträger während der nächsten vierzig Jahre weiterhin bestehen bleiben. Dies liegt vor allem an deren guter Verfügbarkeit und am hohen Entwicklungsstand der fossilen Verbrennungstechniken. Um der globalen Erwärmung entgegen zu wirken, muss die Entwicklung neuer Verbrennungstechniken hinsichtlich Effizienz und Emissionen weiter vorangetrieben werden. Insbesondere müssen die Stickoxidemissionen, auch bekannt als NO_x, reduziert werden.

Diese Aufgabe stellt seit Jahrzehnten eine Herausforderung dar. Für einen spezifischen Betriebspunkt liegt die Effizienz solcher Systeme meist nahe des theoretischen Maximums. Für große Verbrennungssysteme, wie z.B. Gasturbinen, ist der reale Betriebsbereich jedoch sehr weit gefächert. Dies wird in Zukunft durch den kontinuierlichen Zuwachs an erneuerbaren Energiesystemen noch weiter verstärkt. Die aktuelle Herausforderung besteht nun darin, den Betriebsbereich, in dem ein hoher Wirkungsgrad realisiert wird, zu vergrößern.

Eine weitere Herausforderung für Verbrennungssysteme ist die teilweise oder vollständige Verwendung von Bio-Kraftstoffen. Das Verhalten dieser Brennstoffe unterscheidet sich grundlegend von den heute meist verwendeten klassischen Brennstoffen. Daher müssen die zur Vorhersage verwendeten Verbrennungsmodelle, die aktuell entwickelt werden, zum einen die hohe Variabilität der Brennstoffzusammensetzung berücksichtigen, und zum anderen das Verhalten in Bezug auf Flammenstabilisierung richtig vorhersagen.

Unter Berücksichtigung der genannten Aspekte sind das von Alstom entwickelte sequentielle Verbrennungssystem für Gasturbinen sowie homogen aufgeladene Verbrennungsmotoren (engl. HCCI) interessante Konzepte. Leider gestalten sich die Auslegung und die Modellierung solcher Systeme als sehr schwierig, da die starke Interaktion von Chemie und Turbulenz zu Flammenlöschen, Selbstzündung oder Flammenrückschlag führen kann.

Ein großer Durchbruch gelang durch die Verwendung von Grobstruktursimulation (engl. LES) für die Berechnung von Brennkammern. Durch das exponentielle Wachstum der Rechenleistung wird die Berechnung realer Brenner zunehmend möglich. Der damit erreichte tiefere Einblick in die Strömungszustände brachte jedoch auch die Notwendigkeit mit sich, neue Modelle für die Turbulenz-Chemie Interaktion zu verwenden und nach effizienten Wegen zu suchen, den chemischen Quellterm zu berechnen.

Während dieses Projekts wird die Qualität und Genauigkeit des neuen Lösers von R. Kulkarni [66] beurteilt. Das Turbulenz-Chemie-Modell basiert auf dem Transport von Wahrscheinlichkeitsdichtefunktionen (PDF) für die Zusammensetzung unter Verwendung von Euler-stochastischen Feldern. Der Aufwand für die Chemieberechnungen wird drastisch reduziert, indem die Quellterme im Vorfeld in Tabellen gespeichert und während der Simulation aufgerufen werden. Der letztgenannte Ansatz wird anhand von einfachen Konfigurationen überprüft: homogene Reaktoren, Selbstzündung von geschichteten Mischungen und laminare Vormischflammen. Die Exaktheit des Turbulenz-Chemie Modells wird anhand von selbstzündenden Konfigurationen validiert.

Zum Schluss wird eine Erweiterung im Hinblick auf die Emissionsvorhersage eingeführt. Die Notwendigkeit für ein dezidiertes Emissionsmodell resultiert aus der Tatsache, dass sich die Zeitskalen der Verbrennung und der Schadstoffchemie stark unterscheiden. Das entwickelte Modell wird anhand von homogenen Reaktoren und laminaren Flammen getestet.

Abstract

The need of energy to sustain the development of humanity is dramatically increasing. Despite the growing importance of renewable energies, the availability and maturity of the technology for combustion systems will result in the predominance of the fossil energy for the next 40 years. But in order to mitigate the global warming, new developments are needed to improve the efficiency of the combustors while keeping as low as possible the emissions. Among the unwanted species the nitrogen oxides known as NO_x is of primary concern for combustor designers.

This has been a challenge for decades. Therefore for a given nominal operating point the global efficiency is close to the ideal one. But for large combustion systems like gas turbines, the range of operating conditions is quite broad and will be broader with the continuous growth of the renewable energy systems. Therefore the present challenge is to enlarge the range of operating conditions for which the system runs with high efficiency.

Another challenge for the combustion devices is the development of bio-fuel at full or partial proportions. Their behaviors are quite different to the classical fuels used up to now in motors. So the combustion models developed must be able to capture the high variability of the fuel composition and predict correctly the consequences in term of flames stability and emissions production.

In those respects, the sequential combustion system as developed by Alstom Power's GT 24/26 or *Homogeneous-Charge Compression Ignition* engine (HCCI) are interesting concepts. Unfortunately, the design and modeling of such system is quite complex as strong interactions between the turbulence and the chemistry are taking place, leading to no-ignition, self-ignition or even flash-back.

A huge break-through has been achieved by applying Large-Eddy Simulations to combustion chambers. Indeed the exponential growth of computational power made the transient simulations of realistic burners possible. Unfortunately the greater insight on the flow brought also a need for new turbulence-chemistry models and a revival of more efficient ways to deal with the accurate computation of the chemistry source terms.

In this work the quality and accuracy of a new model proposed originally by R. Kulkarni [66] is assessed. The turbulence-chemistry model is based on the transport of the composition probability density function using Eulerian stochastic fields. The cost of the chemistry is radically reduced by storing the source terms in look-up tables. The latter part will be validated solely against simple configurations: homogeneous reactors, auto-igniting mixing layers and laminar premixed flames. Then the accuracy of the turbulence-chemistry model will be evaluated against auto-ignition configurations.

Finally an extension of the model to predict emissions will be presented. The need of a dedicated model for the pollutant formation results of the different range of chemical time scales between the combustion and the pollutants chemistry, e.g. the thermal NO_x. The model will be tested on homogeneous reactors and laminar premixed flames.

Contents

List of Figures

List of Tables

Nomenclature

Latin Characters

C	Normalized progress variable	[-]
C_p	Specific heat capacity at constant pressure	$[\mathrm{J\,kg^{-1}\,K^{-1}}]$
C_v	Specific heat capacity at constant volume	$[\mathrm{J\,kg^{-1}\,K^{-1}}]$
D	Diffusion coefficient	$[\mathrm{kg\,m^{-1}\,s^{-1}}]$
D^{sgs}	Species turbulent diffusion coefficient	$[\mathrm{kg\,m^{-1}\,s^{-1}}]$
$\mathcal{F}$	Favre filtered density function	[-]
$\mathbf{g}$	Gravitational vector	$[\mathrm{m\,s^{-2}}]$
G	Spatial filter operator	[-]
h_s	Sensible enthalpy	$[\mathrm{J\,kg^{-1}}]$
H	Total enthalpy	$[\mathrm{J\,kg^{-1}}]$
k_r	Residual kinetic energy	$[\mathrm{m^2\,s^{-2}}]$
K	Kinetic energy	$[\mathrm{m^2\,s^{-2}}]$
l	Length	[m]
L_{ign}	Auto-ignition length	[m]
N_E	Number of environments	[-]
N_s	Number of species	[-]
N_{sf}	Number of stochastic fields	[-]
p	Pressure	[Pa]
$\mathcal{P}$	Probability density function	[-]
Q_k	Species k mass fraction conditioned on the mixture fraction $Q_k = \langle Y_k \vert \eta \rangle_\Delta$	[-]
Q_h	Sensible enthalpy conditioned on the mixture fraction $Q_h = \langle h_s \vert \eta \rangle_\Delta$	$[\mathrm{J\,kg^{-1}}]$
r	Radial distance	[m]
R	Gas constant	$[\mathrm{J\,kg^{-1}\,K^{-1}}]$
S	Strain tensor	$[\mathrm{s^{-1}}]$
S_L	Laminar flame speed	$[\mathrm{m\,s^{-1}}]$
t	Time	[s]
T	Temperature	[K]
$\mathbf{u}$	Velocity, velocity component	$[\mathrm{m\,s^{-1}}]$

V	Subgrid-scales variance	
$\mathbf{V}_k$	Species k diffusion velocity	$[\mathrm{m\,s^{-1}}]$
w	Weight	[-]
W_i	Molecular/element i weight	$[\mathrm{kg\,mol^{-1}}]$
dW	Wiener process	$[\mathrm{s^{1/2}}]$
$\mathbf{x}$	Distance (Cartesian coordinate system)	[m]
X	Species mole fraction	[-]
Y_c	Progress variable	[-]
Y_k	Species k mass fraction	[-]
z	Axial distance	[m]
Z	Mixture fraction	[-]

Greek Characters

β	Beta function	[-]
δ	Delta function	[-]
Δ	Spatial filter length	[m]
$\Delta h^{f,0}$	Enthalpy of formation	$[\mathrm{J\,kg^{-1}}]$
Δt	Time step	[s]
ϵ	Measure of an error	[-]
η	Mixture fraction	[-]
λ	Thermal conductivity	$[\mathrm{W\,m^{-1}\,K^{-1}}]$
μ	Dynamic viscosity	[Pa s]
μ^{sgs}	Turbulent dynamic viscosity	[Pa s]
ξ	Stochastic field	
ρ	Density	$[\mathrm{kg\,m^{-3}}]$
τ	Viscous tensor	$[\mathrm{N\,m^{-2}}]$
τ_{ign}	Auto-ignition delay	[s]
τ_{sgs}	Mixing time scale	[s]
ϕ	Composition vector (species, temperature and pressure)	
χ	Scalar dissipation rate	$[\mathrm{s^{-1}}]$
ψ	Composition vector (species, temperature and pressure)	
$\dot{\omega}_{hs}$	Heat release	$[\mathrm{W\,kg^{-1}}]$
$\dot{\omega}_k$	Species k mass fraction source term	$[\mathrm{s^{-1}}]$

Abbreviations

AIS	Auto-Ignition Spot
AMC	Amplitude Mapping Closure
CDR	Convection, Diffusion and Reaction balance
CFD	Computational Fluid Dynamics
CMC	Conditional Moment Closure
CSP	Computational Singular Perturbation
DNS	Direct Numerical Simulation
DQMoM	Direct Quadrature Method of Moments
ESF	Eulerian Stochastic Fields method
FDF	Filtered Density Function
FFDF	Favre Filtered Density Function
FGM	Flamelet Generated Manifold
FPI	Flame Prolongation ILDM
HPC	High Performance Computing
IEM	Interaction by Exchange with the Mean
ILDM	Intrisic Low-Dimensional Manifold
LES	Large Eddy Simulation
MR	Most Reactive
PDF	Probability Density Function
RANS	Reynolds-Averaged Navier-Stokes equations
SFPV	Stochastic Field - Progress Variable model
SPDE	Stochastic Partial Differential Equation
WALE	Wall-Adapting Local Eddy-viscosity model

Dimensionless Numbers

Le	Lewis number
Pr	Prandlt number
Pr_t	Turbulent Prandlt number
Sc	Schmidt number
Sc_t	Turbulent Schmidt number

Operators

$\bar{.}$	Spatial filter operator
$E[.]$	Expected value operator
$\langle . \rangle_{\Delta}$	Density weighted spatial filter operator
$\langle . \rangle$	Time average operator
$\tilde{.}$	Density weighted spatial filter operator

Superscripts

b	Related to burnt gas (at thermodynamical equilibrium)
det	Related to detailed chemistry
eq	Related to the final state for the look-up tables' generation
f	Related to fresh mixture (contains only reactants)
$init$	Related to the initial state for the look-up tables' generation
k	Species k
NO	Nitrogen oxide
p	Related to burnt products (at any temperature)
ref	Reference parameter or data
st	Related to stochiometric conditions
tab	Related to tabulated chemistry
u	Related to unburnt gas (before starting the reaction)
Z	Related to the mixture fraction

Subscripts

sgs	Related to the subgrid-scales effect

1 Introduction

Since the beginning of the industrial revolution at the end of 18^{th} century, men have improved their living conditions thanks to complex mechanisms moved by fuel-based energy. The 21^{st} century will be marked by a drastic change in energy resources and management. Indeed, in parallel to the development of renewable energy, a profound reorganization of the energy production will be carried out as more and more countries shut down their nuclear power plants.

Therefore to sustain the energy demands, new gas turbines based on coal or gas will be built. And they will ease the regulation of electricity production thanks to their high flexibility in comparison with the renewable energies. But to be acceptable those combustion systems have to balance three facts: fuel flexibility, reduction of greenhouse gases, and emission production. They all appeal for more efficient designs. Today designing a combustor requires therefore a high efficiency not only at the nominal point but also for a broad range of operating conditions.

A sequential system, in which hot products are mixed with fresh fuel in a second combustion chamber, is a possible solution. In such complex burner lots of phenomena interact like turbulent mixing, chemistry, auto-ignition, heat transfer, radiation ... . Although none of those aspects are new, the interaction between them is a very active research area, especially for auto-ignition regime. But the interest is not limited to the flame and heat transfer. For the gas turbine manufacturers the prediction of pollutants is a primordial point. As most current combustion systems work at lean conditions, the level of unburnt gases is generally very low. However the quantity of NO_x produced cannot be neglected. Therefore a modern combustion model should be able to address the combustion chemistry, its interaction with the turbulence and the pollutants prediction.

The development of combustion model for auto-ignition prediction is built upon the research of M. Brandt [8, 9].

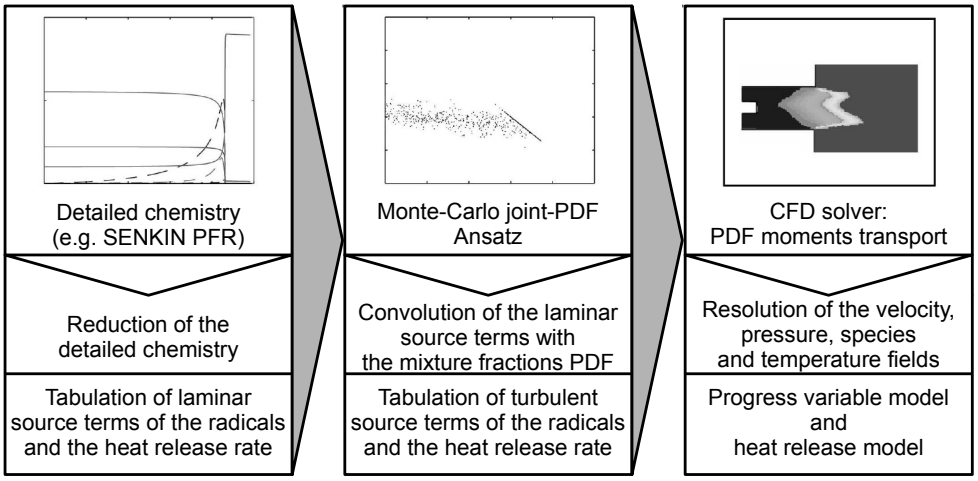

Figure 1.1: Implementation of Brandt's model (translated from [8]).

Auto-ignition event can be divided into three phases: the induction period, the heat release phase and the hot burnt products transport. To predict the occurrence and the position of auto-ignition event, the induction period should be simulated precisely. But in that phase, there is no heat release (temperature is constant) and the concentration of major species is hardly varying. The only parameters evolving are the intermediate species; with most of them reaching a peak around the ignition event. M. Brandt proposes a model in which the turbulent heat release is read in look-up table computed as the convolution of the mixture fractions *joint Probability Density Function* (PDF) and laminar source term computed from SENKIN [72]. And in order to obtain the correct induction period the heat release rate is weighted by a Heaviside function switching from 0 to 1 when the mass fraction of a radical species representative of the radical pool building process reaches a critical level. The formaldehyde, CH_2O, was found to be the best candidate to represent the radical pool in the case of methane.

M. Brandt develops also a new PDF ansatz especially suitable for multi-streams mixing and handling cross-correlations between the parameters. Two approaches were developed in the case of three streams mixing. In the first one, a two dimensional Gaussian PDF is sampled. The samples lying outside the physical bound of the mixture fractions space are projected onto the border of the mixture fractions space (see Figure 1.2). This method can handled δ-PDF for pure composition as well as the Gaussian distribution for mixed composition.

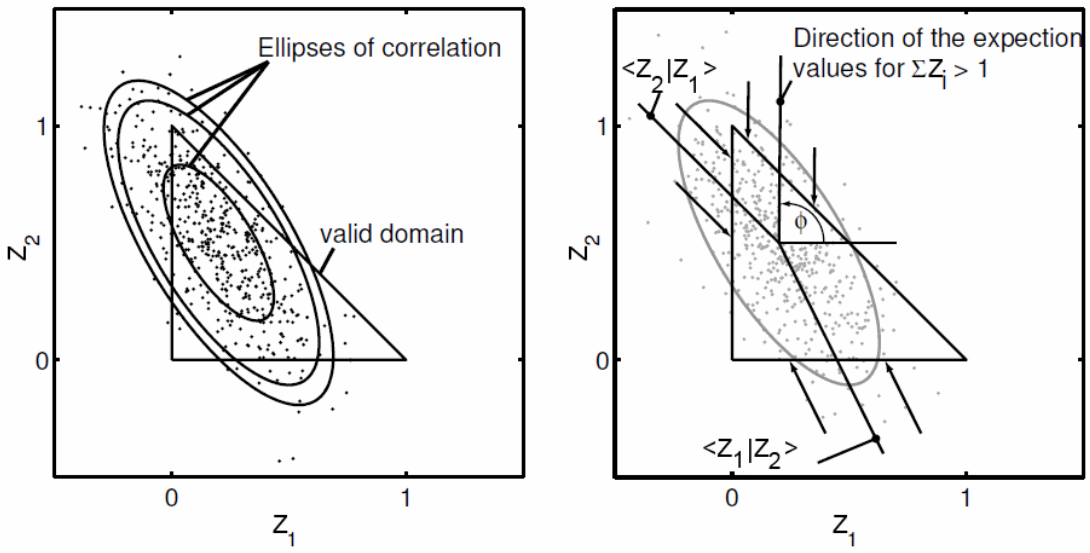

Figure 1.2: Monte Carlo joint-PDF based on Gaussian distribution with projection on the mixture fractions boundaries of the unphysical samples [10].

The other approach to determine the mixture fraction PDF for a given set of first and second moments is obtained by applying for a certain time a mixing model (e.g. modified Curl mixing model) to a 3-δ peaks PDF. The value of the three initials peaks are defined from the first moments of the distribution. Applying the mixing model allows then to get the second order moments desired (see Figure 1.3).

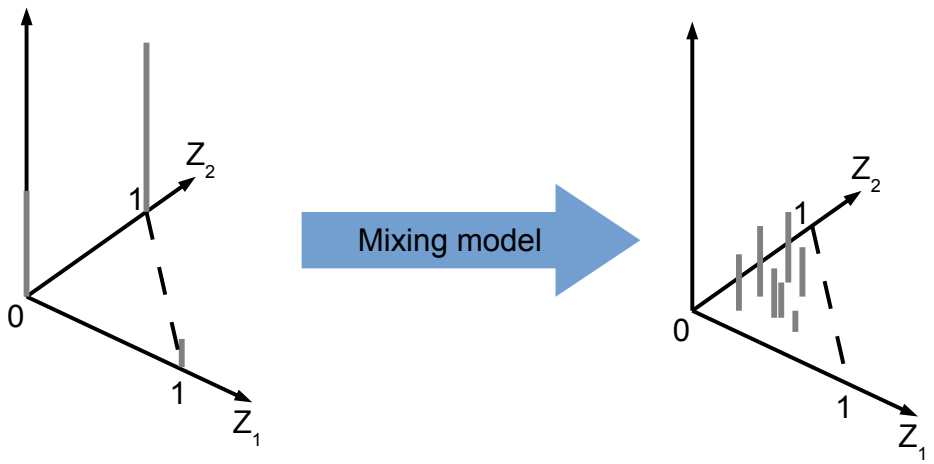

Figure 1.3: Monte Carlo joint-PDF based on the application of a mixing model to an initial 3-δ peaks distribution [10].

In [10], M. Brandt et al. have compared the results of those two joint-PDF models against *Large Eddy Simulation* (LES) data. That validation test case shows that the joint-PDF constructed from the application of the modified Curl mixing model to a 3-δ peaks PDF achieves the best results.

Due to the inhibition of the heat release during the induction period the Brandt's model predicts poorly the propagation of flames sustained by auto-ignition; especially if the propagation has an upstream component. Therefore R. Kulkarni in his effort to adapt the auto-ignition model to LES used an uniform approach for all phases of the auto-ignition event; i.e. tracking of the mixture reactivity through a single progress variable. That progress variable combined intermediate species (like CH_2O), to capture the induction phase (as demonstrated by M. Brandt), and burnt products, representative of the heat release.

The joint-PDF models developed by M. Brandt were all having the ability to avoid any assumptions on the cross-correlations between chemical species. This is particularly important to capture multi-streams flows combining two or more mixture fractions. In such case the joint-PDF shape should not be presumed. This is supported by the better results obtain by M. Brandt using the mixing model approach rather than the multi-dimensional clipped Gaussian. But as the computational power keeps increasing, R. Kulkarni chose to transport the joint-PDF based on *Eulerian Stochastic Fields* (ESF). Those have the advantage to handle multi-streams flows straightforwardly. And the subgrid-scales variance being smaller in LES compared to *Reynolds Averaged Navier-Stokes* equations (RANS), a small number of stochastic fields is sufficient to model joint-PDF. This keeps the computational cost at an affordable level with less assumptions in the combustion model.

In Kulkarni's model, the mixture fraction and the progress variable are transported using Eulerian stochastic fields. Those equations are supplied with source terms read in look-up tables. Then once the new value of the mixture fraction and progress variable are known, the source terms for the chemical species and the heat release rate can be retrieved for each stochastic fields in look-up tables. Taking the average of those source terms gives the filtered source terms needed by the *Computational Fluid Dynamics* (CFD) solver as described in Figure 1.4.

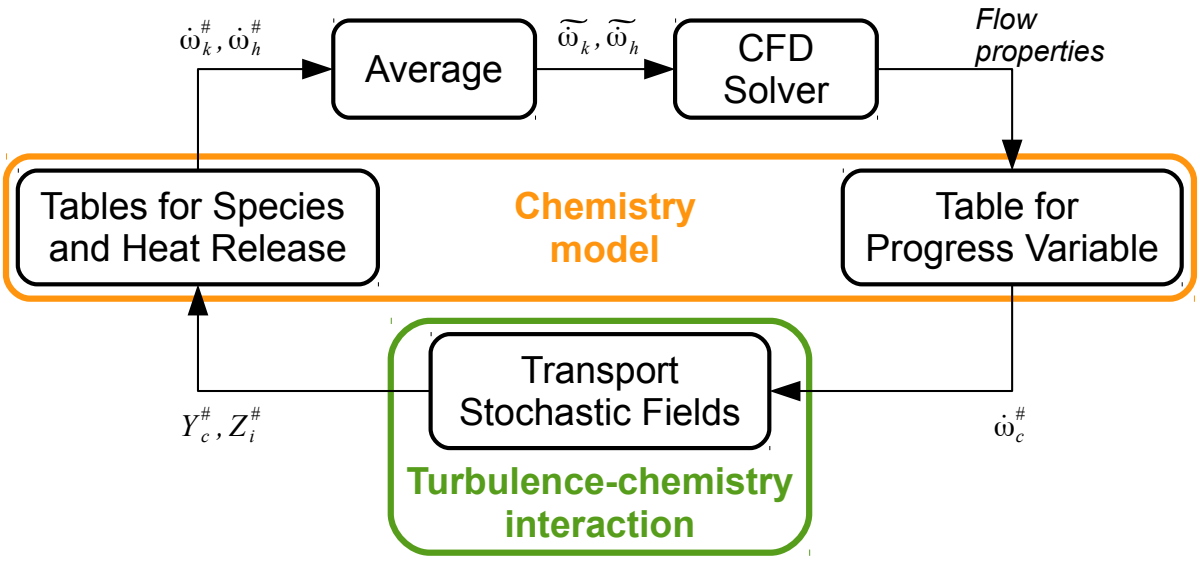

Figure 1.4: Implementation of Kulkarni's model. # represents the index of any stochastic fields.

The following research is the prolongation of the work of R. Kulkarni. The main objectives were:

- The adaptation of the model for the toolbox OpenFOAM®,
- The validation and a deeper analysis of the chemical and turbulence-chemistry interaction models,
- The extension to NO_x prediction.

Those three goals are supplemented with a fourth one: the reduction of the computational cost. Despite the use of *High-Performance Computing* (HPC) system, simulations of combustion in realistic geometries are costly. As a consequence, the model presented here has been chosen to reduce the computational time of a simulation while keeping the flexibility needed for industrial applications.

The structure of this document is as follow. In Chapter 2, the conservation equations will be presented as well as some widely used models for PDF transport. Additively some information about the chemistry modeling and especially the NO_x prediction will be described. After this review of the existing models, the global combustion model including NO_x estimation

will be developed in details in the Chapter 3. The model description will end with some elements on the implementation. The validity of the model will be exposed in the Chapter 4. The validation will start with simple configurations like homogeneous reactor or laminar premixed flame up to more complex flows in which auto-ignition spots appear. The last section of that chapter will assess the accuracy of the NO_x model for non-turbulent cases. And finally, in the Chapter 5, the performance and limitations of the model will be discussed.

2 Fundamentals

The first part of this chapter will introduce the conservation equations solved in the code. The second section will focus on the description of chemistry models, and in particular NO_x prediction. The modeling of the turbulence-chemistry interactions for partially and non-premixed flows based on transported joint probability density function will close this chapter.

2.1 Governing equations

The simulation of reacting flows requires the resolution of the Navier-Stokes equations. Those expressions in conservative form are [93]:

Continuity

$$\frac{\partial \rho}{\partial t} + \frac{\partial \rho u_i}{\partial x_i} = 0, \tag{2.1}$$

where ρ is the density and u_i the i$^{\text{th}}$ component of the velocity.

Species mass fraction

$$\frac{\partial \rho Y_k}{\partial t} + \frac{\partial}{\partial x_i}\left(\rho(u_i + V_{k,i})Y_k\right) = \rho\dot{\omega}_k \qquad \text{for } k = 1...N_s, \tag{2.2}$$

where $V_{k,i}$ is the i$^{\text{th}}$ component of the diffusion velocity and $\dot{\omega}_k$ the chemical source term for the mass fraction Y_k of species k.

Momentum

$$\frac{\partial \rho u_j}{\partial t} + \frac{\partial \rho u_i u_j}{\partial x_i} = -\frac{\partial p}{\partial x_j} + \frac{\partial \tau_{ij}}{\partial x_i} + \rho g_j, \tag{2.3}$$

where p is the pressure, g_j the j$^{\text{th}}$ component of the gravitational acceleration and τ_{ij} the viscous tensor. For compressible flows the latter is defined by:

$$\tau_{ij} = 2\mu S_{ij} - \frac{2}{3}\mu\delta_{ij}S_{kk}, \tag{2.4}$$

where μ is the dynamic viscosity, δ_{ij} the Kronecker symbol and S_{ij} the strain tensor is defined as:

$$S_{ij} = \frac{1}{2}\left(\frac{\partial u_i}{\partial x_j} + \frac{\partial u_j}{\partial x_j}\right). \tag{2.5}$$

Energy - sensible enthalpy form

$$\frac{\partial \rho h_s}{\partial t} + \frac{\partial \rho u_i h_s}{\partial x_i} = \frac{\partial p}{\partial t} - \frac{DK}{Dt} + \frac{\partial u_i \tau_{ij}}{\partial x_j} - \frac{\partial q_i}{\partial x_i} + \rho\dot{\omega}_{hs}, \tag{2.6}$$

where $K = \frac{1}{2}u_k u_k$ is the kinetic energy, $\frac{D_\cdot}{Dt}$ is the material derivative, $\dot{\omega}_{hs}$, the source term due to the chemical reactions. And q_i combines the heat fluxes and the transport of sensible enthalpies by the species diffusion velocities $\mathbf{V}_k$:

$$q_i = -\lambda\frac{\partial T}{\partial x_i} + \rho\sum_{k=1}^{N_s} h_{s,k} Y_k V_{k,i}, \tag{2.7}$$

with T and λ denoting the temperature and the thermal conductivity, respectively.

The following simplifications of the previous equations are made in the developed OpenFOAM® solver:

- The gravitational acceleration effect is neglected.
- The species diffusion velocity is modeled according to Fick's law:

  $$\rho V_{i,k} Y_k \approx -D_k\frac{\partial Y_k}{\partial x_i}, \tag{2.8}$$

  where D_k is the diffusion coefficient.
- The viscous heat source term $\frac{\partial u_i \tau_{ij}}{\partial x_j}$ is neglected.
- The transport of sensible enthalpies by the species diffusion velocities is neglected.
- The heat fluxes are expressed using the sensible enthalpy:

  $$-\lambda\frac{\partial T}{\partial x_i} \approx -\frac{\lambda}{C_p}\frac{\partial h_s}{\partial x_i} \tag{2.9}$$

- The thermal conductivity is derived from the kinetic theory and results in the following algebraic relation $\lambda = \mu C_v(1.32 + 1.77\frac{R}{M_w C_v})$ where C_v is the mass heat capacity at constant volume, R the gas constant and M_w, the mean molecular weight.

The perfect gas law will close that system of conservation equations.

$$p = \rho RT, \tag{2.10}$$

where R is the gas constant defined as $R = C_p - C_v$ with C_p (respectively C_v) being the specific heat at constant pressure (respectively at constant volume).

Turbulent flows in practical applications have generally a Reynolds number too high to carry out a *Direct Numerical Simulation* (DNS). Therefore in the past, most calculations were based on the Reynolds averaged form (RANS) of the previous system of equations. However thanks to the development in micro-electronics and computer science, the power of HPC centers have drastically increased. As a consequence for fluids mechanic users *Large Eddy Simulation* (LES) is now in reach, in particular for academic test cases. The main advantages of LES in comparison to RANS for combustion system are: the capture of transient effects and the reduction of the unresolved fluctuations. As a result, complex flows and in particular combustion systems are better modeled by LES. Unfortunately new problems appeared as for example the need for turbulent inflow generators (see Appendix A for more information).

The Large-Eddy simulation concept is founded on the idea that a turbulent flow is composed of vortices with a large range of sizes - from the Kolmogorov length scale, at which the viscous dissipation occurs, to a size linked to the system geometry and boundary conditions. The latter depending on the geometry should be resolved by the simulation while the former are supposed to be more universal and thus amenable to modeling. By modeling the small scales, the LES cost is drastically reduced in comparison with DNS, as in the latter most of the computation time is dedicated to large wave numbers.

The separation between large and small scales is achieved through a convolution filtering of the fields i.e. a field f will be convoluted by a spatial filter G:

$$\bar{f}(\mathbf{x}) = \int G(\mathbf{x}, \mathbf{x}') f(\mathbf{x}') d^3\mathbf{x}'. \tag{2.11}$$

The fundamental properties of the filter are [31]:

- Consistency
$$\bar{a} = a \Longleftrightarrow \int G(\mathbf{x}, \mathbf{x}')d^3\mathbf{x}' = 1, \tag{2.12}$$
- Linearity
$$\overline{f+g} = \bar{f} + \bar{g}, \tag{2.13}$$
- Commutation with the differentiation time operator
$$\overline{\frac{\partial f}{\partial t}} = \frac{\partial \bar{f}}{\partial t}. \tag{2.14}$$

The commutation with the differentiation space operator is valid only for unbounded domain and homogeneous convolution kernel (i.e. the filtering length Δ is constant in space). Practically, OpenFOAM® as the majority of other codes uses an implicit filtering associated with the computational grid. The assumed commutation with the spacial differentiation will thus introduce a commutation error. That error is presumably small for inhomogeneous grids in which the filtering length evolves smoothly (i.e. in which the cell size varies smoothly).

A density weighted Favre filter, similar to the Favre notation in RANS, will be used to establish filtered equations with a similar structure to the unfiltered equations:
$$\overline{\rho f} = \bar{\rho}\tilde{f}. \tag{2.15}$$

Using the Favre notation[1] and the hypothesis presented earlier, the filtered governing equations are [31, 96]:

Continuity
$$\frac{\partial \bar{\rho}}{\partial t} + \frac{\partial \bar{\rho}\widetilde{u_i}}{\partial x_i} = 0. \tag{2.16}$$

Species mass fraction
$$\frac{\partial \bar{\rho}\widetilde{Y_k}}{\partial t} + \frac{\partial \bar{\rho}\widetilde{u_i}\widetilde{Y_k}}{\partial x_i} - \frac{\partial}{\partial x_i}\left(D_k \frac{\partial \widetilde{Y_k}}{\partial x_i}\right) = -\frac{\partial}{\partial x_i}\left(\bar{\rho}\widetilde{u_i Y_k} - \bar{\rho}\widetilde{u_i}\widetilde{Y_k}\right) + \widetilde{\dot{\omega}_k} \qquad \text{for } k = 1...N_s. \tag{2.17}$$

[1] To ease the reading, the notation $\langle f \rangle_\Delta$ will be sometimes used instead of $\tilde{f}$.

By analogy to the model developed in RANS, the sub-grid term is modeled using Fick's law:

$$\bar{\rho}u_i\widetilde{Y}_k - \bar{\rho}\widetilde{u}_i\widetilde{Y}_k = -D_k^{\text{sgs}}\frac{\partial\widetilde{Y}_k}{\partial x_i}. \tag{2.18}$$

Therefore, if the diffusion coefficients are defined from a laminar and turbulent Schmidt number, the species mass fraction equation becomes:

$$\frac{\partial\bar{\rho}\widetilde{Y}_k}{\partial t} + \frac{\partial\bar{\rho}\widetilde{u}_i\widetilde{Y}_k}{\partial x_i} - \frac{\partial}{\partial x_i}\left(\left(\frac{\mu}{\text{Sc}} + \frac{\mu^{\text{sgs}}}{\text{Sc}_t}\right)\frac{\partial\widetilde{Y}_k}{\partial x_i}\right) = \bar{\rho}\widetilde{\dot{\omega}_k} \qquad \text{for } k = 1...N_s. \tag{2.19}$$

Momentum

$$\frac{\partial\bar{\rho}\widetilde{u}_j}{\partial t} + \frac{\partial\bar{\rho}\widetilde{u}_i\widetilde{u}_j}{\partial x_i} = -\frac{\partial\bar{p}}{\partial x_j} + \frac{\partial\widetilde{\tau_{ij}}}{\partial x_i} - \frac{\partial}{\partial x_i}\left(\bar{\rho}u_i\widetilde{u}_j - \bar{\rho}\widetilde{u}_i\widetilde{u}_j\right). \tag{2.20}$$

Similarly to RANS, the turbulent-viscosity hypothesis of Boussinescq is introduced. The anisotropic residual-stress tensor τ_{ij}^{sgs} is proportional to the filtered rate of strain:

$$\tau_{ij}^{\text{sgs}} = \left(\bar{\rho}u_i\widetilde{u}_j - \bar{\rho}\widetilde{u}_i\widetilde{u}_j\right) - \frac{2}{3}\bar{\rho}k_r\delta_{ij} = -2\mu^{\text{sgs}}\left(\widetilde{S_{ij}} - \frac{1}{3}\widetilde{S_{kk}}\delta_{ij}\right), \tag{2.21}$$

where $k_r = \frac{1}{2}\sum(u_k\widetilde{u}_k - \widetilde{u}_k\widetilde{u}_k)$ is the residual kinetic energy.

The isotropic residual stresses are included in a modified filtered pressure, $\bar{P} = \bar{p} + \frac{2}{3}\bar{\rho}k_r$ resulting in the following law:

$$\frac{\partial\bar{\rho}\widetilde{u}_j}{\partial t} + \frac{\partial\bar{\rho}\widetilde{u}_i\widetilde{u}_j}{\partial x_i} = -\frac{\partial\bar{P}}{\partial x_j} + \frac{\partial}{\partial x_i}2(\mu + \mu^{\text{sgs}})\left(\widetilde{S_{ij}} - \frac{1}{3}\widetilde{S_{kk}}\delta_{ij}\right). \tag{2.22}$$

The subgrid-scale viscosity, μ^{sgs} has to be modeled; e.g. using the dynamic Smagorinsky model [70].

Energy - sensible enthalpy form

The subgrid-scale energy fluxes are modeled using a gradient law based on the subgrid-scale viscosity and a *turbulent Prandlt number*, Pr_t.

$$\frac{\partial \bar{\rho}\widetilde{h_s}}{\partial t} + \frac{\partial \bar{\rho}\widetilde{u_i}\widetilde{h_s}}{\partial x_i} = \frac{\partial \bar{P}}{\partial t} - \frac{D\bar{\rho}\tilde{K}}{Dt} + \frac{\partial}{\partial x_i}\left(\left(\frac{\lambda}{C_p} + \frac{\mu^{sgs}}{\mathrm{Pr}_t}\right)\frac{\partial \widetilde{h_s}}{\partial x_i}\right) + \bar{\rho}\widetilde{\dot{\omega}_{hs}}. \quad (2.23)$$

The filtered equation of state becomes approximatively

$$\bar{P} = \bar{\rho} R \tilde{T}. \quad (2.24)$$

If the subgrid-scale viscosity is known, the equations are closed if the filtered source terms for the species and the sensible enthalpy are known. Combustion modeling comes into play at this stage.

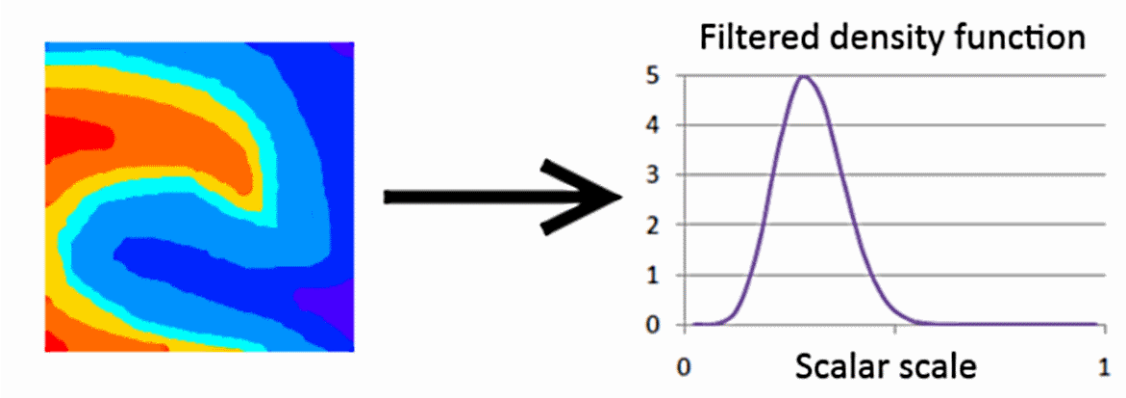

Figure 2.1: Sketch of the real scalar field inside one cell of a typical Large-Eddy Simulation and its model representation using a filtered density function (FDF).

In a direct numerical simulation, the values of all variables and parameters are known. Therefore the fine-grained composition PDF associated to each point at each time is a delta function. In the frame of LES the composition filtered density function is built from the filtering (or G-weighting, if G is the filter) of the fine-grained composition PDF in the vicinity of a point $\mathbf{x}$:

$$F(\phi; \mathbf{x}, t) = \int \delta\left(\psi - \phi(\mathbf{x}', t)\right) G(\mathbf{x}, \mathbf{x}') d^3\mathbf{x}'. \quad (2.25)$$

It follows that the *Favre filtered density function* (FFDF) can be expressed as:

$$\bar{\rho}\mathcal{F}(\phi; \mathbf{x}, t) = \int \rho(\mathbf{x}', t)\delta\left(\psi - \phi(\mathbf{x}', t)\right) G(\mathbf{x}, \mathbf{x}') d^3\mathbf{x}'. \quad (2.26)$$

The FFDF is function of the filter and especially of its filter length.

Consequently the filtered species and energy source terms in every cell can be determined from the integration over the composition space[2] of the FFDF:

$$\widetilde{\dot{\omega}}(\mathbf{x},t) = \int \dot{\omega}(\psi)\mathcal{F}(\psi;\mathbf{x},t)d\psi, \tag{2.27}$$

as well as any filtered scalar, ϕ, (e.g. temperature, species mass fraction,...):

$$\widetilde{\phi}(\mathbf{x},t) = \int \phi(\psi)\mathcal{F}(\psi;\mathbf{x},t)d\psi. \tag{2.28}$$

In order to simplify the notation, the temporal and spatial variation will be dropped from now on.

From Equation (2.27), one can conclude that the combustion model must provide two elements to close the source terms: the filtered density function in every cell and the chemical source terms as a function of the composition. Before describing those two aspects of the turbulent combustion model, key variables will be defined. Then a short review of the common ways to handle the computation of the chemistry source terms in CFD will be exposed. And finally the different solutions to describe the filtered density function will close this chapter.

[2] The composition space is here extended to contain all species, the temperature and the pressure.

2.2 Key-variables definitions

This paragraph introduces common scalars and concepts helping the description of reactive flows. Of particular interest are the parameters characterizing the mixing between different flows and the ones allowing to describe the ignition path in turbulent auto-ignition cases.

2.2.1 Mixture fraction

For security reasons, combustion systems usually keep fuel and oxidant in separated tanks and mix them only at the latest time, namely the entrance of the combustion chamber. Therefore the mixing of the fuel and oxidant and singularly its control play a major role in the dynamics and the stabilization of the flames.

Classically, mixing is described by one or more passive scalars, called "mixture fractions". The strict definition of a passive scalar in reactive flows is based on the element conservation instead of the conservation of a specific species. Indeed those are consumed and produced depending on the local chemistry on the contrary of the element that are conserved. The mass fraction of an element e (e.g. the carbon element, C), Y_e, is defined as [93]:

$$Y_e = \sum_{k=1}^{N_s} a_{ke} \frac{W_e}{W_k} Y_k, \tag{2.29}$$

where a_{ke} is the number of elements e in the species k and W_i, the element or molecular weight.

The corresponding mixture fraction, Z_e is then defined by normalizing Y_e with its values at the fuel and oxidant inlets.

$$Z_e = \frac{Y_e - Y_e^{oxidant}}{Y_e^{fuel} - Y_e^{oxidant}}. \tag{2.30}$$

If there are L (with $L > 2$) inlets with different compositions, L mixture fractions can be defined. For example for the mixture at the inlet i:

$$Z_e^{\text{inlet } i} = \frac{Y_e - \sum_{j \neq i}^{L} Y_e^{\text{inlet } j}}{Y_e^{\text{inlet } i} - \sum_{j \neq i}^{L} Y_e^{\text{inlet } j}}. \tag{2.31}$$

Two singular values are of interest, the "stochiometric mixture fraction" and the so-called "most reactive mixture fraction":

- The stochiometric mixture fraction, Z_{st}, corresponds to the stochiometric mixing of the oxidant and the fuel. At that value of mixing, a complete combustion implies the fully consumption of fuel and oxidant; i.e. the burnt gases consist only of burnt products and inert gases.
- The most reactive mixture fraction, Z_{MR}, is of particular importance for auto-igniting flows. It corresponds to the mixture fraction (and therefore the composition) for which the chemistry is the most active. This is usually related to the mixture resulting in the minimum ignition time. A priori the corresponding composition can be lean or rich. But in practice, auto-ignition occurs often when mixing a hot oxidant with cold fuel, which makes the chemistry more reactive at lean mixture due to the higher temperature.

2.2.2 Scalar dissipation rate

In order to highlight the provenance and the signification of the "scalar dissipation rate" χ the equation for the mixture-fraction subgrid-scale variance will be established first.

The transport equation for the mixture fraction Z is:

$$\frac{\partial \rho Z}{\partial t} + \frac{\partial \rho u_i Z}{\partial x_i} = \frac{\partial}{\partial x_i}\left(D_Z \frac{\partial Z}{\partial x_i}\right), \tag{2.32}$$

where D_Z is the diffusion coefficient of Z.

By multiplying by $2Z$ and using the chain rule on the diffusion term, the conservation equation for Z^2 is formed:

$$\frac{\partial \rho Z^2}{\partial t} + \frac{\partial \rho u_i Z^2}{\partial x_i} = \frac{\partial}{\partial x_i}\left(D_Z \frac{\partial Z^2}{\partial x_i}\right) - 2D_Z \frac{\partial Z}{\partial x_i}\frac{\partial Z}{\partial x_i}. \tag{2.33}$$

The last term of Eq. (2.33) is the scalar dissipation rate χ_Z:

$$2\rho\chi_Z = 2D_Z \frac{\partial Z}{\partial x_i}\frac{\partial Z}{\partial x_i}. \tag{2.34}$$

This term is a sink term decreasing the variation of the scalar up to homogeneity (the gradient will then be zero). Its role to decrease the fluctuations appears more clearly in the equation for the subgrid-scale variance. For example, the mixture-fraction *subgrid-scale variance*, $\widetilde{V}_z = \widetilde{Z^2} - \widetilde{Z}^2$ is

$$\frac{\partial \bar{\rho}\widetilde{V}_z}{\partial t} + \frac{\partial \bar{\rho}\widetilde{u}_i\widetilde{V}_z}{\partial x_i} = \frac{\partial}{\partial x_i}\left(\frac{\mu^{\text{sgs}}}{Sc_t}\frac{\partial \widetilde{V}_z}{\partial x_i}\right) + \frac{\partial}{\partial x_i}\left(D_Z\frac{\partial \widetilde{V}_z}{\partial x_i}\right) + 2D_Z\frac{\partial \widetilde{Z}}{\partial x_i}\frac{\partial \widetilde{Z}}{\partial x_i} - 2D_Z\widetilde{\frac{\partial Z}{\partial x_i}\frac{\partial Z}{\partial x_i}} + 2\frac{\mu^{\text{sgs}}}{Sc_t}\frac{\partial \widetilde{Z}}{\partial x_i}\frac{\partial \widetilde{Z}}{\partial x_i}. \tag{2.35}$$

The first term on the right is the transport due to the unresolved fluctuations, the second and third ones are the molecular diffusion effects, the fourth one is the filtered scalar dissipation rate and the latest the production term.

The filtered scalar dissipation rate is classically modeled as:

$$2\bar{\rho}\widetilde{\chi}_Z = 2D_Z\widetilde{\frac{\partial Z}{\partial x_i}\frac{\partial Z}{\partial x_i}} = 2D_Z\frac{\partial \widetilde{Z}}{\partial x_i}\frac{\partial \widetilde{Z}}{\partial x_i} + C\frac{\mu^{\text{sgs}}}{Sc_t}\frac{\widetilde{V}_z}{\Delta^2}, \tag{2.36}$$

with the model constant $C = 2$.

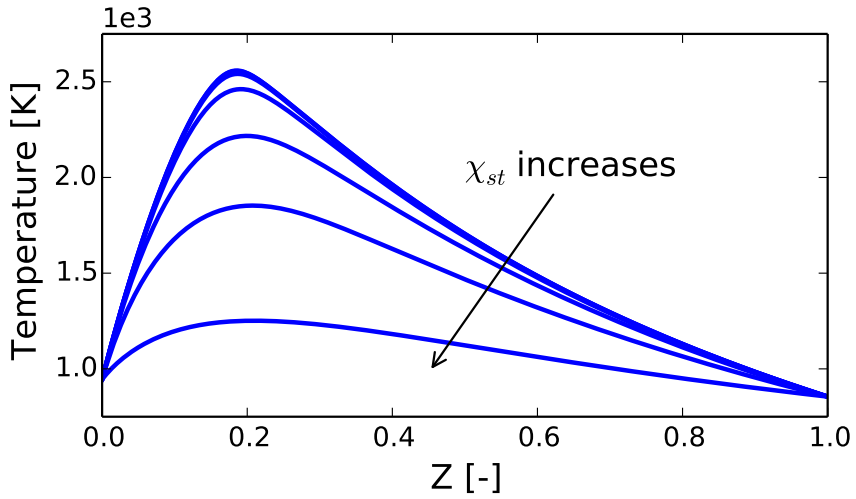

Figure 2.2: Temperature profiles of a counter-flow flame for different values of scalar dissipation rates (0.01, 0.1, 1, 10, 100, 1000 and χ_q). The oxidant is standard air at 955K and the fuel is diluted hydrogen ($Y_{\text{H}_2} = 0.14$ and $Y_{\text{N}_2} = 0.86$) at 855K. The simulation were carried out at atmospheric pressure.

The scalar dissipation rate plays and important role in the modeling of non-premixed flames. If one considers the simple counter-flow flames configuration in which oxidant is injected on one side and fuel on the other side,

the steady-state distribution of all thermodynamical and chemical properties (temperature, species mass fractions,...) on the axis between the two injectors is entirely defined from two parameters: the mixture fraction and the scalar dissipation rate. This is the basis of the flamelets model of Peters [88, 89]. In that model, the species mass fraction conservation equations for a laminar counter-flow flame reduce to:

$$\rho\frac{\partial Y_k}{\partial t} - \frac{1}{2}\rho\chi_Z\frac{\partial^2 Y_k}{\partial Z^2} = \dot{\omega}_k. \tag{2.37}$$

The mixture fraction is related to the position on the central axis; the oxidant injector corresponds to $Z = 0$ and the fuel injector to $Z = 1$. The scalar dissipation rate is linked to the strain rate which depends on the injection velocities of the fuel and the oxidant. Assuming constant density, the scalar dissipation rate for a one-dimensional strained flame as an analytical solution [93]:

$$\chi_Z = \frac{a}{\pi}\exp\left[-2\left(\mathrm{erf}^{-1}\left[1-2Z\right]\right)^2\right], \tag{2.38}$$

where a is the strain rate.

In order to solve Equation (2.37) the scalar dissipation rate distribution must be known. This is usually done by prescribing its value at the stoichiometric mixture fraction, Z_{st}. Then using Equation (2.38), the distribution of χ_Z with Z is given by:

$$\chi_Z = \chi_{st}\exp\left[2\left(\left[\mathrm{erf}^{-1}\left(1-2Z_{\mathrm{st}}\right)\right]^2 - \left[\mathrm{erf}^{-1}\left(1-2Z\right)\right]^2\right)\right]. \tag{2.39}$$

As can be seen in Figure 2.2, the temperature profile decreases with the raise of the scalar dissipation rate. Eventually, extinction of the flame will occur for the so-called "quenching scalar dissipation rate", χ_q. But this is not a threshold between χ associated with a burning flame solution and χ for which only non-reacting solution exists. Indeed there is an "ignition scalar dissipation rate", $\chi_i < \chi_q$, below which only the burning flame exists. For intermediate values, both reacting and non-reacting solution can exist. This is usually highlighted by drawing the maximal temperature of the steady flamelet versus the scalar dissipation rate at stoichiometric conditions (see for example Figure 2.3).

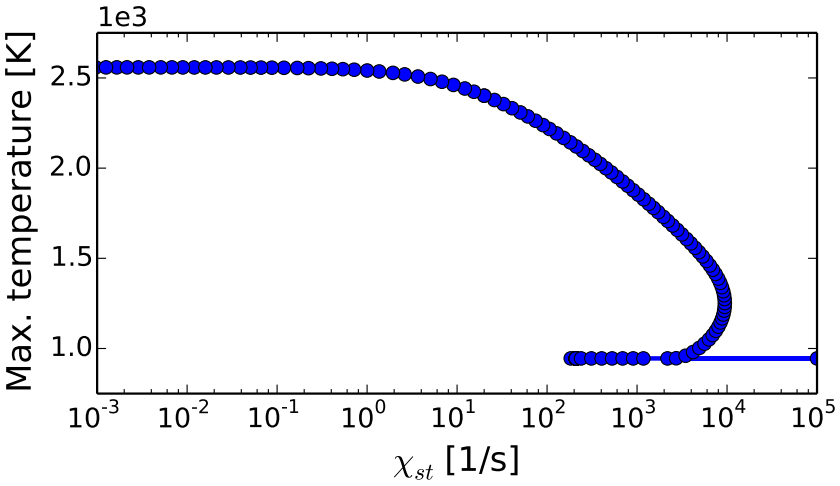

Figure 2.3: Maximal temperature as a function of the scalar dissipation rate at stoichiometric conditions. The mixture used was at atmospheric pressure with standard air as oxidant at 955K and diluted hydrogen ($Y_{H_2} = 0.14$ and $Y_{N_2} = 0.86$) at 855K as fuel.

2.2.3 Progress variable

The completion of the combustion can be monitored using a "reaction progress variable", Y_c. The concept was first used in models for premixed flames in which the usual definition was based on the temperature; $Y_c = \frac{T-T_u}{T_b-T_u}$. It takes the value of 0.0 in unburnt gas (subscript u) and 1.0 in burnt gas (subscript b).

The definition was later extended for partially premixed flames by defining the progress variable as a linear combination of species evolving monotonically with the combustion completion; e.g. for a mixture of methane and air, a possible definition can be $Y_c = Y_{CO} + Y_{CO_2}$.

Unfortunately in the latter case the scalar varies between limits function of the mixture. To compare the progression of the reaction independently of the local mixture, the progress variable can be normalized to take values between 0.0 and 1.0 : $C = \frac{Y_c-Y_{c,init}}{Y_{c,eq}-Y_{c,init}}$ in which $Y_{c,init}$ is the value of Y_c in the unburnt mixture and $Y_{c,eq}$ the one at equilibrium. The two latter parameters are function of the mixture fraction in case of partially premixed flames. Consequently the transport of the *non-normalized* progress variable must be used for partially and non-premixed flames. Its normalized form can be transported solely for premixed cases.

2.3 Chemistry models

The precise computation of the chemistry is by itself a challenge. Indeed a simple phenomena as the combustion of hydrogen in the air implies already a complex mechanism of 19 reactions and 9 species. The description of combustion for more realistic fuels like methane or n-heptane contains tens of species and hundreds of reactions; e.g. [105, 118]. Consequently the resolution of detailed chemistry mechanism for classical LES is usually prohibitively expensive. Therefore some modeling and hypothesis are required to reduce the computational cost of the chemistry calculations.

2.3.1 Chemistry models in practice

In the past, the main approach to decrease the computational time needed by the chemistry was the reduction of the chemical mechanism. Indeed, depending on the operating conditions some hypothesis on the importance of reactions and species can be done to reduce the number of reactions and species. Using curve fitting, the combustion mechanism can even be reduced to a single "global" reaction yielded satisfactory results. Methane is probably the gas for which the most reduced mechanisms have been developed [46, 51, 106].

The major drawbacks of those reduced mechanisms are:

1. The work required to build them
2. Their application range
3. Their ratio cost over accuracy

Indeed, although some automatic algorithms exist, the research and choice of the best model still require lots of time and strong experience to be derived. The resulting mechanisms are usually valid for a restrained range of pressure and temperature that are often not matching burner conditions — strong reductions can usually be obtained only for high temperature see e.g. [118]. And even by selecting one reduced mechanism tuned for the conditions of interest, the computational cost can still be high in comparison with the flow resolution.

Simultaneously to the development of reduced mechanisms, the combustion community moved forward towards simulations of "flames" featuring more complex phenomena such as extinction, auto-ignition spots, lifted flames,... . Most of the recent experiments analyze reactive configurations with strong interaction between turbulence and chemistry. Thereby extreme simplifications of the chemistry mechanism are usually inaccurate as the capture of key radical species becomes crucial. The community was therefore in need for new ways to reduce the cost of the chemistry, easier to use and more accurate.

At the beginning of the 90's the concept of tabulated chemistry appears. The initial idea was proposed by Bradley et al. [7]. The concept separates the resolution of the chemistry and physical properties from the CFD simulation. For instance Bradley et al. used laminar flamelets to generate look-up tables for the species and the heat release. The values were retrieved from a dimensionless reaction progress variable based on the rising temperature.

A more rigorous establishment of the method was provided by the so-called *Intrinsic Low-Dimensional Manifold* (ILDM) theory developed by Maas and Pope [73]. Remarking that time scales of the chemistry range usually from 10^{-9} to 100 s, the ILDM decoupled automatically the fastest time scales of the large ones. Only the latter are kept as they are driving the reactions and forming in the composition space an attracting manifold of the reaction trajectories (see Figure 2.4). That hyper-surface can be described with few parameters (usually some species mass or mole fractions see for example Figure 2.4). Therefore the evolution of the chemistry reduced to motion on the manifold that can be stored in look-up tables. Any chemical source term can then be retrieved quickly from those tables.

The major restriction of the ILDM method is the range of temperature. Indeed at low temperature the chemical kinetics is very stiff. And most of the time scales are large. Therefore the dimensions of the manifold are important and result in huge look-up tables. O. Gicquel et al. [33] tackles that problem by prolongating the ILDM in the low temperature range based on laminar premixed free flame. This new method, called *Flame Prolongation ILDM* (FPI), is similar to the *Flamelet Generated Manifold* (FGM) proposed by van Oijen et al. [112].

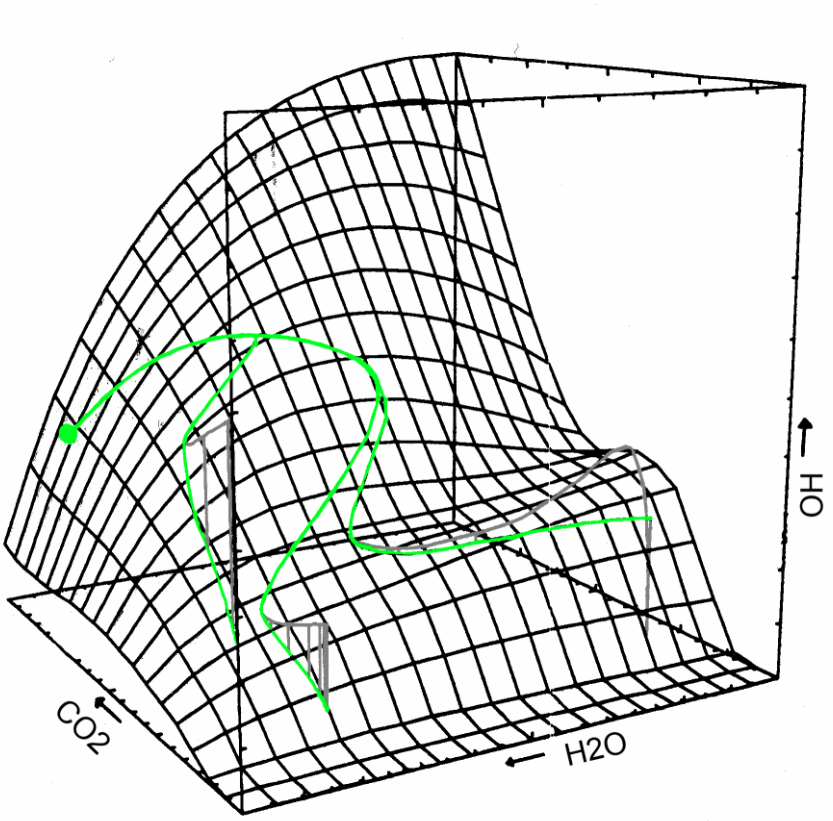

Figure 2.4: Plot of a two dimensional manifold with some trajectories (in gray) and their projection on the manifold (in green) for the specific mole fraction of OH. The big point represents the equilibrium value. This plot is a modified version of Fig. 9 (b) in [73].

The major difference of FPI/FGM with ILDM comes from the generation method of the manifold. Indeed when ILDM uses the eigenvalues of the reaction mechanism to determine the manifold, the manifold of FPI/FGM results from canonical "flames" (laminar premixed free flames, counter-flow flames, homogeneous reactors,...). As a consequence FPI/FGM should be applied only to flames having the same balance between the convection, diffusion and reaction terms as the canonical test case used; e.g. it is not advisable to apply homogeneous reactors based look-up tables on diffusion flames.

As most of the experiments and industrial systems in combustion operate at low temperature, the method FPI/FGM should be preferred to ILDM. And as fewer hypotheses are done in FPI/FGM in comparison to reduced chemistry mechanisms, the range of application and the accuracy of FPI/FGM

are generally higher. For those two reasons, the chemistry model chosen is the FPI/FGM method, known also as tabulated chemistry.

The tabulated chemistry results in a projection of the composition space to a low-dimension parameter space, and Equation (2.27) simplifies greatly. Indeed if we assume that the mixture fraction and the progress variable are such two parameters, Equation (2.27) becomes

$$\begin{aligned} \widetilde{\dot{\omega}}(\mathbf{x},t) &= \int \dot{\omega}(\psi)\mathcal{F}(\psi)d\psi \\ &= \iint \dot{\omega}(Y_c,Z)\mathcal{F}(Y_c,Z)dY_c dZ. \end{aligned} \tag{2.40}$$

2.3.2 Pollutant chemistry

One of the key information expected from numerical simulations of reactive flows is a quantitative prediction of the pollutants. Amount those unwanted species oxides of nitrogen, in particular NO and NO_2 (called also NO_x[3]), are of primary concern. Indeed those species react with the vapor water to form nitric acid responsible for the acid rain. They also form with other chemicals small particles causing or worsening respiratory diseases. And finally NO_x is an ozone precursor; the ozone having also negative impact on the human respiratory organs [23]. Consequently the NO_x emissions of combustors are strictly regulated; the maximal concentration allowed is reduced regularly in major countries.

The formation of NO during the combustion of a fuel is ruled by four mechanisms: the fuel NO_x, the nitrous oxide [74], the Zeldovich (or thermal) [117] and the Fenimore (or prompt) [24] mechanisms [94, 102]. If the fuel contains nitrogen atoms, their oxidation will create fuel NO_x. The second one denotes of the conversion of nitrous oxide to NO. The third is linked to the direct oxidation of nitrogen molecules. Its name comes from the high temperature sensitivity of that mechanism (a slight rise of the temperature results in a high increase of NO). The last one, called prompt, occurs in the very front of the flame. It results from the fixation of N_2 by hydrocarbon fuels that will be later converted to NO.

[3] NO_x is a generic term defining the group of species NO and NO_2.

Those mechanisms are not of equal importance. But their respective strengths depend on the conditions — especially on the fuel concentrations and pressure. For example for lean mixtures at atmospheric pressure, the nitrous oxide and thermal paths are of similar order with the prompt being of less importance. But at lean condition and high pressure (typical of modern combustion chambers), the nitrous oxide path is the major one followed by the thermal path, the prompt mechanism being unimportant.

In the past, models took advantage of that to focus on the computation of relevant mechanisms only. Consequently the early NO_x model were composed of reactions for some of the 4 mechanisms; often reduced to the driven reactions. For example, as the radical N is highly reactive, a quasi-steady state assumption can be made. Therefore the Zeldovich mechanism can be approximated by its rate limiting step (the dissociation of N_2 molecules):

$$\frac{dX_{\mathrm{NO}}}{dt} = 2k_1 X_{\mathrm{N_2}} X_{\mathrm{O}}, \tag{2.41}$$

where k_1 is the rate constant of the initiation step.

As the amount of NO_x produced is typically some orders smaller than the main species, the thermodynamics of a reactive flow is barely modified by the NO_x chemistry. Therefore most of those models were developed as post-processor, evaluating the pollutant from the converged simulation of the flame.

Thereby they could be used with new chemistry models like the tabulated chemistry. But the accuracy allowed by the tabulated chemistry will be wasted. In addition, a prediction model based on look-up tables will be more coherent as the basis for the combustion and pollutant chemistry will be identical. Unfortunately the chemical time scales of the NO_x ranges from time scales similar to the one of the combustion to time scales far higher. To overcome this problem, similarly to ILDM, a new dimension (usually Y_{NO}) can be added to the table space. However the introduction of Y_{NO} raised some troubles to generate the chemical tables. Zoller et al. [119] first generate the combustion tables based on flamelet computation in a 3D parameters space: mixture fraction, scalar dissipation rate, and radiation heat losses. Then for each point of that table, a homogeneous reactor was set at the temperature and pressure of the 3D table; the composition being the one of the table except that all species containing nitrogen (other than N_2)

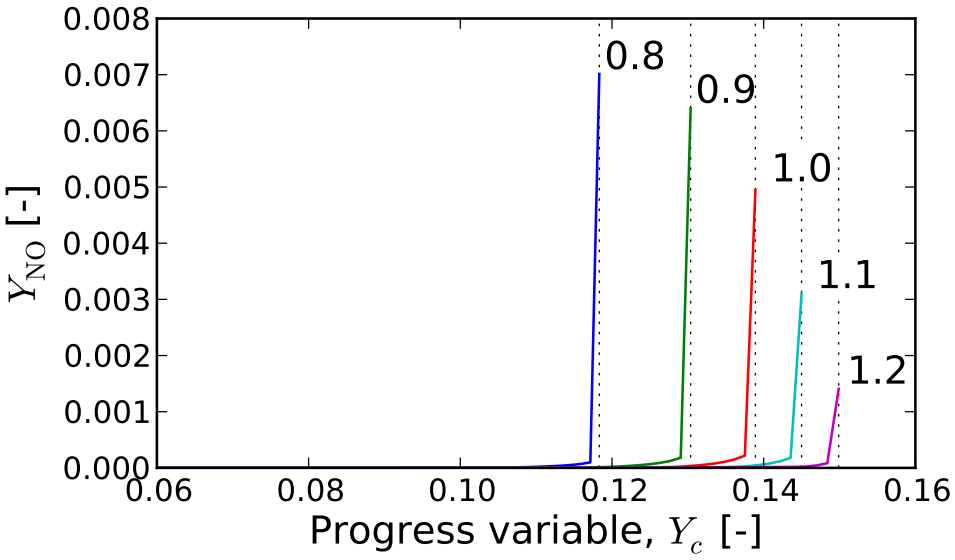

Figure 2.5: Variation of NO mass fraction with the progress variable for different equivalent ratios of methane-air mixture at atmospheric pressure. The tabulated data are used to plot these curves. The main variation of Y_{NO} occurs for Y_c close to Y_c^{eq}. The latter is highlighted by the vertical dashed lines.

are set to zero. Then from the reactors computations, the NO source term were tabulated as a function of Y_{NO}. And the resulting table for $\dot{\omega}_{NO}$ had consequently 4 dimensions. That method is limited to flame with moderate NO concentration as the chemical equilibrium composition will be different of the one obtained from the flamelet calculation.

Another disadvantage is the increased size of the table. Indeed, using the same example, if the 3D table has 202 points in mixture fraction dimension, 22 in scalar dissipation and 32 in radiation heat losses, its size is 1.1 Mo. The fourth dimension is discretized in 196 points, bringing the table size to 223 Mo. Although this number is acceptable for a modern computer, the reader has to remember that the look-up table must be stored as many time as the number of processors used to carry out the simulation. Therefore the huge increase of working memory for the computation of a minor species can be questioned.

In this work, an original method based on look-up tables with a special treatment in the burnt products, where NO is unrelated to the progress variable, was devised. That new model will be described in Section 3.2.

2.4 Turbulence-chemistry interaction

As said previously, the conservation equations are closed if the composition Favre filtered density function can be determined in every cell at every time. As for any other variable a transport equation for the FFDF can be derived [37] (see Appendix B for the derivation of the equation):

$$\begin{aligned}\frac{\partial \bar{\rho}\mathcal{F}(\psi)}{\partial t} &+ \frac{\partial \bar{\rho}\tilde{u}_i\mathcal{F}(\psi)}{\partial x_i} - \frac{\partial}{\partial x_i}\left(\bar{\rho}\tilde{u}_i - \bar{\rho}\left\langle u_i|\psi\right\rangle_\Delta\right)\mathcal{F}(\psi) \\ &= -\frac{\partial}{\partial \psi_k}\left\langle \frac{\partial}{\partial x_i} D_k \frac{\partial \phi_k}{\partial x_i}\middle| \psi \right\rangle_\Delta \mathcal{F}(\psi) + \frac{\partial}{\partial \psi_k}\bar{\rho}\dot{\omega}_k\mathcal{F}(\psi). \quad (2.42)\end{aligned}$$

The first term is the temporal variation. The two others terms on the left hand side are the convective transport terms due to the filtered and the subgrid-scale velocities. On the right hand side are the terms modifying the FFDF in composition space due to the molecular mixing and reactions. The latter term is closed. But the former is not and its closure is still an active area of research.

The solution of the transport equation can be done using either a Lagrangian or an Eulerian approach. The "Lagrangian particles method" will be described first. Then the different possibilities to model the FFDF using Eulerian fields will be presented.

2.4.1 Lagrangian approach

Historically the *Lagrangian method* is the most developed to transport the joint one-point one-time probability density function. It relies on the transport of particles concurrently with the solution of the conservation equations. Those particles carry a composition and are therefore a realization of the joint-PDF. The local joint-PDF can be approximated by looking at the composition of all particles contained in the cell.

The main advantage is the possibility to transport PDF's of any shape. But the disadvantages are numerous:

- Use of Lagrangian solver in parallel with Eulerian solver: high computational cost for interpolating from Eulerian fields to particle positions

Advantages	Challenges
PDF of any shape	Coupling cell/particle
Coupling with detailed chemistry	Micro-mixing closure
Simple particles equation	Valid statistic in all cells

Table 2.1: Pros and cons of the Lagrangian approach.

and vice-versa, troubles to manage the boundary conditions, dispersion term due to the sub-grid scales/turbulent velocities...

- The closure of the molecular mixing term is crucial and not trivial. This is reflected by the number of publications on the subject (see Meyer and Jenny's review [84]).
- The statistical convergence is difficult to achieve. Indeed the convergence depends on the number of particles per cell. Unfortunately the density of particles can be locally too low as it is unknown a priori – although some model allows the duplication of particles to ensure a minimal density of particles per cell.

This method is quite established now. And many accurate simulations have been performed based on particle transport in both RANS and LES. For example, the lifted Berkeley flames were successfully simulated in RANS by Masri et al. [81] and Gordon et al. [35, 36].

2.4.2 Eulerian approach

In the framework of LES, for which the cell size is very small and thus requires more particles than in RANS, the Lagrangian method has an important computational cost that is barely affordable in realistic geometries. To reduce it, models using Eulerian fields should be preferred. Some of them will be presented here after.

2.4.2.1 Presumed PDF

The computational cost can be drastically reduced by presuming the shape of the joint-PDF. Indeed distributions like the β-PDF or the Gaussian PDF

are fully characterized by their mean and variance. Therefore, the transport of only two additional fields allows the determination of one dimension of the joint-PDF.

Going back to the example of a composition space being defined by one mixture fraction and one progress variable, the joint-PDF has two dimensions. If independence can be assumed between those two parameters (Eq. (2.43)), the full joint-PDF can be modeled with for example a double β-PDF (Eq. (2.44)). Hence four additional fields must be transported in the simulation. In this case, Equation (2.40) can be simplified further.

$$\begin{aligned}
\widetilde{\omega}_k &= \iint \dot{\omega}_k(Y_c, Z)\mathcal{F}(Y_c, Z)dY_c dZ \\
&= \iint \dot{\omega}_k(C, Z)\mathcal{F}_C(C)\mathcal{F}_Z(Z)dC dZ \qquad (2.43) \\
&= \iint \dot{\omega}_k(C, Z)\beta_C(C; \widetilde{C}, \widetilde{V_c})\beta_Z(Z; \widetilde{Z}, \widetilde{V_z})dC dZ \qquad (2.44)
\end{aligned}$$

As the progress variable is not independent of the mixture fraction, a variable change is made from the progress variable Y_c to its normalized version $C = Y_c/Y_{c,eq}$, that supposedly is independent of the mixture fraction.

Combined with a tabulated chemistry model, the presumed multidimensional β-PDF is one of the most used model for LES. It requires the determination of 4 fields [19]:

- The mixture fraction, $\widetilde{Z}$,
- The mixture fraction variance, $\widetilde{V_z}$,
- The progress variable, $\widetilde{Y_c}$,
- The second moment of the progress variable distribution, $\widetilde{Y_c^2}$.

When the β-PDF for the mixture fraction is retrieved directly from the transported fields, the β-PDF for the normalized progress variable requires some intermediate steps. First the equilibrium values of the progress variable $\widetilde{Y}_{c,eq}$ and its second moment $\widetilde{Y_{c,eq}^2}$ should be found in a table function

of the mixture fraction and its variance. Then the normalized progress variable and its variance can be determined:

$$\widetilde{C} = \frac{\widetilde{Y_c}}{\widetilde{Y_{c,eq}}}, \tag{2.45}$$

$$\widetilde{V_c} = \frac{\widetilde{Y_c^2}}{\widetilde{Y_{c,eq}^2}} - \widetilde{C}^2. \tag{2.46}$$

This example shows a combination of two β-PDF's. But other possibilities were also suggested. For example, Pierce and Moin [90, 91] argue that the variance of the progress variable in LES is negligible. Therefore the joint-PDF reduces to the combination of a δ and a β-PDF's.

The computational cost of the chemical properties can be drastically reduced by integrating prior to the simulation the convolution equation (2.44). Unfortunately this results in bigger tables; e.g. when assuming a double-β-PDF, the tables have 4 dimensions instead of 2 for the tables prior to the convolution operation.

When using more than two parameters this can become a real problem, Ribert et al. [98, 99] and Veynante et al. [113] suggest taking profit of the self-similar properties of turbulent premixed flames to decrease the chemical tables size.

Advantages	**Challenges**
Need few additional transport equations	Presumed the shape of the joint-PDF
Very low computation cost of the chemistry	Usually neglect cross-correlations
	Chemistry table of large size

Table 2.2: Pros and cons of the presumed-PDF model.

The Brandt's model for joint-PDF based on Monte Carlo method [10] described in the introduction is part of the presumed-PDF group. Indeed if the statistical error of the Monte-Carlo method is zero, the joint-PDF will be the multi-Gaussian clipped by projection of the non-physical probability space on its boundaries. However in the opposite of the double-β-PDF the effect of the cross-correlations is taken into account.

The other method propose by Brandt et al. [10] based on the mixing of a multi-dimensional δ-peaks distribution falls also in the category of

presumed-PDF. But on the contrary with the *classical* presumed-PDF, the shape of the PDF is not constrained to a mathematical distribution. This is a powerful property allowing to get any shape from multi-dimensional δ-peaks for unmixed cells to Gaussian distribution in highly mixed cells.

2.4.2.2 Conditional Moment Closure - CMC

Klimenko and Bilger [58] developed independently a method based on the transport of the conditional values of species and enthalpy with the mixture fraction. The interest of that idea is particularly obvious in diffusion flames. Indeed, in such flames, the fluctuations of temperature for example are great. But the fluctuations of the temperature conditioned on the mixture fraction are very small (see for example Fig. 1 in [58]). The *Conditional Moment Closure* consequently solves transport equations for the conditional average of the species and enthalpy against the mixture fraction. When neglecting the conditional fluctuations of the density, the conservation equations of $Q_k = \langle Y_k|\eta\rangle_\Delta$ takes the form [3]:

$$\frac{\partial Q_k}{\partial t} + \langle u_i|\eta\rangle_\Delta \frac{\partial Q_k}{\partial x_i} - \langle \chi|\eta\rangle_\Delta \frac{\partial^2 Q_k}{\partial \eta^2} + e_f = \langle \dot{\omega}_k|\eta\rangle_\Delta \qquad \text{for } k = 1...N_s, \quad (2.47)$$

with

$$e_f = \frac{1}{\bar{\rho}\mathcal{P}_Z(\eta)} \frac{\partial}{\partial x_i} \left[\bar{\rho}\mathcal{P}_Z(\eta) \left(\langle u_i Y_k|\eta\rangle_\Delta - \langle u_i|\eta\rangle_\Delta Q_k\right)\right]. \quad (2.48)$$

The first term is the temporal variation of the conditional value, the second is its transport due to the conditional velocity, e_f is the subgrid conditional flux and the last term on the left is due to the molecular transport.

The chemical source term appears on the right hand-side and, if closed at the first order, becomes:

$$\langle \dot{\omega}(\mathbf{Y}, h_s)|\eta\rangle_\Delta \approx \langle \dot{\omega}(\mathbf{Q}, Q_h)|\eta\rangle_\Delta = \dot{\omega}(\mathbf{Q}, Q_h). \quad (2.49)$$

The closure of the other terms can be achieved through different models.

In LES, the conditional velocity is approximated by its unconditional value [3]:

$$\langle u_i|\eta\rangle_\Delta = \widetilde{u_i}. \quad (2.50)$$

The sub-grid conditional flux is given by a classical gradient formula:

$$\langle u_i Y_k|\eta\rangle_\Delta - \langle u_i|\eta\rangle_\Delta Q_k = -D_k^{\text{sgs}} \frac{\partial Q_k}{\partial x_i} \tag{2.51}$$

And finally the conditional scalar dissipation rate can be closed using the *Amplitude Mapping Closure* model (AMC) in which the conditional scalar dissipation rate has a given shape in mixture fraction. This shape is then scaled as a function of the local unconditional scalar dissipation rate, $\tilde{\chi}$:

$$\langle \chi|\eta\rangle_\Delta = \chi_0(\tilde{\chi}) A(\eta). \tag{2.52}$$

In order to reconstruct the filtered value of a scalar in any cell, the PDF for the mixture fraction has to be known; a β-PDF is usually presumed. Finally, the filtered scalar can be computed, using Bayes' theorem:

$$\begin{aligned} \tilde{\phi} &= \int \phi(\psi)\mathcal{F}'(\psi|\eta)\mathcal{F}_Z(\eta)d\psi d\eta \\ &= \int_0^1 \left(\int \phi(\psi)\mathcal{F}'(\psi|\eta)d\psi \right) \mathcal{F}_Z(\eta)d\eta \\ &= \int_0^1 \langle \phi|\eta\rangle_\Delta \mathcal{F}_Z(\eta)d\eta. \end{aligned} \tag{2.53}$$

Advantages	**Challenges**
Preserve the cross-correlation	Important modeling effort
Coupling with detailed chemistry	High computational cost
	Presumed PDF for the mixture fraction
	Difficult to extend to multi-stream mixing

Table 2.3: Pros and cons of the CMC model.

The CMC method has the advantage of preserving the cross-correlation between the composition-space dimensions. Therefore, unlike the presumed-PDF, all species can be transported and a reduced or detailed mechanism can be used to compute the chemistry source terms.

Unfortunately, the conservation equations are much more complicated and require lots of modeling (conditional velocity, scalar dissipation rate,...) in order to close all terms. In addition the cost of the simulation increases sharply as between 30 to 50 conditional moments for all scalars have to be transported to reconstruct its distribution in mixture fraction. Finally, the PDF for the mixture fraction is still assumed.

In order to reduce the computational cost of the CMC method, the CMC equations can be solved on a coarser mesh than the LES mesh. This unfortunately increases the memory cost and makes the implementation of the model more difficult.

More recently, the so-called *0D-CMC* was used successfully – e.g. in [3]. In that case, Equation (2.47) is simplified by removing the flow effects (convection and sub-grid terms). The solution for the scalars (in particular the temperature and the density) can be tabulated as a function of the filtered mixture fraction, its variance, and the scalar dissipation rate. This model is equivalent to the steady flamelet/progress variable method developed by Ihme et al. [41].

Although most of the practical systems imply the mixing between one fuel and one oxidant streams, some systems require additional streams to be simulated. In that case, the CMC starts to show its limits in terms of modeling and assumption.

2.4.2.3 Direct Quadrature Method of Moments - DQMoM

Initially introduced by Fox [28], the *Direct Quadrature Method of Moments* approximates the composition PDF by:

$$\mathcal{F}(\phi;\mathbf{x},t) \approx \sum_{n=1}^{N_E} w_n(\mathbf{x},t) \prod_{k=1}^{N_s} \delta[\psi_k - \phi_{n,k}(\mathbf{x},t)]. \tag{2.54}$$

The composition PDF is represented by N_E *environments* characterized by a weight w_n[4] and a given composition ϕ. Those elements are transported according to:

$$\frac{\partial \bar{\rho} w_n}{\partial t} + \frac{\bar{\rho}\tilde{u}_i w_n}{\partial x_i} = \frac{\partial}{\partial x_i}\left[D^{\text{sgs}}\frac{\partial w_n}{\partial x_i}\right] + \bar{\rho}a_n, \tag{2.55}$$

$$\frac{\partial \bar{\rho} w_n\phi_{n,k}}{\partial t} + \frac{\bar{\rho}\tilde{u}_i w_n\phi_{n,k}}{\partial x_i} = \frac{\partial}{\partial x_i}\left[D^{\text{sgs}}\frac{\partial w_n\phi_{n,k}}{\partial x_i}\right] + \bar{\rho}b_{n,k}. \tag{2.56}$$

[4] The weight is equivalent to a probability and must satisfy $\sum_{n=1}^{N_E} w_n = 1$.

The source terms a_n and $b_{n,k}$ are solutions of an algebraic linear system derived from a set of $M = N_E(N_s + 1)$ empirical moments (usually the lowest-order) [1]:

$$\langle \phi_1^{m_{m1}} \dots \phi_{N_s}^{m_{mN_s}} \rangle_\Delta = \sum_{n=1}^{N_E} w_n \prod_{k=1}^{N_s} \phi_{n,k}^{m_{mk}} \qquad \text{for } m = 1...M, \tag{2.57}$$

to force the environments to follow the equivalent moment transport equations corresponding to a given modeled PDF transport equation.

The source terms a_n are only functions of the mixing model while $b_{n,k}$ depend on the mixing model and the chemical source terms.

Advantages	**Challenges**
Few environments sufficient (2 or 3)	Boundedness not guarantee
Low computational cost	Linear system poorly conditioned
Coupling with detailed chemistry	

Table 2.4: Pros and cons of the DQMoM model.

The DQMoM approach requires low computational resources as a little number of environments (2 or 3) gives acceptable solution. But constraining more moments (implying more environments) is troublesome, as the linear system determining the source terms a_n and $b_{n,k}$ becomes poorly conditioned for higher N_E. An additional consequence of the low N_E is the restriction to simple mixing model.

2.4.2.4 Eulerian Stochastic Fields method - ESF

The first description of the ESF method was introduced by Valino [111]. Later, Sabel'nikov and Soulard [101] carried out a study on the effect of each term in the *Stochastic Partial Differential Equations* (SPDE) used to solve Eq. (2.42). That study was carried out by using a different integration approach (*Stratonovich integration*) than the one of Valino (*Ito integration*). Those two approaches will be described next.

Knowing that in the ESF method the FFDF is decomposed for each dimension of the composition space (in our example the dimension of the space is $N_s = 2$) in N_{sf} stochastic fields:

$$\mathcal{F}(Y_c, Z; \mathbf{x}, t) = \frac{1}{N_{\text{sf}}} \sum_{n=1}^{N_{\text{sf}}} \prod_{k=1}^{N_s} \delta[\psi_k - \xi_{n,k}(\mathbf{x}, t)], \tag{2.58}$$

with $\xi_{n,k}$ denoting the n'th realization of the variable at index k.

Then the filtered value in each cell can be computed using[5]:

$$\widetilde{Y_k} = E\left[\xi_{n,k}\right] = \frac{1}{N_{\text{sf}}} \sum_{n=1}^{N_{\text{sf}}} \xi_{n,k}. \tag{2.59}$$

To present the two integral forms of a SPDE the *general Fokker-Planck equation* in one dimension will be taken as example:

$$\frac{\partial f(x,t)}{\partial t} = -\frac{\partial}{\partial x}[A(x,t)f(x,t)] + \frac{1}{2}\frac{\partial^2}{\partial x^2}[B(x,t)f(x,t)], \tag{2.60}$$

where $f(x,t) = \mathcal{F}(x,t;x_0,t_0)$ is the probability function at a given position and a given time conditioned on the initial conditions, $A(x,t)$ the *drift vector* and $B(x,t)$ the *diffusion matrix*.

That equation is equivalent to the Ito stochastic differential equation:

$$dx = A(x,t)dt + B(x,t)dW(t), \tag{2.61}$$

where $dW(t)$ is a *Wiener process*; i.e. a Gaussian random number with mean equal to zero and variance equal to dt.

In the Stratonovich calculus, the equivalent equation is:

$$dx = \left[A(x,t) - \frac{1}{2}B\frac{\partial B}{\partial x}\right]dt + B(x,t)dW(t). \tag{2.62}$$

The different formulations for SPDE rise because the Riemann-Stieltjes integral is no more applicable; i.e. the result of the integration depends on the point chosen inside the time interval to approximate the value of the function. As shown in Figure 2.6, for the Ito integration the first point of the interval is chosen while Stratonovich selected the mid-point.

[5] $E[X]$ is the expected value of the stochastic variable X.

The Ito formulation has the property of non-anticipation; i.e. the Wiener process value is independent of the diffusion matrix, as the random values are computed independently of the diffusion matrix[6]. The advantage of the Stratonovich formulation is that the integration is identical to the results of the Riemann-Stieltjes integral.

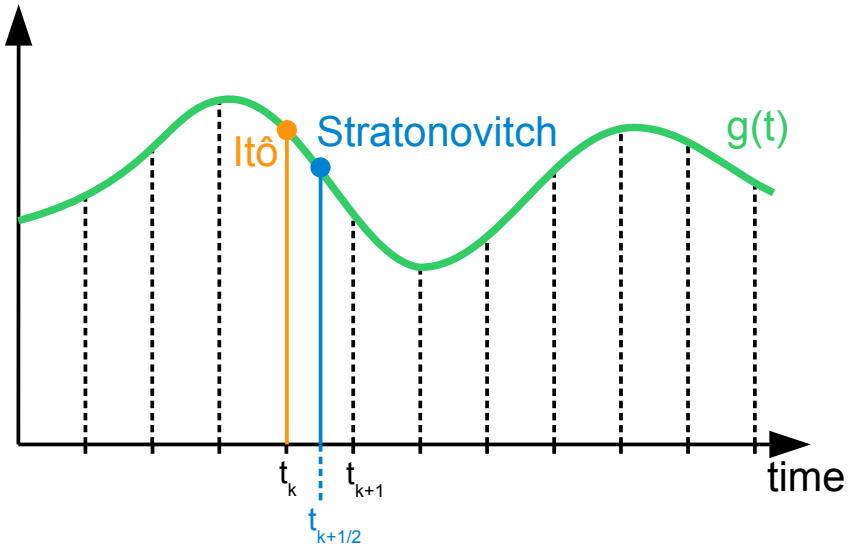

Figure 2.6: Difference between the Ito and the Stratonovich integrals.

The interested reader will find more information about Stochastic Differential Equations in [30].

The two calculi will be applied to Eq. (2.42). But beforehand the modeling used for some terms of that equation will be exposed.

The unresolved fluxes can be computed using the analogy with the diffusive term:

$$\frac{\partial}{\partial x_i}\left(\bar{\rho}\tilde{u}_i - \bar{\rho}\left\langle u_i|\psi\right\rangle_\Delta\right)\mathcal{F}(\psi) = -D_\psi^{\text{sgs}}\frac{\partial\mathcal{F}(\psi)}{\partial x_i}. \tag{2.63}$$

[6] More precisely, C. Gardiner's definition is: "*A function $G(t)$ is called a non-anticipating function of t if $G(t)$ is statistically independent of $W(s) - W(t)$ for all s and t such that $t < s$.*" [30]

If the diffusion in the composition space is modeled using the *Interaction by Exchange with the Mean* (IEM) model [28], the transport equation for a stochastic field is, according to the Ito calculus used by Valino [111]:

$$\begin{aligned} d\xi_{n,k} &= -\tilde{u}_i \frac{\partial \xi_{n,k}}{\partial x_i} dt + \frac{1}{\bar{\rho}} \frac{\partial}{\partial x_i} \left[D_k^{\text{sgs}} \frac{\partial \xi_{n,k}}{\partial x_i} \right] dt + \dot{\omega}_k dt \\ &- \frac{C_\phi}{2\tau_{\text{sgs}}} (\xi_{n,k} - \tilde{Y}_k) dt + \sqrt{2\bar{\rho}^{-1} D_k^{sgs}} \frac{\partial \xi_{n,k}}{\partial x_i} dW_i^n, \end{aligned} \tag{2.64}$$

where the mixing time scale τ_{sgs} is given by $\tau_{\text{sgs}}^{-1} = \frac{\mu + \mu^{\text{sgs}}}{\bar{\rho}\Delta^2}$ and the model constant C_ϕ has typically a value of 2.0. dW_i^n is a vector of Wiener processes varying in time but not in space. It is approximated by a random number equal to $\pm dt^{1/2}$.

The Stratonovich formula[7] is:

$$\begin{aligned} d\xi_{n,k} &= -\tilde{u}_i \frac{\partial \xi_{n,k}}{\partial x_i} dt + \frac{1}{2} \frac{\partial \bar{\rho}^{-1} D_k^{\text{sgs}}}{\partial x_i} \frac{\partial \xi_{n,k}}{\partial x_i} dt + D_k^{sgs} \frac{\partial \bar{\rho}}{\partial x_i} \frac{\partial \xi_{n,k}}{\partial x_i} dt + \dot{\omega}_k dt \\ &- \frac{C_\phi}{2\tau_{\text{sgs}}} (\xi_{n,k} - \tilde{Y}_k) dt - \sqrt{2\bar{\rho}^{-1} D_\psi^{\text{sgs}}} \frac{\partial \xi_{n,k}}{\partial x_i} \circ dW_i^n. \end{aligned} \tag{2.65}$$

The Stratonovich formula shows clearly the advective nature of a SPDE.

The numerical implementation of the SPDE has to be carried out carefully and consistently with the chosen formulation. For instance, the Ito formulation requires the generation of the Wiener term at the beginning of the time step and to advance explicitly in time. In the Stratonovich formulation, the coefficients have to be evaluated at mid-point of the time-step.

Advantages	**Challenges**
Eulerian formulation	Advective nature of the SPDE
Coupling with detailed chemistry	High computational cost
Statistics per cell constant	

Table 2.5: Pros and cons of the ESF model.

As all Eulerian approaches, ESF is quite easy to implement. Unfortunately the advective behavior of the SPDE makes the solver less robust especially as only first order in time can be used. Indeed the stochastic fields are non-continuous in time.

[7] The notation $\circ$ is used to emphasize the difference between the Ito and the Stratonovich formulations.

The joint-PDF being approximated by δ functions inevitably a statistical error appears. The number of stochastic fields (i.e. δ functions) to transport should be high enough to keep that error low. For RANS simulations, Soulard and Sabel'nikov [108] have reached statistical convergence on the mean and variance values transporting at least 50 fields.

In LES most of the authors used 8 or 16 fields. This was confirmed by a validation test presented in Section 4.2.1. The number of fields transported has an important impact on the computational time as the total number of fields to solve is N_{sf} x N_s. So if the number of fields required to reach statistical convergence is high, the computation cost of this method can become a problem.

Due to numerical resolution, the stochastic term can bring the species mass fractions below or above its physical bounds. Therefore a correction should be implemented to ensure the bounding of the scalar. This introduce an additional error on the joint-PDF moment calculation.

2.4.3 Comparison of the PDF transport models

After this review of possible approaches to transport a PDF, a short comparison between the different models supplied by published results will follow to explain the final choice for the joint PDF transport.

In Figure 2.7, an example of PDF for a reduced composition space (i.e. mixture fraction and normalized progress variable) is shown using the previously described models. The presumed PDF is usually very accurate and computationally efficient for composition spaces with one or two dimensions. But the targeting flows to be simulated were multi-streams mixing configurations in which the independence between the composition dimensions cannot be assessed. So the shape of the joint-PDF is unknown and cannot be presumed. Consequently that model was discarded. But for simple mixing, it is definitely a very effective method with a low computational cost.

The CMC model was left aside for similar reasons. Indeed, the transport equations for the conditional values on one mixture fraction are already complicated and require multiple closure models. The addition of a sec-

ond mixture fraction in case of ternary-mixing will increase drastically the complexity of the transport equations as well as the closure models required.

The major drawback of the Direct Quadrature Moment Method is the numerical instability of the algorithm and the possibility to face unphysical distribution of species ($\sum_{k=1}^{N_s} Y_k \neq 1$). In the future this method could become a very competitive method thanks to its low computational cost and high flexibility of the PDF shape.

To be able to model multi-streams mixing with a limited amount of numerical troubles, a Markovian modeling of the PDF was chosen. In a recent publication Jaishree and Haworth [42] compare the Lagrangian method, the

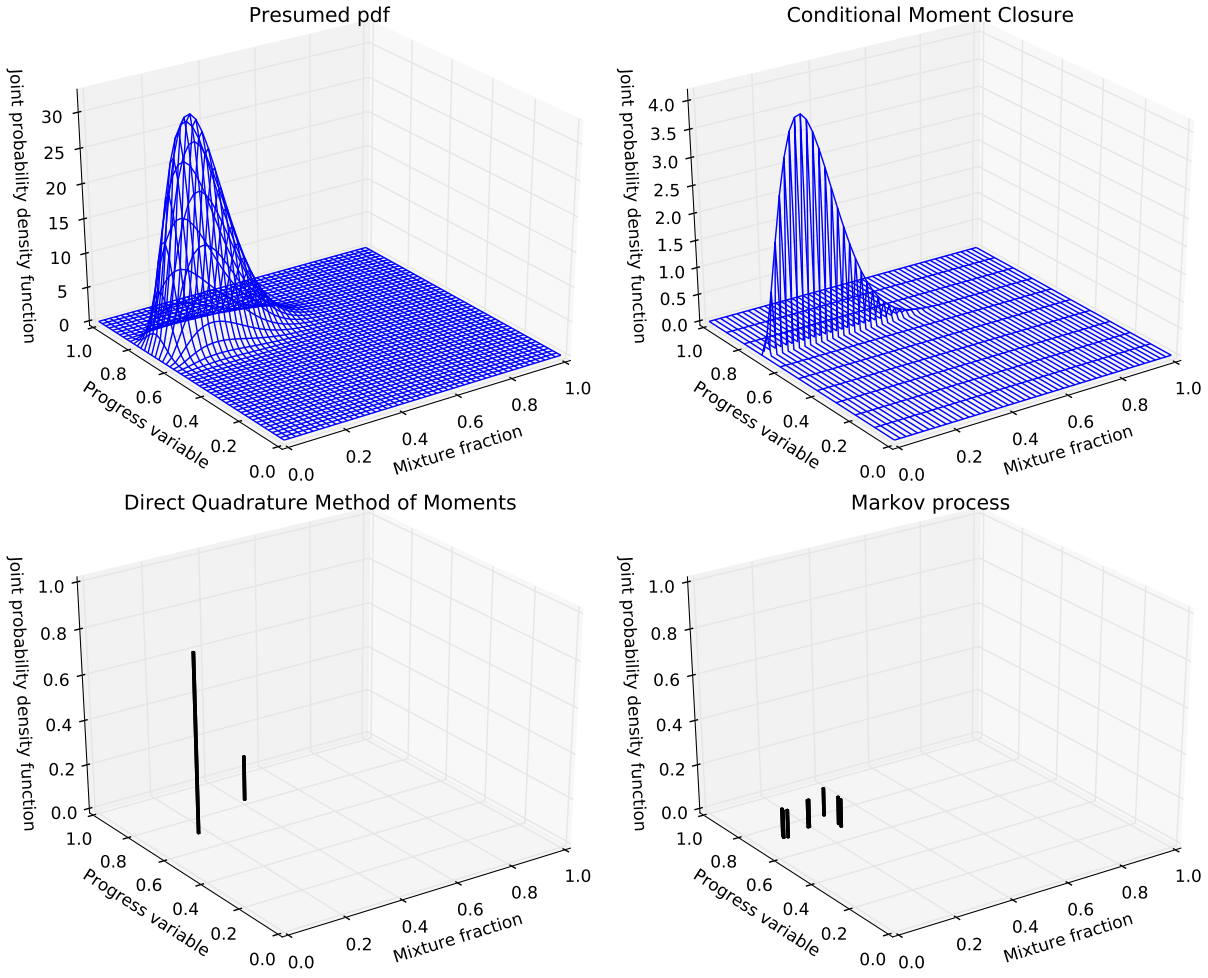

Figure 2.7: Visual comparison of the modeled PDFs. The figures represent from top-left to bottom-right: a double β-PDF, a CMC-PDF, a DQMoM PDF and a Markovian PDF (Lagrangian particles or stochastic fields).

Eulerian stochastic fields and the DQMoM model based on the simulation of the Sandia flames D, E and F using RANS simulation.

Some key conclusions are:

- DQMoM method is the fastest (up to one order of magnitude faster) but has the lowest accuracy (especially when estimating the RMS of the scalars).
- Particles and stochastic fields approach have good and similar accuracy when the number of particles, N_{PC}, per cell is similar to the number of stochastic fields, N_{sf}.
- The turbulent diffusion is modeled by introducing randomness, in physical space for particle methods and in composition space for stochastic fields methods. Consequently for the latter case, some precautions have to be taken to conserve physical compositions.
- The stochastic fields method is more expensive than the particles approach (by approx. 50%). Jaishree and Haworth argue that the computational cost should be similar if the chemistry computation is more costly than the Navier-Stokes equations. But as in this case, they used the "In-Situ Adaptive Tabulation" method [95], the computational cost using particles is only a weak function of N_{PC} when it increases linearly with N_{sf}.
- For LES, the advantage of the particle method may be reduced since less stochastic fields are required. At the same time more problems rise to ensure a minimum number of particles per cells.

From those conclusions, the Eulerian stochastic fields' method is a good option to model accurately the turbulence-chemistry interactions in LES context, and in particular for multi-streams mixing. Moreover, its numerical implementation is fairly easier than for a coupled Lagrange-Euler solver.

2.5 Summary

From this review on chemistry and turbulence-chemistry models, it is possible to choose and develop a model adequate to our problem; namely "auto-ignition in multi-streams mixing turbulent flows". The choice was discussed and carried out by R. Kulkarni [63] guided by the necessity to simulate the reheat combustor in Alstom's GT24/GT26 sequential gas turbine power plant.

This combustor presents the particularity to ignite the fuel using the residual heat of burnt gas coming from the primary chamber (see Figure 2.8). In addition the fuel is shielded by a cylindric film of air. Therefore the auto-ignition is delayed increasing the distance between the flame and the injector. From modeling point of view, the solver should handle three-streams mixing (i.e. 2 mixture fractions). In the Figure 2.8, the proportion of burnt gas are described by the mixture fraction Z_2 and the proportion of fresh fuel by the mixture fraction Z_1. Moreover if one is interested in the cooling effects due to air cooling and heat losses, an additional mixture fraction will be needed as well as one parameter for the heat losses.

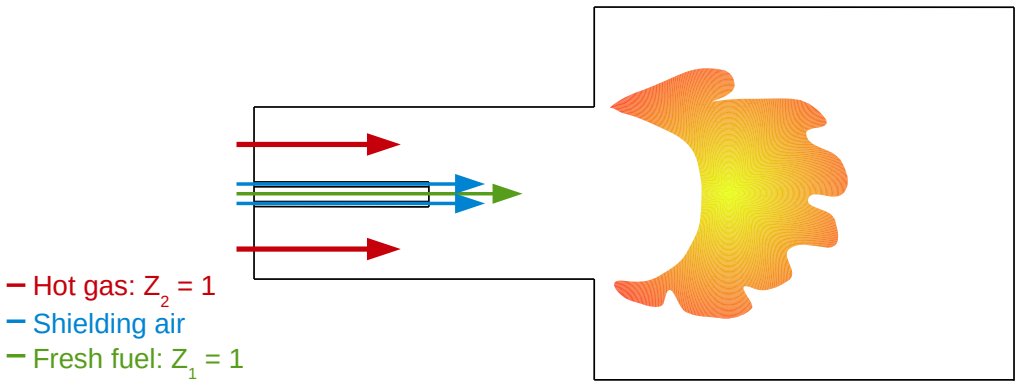

Figure 2.8: Schema of the secondary burner in a sequential burner as used in the Alstom's GT24/GT26 sequential gas turbine.

To summarize the following phenomena should be handled by the model:

- Low computational cost (in comparison with a cold flow LES simulation)
- Applicable in complex geometries

- Flexible number of inlet flows
- Extensible to new phenomena such as heat losses

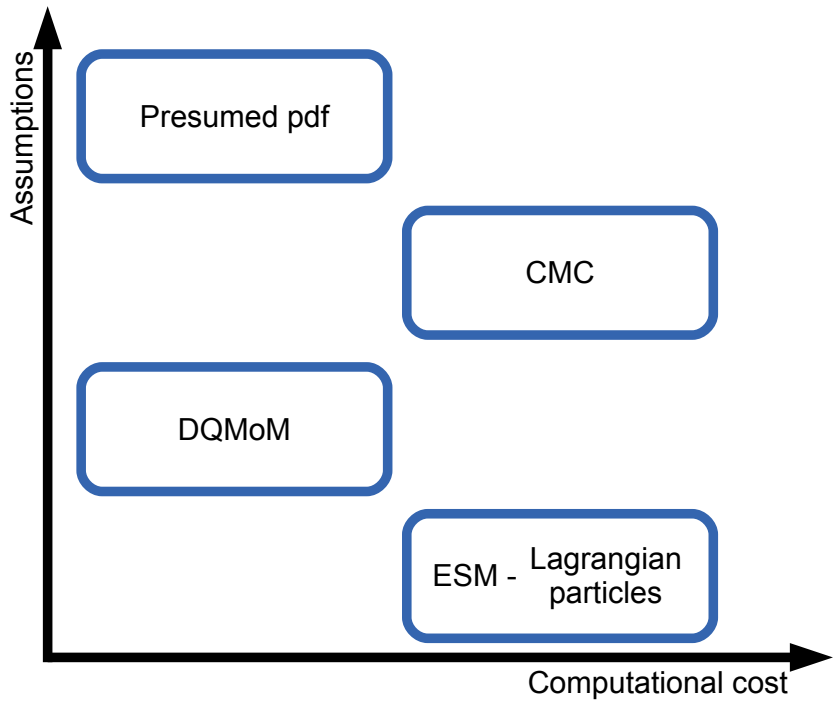

Figure 2.9: Trade-off between the composition PDF models.

Due to the two first requirements, the Lagrangian approach is discarded as its application to LES introduced lots of trouble to maintain an acceptable statistical accuracy at a reasonable computation cost. The third requirement (multi-stream mixing) increases the complexity and modeling effort for the presumed PDF and the CMC models. Therefore they were discarded too. Finally the DQMoM approach is badly conditioned. Eventually the ESF method was chosen. That model provides a good trade-off between computational cost and flexibility/level of assumption as summarized in Figure 2.9.

For the chemistry, the tabulated chemistry ansatz was chosen. Indeed, in comparison with reduced chemistry the computational cost is even lower. In addition tabulated chemistry can model easily auto-ignition while reduced mechanisms usually have troubles to correctly predict the radical build-up during the induction phase.

The combination of the two previous element is called the SFPV model. In the course of this project, it was implemented using the OpenFOAM® toolbox. The implementation is as close as possible to Kulkarni's model, except in the way of species mass fraction source terms calculation. And a new feature has been developed; prediction of NO_x emissions. The model and those two points will be described at length in the next chapter.

3 Model and its implementation

The SFPV model developed by R. Kulkarni [63] combines a tabulated chemistry approach with a composition PDF transported thanks to Eulerian stochastic fields. This chapter will describe in detail its two major aspects: the generation of the look-up tables for the chemistry and the transport equations to solve in addition with the Navier-Stokes system. Then its extension to NO_x modeling will be depicted. The last section will present the code architecture. The code was designed in different modules allowing a great flexibility and extensibility of the solver for future development.

3.1 Combustion Model

3.1.1 Chemistry modeling

When using the tabulated chemistry, the critical point to answer is: Which canonical test case has a similar chemistry as in my CFD simulation? The answer to that question is not straightforward. In the literature [85], tabulation is usually obtained from the following simple test cases:

- Homogeneous reactors [10, 20, 64]: adequate for auto-igniting flames. But it is not valid anymore when the mixture fraction dissipation rate is high [25].

- One-dimensional laminar premixed flame [7, 20, 26]: acceptable for flame propagation.

- Laminar counter-flow flame / (un-)steady flamelets[1] [39, 91]: acceptable for diffusion flame, auto-igniting mixing layers and extinction in which the mixture fraction dissipation rate plays a major role.

[1] This group includes the steady flamelets and the 0D-CMC models.

In this work homogeneous reactors were used (except if mentioned otherwise). Indeed the auto-ignition spots configurations studied here appear to be only weakly influenced by the mixture fraction dissipation rate.

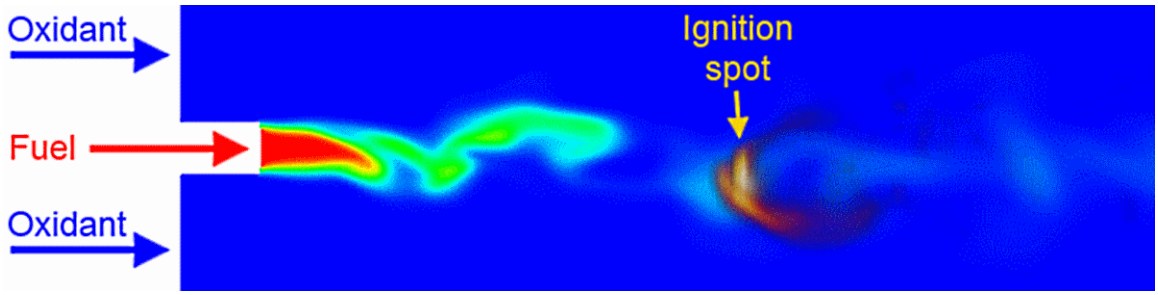

Figure 3.1: Schema of an ignition spot in a partially premixed flow. The background slice represents the mixture fraction (scale from blue to red) on top of which appears the heat release rate in volume rendering.

Once the canonical test case is chosen, the table parameters have to be defined. The set of parameters is the minimal number of variables that define a bijection[2] between the CFD composition space and the tabulated composition space.

A typical snapshot of auto-ignition spots in partially premixed flow is shown in Figure 3.1. Obviously one of the parameters in composition space should be the mixture fraction, $\widetilde{Z}$, describing the mixing between oxidant and fuel. But this parameter alone cannot predict the advancement of the chemistry between pure mixing and equilibrium. Therefore at least one additional parameter should be used. That parameter will be the progress variable, $\widetilde{Y}_c$.

In one cell, the mixture fraction provides with the reference of the homogeneous reactor from which chemical variables should be extracted. And the progress variable gives the reactive mixture state between the initial reactor time (no reaction) and the final reactor time (chemical equilibrium).

Of course in other cases, other parameters could be needed: additional mixture fractions for multi-streams mixing, enthalpy for simulation with heat losses, scalar dissipation rate for diffusion flames, etc... .

[2] By definition "*a bijection is a mapping that is both one-to-one (an injection) and onto (a surjection), i.e. a function which relates each member of a set S (the domain) to a separate and distinct member of another set T (the range), where each member in T also has a corresponding member in S*" [Definition from Oxford dictionary].

Questions	Answers
Canonical case	Homogeneous reactor
Table parameters	Mixture fraction & Progress variable
Progress variable definition	$HO_2 + H_2O$ or $CH_2O + CO + CO_2$

Table 3.1: Summary of the default tabulated chemistry settings for this work.

The last point to answer is the modeling of the parameters. For the mixture fraction, the definition has been presented earlier (see Section 2.2). But the definition of the progress variable is more critical. As it will be shown in Sec. 4.1, for auto-ignition cases, it is primordial to define the progress variable with a combination of product and intermediate species. In this work HO_2+H_2O is used for hydrogen combustion and $CH_2O+CO+CO_2$ for hydrocarbons. In the simulations, the non-normalized progress variable will be transported. Its normalized form is only used to look into the chemistry tables.

The Table 3.1 summarizes the choices made for simulating auto-ignition spots regimes presented in this work.

3.1.2 Turbulence-chemistry interaction

As mentioned previously, the inhomogeneity inside a cell due to the unresolved subgrid-scales has a great influence on the chemistry. The ESF method was chosen to model those fluctuations. In the present case, using a tabulated chemistry based on mixture fraction and progress variable implies the transport of a set of stochastic fields for those two parameters. As described in Section 2.4.2.4, two formulations are possible: the Ito or the Stratonovich formulations. Although Sabel'nikov and Soulard [101] argue that the Stratonovich formulation should be preferred to the Ito formulation, most of the simulations carried out with success in LES [44, 45, 47–50, 64–66] were based on the Ito formulation. The latter formulation was therefore chosen. Another advantage is a simplification of the implementation as the time integration is carried out from the known values of the fields and do not need to be evaluated at the mid-time step.

To close the transport equation only one term requires modeling: the *micro-mixing term*. The IEM model complemented with a *drift term* as suggested by Mc Dermott [83] was chosen. The drift term increases the accuracy for fine LES[3].

The transport equation used is:

$$\begin{aligned} d\xi_{n,k} &= -\tilde{u}_i \frac{\partial \xi_{n,k}}{\partial x_i} dt + \frac{1}{\bar{\rho}} \frac{\partial}{\partial x_i} \left[(D + D_k^{\text{sgs}}) \frac{\partial \xi_{n,k}}{\partial x_i} \right] dt + \dot{\omega}_k dt \\ &- \frac{C_\phi}{2\tau_{\text{sgs}}} (\xi_{n,k} - \tilde{Y}_k) dt + \sqrt{2\bar{\rho}^{-1} D_k^{\text{sgs}}} \frac{\partial \xi_{n,k}}{\partial x_i} dW_i^n, \end{aligned} \tag{3.1}$$

where $C_\phi = 2$ and $\tau_{\text{sgs}} = \frac{\bar{\rho}\Delta^2}{\mu + \mu^{\text{sgs}}}$, following Jones [49]. The diffusivity of the table parameters are identical and determined using Schmidt numbers: $D = \frac{\mu}{\text{Sc}}$ and $D^{\text{sgs}} = \frac{\mu^{\text{sgs}}}{\text{Sc}_t}$. And finally the turbulent dynamic viscosity μ^{sgs} is determined from a dynamic Smagorinsky model for compressible flows based on the Germano model [32]:

$$\mu^{\text{sgs}} = C_d \bar{\rho} \Delta^2 |\tilde{S}|, \tag{3.2}$$

with $\tilde{S}$ denoting the resolved strain rate tensor and C_d being calculated by a least-squares method as proposed by Lilly [70].

An acceptable statistical representation of the PDF was obtained using 8 stochastic fields per table parameters. This is similar to solving simultaneously 8 realizations of the composition space. And this one being defined by two parameters, the combustion model requires the transport of 16 scalars in addition to the classical conservation equations (mass, momentum, species, and energy).

3.1.3 Link between the CFD solver and the combustion model

Figure 3.2 represents the interaction between the chemistry model, the turbulence-chemistry interaction model and the CFD solver.

At the beginning of the time step, the source terms for every pair[4] of stochastic fields are obtained from look-up tables. Then the stochastic fields can

[3] When the filter size is of the order of the Kolmogorov scale.

[4] The stochastic fields are grouped by indexes. For example the source term for the i$^{\text{th}}$ stochastic field of progress variable, $Y_{c,i}(\mathbf{x}, t)$, is given by the value of the table corresponding to the pair $(Z_i(\mathbf{x}, t), Y_{c,i}(\mathbf{x}, t))$.

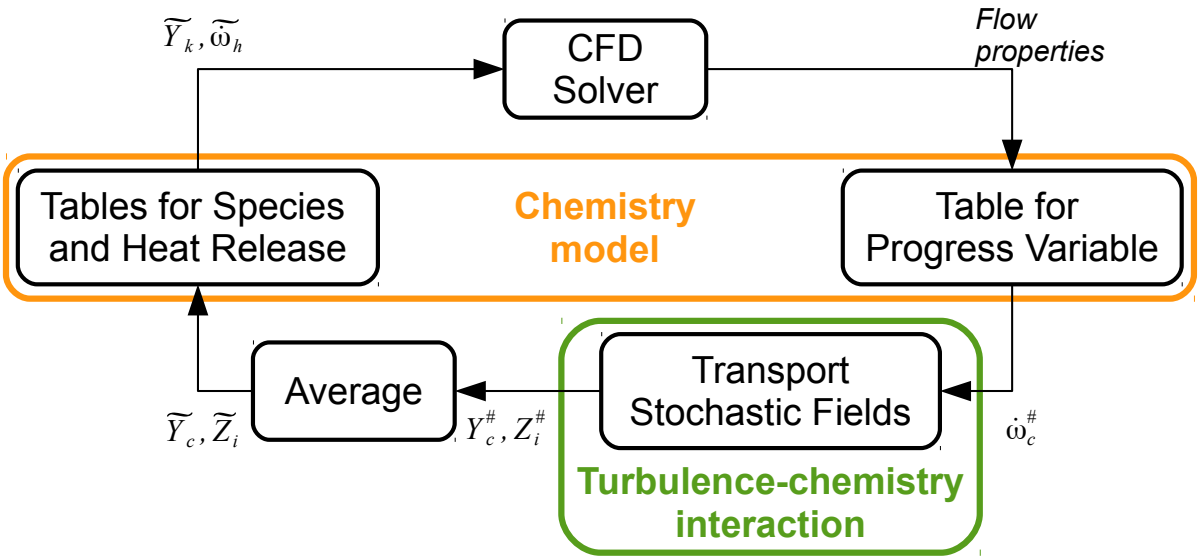

Figure 3.2: Link between the solver and the combustion model.

be transported using Eq. (3.1). So the filtered values of the progress variable $\widetilde{Y}_c$ and the mixture fraction $\widetilde{Z}$ can be calculated. At this point, there are two possibilities to provide the CFD solver with the physical properties (species mass fractions, viscosity, heat capacity, density,...) [29]:

1. The physical properties are stored directly in look-up tables. And they are retrieved using the filtered values of the table parameters. This is the most efficient way to implement the coupling. Unfortunately setting properties like this can introduced high frequency errors rendering the solver unstable; especially in the flame, where the physical values evolve rapidly. Indeed the linear interpolation in the tables can result in interpolated fields with important jumps for one cell to another. This in turn can deteriorate the stability of the numerical solver.

2. The species mass fractions are transported. But their source terms are computed in order to relax the species mass fractions toward the tabulated values [14]:

$$\widetilde{\dot{\omega}}_k = \frac{\widetilde{Y}_k^{\text{table}} - \widetilde{Y}_k^{\text{CFD}}}{\Delta t}, \tag{3.3}$$

   where Δt is the CFD time step.

The latter approach was chosen as the OpenFOAM® solver was becoming unstable for every trial of the first methodology. In addition the second

approach allows integrating much more existing code from the OpenFOAM® toolbox. Consequently the probability of introducing bugs is reduced.

The drawback of the second approach is the necessity to transport additional scalars – the filtered species mass fractions and the filtered sensible enthalpy. But it is not necessary to transport all species to reconstruct correctly thermodynamic states. So only a subset of $N_s^\star$ species are solved. Galpin et al. [29] perform an extensive study of the best combination of species to be carried in the case of methane burning in air. Their recommendations were followed in this work. Therefore in the case of methane, the species CH_4, CO, CO_2, C_2H_2, H_2O, H_2, H, O_2 and N_2 are transported. The source terms are computed from look-up tables for CH_4, CO, CO_2, H_2O, and H mass fractions and atomic budgets for C, H and O – N_2 being considered as an inert gas.

For other hydrocarbon fuels, the same set of transported species and tables were chosen[5]. In the case of hydrogen, H_2, O_2, H_2O, and N_2 were solved. And the source terms were calculated from a look-up table for H_2O and atomic balances for H and O.

The source term for the energy equation, $\dot{\omega}_{hs}$, is computed from the species source terms and their enthalpy of formation, $\Delta h_k^{f,0}$.

$$\dot{\omega}_{hs} = -\sum_{k=1}^{N_s^\star} \Delta h_k^{f,0} \dot{\omega}_k. \tag{3.4}$$

Those "fake" source terms relaxing the species towards the tabulated values consists a major difference with the implementation of R. Kulkarni. Indeed in his implementation the source terms for the species were the chemical source terms read directly from look-up tables for all pairs of stochastic fields. Then the filtered source terms were computing using Equation (2.59):

$$\tilde{\dot{\omega}}_k = \frac{1}{N_{\text{sf}}} \sum_{n=1}^{N_{\text{sf}}} \dot{\omega}_{n,k}^{\text{table}}. \tag{3.5}$$

On the contrary of the relaxation technique (Eq. (3.3)), that implementation doesn't insure that the chemical state in the CFD corresponds to a tabulated state. Indeed as shown in Figure 3.3, the time integration of the source

[5] CH_4 is replaced by the hydrocarbon molecule.

terms, $Y_{2'}$, will introduced a small error compare to the true value, Y_2. As this small error occurs at each time step, it will get bigger and bigger with time. Using relaxation source terms avoid such error and insure the analogy between the instantaneous look-up tables parameters and the instantaneous chemical mixture. Moreover the physical bound of the species mass fractions could be crossed (e.g. the mass fraction of a product can be higher than its equilibrium value).

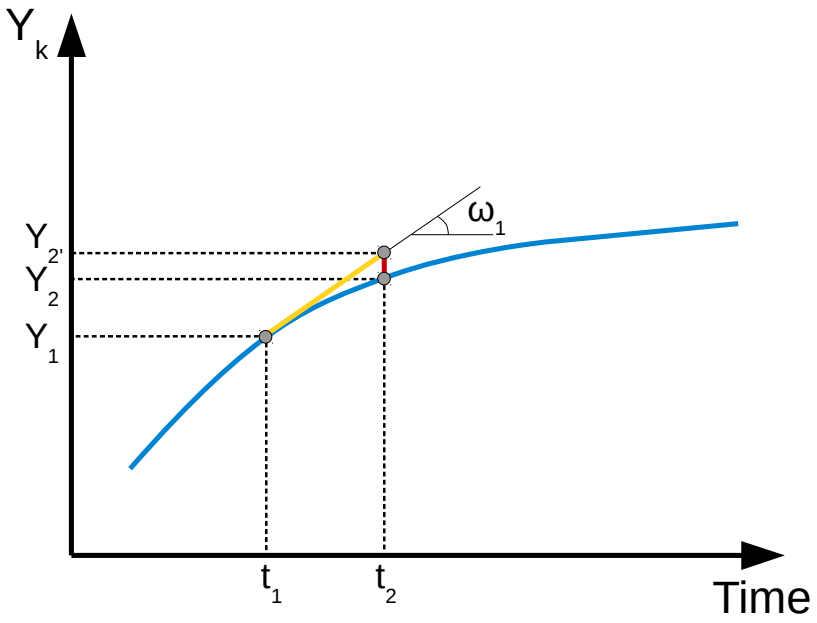

Figure 3.3: Comparison of the relaxation approach and the instantaneous source term method for computing the chemical source terms.

3.2 NO_x model

From the short review of the pollutant modeling approach based on look-up tables (see Section 2.3.2), NO_x emissions are best predicted when:

- an additional transport equation for NO_x is solved,
- with its source term read from a table having NO_x as additional dimension.

Unfortunately adding a dimension implies a huge increase in storage requirement for predicting a minor species such as NO_x. Therefore this paragraph will present a new modeling approach combining a look-up table without additional dimension, but supplemented by algebraic relations.

When using the tabulated chemistry model, one of the important points is the configuration used to generate the tables. The logic behind the model will be exposed in the case of homogeneous reactors. Then it will be extended for 1D premixed flame.

3.2.1 Tabulation based on homogeneous reactors

Let's consider different mixtures of methane and air close to the stoichiometric conditions at a temperature of 800K and atmospheric pressure. The major variation of NO mass fraction is nearly insensitive to the variation of the progress variable[6] as shown in the left graphic of Figure 3.4. But when plotting the evolution of the NO source term as a function of the progress variable, it seems that most of the source term variation is captured except the far end where a discontinuity occurs. Those last segments of the curves are related to the evolution of the source term in the homogeneous reactor between the latest tabulated point (corresponding at $C = Y_c/Y_c^{eq} = 99\%$) and the thermodynamics equilibrium state. This is the time during which most of Y_{NO} is produced. Therefore to improve NO_x prediction based on look-up tables, the variation of $\dot{\omega}_{NO}$ for high progress variable value, i.e. for a composition close to the burnt products, should be accurately captured.

[6] Here the progress variable is defined as $Y_c = CO + CO_2$

Figure 3.5 shows the time evolution of the progress variable and the NO source term for the stochiometric mixture of methane and air. It is clear that $\dot{\omega}_{\mathrm{NO}}$ varies still greatly for very slight evolution of the progress variable[7] in the burnt products. And therefore $\dot{\omega}_{\mathrm{NO}}$ reconstructed from the table cannot follow accurately the real $\dot{\omega}_{\mathrm{NO}}$.

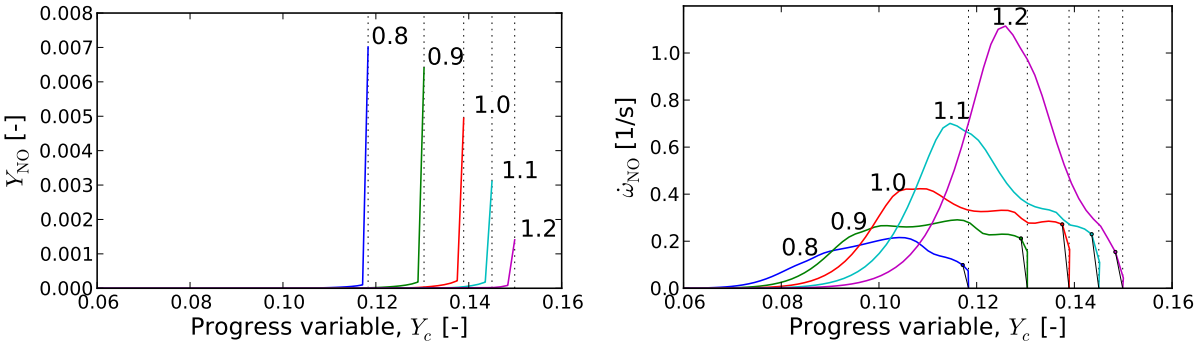

Figure 3.4: Variation of NO mass fraction (left) and its source term (right) with the progress variable for different equivalent ratios of methane-air mixture at atmospheric pressure. The points mark the last tabulated values. The black solid lines depict the interpolated source terms. The dotted vertical lines highlight Y_c^{eq} for the different mixture fractions.

In the burnt products, the major species, the temperature and the pressure are roughly constant and close to their equilibrium values. Therefore the residual chemical reaction rates are all relaxing towards zero. Due to the interaction between different reactions, that drop contains different time scales. Consequently it should be possible to approximate the evolution of $\dot{\omega}_{\mathrm{NO}}$ in the burnt products as a series of exponentials:

$$\dot{\omega}_{\mathrm{NO}} = \sum_i a_i \exp\left(-\frac{t^\star}{\tau_i}\right), \tag{3.6}$$

where $t^\star = 0$ when the composition is close to the burnt products. The definition of that composition is a major hypothesis of the model. After different tests, it was chosen to make it corresponds to time at which C=99%. So $t^\star$ is the time elapsed since the threshold C=99% has been crossed.

The parameters a_i and τ_i can be estimated by curve fitting from a least-square algorithm. The number of terms in the series is chosen according to two criteria: the accuracy of the curve fitting and the number of parameters to be stored. Currently the curve fitting is done with 3 time scales except

[7] At C=99%, $\dot{\omega}_{\mathrm{NO}}$ is equal to 0.27 s^{-1} and will decrease toward zero much more slowly than C tends to 100%.

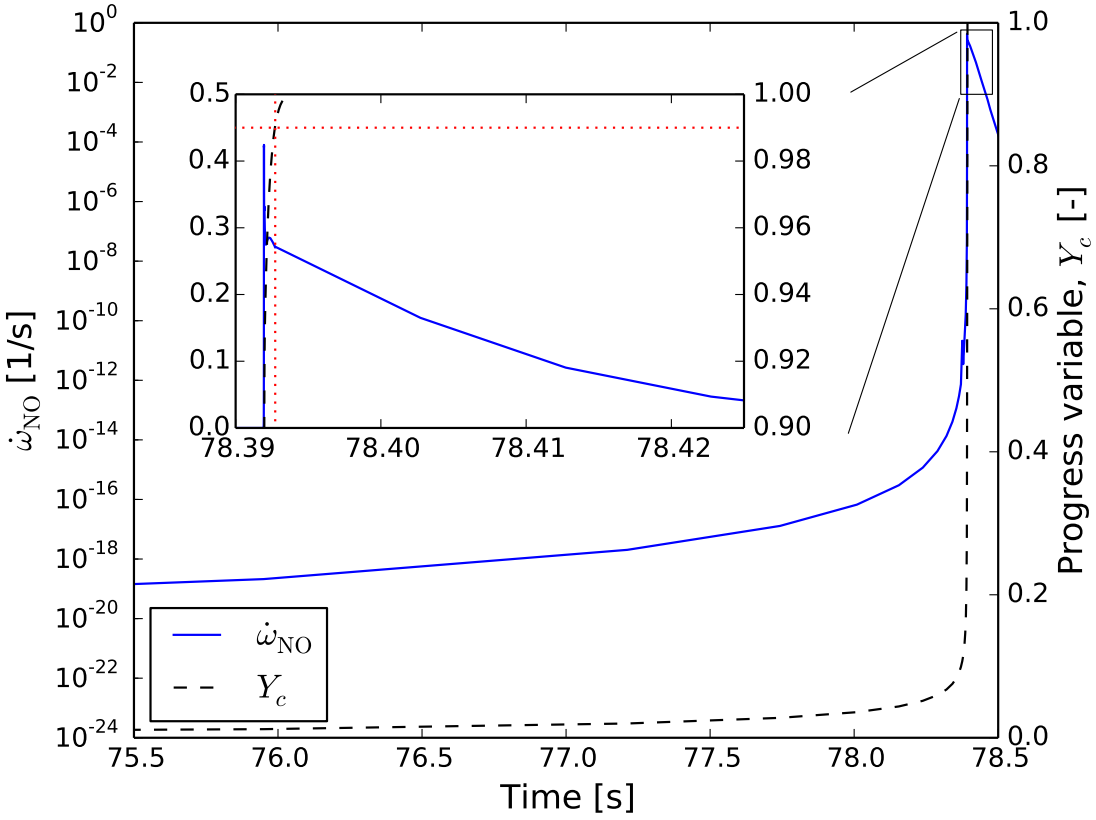

Figure 3.5: Temporal evolution of NO mass fraction source term (blue solid line) and the normalized progress variable (dashed black line) for a methane-air mixture at stochiometry and an initial temperature of 800K. The subgraph shows a zoom on the time interval [78.39, 78.425]. This detail highlights the variation of $\dot{\omega}_{NO}$ for value of the progress variable in the neighborhood of 99 % (dotted red lines).

if 1 or 2 time scales are more accurate. The Figure 3.6 presents an example of curve fitting results.

The curve fitting parameters obtained for this test case at stoichiometric conditions are listed in Table 3.2. If the data set contains less than three time-scales, the curve fitting algorithm tends to have similar time-scales. And unfortunately the weighting parameters are of opposite signs, resulting in larger discrepancies.

For a homogeneous reactor, the evolution of NO mass fraction is nothing else than the time integration of its source term. So the integration of Equation (3.6) provides an algebraic formula for Y_{NO} and a possibility to verify the accuracy of the series approximation (see Figure 3.6):

$$Y_{NO} = \int_0^{t^\star} \dot{\omega}_{NO} dt = -\sum_i a_i \tau_i \exp\left(-\frac{t^\star}{\tau_i}\right) + Y_{NO}^{t^\star=0}. \tag{3.7}$$

a_1	τ_1 [ms]	a_2	τ_2 [ms]	a_3	τ_3 [ms]
0.2716	17.76	-	-	-	-
20.43	24.94	-20.16	25.08	-	-
0.1282	21.23	0.2548	21.38	-0.1114	32.25

Table 3.2: Fitting parameter sets a_i and τ_i for fitting the NO formation rate $\dot{\omega}_{\mathrm{NO}}$ according to Eq. (3.6) with up to 3 time scales. The mixture considered here is a stoichiometric mix of methane and air at 800K and 1 atm.

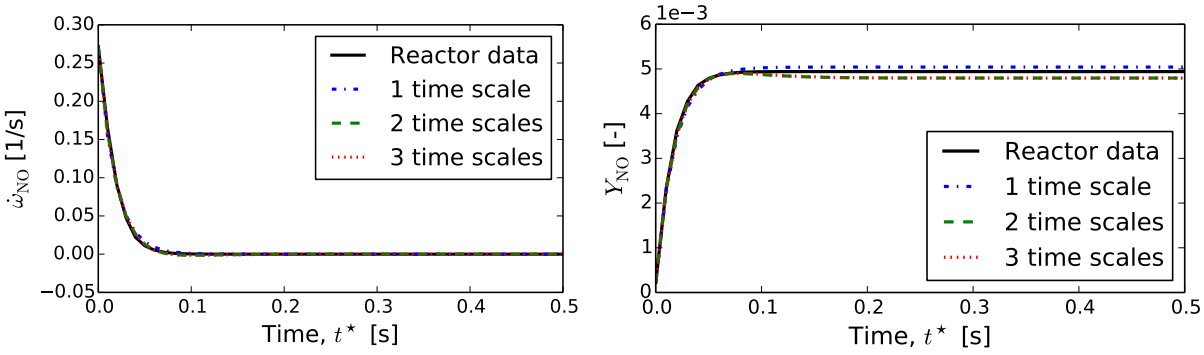

Figure 3.6: Curve fitting with 1 to 3 time scales for the variation of $\dot{\omega}_{\mathrm{NO}}$ (left) and Y_{NO} (right) in a homogeneous reactor. In those figures $t^\star = 0$s is the time at which the normalized progress variable is equal to 99 %.

The remaining question is: how can we use the Equations (3.6) and (3.7) in a CFD code?

In order to retrieve $\dot{\omega}_{\mathrm{NO}}$ in a given cell, $t^\star$ must be known in the cell. For that, a possibility would be to transport an equation for $t^\star$ with a source term appearing only in the burnt products. This was done for example by Enjalbert et al. [22] to transport the residence and mixing times in a lifted flame. On the other hand Y_{NO} will be transported anyway. So by finding the roots of Eq. (3.7) — e.g. using a Newton algorithm — the local $t^\star$ can be found. Then knowing $t^\star$, $\dot{\omega}_{\mathrm{NO}}$ can be obtained from Eq. (3.6).

3.2.2 Tabulation based on 1D laminar premixed flame

The scalar transport equation solved for a 1D laminar premixed flame can be expressed as:

$$\frac{d\rho_u S_L Y_k}{dx} - \frac{d}{dx}\left(D_k \frac{dY_k}{dx}\right) = \rho\dot{\omega}_k, \tag{3.8}$$

with ρ_u is the density of the unburnt gas, S_L the laminar flame speed for the specified conditions and D_k is the diffusive coefficient of the species k.

This time again, NO lacks sensitivity with the progress variable in the burnt products. But applying the same hypothesis as for the homogeneous reactor, the source term for NO mass fraction can be approximated by a combination of decreasing exponentials parametrized by a coefficient, b_i, and a length scale, λ_i:

$$\dot{\omega}_{\mathrm{NO}} = \sum_i b_i \exp(-\frac{x^\star}{\lambda_i}), \tag{3.9}$$

with $x^\star$ equal to zero when C equals 99%.

Then by integrating twice Equation (3.8), the NO mass fraction evolves as:

$$Y_{\mathrm{NO}} = -\sum_i \frac{\rho_b b_i \lambda_i^2}{\rho_u S_L \lambda_i + D_{\mathrm{NO}}} \exp(-\frac{x^\star}{\lambda_i}) + Y_{\mathrm{NO}}^{x^\star=0}, \tag{3.10}$$

with ρ_b denoting the density of the burnt gas.

To carry out the integration, the diffusion coefficient and the density were supposed constant in space and equal to their value at equilibrium[8]. As mentioned before, this hypothesis is acceptable as the temperature and the major species are roughly constant in the burnt products.

To summarize, the mass fraction of NO is transported in the CFD solver according to:

$$\frac{\partial \bar{\rho}\widetilde{Y}_{\mathrm{NO}}}{\partial t} + \frac{\partial \bar{\rho}\widetilde{u_i}\widetilde{Y}_{\mathrm{NO}}}{\partial x_i} - \frac{\partial}{\partial x_i}\left(\left(\frac{\mu}{\mathrm{Sc}} + \frac{\mu^{sgs}}{\mathrm{Sc}_t}\right)\frac{\partial \widetilde{Y}_{\mathrm{NO}}}{\partial x_i}\right) = \bar{\rho}\tilde{\dot{\omega}}_{\mathrm{NO}}, \tag{3.11}$$

in which the source term $\tilde{\dot{\omega}}_{\mathrm{NO}}$ is calculated using a look-up table when the local normalized progress variable is lower than 99%. Otherwise, for look-up tables based on homogeneous reactors, the local $t^\star$ is computed by solving for the root of Eq. (3.7). Then the source term is computed from Eq. (3.6). The parameters a_i and τ_i are found in look-up lists as functions of the mixture fraction.

Three steps are necessary to generate the required parameters:

[8] Other definitions were tried like taking the value at the point for which C=99%. But the best results were obtained when evaluating the parameters at equilibrium

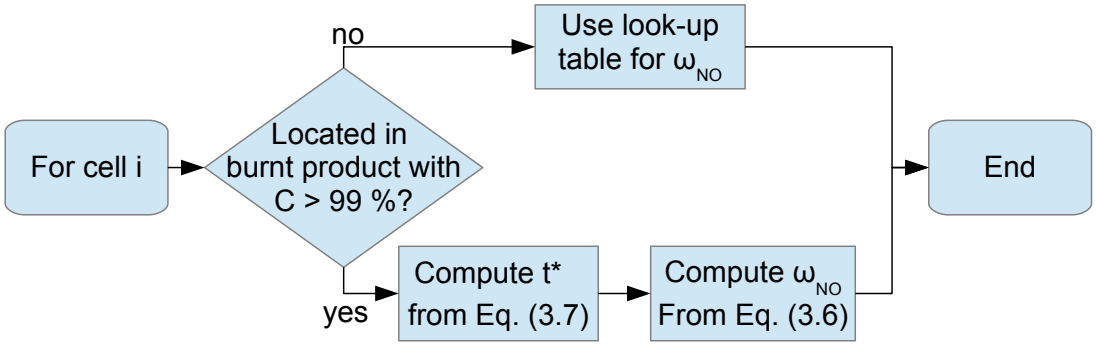

Figure 3.7: Algorithm of the NO model.

1. Generate the table for $\dot{\omega}_{\mathrm{NO}}$ from homogeneous reactors.
2. For each reactor, extract the temporal evolution of $\dot{\omega}_{\mathrm{NO}}$ for $C > 99\%$.
3. Using a curve fitting algorithm, determine the coefficients a_i and τ_i for each reactor.

For look-up tables based on laminar premixed flames, the algorithm is similar. Only the equation are different; Eq. (3.7) have to be substituted by Eq. (3.10) and Eq. (3.6) by Eq. (3.9).

As shown by Veynante et al. [113], algebraic relations are simply an extension/approximation of tabulated chemistry. Indeed if a relation can be found that allows retrieving the source terms from the table parameters, the look-up tables are not needed. Although Veynante et al. have found parametrized functions for computing the progress variable source term, the complexity of the functions can lead to a longer time to compute a value from the relation than to retrieve it from the tables. Therefore this new model combining a table and simple algebraic relations seems to be a good compromise.

3.3 Table optimization

In computer science a trade-off between computation and storage should often be determined. This is the case when comparing reduced chemistry against look-up tables. But choosing the look-up tables approach requires an optimization of the points discretization used in order to maximize the accuracy for a minimal table size. Indeed the chemistry evolution depends greatly for example on the mixture fraction. In the vicinity of the most reactive mixture fraction, the chemistry evolution changes rapidly with small change in mixture fraction. On the contrary for very rich mixture fraction, the chemistry is almost not active. Therefore to cover accurately the mixture fraction space, a non-uniform discretization should be more efficient than an uniform one.

The starting point of the optimization is the sensibility of the chemistry to the mixture fraction. Indeed the chemistry is faster for the so-called most-reactive mixture fraction, Z_{MR}. Assuming that the *auto-ignition delay*[9] τ_{ign} is a good indicator for the reactivity of a reactor, a preferential distribution could be defined using the inverse of the auto-ignition delay normalized to obtain a probability density function for the discretization points (see Figure 3.8) such as:

$$\frac{1}{K}\int_0^1 \tau_{\mathrm{ign}}^{-1}(Z)dZ = 1, \tag{3.12}$$

where K is the value of the integral normalizing the curve.

That curve cannot be used directly because to retrieve quickly a value in the chemical table, the correspondence between indexes and values of Z has to be easy. The idea is consequently to approximate that curve using a function. As the most reactive mixture fraction is shifted on the lean side, a non-symmetric function is needed. The one tested are a parabola added to an exponential law, named *expparab* later, and a beta function. The reconstructed curves are drawn in the Figure 3.8.

The expression for the *expparab* function is:

$$f = q(x-1)^2 + a - K\exp(-x/\tau), \tag{3.13}$$

[9] The definition of the auto-ignition delay is here the time at which the heat release is maximal.

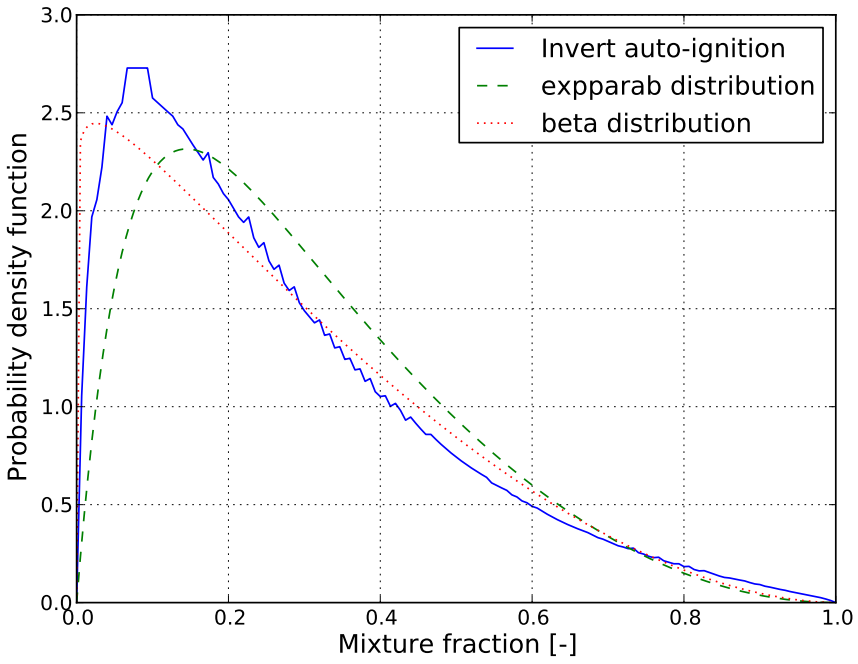

Figure 3.8: Optimization of the table based on the sensitivity of the chemistry on the mixture fraction. Mix at 1 atm of diluted hydrogen (mass fractions: 14% H2 + 86% N2) at 1000K and air (mass fractions: 0.233% O2 + 0.767% N2) at 1100K.

where q, a, K and τ are parameters to be determined using the 3 following conditions:

1. $f(0) = 0$,
2. $f(1) = 0$,
3. $\int_0^1 f dx = 1$.

That allows to have an undetermined parameter fixed using an optimization algorithm. It conforms the shape of f as much as possible to the one determined by the auto-ignition delay.

The Figure 3.9 presents the distribution of points when reducing the total number of them and using the *expparab*.

To retrieve the index of a given mixture fraction, it's actually the cumulative distribution function that is used and so stored for the simulation. Indeed for a given mixture fraction, the cumulative distribution function

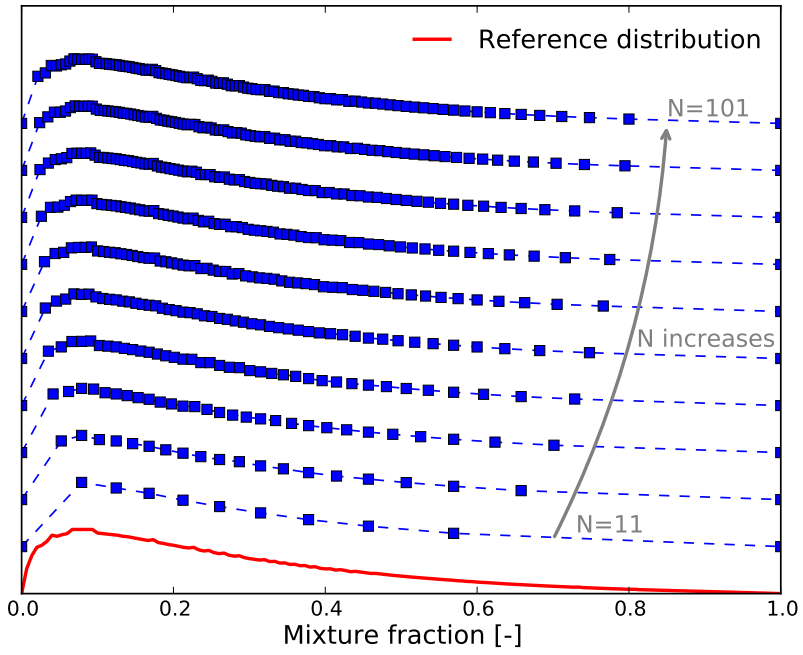

Figure 3.9: Example of points distributions in the mixture fraction space when increasing the number of them based on a *expparab* distribution. For clarity the different curves are shifted in the vertical direction.

will provide us with a value equivalent to the position of the given mixture fraction in the table.

The goal is to reduce the size of the table with a finer discretization where the chemistry is faster. To evaluate the error due to the reduction, the integral of the source term for the progress variable over the space (Z, C) was compared to a reference case using 100 points distributed uniformly in the two sub-spaces. Following Naudin [86], that measure is expressed:

$$\epsilon = \int_0^1 \int_0^1 \left| 1 - \frac{\dot{\omega}_c}{\dot{\omega}_c^{\text{ref}}} \right| dC dZ.$$

The results for the uniform and the *expparab* distribution are presented in the Figures 3.10. The use of non-uniform distribution appears to produce a slightly bigger error than the uniform one[10]. But the size of the table could be easily reduced from a reference of 100 $\times$ 100 points to 40 points in the mixture fraction space and 30 in the progress variable space.

[10] The results for the beta distribution are not better than the uniform distribution.

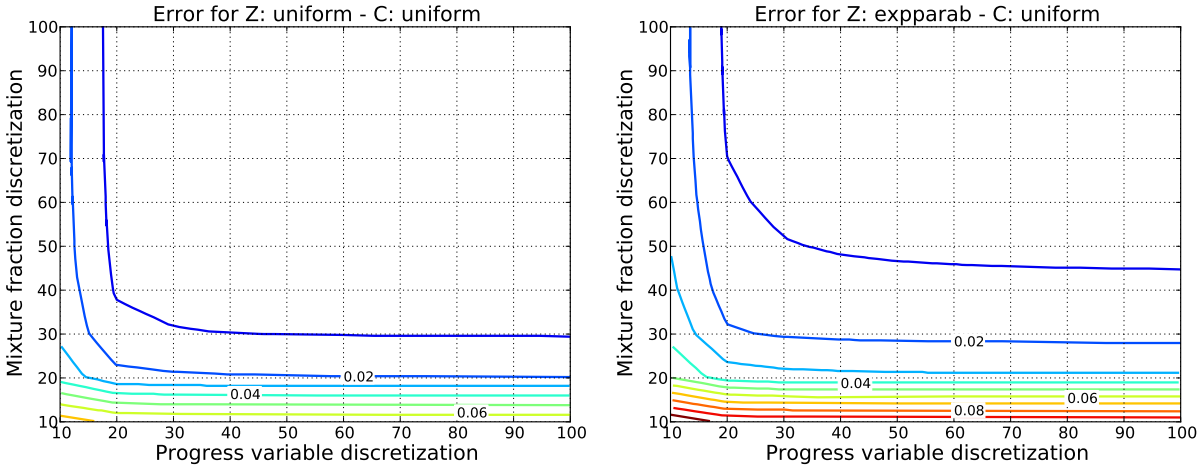

Figure 3.10: Error on the progress variable source term as a function of the discretization in mixture fraction and progress variable space. On the left both Z and C are uniformly distributed using 100 points for each parameter. On the right Z is distributed according to an *expparab* function with 40 points and C is uniformly distributed with 30 points.

Quite a few distributions were designed during this project:

- `uniform`: uniformly distributed parameter,
- `loguniform`: uniformly distributed parameter + logarithmic distribution between zero and the first point. For example (0, 1e-4, 1e-3, 0.01, 0.02,... , 1),
- `uniformlast`: uniformly distributed parameter on a reduced interval + latest physical value,
- `polynom`: approximation of the invert ignition curve based on a 3^{rd} order polynom,
- `beta`: approximation of the invert ignition curve based on a beta function,
- `expparab`: approximation of the invert ignition curve based on the combination of a parabola and an exponential as presented earlier.

After some trials, the mixture fraction space was discretized using an uniform distribution for the rest of this work. And the progress variable was discretized using `loguniform` to predict accurately the ignition delay.

3.4 Code architecture

The previous section detailed the implemented combustion model. But in order to help the potential future users of the code, the last section of this chapter will describe the implementation and the different parameters. As the look-up tables have to be generated prior to a CFD simulation. The Cantera [34] scripts will be presented first followed by the CFD solver.

3.4.1 Tabulation scripts

The generation of the tables can be done using any kind of dedicated chemistry softwares. During this project, Cantera [34] was chosen due to its performance (accuracy similar to Chemkin), its ease of use (availability of Python and Matlab interfaces), and its high quality documentation (the code is heavily commented and lots of tutorials are shipped with the code). All scripts were written in Python due to its high flexibility (scripting language similar to Matlab language), the number of packages existing (especially *Numpy* and *Scipy* [43] for mathematical operations and *Matplotlib* [38] to produce figures), and its availability (it is a cross-platform open-source program pre-installed in all Linux distributions).

To reduce the load of modifications from one test case to another, the scripts are articulated around one based class, called `createTable` and some libraries:

- `ReactorOD` for the functions linked to homogeneous reactor at constant pressure
- `oneDFlame` for those linked to free laminar premixed flame
- `tableLibrary` for miscellaneous functions (computation of thermophysical properties, automatic optimization of a parameter distribution,...)

A particular effort was put into the documentation of the functions. Therefore people interested should refer directly to the code for detailed information on the API.

New conditions can be easily defined by creating a new class derived from `createTable` in which the members are set according to the new requirements

and some functions are redefined (typically the progress variable definition). Consequently all the members and the important functions will be now exposed followed by a *howto* generate a table set.

Class members

There are 6 sections of members to be defined: the chemistry parameters, the tabulated chemistry space discretization, output options, general options, parameters used only with homogeneous reactors or only with premixed flame. The different sections are mentioned below using the default values for all parameters; i.e. you must only redefine the ones having a non-default values.

1. Chemistry parameters to specify the chemistry mechanism, the fuel and air composition

```
# Chemical mechanism
 #Filename containing the chemistry mechanism
self.mechanism = "gri30.cti"
 #Name of the mixture
self.mixtureName = "gri30_mix"
 #Name of the transport model
self.transportModel = "Mix"

# pressure
self.p = OneAtm
# fuel
reactorf = importPhase(self.mechanism, self.mixtureName)
reactorf.set(T = 1000.0, P = self.p, Y = 'H2:0.14,N2:0.86')
# air
reactora = importPhase(self.mechanism, self.mixtureName)
reactora.set(T = 1100.0, P = self.p, X = 'O2:0.21,N2:0.79')
```

2. Distribution of the table parameters

```
# How to specified a distribution?
# It's a dictionary with 4 entries:
#  name: Name of the variable
#  distribution: Type of distribution (available are: uniform,
#   uniformlast, loguniform, geometric, polynom, expparab,
#   beta and values)
#  values: Variable distribution (only for distribution::values)
#  parameters: Parameters needed to compute the distribution
#   (for example alpha, beta for distribution::beta)
# N.B.: If the distribution is not bounded between 0 and 1,
```

```
# add the two bounds at the end of the parameters list.

# number of intervals in the mixture fraction space
self.Z = {'name':"ft", 'n': 100, 'distribution': 'uniform',
     'values': array([]), 'parameters': array([])}
# To optimize the mixture fraction (only with 0D reactors)
self.optimizeZ = False

# number of intervals in the progress variable space
self.C = {'name':"Yc", 'n': 100, 'distribution': 'loguniform',
    'values': array([]), 'parameters': array([4, 100])}
# To optimize the progress variable (only with 0D reactors)
self.optimizeC = False
```

3. General options

```
self.options = {
     "SMALL": 1e-8,          # Small float value
     # Margin to detect parameter boundary values
     "BCMargin": 1e-4,
     # Check that the progress variable is monotonous
     "checkPV": True,
     # If reactor/flame crashes, shift the parameter by
     # tolParameter and try again (0.0 turns this off)
     "tolParameter": 0.0
}

# Print additional information
self.verbose = False
```

4. Output options

```
# Names in order of the files to be output
self.outputNames=('Yc', 'T', 'H2O', 'OH')
# Generate the output from the outputNames? (see
#  tableLibrary::interpretOutputNames)
self.interpretOutput = True
# Name of the output directory
self.outputDir = "constant"

# NO modeling
self.NOxModel = {
    "source":False,    # Output the table for wNOx
    "Ihme":False,      # Output tables for Ihme model
    "curveFitting":False, # Output NOx curve fitting model
    # Threshold of normalized progress variable for curve
    #  fitting
    "thresholdC":0.99,
    # Filename storing raw curve fitting parameters
```

```
    "fileCurveFit": "NOxCurveFitting.dat",
    # Definition of NOx - for NO ["NO"],
    #  for NO+NO2 ["NO", "NO2"]
    "NOxSpecies":["NO"]
}
```

5. Options for tabulation based on homogeneous reactors

```
# Maximal time of integration / negative value to deactivate
self.maxIntTime=-1. # e.g.: set to 0.01 s

# Characteristic time step of the CFD
# Pre-integration on a characterized time step of the source
#  term instead of instantaneous value.
# 0.0 = instantaneous source term
self.dtCFD=0.0

# Compute the ignition delay time for the different reactors
self.ignitionTime = False
```

6. Options for tabulation based on free premixed flames

```
# Minimal temperature to use when generating the table
# with heat losses
self.minTHL = 300.

# List of species introduced when recirculating burnt gases
#  e.g. ("N2","O2","CH4","H2O","CO","CO2")
# - None to recirculate equilibrium state
self.productsAllowed = None

# If True, flames computed with hypothesis that Lewis = 1
# i.e. for all species Yk, Dk = thermalConductivity/rho/Cp
self.LewisOne = False
```

Class functions

The function defining the progress variable should be adapted for every case. But others functions, like the one specifying the output of the script or the formatting of the data output, may require some tuning.

1. `defPV` returns the current value of the progress variable Y_c and its source term. The two variables to set to define a progress variable is a list of strings containing the specie names used to define Y_c and their weights. The following example corresponds to $Y_c = 1\,Y_{\mathrm{CH_2O}} + 1\,Y_{\mathrm{CO}} + 1\,Y_{\mathrm{CO_2}}$.

```
def defPV(self, mixture, source=False, yOld=zeros(0)):
  # To be adapted
  namesPV=['CH2O', 'CO', 'CO2']
  # Coef. to weight the species in PV definition
  coefPV=sc.ones(len(namesPV))
```

Remark: Remember that for an auto-ignition case, an intermediate species (HO_2 for hydrogen or CH_2O for methane) should be included in the definition.

2. The output data can be tuned at two levels. In `outputData` are extracted all wanted variables for a given point in time (respectively in space) of a homogeneous reactor (respectively a premixed flame). Or if you want to modify the way the full set of data are handled, you will have to modify `outputReactorData` (respectively `outputFlameData`) for table based on homogeneous reactors (respectively premixed flames).

3. To modify the format of the output data, the modifications should be made in the `writeBlablabla` functions; more specifically in `writeTableParameters` for the table parameters distributions specifications and in `writeTable` for the tables' format.

Run the tabulation

To facilitate the comprehension of this paragraph, the parameters for a given test case are presumed to be defined in a new class, `myCreatorTable`. From that new class, you can create three types of tables depending on the function called:

1. Tables based on homogeneous reactors:
   `createFromReactor(outputInText=False, writeForCFD=True, writeReactor=False)`

   - If `outputInText`, write the table in raw data.
   - If `writeForCFD`, write them in OpenFOAM® friendly format.
   - If `writeReactor`, write the raw data of each reactor in separated files.

2. Tables based on free premixed flames:

```
createFromFlame(outputInText=False, writeForCFD=True, writeFlame=False)
```

   - If `outputInText`, write the table in raw data.
   - If `writeForCFD`, write them in OpenFOAM® friendly format.
   - If `writeFlame`, write the raw data of each flames in separated files.

3. Pre-integrated tables for presumed β-PDF (experimental):

```
createDblBetaTables(outputInText=False,
    writeForCFD =True, writeOneDCase=False,
    reactorBased=True, mixReactorAndFlame=False)
```

   - If `outputInText`, write the table in raw data.
   - If `writeForCFD`, write them in OpenFOAM® friendly format.
   - If `writeOneDCase`, write the raw data of each canonical case used (reactors and/or flames) in separated files.
   - If `reactorBased`, tables based exclusively from homogeneous reactor; else exclusively from premixed flame.
   - If `mixReactorAndFlame`, the resulting table is the weighting of a table from homogeneous reactor and from premixed flame; the weight being the normalized progress variable (see [20]).

In order to generate look-up tables based on homogeneous reactors (with output in raw and Foam format), the syntax will be:

```
c = myCreatorTable()
c.createFromReactor(True, True, False)
```

Algorithm of tabulation

The tables are generated for all the discretized points in the table parameters space. Therefore boundary cases will be set to default values (0.0 for source terms, latest known value for the other parameters) in order to avoid lattices in a table. The second problem is the variation of the progress variable scale for each canonical test (i.e. homogeneous reactor or premixed flame). To store consistently and retrieve efficiently a value in the tables, the progress variable distribution should be identical for all canonical tests. The only way of fulfilling that requirement is to work with the normalized progress variable varying from 0 to 1 in each case as it is defined by

$$C = \frac{Y_c - Y_{c,init}}{Y_{c,eq} - Y_{c,init}}.$$

Therefore the data of all cases will be linearly interpolated to match the prescribed normalized progress variable distribution before being saved.

A good table requires an accurate capture of the evolution of the flame or reactor profile. In the former case, the standard solver of Cantera does a very good job making use of a dynamic refinement of the discretization space. But in the case of the homogeneous reactor a dynamic refinement in time is not available. Therefore a strategy[11] was devised. Prior to a reactor computation, the time before ignition is evaluated. This induction time is defined as the time needed to have an increase of 1% in temperature relative to the total temperature rise. Once the induction time is known, the computation of the reactor can be carried out. Up to the induction time, the reactor states are saved according to a uniform distribution in time. Then the reactor is run time step by time step[12]. The states are then stored following a uniform distribution in progress variable space from the value at the induction time to equilibrium value. The latest point will be the state of the mixture at thermodynamical equilibrium.

In the case of homogeneous reactor, the first progress-variable source term stored in the table is critical to predict the auto-ignition time. In the current script, the first source term is not the instantaneous one but the

[11] The idea was first introduced by R. Kulkarni and improved further.
[12] The time step used is the one estimated by the ODE solver.

time-averaged source term between 0s and the second point of the table as suggested by Colin et al. [14].

The time integration of Cantera can fail for specific conditions. Therefore to improve the robustness of the scripts, errors rising from time integration are automatically caught and treated. A slight variation[13] on the table parameters is performed to overcome the troublesome conditions. A very small variation e.g. 10^{-5} is usually sufficient to obtain a solution and induces only a tiny error in the tabulated values.

3.4.2 Solver structure

In an effort to gain the maximal compatibility between the new code and the standard OpenFOAM® (in version 2.1.x), the new code was implemented using high level of C++ programming. The resulting code should therefore be compatible with the future versions of OpenFOAM® and easily extended. To meet those requirements two main class hierarchies were created, one deriving from the abstract existing class `combustionModels` to implement the turbulence-chemistry interaction model and another branch deriving of an abstract class `tableSolver` allowing to implement the tabulated chemistry with various sets of parameters.

Class diagram

Figure 3.11 shows the hierarchy and the interactions between the two sets of classes. An abstract main class `eulerianPDFCombustion` defines the interface between the solver and the turbulence-chemistry model. The former can be either `reactingTableFoam` or `rhoReactingTableFoam`. They are a variation of the existing `reactingFoam` and `rhoReactingFoam`. The latter can be `deltaPDFModel`, `stochasticIto`, `doubleBetaPDF` or any model you want to implement.

The interaction between the combustion model and the table solver is not direct for two reasons. Firstly it could be interesting for post-processing to interpolate into a table outside of the main solver. Secondly, another chemistry solver (like an ODE solver) to determine the chemical source terms could be implemented more easily. Therefore the combustion model

[13] The parameter is shifted according the value of the option `tolParameter`.

interacts firstly with the class `pdfChemistrySolver` that interacts only for the interpolation with the tabulated chemistry class.

To prove the flexibility of the tabulated chemistry solver, different kinds of table solver were implemented:

- `tableFtYc` for tables based on a mixture fraction and a progress variable.
- `tableHLYc` for tables based on an enthalpy dimension and a progress variable.
- `tableDoubleBeta` for tables based on a mixture fraction, a progress variable, and their variances.

The class `pdfChemistrySolver`, having access to the thermodynamical properties, is computing the source terms of all transported species from the tabulated subset to maintain the atomic budget. For that a "fake" reaction mechanism should be defined (syntax identical to the one needed for `reactionFoam`) that will conserve the atomic budget.

To describe the major functions and the parameters needed, the flow sequences of the combustion model construction and the calls by the solver to the combustion model will be detailed in the following two sections.

Combustion model construction

The construction of the combustion model is happening when the following line in the `createFields.H` solver[14] is executed:

```
Info<< nl << "Creating␣combustion␣model\n" << endl;

autoPtr<combustionModels::rhoCombustionModel> combustion
(
    combustionModels::rhoCombustionModel::New(mesh)
);
```

At that point the dictionary `combustionProperties` is read to select the combustion model; e.g. to select the Eulerian stochastic fields model:

```
combustionModel stochasticIto<rhoCombustionModel,incGasThermoPhysics>;
```

[14] Here `rhoReactingTableFoam`.

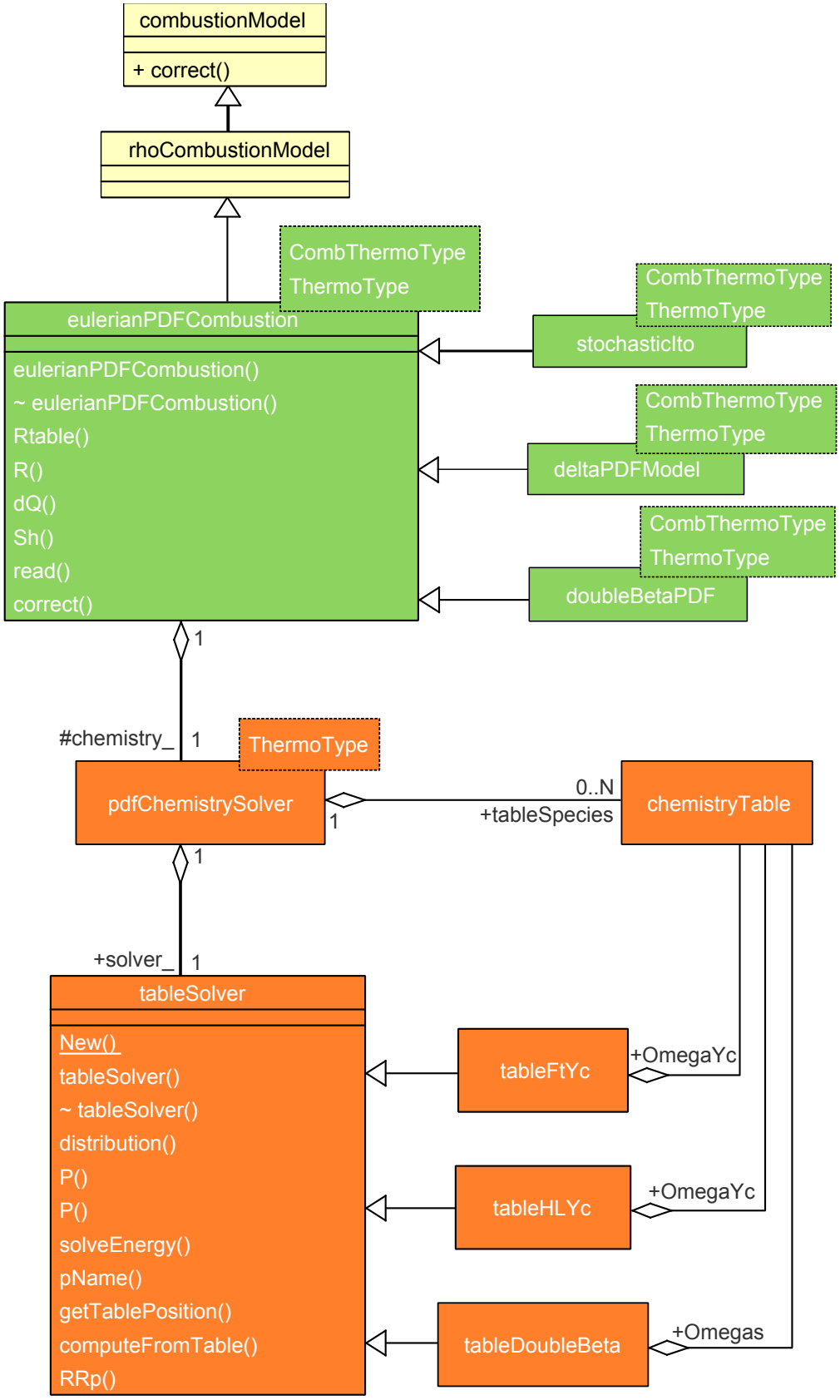

Figure 3.11: Classes hierarchy and interactions of the combustion model when using `rhoReactingTableFoam`. Remark: with `reactingTableFoam`, the only change is a switch between `rhoCombustionModel` and `psiCombustionModel`.

Then, the constructor of `stochasticIto` is called. That will trigger a cascade of constructors in the following order:

1. `combustionModel`
   Read the dictionary `combustionProperties`.
2. `thermoType`
   The thermophysical model will be defined in `thermophysicalProperties`; here `hsRhoMixtureThermo<reactingMixture<incGasThermoPhysics>>`. The multi-species class `reactingMixture` must be chosen.
3. `rhoCombustionModel`
4. `tableSolver`
   The table parameters are defined in a dictionary, `tableProperties`.
5. `pdfChemistrySolver<incGasThermoPhysics>`
6. `eulerianPDFCombustion<rhoCombustionModel,incGasThermoPhysics>`
7. `stochasticIto<rhoCombustionModel,incGasThermoPhysics>`

The table parameters, simply called `P`, are hard coded in the chosen `tableXYZ` model; e.g. `tableFtYc` for tables with one mixture fraction and a progress variable as parameters. Therefore the average fields of those two parameters are created and stored in `tableFtYc`. In addition to the model selection, the dictionary `tableProperties` contains the `distribution` of the parameters as well as some useful parameters (for instance the value of the progress variable at equilibrium to be able to compute the normalized progress variable).

As mentioned previously, only a subset of species is transported. And the source terms of all of them is computed from relaxed source terms using tables and atomic budgets. Therefore a relation between the source terms provided by the tables and all needed source terms has to be found. To achieve this, two elements should be specified: the tables to be used and that relation. The tables list is defined in the sub-dictionary `combustionProperties::stochasticItoCoeffs` by a list of string corresponding to the keyword `tables`; e.g. for hydrogen combustion `tables ( H2O )`. And the atomic budgets are conserved by introducing surrogate reactions. For example, if hydrogen is burnt in air with H_2O stored in a table, the "mechanism" will be:

```
species    4( H2 O2 H2O N2 );

reactions
{
    hydrogenReaction
    {
        type    irreversibleArrheniusReaction; //Doesn't matter
        reaction "2H2 + O2 = 2H2O";
        A       1.16e+09; //Doesn't matter
        beta    1; //Doesn't matter
        Ta      37890.3; // Doesn't matter
    }
}
```

Only the entry `reaction` is used in this case. The other parameters are needed because existing classes are reused to interpret chemistry mechanisms.

An example of the dictionaries needed to run a simulation is presented in Appendix C.

Interactions solver – combustion model

The `combustionModel` class has four public functions called by the solver: `correct`, `R`, `Sh` and `dQ`. The three latest return fields computed during the execution of `correct`.

- `R(const volScalarField& Y)`: returns the source term for the species mass fraction `Y` transport equation.
- `Sh()`: returns the source term for the sensible enthalpy equation.
- `dQ()`: returns the heat release rate (for post-processing only).

A function `Rtable(const label& i)` was added to return the mean source term of the i^{th} table parameter; e.g. to get the filtered source term of the progress variable.

But those functions are only access functions. The core of the combustion model is solved when the function `correct()` is called.

That function is redefined in every turbulence-chemistry interaction model. So for clarity the focus will be put on `stochasticIto` only. Figure 3.12 explains graphically the steps carried out.

1. To ensure compatibility with the Ito formulation, the micro-mixing term, the stochastic term, and the source term of Equation (3.1) are computed only once – the first time the function `correct` is called[15].
2. Equation (3.1) is solved for all stochastic fields.
3. The averaged values (i.e. the filtered value) of the table parameters are computed from the stochastic fields using Eq. (2.59).
4. As the value of the table parameters are now known at $t + \Delta t$, the relaxation source terms for the species can be computed.

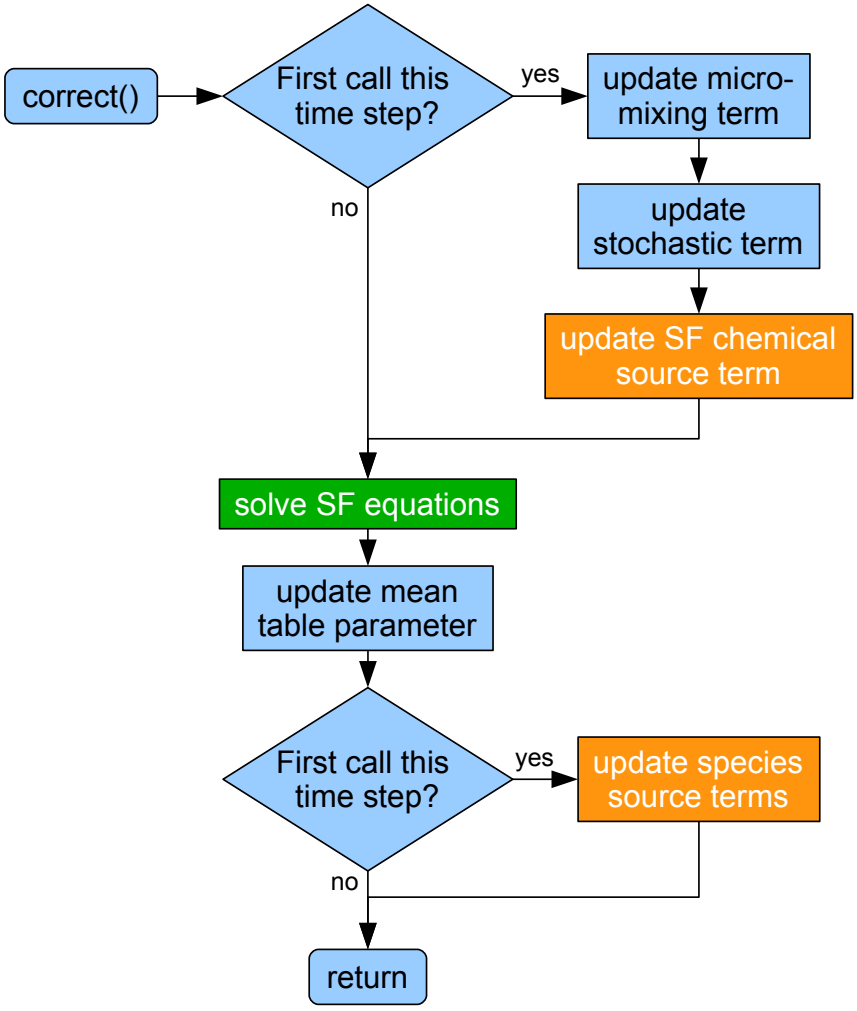

Figure 3.12: Flow chart of the function `correct` to solve the turbulence-chemistry interaction.

Values must be retrieved at two points using look-up tables (orange boxes in Fig. 3.12). The procedure to do so is the following. For each cell of

[15] This function is called every iteration of the PISO loop in standard OpenFOAM® solvers.

the CFD mesh, a vector with the local table parameters is built. From that vector, the function `tableSolver::getTablePosition` first normalizes the table parameters (i.e. compute the normalized progress variable from the progress variable). Then it finds the position and weights to interpolate in the tables. Finally the look-up tables (class name `chemistryTable`) are directly interpolated to get the progress variable source term or process by `pdfChemistrySolver` to calculate the source terms of all species by respecting atomic budgets.

3.4.3 NO_x with OpenFOAM®

The amount of nitrogen oxides produced is usually very low in comparison with the main species like CO_2, N_2,... . The fluctuations of thermo-physical properties due to the NO_x are consequently unimportant. Hence the variation of NO_x can be computed in a post-processing step.

OpenFOAM® provides a framework for post-processing tools on the run, called `functionObjects` that fits perfectly with the present requirement; i.e. an one-way coupling between the CFD solver and an independent scalar equation. The parameters are specified in `controlDict`.

```
functions
{
  NOxCurveFit
  { //Type of the functionObject - here NOx new model
    type           NOxCurveFittingModel;
    functionObjectLibs ( "libuserFunctionObjects.so");
    enabled        true;
    //Write NOx field at the same time than the other flow fields
    outputControl outputTime;
    //Name of the file storing the NOx source terms
    RRNOx          RRNOx;
    // Name of the file where the coefficients for the curve
    // fitting are saved
    NOxCoeffs      NOxCurveFittingDict;
    // Threshold of normalized progress variable for the curve
    // fitting model
    thresholdC     0.99;
  }
}
```

3.5 Summary

This chapter described in more details the equations transported and hypotheses used to implement the SFPV combustion model. In particular the logic and theory behind the new approach for NO_x modeling, namely a transported scalar with a source term obtained from look-up table and algebraic relation, was described at length.

In addition to the theoretical background, a short review of the code structure for generating the tables in Cantera and to complete CFD simulation with OpenFOAM® was written to help interested readers in their effort to use and develop further the model.

The next chapter will validate the solver against various test cases from simple homogeneous reactor to auto-ignition spots in hot turbulent flows. That validation will be also the occasion to look at the influence of different hypotheses like the number of stochastic fields.

4 Application and validation

Now that the SFPV model and the code structure has been described, their validation will be depicted in this chapter. The first tests focus on the validation of the look-up tables generation and their accuracy compared to detailed chemistry results. Those points will be assessed with homogeneous reactors calculation and with auto-igniting diffusive mixing layers.

The mixing effect in mixture fraction space will receive a special attention. Indeed, the look-up tables are based on homogeneous reactors of different mixture fraction but solved independently. Therefore the mixing in mixture fraction space is not explicitly taken into account in the tables.

The second phase of validation cases will evaluate the performance of the turbulence-chemistry model for predicting auto-ignition spots. First a comparison of the implementation of R. Kulkarni's model in FLUENT® [63] and its adaption to OpenFOAM® described in the previous chapter will be carried out. The relative efficiency and accuracy of the two codes will be highlighted. Then some of the experiments of Markides et al. [76, 78] of random auto-ignition spots appearing in fuel injected into hot air will be simulated. The range of temperature boundary conditions will be broad to cover the regime from random auto-ignition spots to flash-back.

In the literature [56, 82], the auto-igniting kernels appearance is reported to be possible in region with a composition close to the most reactive mixture fraction and where the scalar dissipation rate is low. The most reactive mixture fraction is a value that can be determined. But a threshold of scalar dissipation rate to separate values inhibiting the auto-ignition from those allowing it seems unlikely to be found as it will depend on the boundary conditions of the simulation.

As the present tabulation process is not taking explicitly into account the scalar dissipation rate, the relation between the scalar dissipation rate and the auto-ignition events will be closely analyzed in order to validate the use of chemistry look-up tables based on homogeneous reactors for auto-igniting

turbulent flows; i.e. neglecting direct effect of the scalar dissipation rate on the chemistry.

In the last section, the extension of the model to predict NO_x will be validated. In that purpose, simple validation against detailed chemistry in the case of homogeneous reactors and laminar premixed flames will be described. The section will be closed with preliminary results on the turbulent methane lifted flame experiments of Cabra et al. [12].

4.1 Chemistry validation

The present model computes chemical and sensible enthalpy source terms from look-up tables. The validation against source terms computed from detailed chemistry is affordable for simple configurations. Here after are described validation test cases based on the time evolution of homogeneous reactors and mixing layers.

Those test cases were extensively used to tune the implementation of the model as well as an appropriate definition for the progress variable in the framework of auto-ignition.

4.1.1 Homogeneous reactors

The time evolution of homogeneous reactors at constant pressure is driven by the following equations:

$$\begin{cases} \frac{dY_k}{dt} = \dot{\omega}_k & \text{for } k = 1...N_s \\ \frac{dh_s}{dt} = \dot{\omega}_{hs} \end{cases} \tag{4.1}$$

For this first validation test case, the Equations (4.1) have been integrated by computing the source terms in three different ways:

- Detailed chemistry using the Sandiego mechanism [103] containing 21 equations and 8 reacting species
- Reduced chemistry derived from the detailed mechanism by Boivin et al. [5]
- Tabulated chemistry built on the Sandiego mechanism

The reduced chemistry mechanism of Boivin et al. is carried out in two steps. Firstly for practical conditions of premixed and non-premixed flames, autoignition and detonations, some elementary reactions have a negligible contribution. Therefore the full mechanism can be reduced to a skeletal mechanism of 12 reactions. In a second step, steady-state assumptions are introduced for O, OH and H_2O_2. With those assumptions, the different

elementary reactions source term can be linearly combined from three independent source terms. Those three source terms defined the following three overall steps:

$$\begin{aligned} 3H_2 + O_2 &\leftrightarrow 2H_2O + 2H \\ H + H + M &\leftrightarrow H_2 + M \\ H_2 + O_2 &\leftrightarrow HO_2 + H \end{aligned}$$

The previous three steps mechanism results in highly underestimated autoignition time delays, especially at rich conditions. This comes from the steady-state assumptions for O and OH being inaccurate in the initial period of radical branching. To circumvent that problem, Boivin et al. have defined a correction factor to apply to the three global steps based on the 3 elementary reactions responsible of the radical growth when the steady-state assumption is poor. The indicator determining when the steady-state assumption is applicable has been construct on HO_2. If HO_2 is in quasi steady-state (i.e. its production term is nearly equal to its destruction term), then the steady-state assumption for O and OH is acceptable and the original three steps mechanism is used; otherwise the correction factor should be applied.

When using the tabulated chemistry, not all species are transported as described in Section 3.1.2. The number of source terms, N_ω, depends on the number of species, N_s, and the number of elements, N_e, (O, H,...) such that $N_s = N_\omega + N_e$. So for this test case, different implementations of the tabulated chemistry were given special consideration:

- $\dot{\omega}_{H_2O}$ is tabulated and H_2, O_2 and H_2O are transported,
- $\dot{\omega}_H$ table is added and H is transported,
- hs the heat release is read from a table instead of being computed from the species source terms,
- T the energy source term is computed by relaxation of the temperature.

The results match perfectly if the reactor simulated is one of the reactors used to generate the table (not shown). The agreement is very good if the mixture fraction simulated is around the stoichiometric mixture fraction as

shown in the Figure 4.1. The reduced mechanism is describing the chemistry with a bigger error than the tabulated chemistry model due to the assumptions made on some intermediate species. Especially the reduced mechanism underestimates the ignition delay.

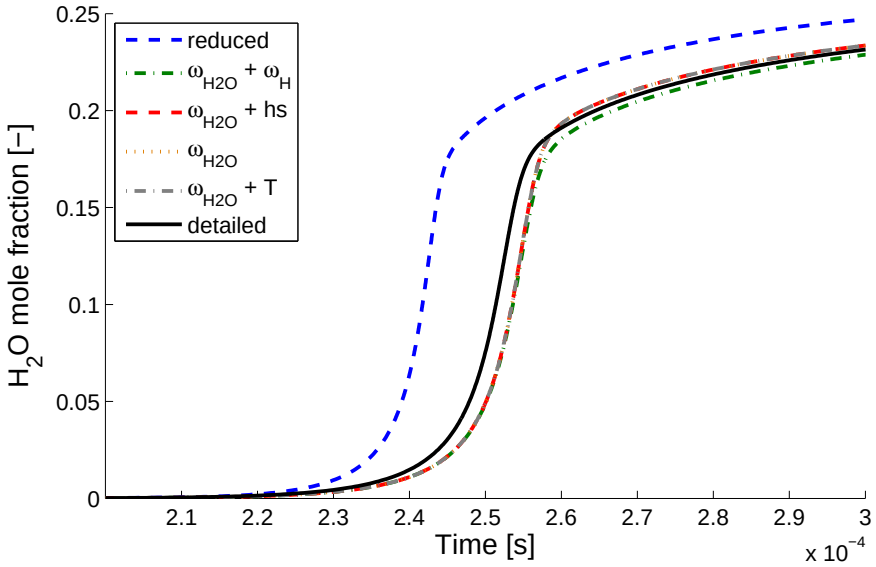

Figure 4.1: Profile of H_2O mole fraction for a reactor at $Z = Z_{st}$. The different curves are results from: the Sandiego mechanism [103] (black solid line), the reduced mechanism of Boivin et al. [5] (blue dashed line) and the tabulated chemistry with the source terms for H_2O and H (green dot-dashed line), for H_2O and h_s (red dashed line), for H_2O (orange dashed line) and H_2O and T (gray dot-dashed line).

When the reactor has a very lean or very rich mixture fraction, the accuracy of the linear interpolation is not as great, see Figure 4.2. The reduced mechanism is again too fast especially for lean mixture fraction. But it recovers correctly the evolution slopes of the species and the temperature. And the equilibrium state reached by the reduced mechanism is nearly identical with the one of the detailed mechanism.

Concerning the tabulated chemistry, for the lean reactor the source terms are overestimated, resulting in the consumption of reactants that are not present in reality. For the rich reactor, the choice of H_2O for the progress variable was not adequate because it reaches its equilibrium value before other scalars. Therefore all source terms were set to zero although some species and the temperature did not reached their equilibrium values.

To overcome those problems, the correction made was to define the progress variable based on $H_2O + HO_2$ and to have a threshold to stop the chemistry

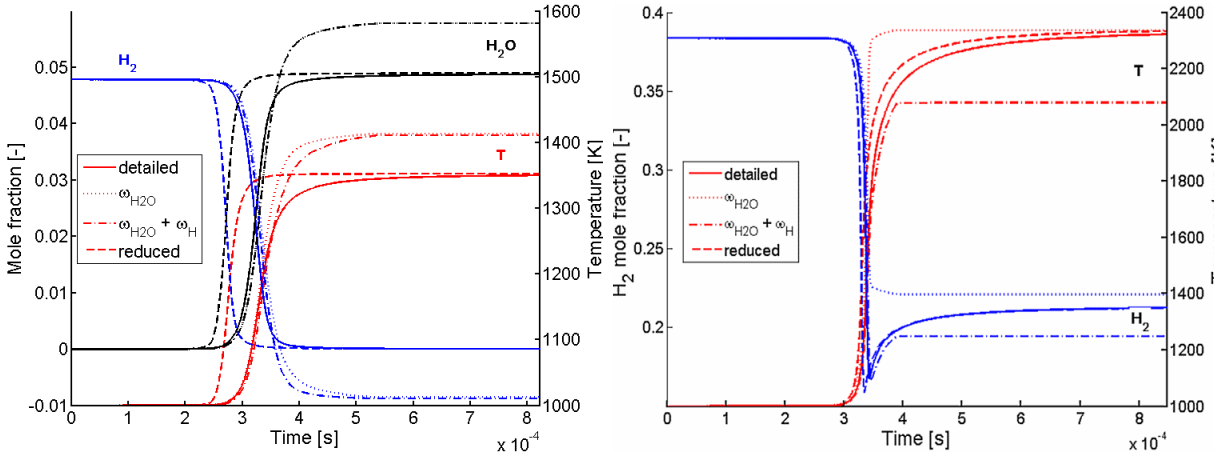

Figure 4.2: Profiles of H_2 and H_2O mole fractions and the temperature for lean (left) and rich (right) reactors. The different curves are results from: the Sandiego mechanism [103] (solid line), the reduced mechanism of Boivin et al. [5] (dashed line) and the tabulated chemistry with the source terms for H_2O and H (dot-dashed line) and for H_2O (dotted line).

(i.e. set source term of the progress variable to zero) when the equilibrium is reached. The implementation was further improved by relaxing the species mass fractions instead of interpolating their source terms into tables. This allows in particular to reach the proper equilibrium values. The results for the temperature are shown in Figure 4.3.

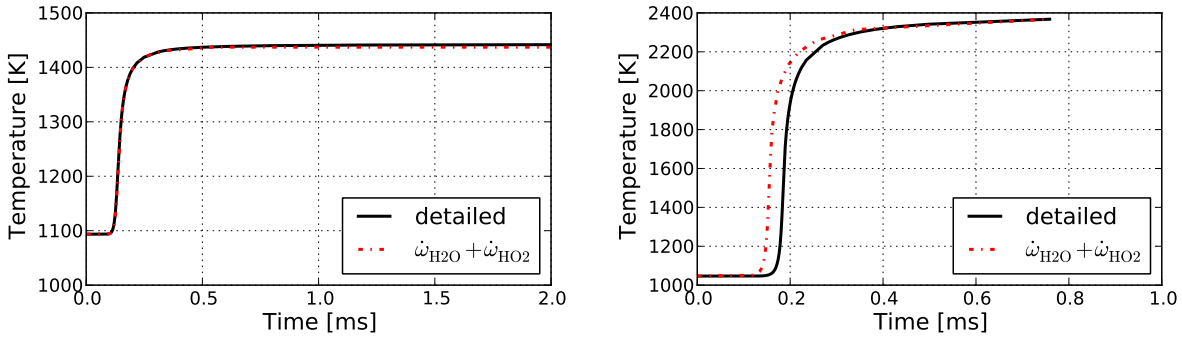

Figure 4.3: Temperature profiles in the homogeneous lean (left) and rich (right) reactors after correction.

These first tests highlight the importance of defining the progress variable from a product species combined with an intermediate one for auto-ignition cases. The choice of the intermediate molecules can be based on the analysis of the initiation reactions as done by Brandt [8] for methane. Those studies

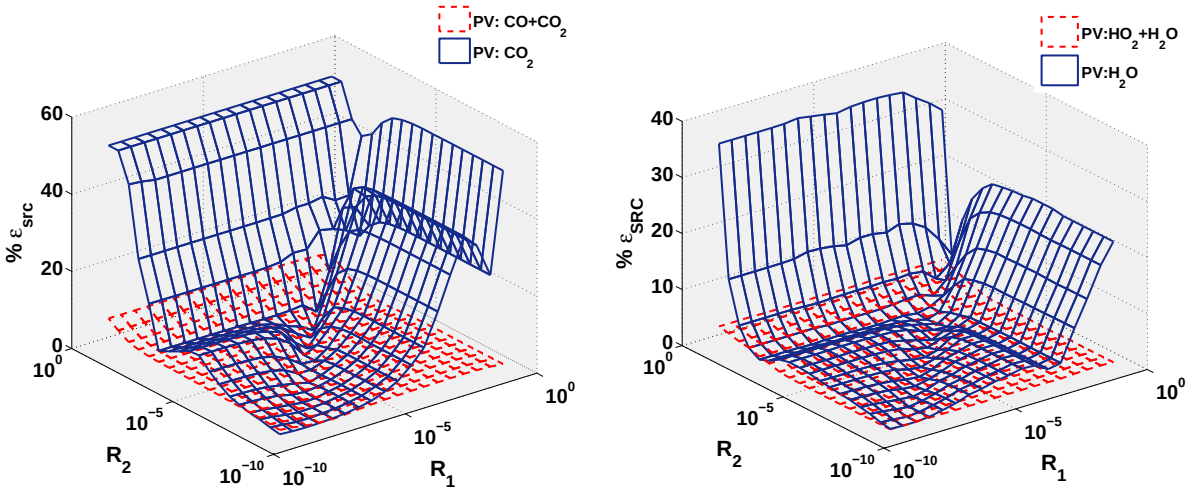

Figure 4.4: Errors in source terms for methane (left) and hydrogen (right) for different definition of the progress variable. R_1 and R_2 are the reactivities of the reactors before mixing. The reactivity is defined here as $R = Y_c/Y_c^{\text{ign}}$, with Y_c^{ign} the value of the progress variable at ignition.

identified CO and CH_2O as crucial intermediates for methane and HO_2 for hydrogen.

In a 3D simulation, mixing and reactions take place simultaneously. However the current model separates them. Therefore the mixing might lead states not covered by the look-up tables generation. To investigate the simultaneous effect of mixing and reaction, a test case based on homogeneous reactors at constant pressure was designed.

Two homogeneous reactors with different initial compositions (i.e. different mixture fractions) are run in time up to given progress variable values (different for each reactor). Then those two reactors with different mixture fraction and progress variable states are mixed together to create a new homogeneous reactor, called "*mixed reactor*". That mixed reactor is run in time up to equilibrium once computing the chemical source terms with detailed chemistry (subscript *det*) and once interpolating them from tabulated chemistry (subscript *tab*). An error can be defined based on the evolution of the progress variable source term after the mixing of the two initial reactors have been carried out[1]:

$$\epsilon = \left| \frac{\dot{\omega}_{\text{det}} - \dot{\omega}_{\text{tab}}}{\dot{\omega}_{\text{det}}} \right| \tag{4.2}$$

[1] Another definition based on the ignition time of the mixed reactor gave similar results.

That error is always drastically reduced when adding an intermediate species to the progress variable definition, see Figure 4.4.

4.1.2 One-dimensional mixing layer

From the previous test case, the best implementation of the tabulated chemistry model have been chosen; i.e. the species source terms are computed by relaxation insuring the element balances and the source term for the energy is derived from Equation (3.4).

This second test case was used to assess the accuracy of the model when mixing and reactions were taking place simultaneously in a more realistic configuration than the arbitrary mixing of reactors. Moreover this test case will validate the definition of the composite progress variable (i.e. composition of a product and an intermediate species).

For 1D mixing layers, the equations of conservation Eq. (2.1), (2.2), (2.3) and (2.6) have to be solved in time and along one space dimension. The initial solution has a step shape with on one side the oxidant conditions and on the other the fuel conditions. The time evolution of the system can be divided into three phases:

1. A mixing period in which initiation reactions are active without heat release.
2. The auto-ignition event occurs.
3. The system stabilized in a diffusion flame configuration.

4.1.2.1 Comparison of the chemistry models

The validation test case is a one-dimensional mixing layers with fuel (14% in mass of hydrogen diluted in nitrogen) on one side at 1000K and on the other side hot air at 1100K. The pressure is constant and equal to 1 atm. The hydrogen mixes with the air by diffusion only. Due to the elevated temperature, the chemistry quickly produces radicals up to ignition. The ignition has the characteristic pattern of a triple flame with two premixed branches appearing at the ignition spot for a short time followed by a diffusion flame. The ignition spot appears at a mixture fraction smaller than the stoichiometric value. This is expected, since the chemistry is faster at lean conditions for this initial settings; this is the most reactive mixture fraction.

As for the homogeneous reactor test case, the simulation was carried out using three different models for the chemical source terms: the Sandiego mechanism [103], a reduced mechanism [5] and the tabulated chemistry.

The code used to simulate the mixing layers is based on CHEMKIN routines. It was chosen to take H_2O as progress variable. And the variables transported for the tabulated chemistry were H_2, O_2, H_2O, and the temperature.

Figures 4.5 and 4.6 compare the production of H_2O with and without consideration of differential diffusion, respectively. In both cases the reduced mechanism is achieving accurate results. Two discrepancies can nevertheless be seen:

- A small overestimation of the autoignition delay,
- A quicker production of H_2O; the delay between the ignition and the peak of H_2O production rate is smaller than in the case of the detailed chemistry.

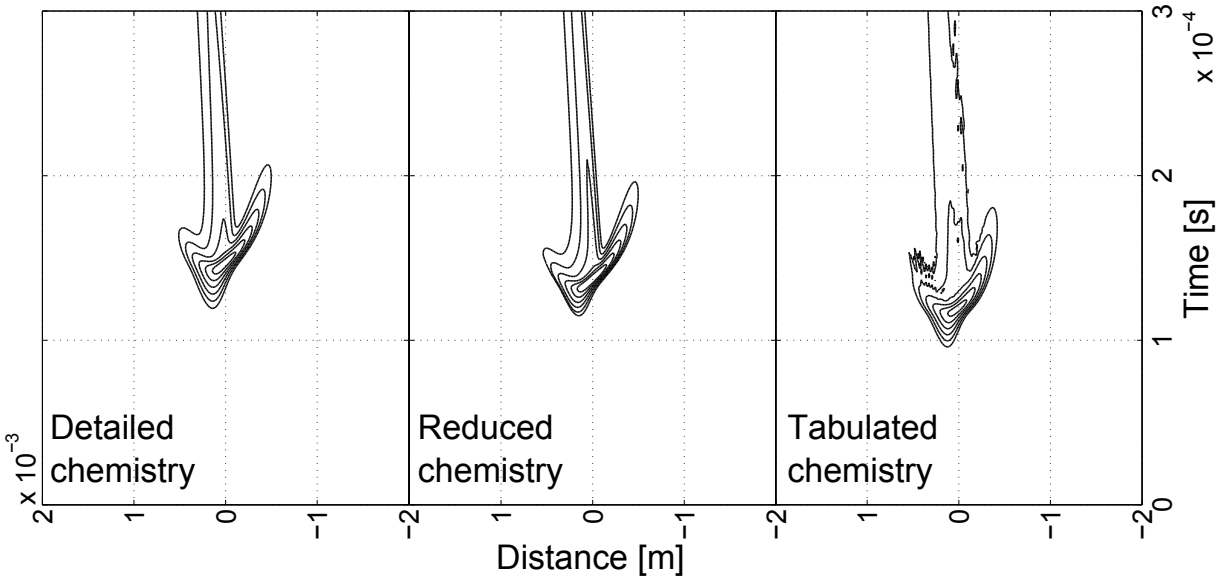

Figure 4.5: Iso-contours of H_2O mole fraction net production rate corresponding to $2^n \times 10^4$ mol/m^3/s for $n = 2$ to 7 in auto-igniting mixing layer – Air at 1100 K (left) / Fuel (right) at 1000 K – Le = 1. The horizontal axis is the space dimension and the vertical axis being the time one.

The main results from this test case are the overall good agreement of the tabulated chemistry with the detailed chemistry except in the diffusion

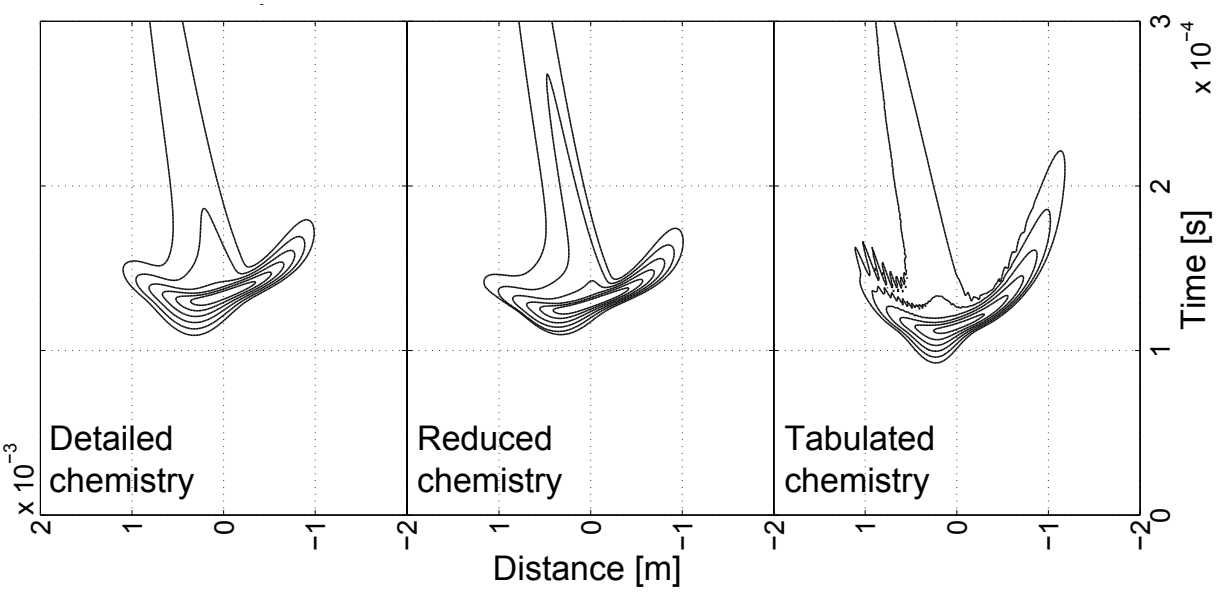

Figure 4.6: Iso-contours of H_2O mole fraction net production rate corresponding to $2^n \times 10^4$ mol/m^3/s for $n = 2$ to 7 in auto-igniting mixing layer – Air at 1100 K (left) / Fuel (right) at 1000 K – Differential diffusion. The horizontal axis is the space dimension and the vertical axis being the time one.

part of the flame. In the CHEMKIN routines, the progress variable was reconstructed from a unique species, H_2O. And so the differential diffusion coefficient of that species was applied to the progress variable. This explains the high fidelity obtained in the differential diffusion case. But if the progress variable is defined from a combination of species, the resulting differential diffusion coefficient will not be easily calculated. Therefore the results may be less accurate.

The auto-ignition delay is slightly underestimated by the tabulated chemistry. It was found to be an error when generating the table. The initial temperature was set using a linear interpolation with the mixture fraction. However it is the sensible enthalpy that has to be linearly interpolated to provide the initial energy state. This was corrected latter and tested on the same test case but using the implementation described in Chap. 3, see Figure 4.7 for the results with the correction.

The results for the detailed chemistry, for the reference table (101 points in Z space and 106 in C) and for the reduced table (41 points in Z space and 36 in C) are presented in Figure 4.7[2]. It can be seen that the agreement is acceptable up to ignition. But the diffusion flame is not captured correctly.

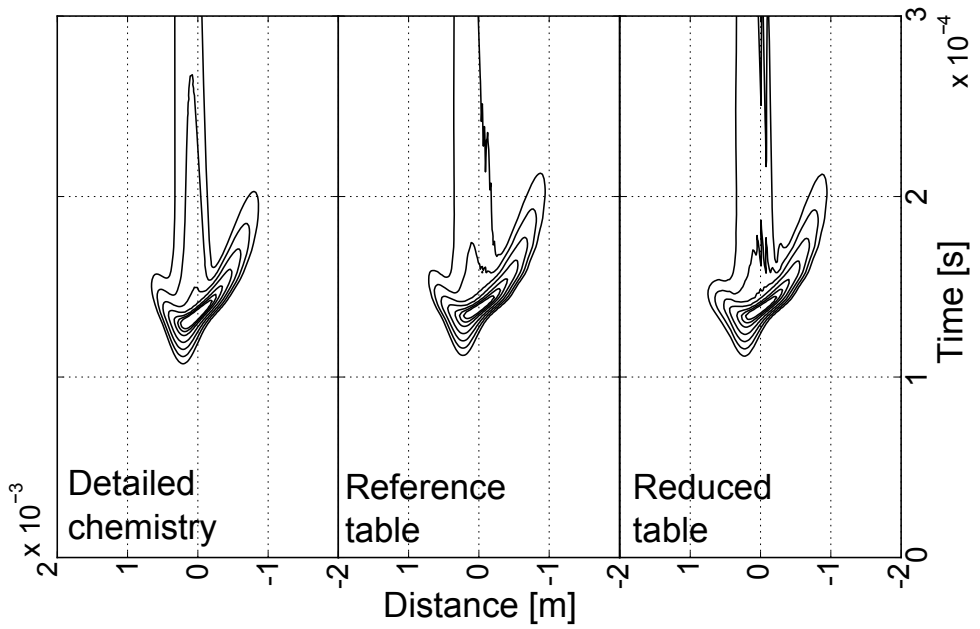

Figure 4.7: Iso-contours of Y_c source term corresponding to $2^n \times 62.5$ s^{-1} for $n = 1$ to 7. Comparison of the progress variable source term for the reduced table (41 × 36 points in (Z,C) space) against the reference one (101 × 106 points) – Air at 1100 K (left) / Fuel (right) at 1000 K – Le = 1. The horizontal axis is the space dimension and the vertical axis being the time one.

Moreover in the diffusion region the reduction of the table induced some erratic behavior of the source term in the rich area.

The discrepancy in the diffusion flame comes from an inadequate chemistry stored in the look-up tables. Indeed, in the diffusion flame, the reactants have to diffuse through a layer of burnt products to come into contact and react with each other. The presence of the burnt products change the reaction paths towards complete combustion in comparison with the chemistry happening in homogeneous reactor. Therefore the chemistry stored in the tables does not represent accurately the chemistry taking place in the diffusion flame. But the part related to the building of the radicals pool up to ignition is well captured. Consequently the chances are high that look-up tables based on homogeneous reactors predict correctly the auto-ignition spots regime observed in experiments.

[2] The point in progress variable dimension are distributed using the `loguniform` law with 5 points between 0 and 0.01.

4.1.2.2 Validation of the progress variable definition

This test case was also used to validate the definition of the progress variable based on an intermediate and a product species rather that a single product molecule [16]. This was done for methane and hydrogen using the boundary conditions for the hydrocarbon and hydrogen fuels given in Tables 4.1 and 4.2

	Species & Temperature	
Fuel	X_{CH_4}=0.33; X_{O_2}=0.15	320K
	X_{H_2O}=2.9e-4; X_{N_2}=0.52	
Oxidizer	X_{O_2}=0.12; X_{H_2O}=0.15	1350K
	X_{CH_4}=3e-4; X_{N_2}=0.73	

Table 4.1: Methane conditions

	Species & Temperature	
Fuel	X_{H_2}=0.69; X_{N_2}=0.31	750K
Oxidizer	X_{O_2}=0.21; X_{N_2}=0.79	950K

Table 4.2: Hydrogen conditions

The hydrocarbon case boundary conditions are from the Cabra methane flame [11] and the hydrogen case from the Cambridge experiment [78].

The errors between the tabulated chemistry and the detailed chemistry is assessed from the temperature field. Its definition is

$$\epsilon_T = \left| \frac{T_{\text{det}} - T_{\text{tab}}}{T_{\text{det}}} \right| \tag{4.3}$$

The evolution of this error will be analyzed from the initial state to the auto-ignition event.

Hydrocarbon

Figure 4.8 shows the errors in temperature between the tabulated chemistry approach and the detailed chemistry over the physical and the time dimensions. When the progress variable is only based on CO_2, the auto-ignition delay is underestimated and the acceleration of the chemistry is very stiff. This is seen as an early and faster increase in the error in the figure. In the contrary, when CO is added, the chemistry evolution during the initialization period as well as the acceleration (heat release) at the ignition point is captured more accurately.

Formaldehyde could have also been added to the definition of the progress variable. But the improvement is not as large as for CO.

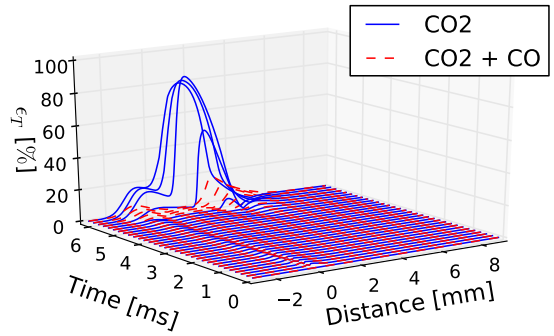

Figure 4.8: Error in temperature estimation between the detailed chemistry and the tabulated chemistry for autoignition of air and methane mixing layers.

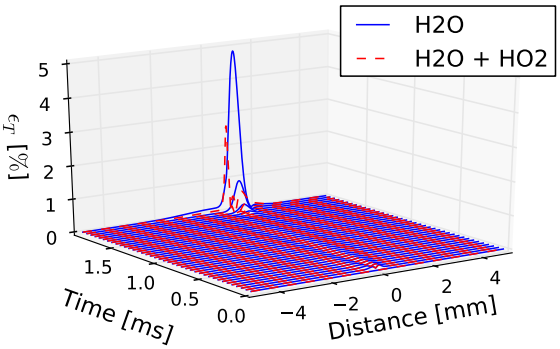

Figure 4.9: Error in temperature estimation between the detailed chemistry and the tabulated chemistry for autoignition of air and hydrogen mixing layers.

Hydrogen

The Figure 4.9 shows the results for the hydrogen mixing case. The error is very small during the initial state. This period corresponds to the mixing of the reactants by diffusion and the building of the intermediate species. The initialization reactions does not produce or absorb much energy. Consequently the temperature is constant in all simulations and the errors are low.

At the ignition point the temperature rises rapidly along with a faster build-up of the progress variable. The error is larger if only the final product, H_2O, is taken as progress variable. But it is reduced by adding a proper intermediate; in this case HO_2.

4.2 Turbulence-chemistry validation

At this point the generation of accurate and optimized look-up tables from homogeneous reactors is mastered. Therefore the validation can focus on the next step: the turbulence-chemistry interaction. Most of the tests were carried out on a configuration of auto-ignition spots simulated with a DNS code by S.G. Kerkemeier et al. [54, 56]. Those tests will be described first followed by simulations of the Cambridge experiments on the same kind of setup [75, 78].

4.2.1 Preliminary tests

Basic test case description

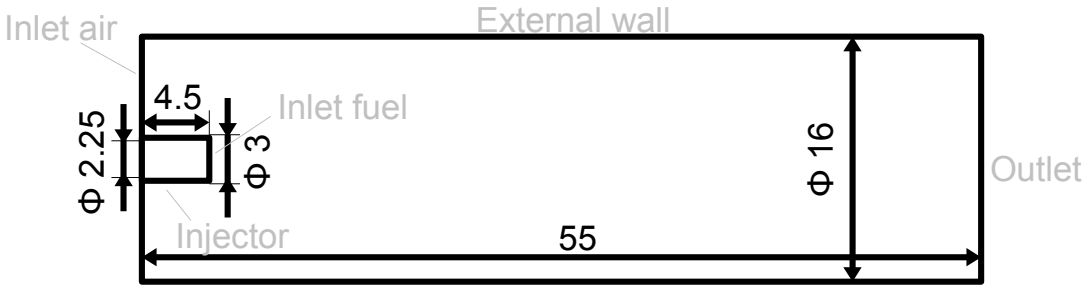

Figure 4.10: Description of the ETH DNS test case geometry (dimensions in mm). The turbulent inlet plane is shifted 4.5 mm upstream of the injection plane. The external tube has a diameter of 16 mm and a length of 55 mm.

The basic validation test case of the turbulent-chemistry interaction model is the one of S.G. Kerkemeier et al. [54, 56] – called later "*ETH case*". They carried out a DNS of auto-ignition spots appearing in a diluted hydrogen jet mixing with a turbulent co-flow of heated air. The settings are inspired from the experiments of Markides et al. [78] with small changes allowing a reduction of the geometry size. The external cylinder has a diameter of 16 mm and a length of 55 mm. A cylindrical injector of outer diameter 3 mm and inner diameter 2.25 mm is introduced within the tube as described in Figure 4.10. The boundary conditions are summarized in Table 4.3. The turbulence at the air inlet is generated using a digital filter approach [57] in the DNS. But another turbulence inflow generator was chosen in

OpenFOAM® – the vortex generator of Kornev et al. [59–62] – as its code source was available.

The injector is considered as an adiabatic wall with no-slip boundary condition. The external slip wall is set to zero-gradient for all scalar fields. At the outlet, the so-called `waveTransmissive` boundary condition was used for the pressure to let numerical pressure waves exit the computational domain. A further stabilization of the pressure field was obtained by using a reference pressure in the perfect gas law instead of the local pressure.

	Flow	**Species**	**Temperature**
Air inlet	$\langle u_{\text{air}} \rangle = 26$ m/s	$Y_{O_2} = 0.233$	945 K
	Turbulence intensity = 15%	$Y_{N_2} = 0.767$	
	Integral length scale $l_t = 3$ mm		
Fuel inlet	Parabolic profile with	$Y_{H_2} = 0.14$	855 K
	$\langle u_{\text{fuel}} \rangle = 26$ m/s	$Y_{N_2} = 0.86$	
Injector	Non-slip	No fluxes	No flux
External wall	Slip	No fluxes	No flux
Outlet	Fixed pressure (`waveTransmissive`)	No fluxes	No flux

Table 4.3: Boundary conditions for the ETH case

The DNS solver is a low Mach number code based on the spectral element method. The domain is discretized into 963,264 spectral elements approximated with 4^{th} order Lagrange polynomials.

The total time of simulation is 9 ms preceded by 4.23 ms of simulation without injection of hydrogen.

For the LES simulations, the generated O-grid mesh contains 183,696 cells with 134 x 52 x 32 cells in the axial, azimuthal and radial direction respectively. The cells are clustered towards the center line to accurately resolve the shear layer between the fuel jet and the hot co-flow.

The time-step was 1 µs and the total simulation time was 12 ms to obtain accurate time averaged data.

The ETH test case was first used to validate the micro-mixing model in the stochastic partial differential equation. The optimized number of stochastic fields will be then determined. Finally the influence of the turbulence model

will be analyzed. At that point, the model hypothesis will be frozen in order to move to the validation of the model and some physical analysis.

Stochastic differential equation

The Ito's formulation of the stochastic partial differential equation for scalar fields is:

$$\begin{aligned} d\xi_{n,k} &= -\tilde{u}_i \frac{\partial \xi_{n,k}}{\partial x_i} dt + \frac{1}{\bar{\rho}} \frac{\partial}{\partial x_i} \left(D_1 \frac{\partial \xi_{n,k}}{\partial x_i} \right) dt + \dot{\omega}_k dt \\ &- \frac{C_\phi}{2\tau_{\text{sgs}}} (\xi_{n,k} - \tilde{Y}_k) dt + \sqrt{2\bar{\rho}^{-1} D_2} \frac{\partial \xi_{n,k}}{\partial x_i} dW_i^n. \end{aligned} \tag{4.4}$$

In the literature, different values can be found for D_1 (coefficient of diffusion) and D_2 (coefficient in the Wiener term). From the theory [37, 111], $D_1 = D_2 = D^{\text{sgs}}$. But Jones et al. [44, 45, 47–50] are using $D_1 = D_2 = D + D^{\text{sgs}}$. Finally the theoretical formulation has been retained. But a drift term was added to the micro-mixing model following McDermott and Pope [83]; i.e. $D_1 = D + D^{\text{sgs}}$ and $D_2 = D^{\text{sgs}}$.

Figure 4.11 shows the instantaneous[3] mixture fields for the ETH test case. On top of it, three iso-contours of temperature – 1000, 1500 and 2000K – are plotted.

The formulation of Jones et al. yields the worst results as the simulation predicts a flash-back instead of auto-ignition spots. That inaccuracy can be also seen in Figure 5 of [48], where the ignition length reduces with time for boundary conditions corresponding to auto-ignition spots. As the Wiener term should be null in laminar flow[4], D_2 must be only related to the subgrid-scale diffusion coefficient. Therefore the formulation of Jones et al. was discarded.

The theoretical formulation does not capture properly the mixing of the fuel. Indeed as the jet coming from the injector is laminar, the diffusion acting close to the injector is mainly due to the molecular diffusion absent in the theoretical formulation. Therefore the spatial diffusion of the mixture fraction is not proper, leading to a higher penetration of the jet inside the co-flow. This effect is greatly enhanced in this case as the mesh resolution

[3] The snapshots are taken after 12 ms of simulation.
[4] In laminar flow, the turbulent composition PDF degenerates in a δ-PDF.

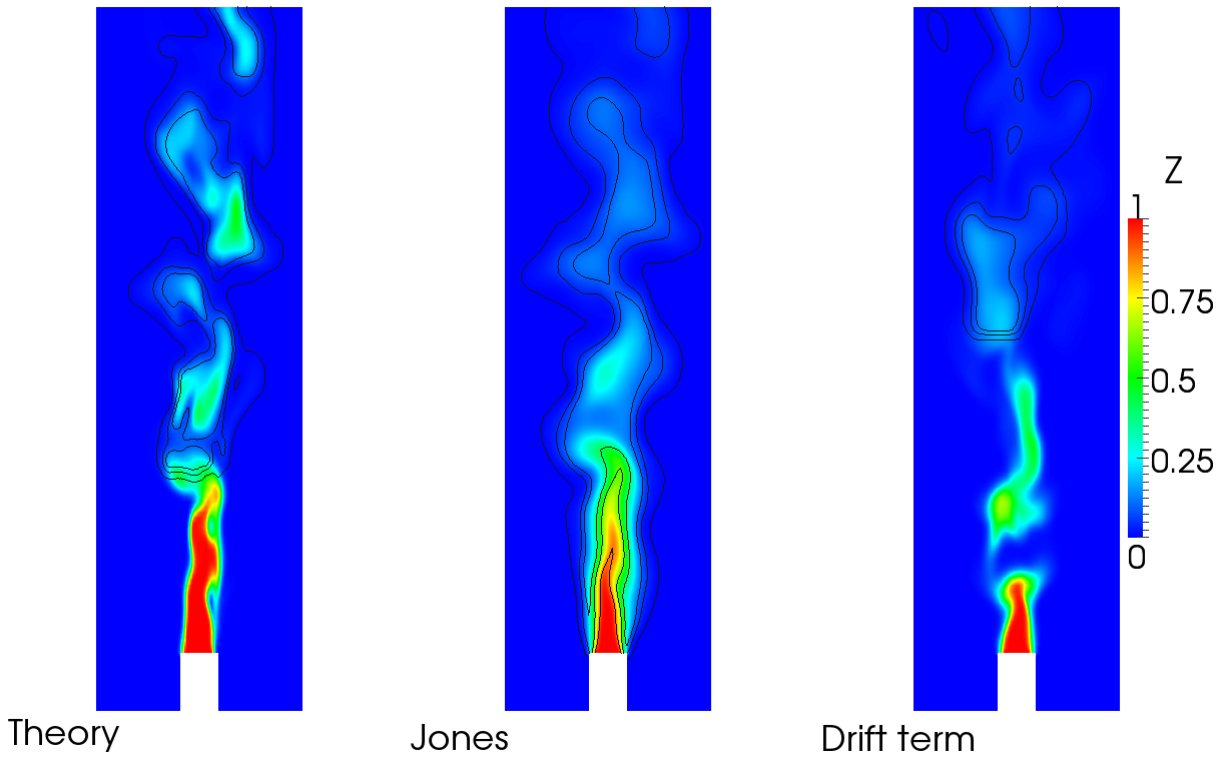

Figure 4.11: Comparison of different stochastic partial differential equation formulations: left from the theory [37, 111] – middle from Jones et al. [44, 45, 47–50] – right from the theory + drift term. The figures represent the instantaneous mixture fraction field after 12 ms of simulation on top of which are drawn in black iso-contours of temperature (1000, 1500 and 2000K).

is high. This is also the reason of adding a drift term as suggested by McDermott and Pope [83] to insure the convergence of the filtered equations towards the physical equations when the LES tends towards DNS.

Mathematically this can be proven by taking the expected value of the stochastic fields equation (Eq. (4.4)) to fall back to the filtered equation. As by definition, $E[\xi_{n,k}] = \widetilde{Y}_k$ and the Wiener process is zero in average.

$$\begin{aligned} dE[\xi_{n,k}] &= -\tilde{u}_i \frac{\partial E[\xi_{n,k}]}{\partial x_i} dt + \frac{1}{\bar{\rho}} \frac{\partial}{\partial x_i} \left(D_1 \frac{\partial E[\xi_{n,k}]}{\partial x_i} \right) dt \\ &\quad + E[\dot{\omega}_k] dt - \frac{C_\phi}{2\tau_{sgs}} (E[\xi_{n,k}] - \widetilde{Y}_k) dt \\ &= -\tilde{u}_i \frac{\partial \widetilde{Y}_k}{\partial x_i} dt + \frac{1}{\bar{\rho}} \frac{\partial}{\partial x_i} \left(D_1 \frac{\partial \widetilde{Y}_k}{\partial x_i} \right) dt + E[\dot{\omega}_k] dt. \end{aligned} \tag{4.5}$$

Equation (4.5) is identical to Eq. (2.19) if $D_1 = (D + D^{sgs})$.

Statistical convergence

An important but open question is the number of stochastic fields to be transported per scalar [49]. For this test case and the mesh used, the results are barely affected when varying the number of stochastic fields from 4 to 40 (see Figure 4.12). Two stochastic fields yield also acceptable results. But the heat release is more concentrated in comparison with the other simulations. This probably results of the underestimation of the subgrid-scale variance.

Despite the good results obtained for four stochastic fields, following Jones et al. [44, 45, 47–50], the default choice has been 8 fields to lower the statistical error while keeping the computational cost at an acceptable level.

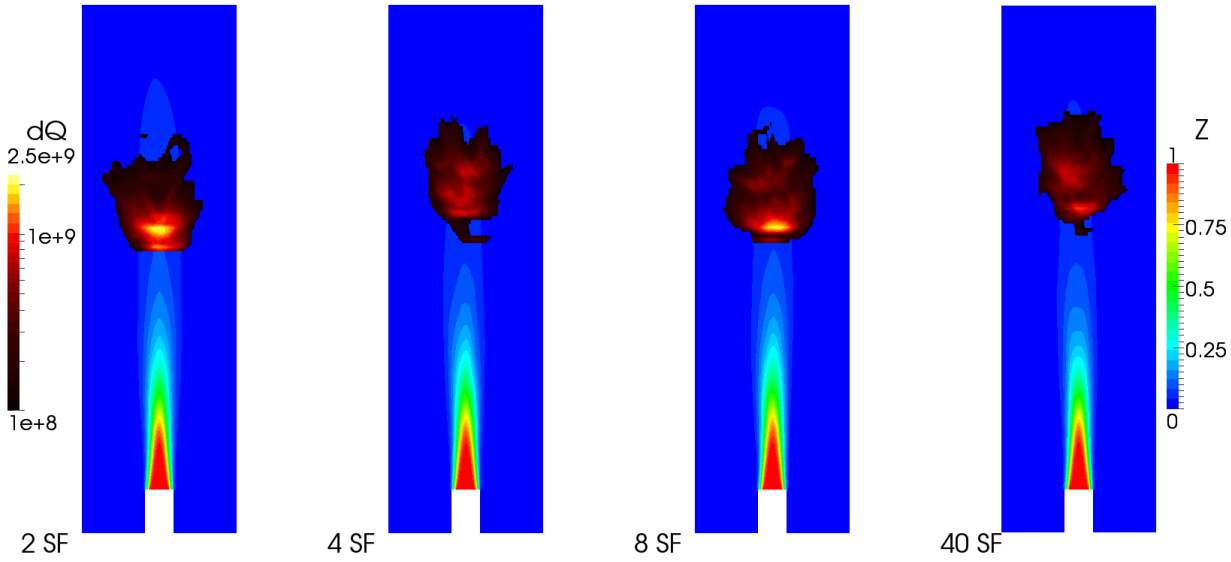

Figure 4.12: Influence of the number of stochastic fields. From left to right, 2, 4, 8 and 40 stochastic fields have been transported for each table parameters. The slices are painted according to the time averaged mixture fraction fields. Then on top of it, the cells in which the time averaged heat release is greater than $10^8\,W/m^3$ are shown.

As the influence of the number of stochastic fields was barely discernible, the mesh quality was assessed. In this case the so-called M criterion of Pope [97] and the M_z criterion of Boudier et al. [6] were used. The former estimates the proportion of turbulent kinetic energy modeled in the total turbulent kinetic energy. The latter is similar but for the proportion of

turbulent modeled mixture-fraction fluctuations in the total level of turbulent mixture-fraction fluctuations. Therefore M and M_z are equal to 1 in Reynolds average flows and 0 for resolved flows. Pope defines the threshold for a good simulation at 0.2; i.e. a good LES should resolve at least 80 % of the turbulent kinetic energy.

The results for the ETH test case are really good (Fig. 4.13). Only a small region close to the injection plane lacks in resolving a sufficient proportion of the turbulent fluctuations

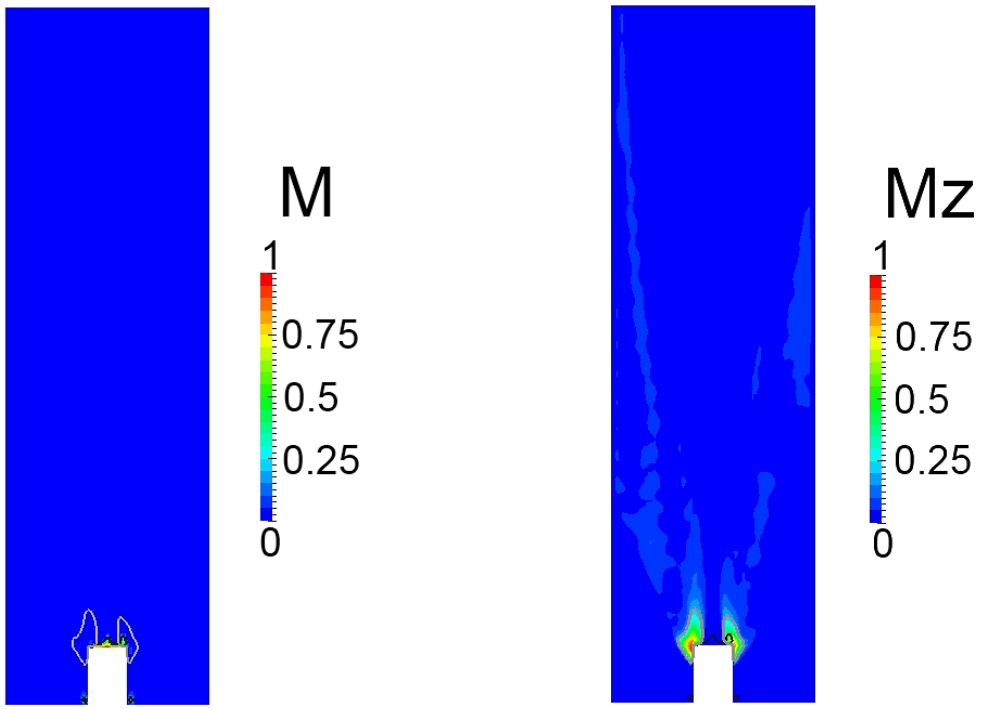

Figure 4.13: Mesh quality tests: left, M criteria of Pope [97] - right M_z criteria of Boudier et al. [6]. The black line corresponds at $M = 20\%$, the gray line at $M_z = 20\%$.

As suggested by Jones et al. [44, 45, 47–50], the Wiener process is approximated by dichotomic random values $\pm\sqrt{dt}$. But as the Wiener term should be statistically zero, the dichotomic values were not chosen randomly. Instead a list containing an equal number of $+\sqrt{dt}$ and $-\sqrt{dt}$ were randomly shuffled before being used in the stochastic differential equations. This improves the statistical convergence of the ESF method as shown by Akroyd et al. [2].

Turbulence models

The final test carried out was the influence of the turbulence model. The *dynamic Smagorinsky model* [70] and the *Wall-Adapting Local Eddy-viscosity model* (WALE) [87] were tested[5]. Two values of the constant for the WALE model were tried; 0.45 and 0.5. The Table 4.4 summarizes the average height of the *Auto-Ignition Spots* (AIS) for the different scenarios. The best results were found with WALE taking $C_w = 0.5$.

The results indicate that the turbulence model has a greater influence than the number of stochastic fields.

Model of turbulence	**Average AIS height**
Reference DNS	26.25 mm
Dynamic Smagorinsky	40.21 mm
WALE with $C_w = 0.45$	30.65 mm
WALE with $C_w = 0.5$	27.24 mm

Table 4.4: Average height of the auto-ignition spots (AIS) for different models of turbulence.

The turbulent inlet generator parameters (i.e. the integral turbulent length scale and the turbulent time scale) were kept constant for those tests and are identical to the one of the DNS. But Kulkarni et al. [63, 66] have performed an extensive study on those parameters, showing a non-monotonous dependence of the mean auto-ignition length with both the integral turbulent length and the turbulent intensity. The auto-ignition length was found to depend strongly on the turbulent time scale; showing a minimum when it was similar to the auto-ignition delay at $Z = Z_{\mathrm{MR}}$.

4.2.2 Validation on the ETH test case

The ETH test case was simulated in Fluent® and in OpenFOAM®. The comparison between the reference DNS and the two LES simulations was presented at the *Open Source CFD International Conference* 2011 [17]. The following section will summarize the main results.

[5] Those two were the one providing the best results in the simulations done by R. Kulkarni with Fluent.

The parameters in Fluent® and OpenFOAM® were chosen as alike as possible. In particular the subgrid-scale stress tensor is determined from the WALE model [87] with the constant equals 0.5. The Lewis number is assumed to be equal to 1. The subgrid-scale Schmidt number, Sc_t, is set to 0.85. The numerical schemes chosen are implicit second order in time, central schemes for the momentum equation and TVD schemes for the scalar equations in order to maintain the boundedness. One important difference between the 3 simulations is the turbulent inlet generator. The *digital filter* of Klein et al. [57] was used for the DNS, the *vortex generator* of Kornev et al. [60] for OpenFOAM® and the *spectral synthesizer* of Smirnov et al. [104] for Fluent®.

The generation of the tables based on homogeneous reactors was accomplished using Cantera [34] with the chemistry mechanism of Li et al. [69].

In this case, the tables are parametrized by the mixture fraction and the progress variable, Y_c. The latter has a composite definition: $Y_c = Y_{\mathrm{H_2O}} + Y_{\mathrm{HO_2}}$.

All following results are non-dimensionalized. The reference length l_{ref} is equal to the injector inner radius ($l_{\mathrm{ref}} = 1.125$ mm). The reference velocity is the average air flow velocity, $u_{\mathrm{ref}} = 26$ m/s. Consequently the reference time is $t_{\mathrm{ref}} = l_{\mathrm{ref}}/u_{\mathrm{ref}} \approx 43\text{e-}6$ s. Finally, the inlet fuel temperature ($T_{fuel} = 855$ K) is the reference temperature.

Phenomenology

Before presenting quantitative results, a qualitative study of the auto-ignition event will be carried out. A relevant auto-ignition spot appearance and its development are shown in the instantaneous snapshots of Figure 4.14. The slices are colored according to the progress variable source term in the cells and the two contours represent Z_{MR} (solid line) and Z_{st} (dashed line). The left figure is taken when auto-ignition occurs; i.e. the progress variable source term in one cell increases steeply. The right figure shows the propagation of the same auto-ignition spot.

Table 4.5 compares the observation done by Kerkemeier et al. [55] on auto-ignition spots occurring in turbulent flows (2D DNS) and the LES results.

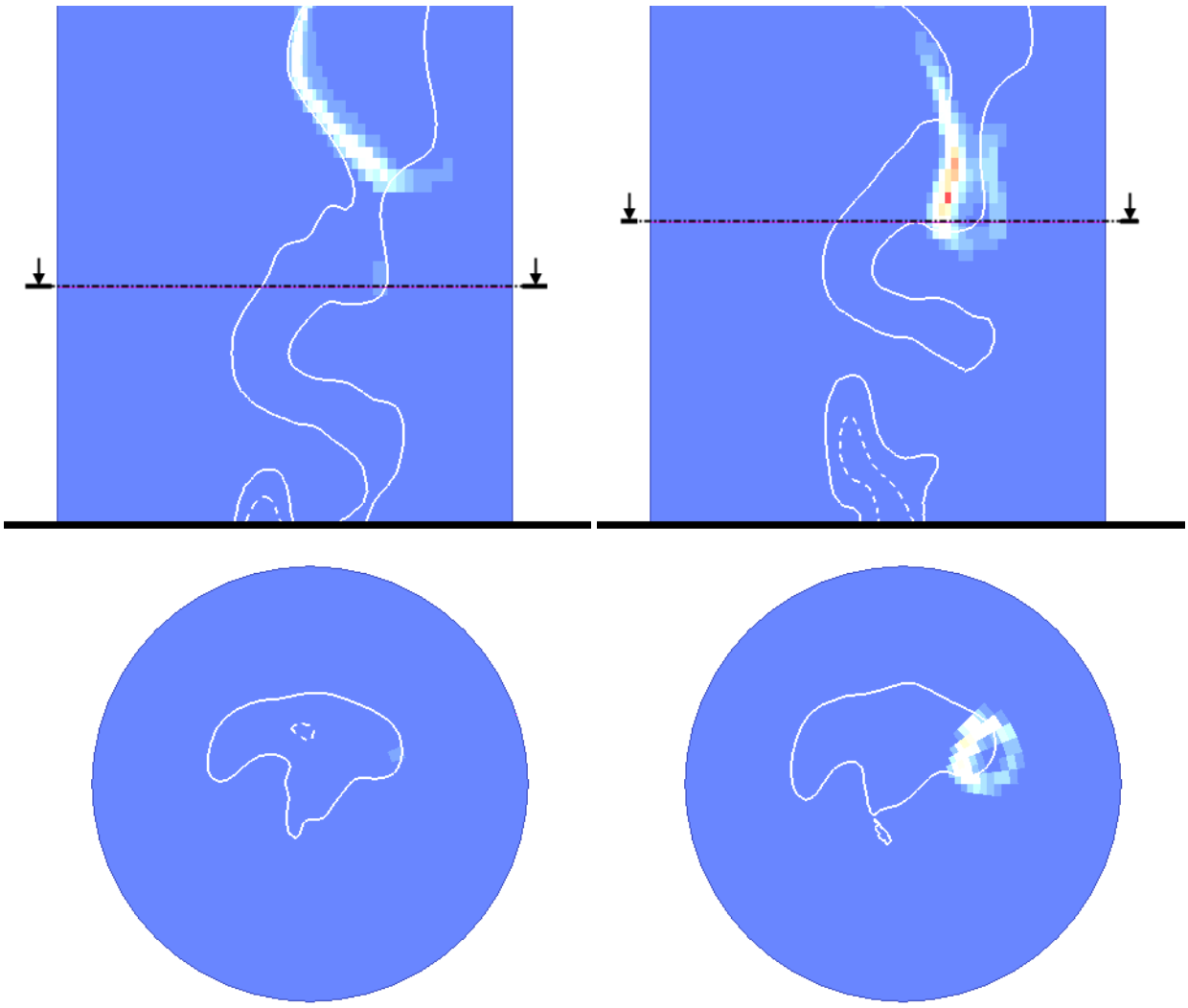

Figure 4.14: Initiation (left) and propagation (right) of an auto-ignition spot. The solid line is the most reactive mixture fraction iso-contour (Z_{MR}=0.04) and the dashed line the stoichiometric mixture fraction iso-contour (Z_{st}=0.17).

Observations	2D DNS	LES
AIS on Z_{MR}	X	X
AIS only at low χ_Z	X	X
AIS in regions concave towards the air	X	-
Spherical propagation	X	X
Stronger propagation on the rich side	X	X

Table 4.5: Comparison of auto-ignition spots structure between the LES simulation and the 2D DNS of Kerkemeier et al.[55].

All observations done in DNS simulation of auto-ignition are retrieved in the LES except one. It was seen in the DNS that a region concave towards

the air has a higher probability to be an auto-ignition site. The reason invoked is the higher concentration of radicals into a lean-mixture volume due to the diffusion. The discrepancy may be related to the resolution of the LES and the subgrid-scale model.

Once the auto-ignition spot appears, it develops roughly spherically with a stronger chemistry on the richer side – the lean side lacks fuel to sustain the reaction. Eventually it expands through the tube formed by the mixture-fraction iso-contour $Z = Z_{\mathrm{MR}}$ forming a flamelet that can survive in the flow for a certain amount of time (see upper-left figure in Fig. 4.14). That flamelet may stay in place; its propagation compensating the convection by the flow. But most of the time the convection is too strong and transports the structure outside the computational domain or extinction occurs.

In the Cambridge experiments, the flamelets grew around a kernel with an average cross-stream flame speed between 0.6 and 1.2 S_L [82]. A simple estimation in the LES simulation was done by approximating at different instants the surface of the spots in the cross section (similar to the lower part of Fig. 4.14). By presuming that the surface is a disc, a radius can be computed. Its time variation allows an estimation of the cross-stream flame speed. At an early stage, i.e. when the spot keeps a spherical shape, the flame speed is found to be between 1.0 and 1.3 S_L. The reference laminar flame speed was computed for the stoichiometric mixture corresponding to the inlet boundary conditions of the ETH test case.

In the 2D DNS, the tip of the established flamelets has the structure of a triple flame. This is not the case in the LES for two reasons. First, those structures are small and may not be resolved in the LES. Second element, the mixing in the 2D DNS is not as strong as in the 3D case. Therefore in the former case a structure of diffusion flame with the core of the jet remaining rich can occur. This is not possible in the 3D case (LES and DNS).

Flow field

The radial average velocity profiles for different heights are plotted in Figure 4.15. The LES simulations of Fluent® and OpenFOAM® are very similar at low heights. But further downstream the jet mixes more slowly in the two LES simulations than in DNS: the Fluent® simulation predicts the slowest decay of the jet velocity.

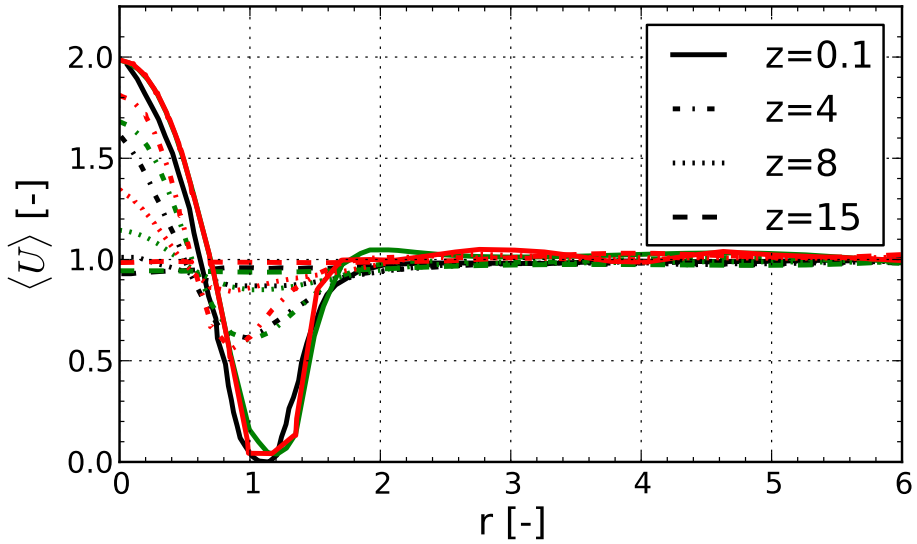

Figure 4.15: Radial average velocity profiles for z=0.1 (solid line), z=4 (dot-dash line), z=8 (dotted line) and z=15 (dashed line). DNS (black); OpenFOAM® (green); Fluent® (red)

Fuel mixing

The evolution of the average mixture fraction along the center line is well captured by the OpenFOAM® simulation (see Figure 4.16). The mixing is again faster in Fluent. For high values of z, both LES simulations reach a lower value than the DNS.

Directly at the injector, the mixture fraction stays constant, since the jet is not yet perturbed by the turbulent co-flow. But starting around $z = 4$, the vortices of the co-flow enter the fuel jet and the mixing takes place quickly.

Figure 4.17 illustrates the average scalar dissipation rate χ on the center line. In LES, the scalar dissipation rate is determined from $\chi = 2(D +$

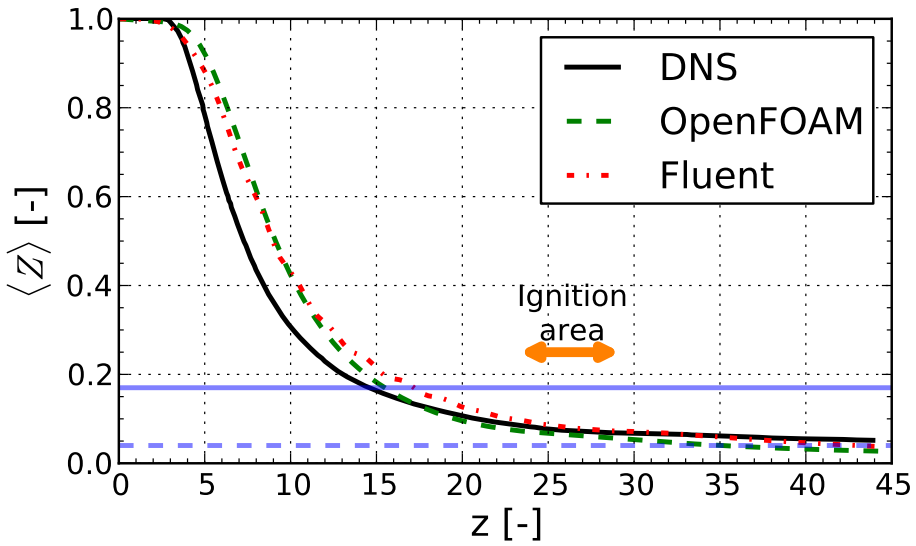

Figure 4.16: Average mixture fraction along the center line in the ETH test case. DNS (solid line); OpenFOAM® (dashed line); Fluent® (dot-dash line)

$D^{sgs}) \|\nabla Z\|^2$. Table 4.6 compares the magnitude and axial position of the peak. It is located where the turbulence is distorting the jet. The diffusion in the Fluent® simulation seems higher than in OpenFOAM®. Consequently, the slope of the mixture fraction decay is smaller. And the scalar dissipation peak is lower.

Max χ	DNS	OpenFOAM®	Fluent®
Peak position	5.8	7.2	6.5
Peak value	0.014	0.016	0.005

Table 4.6: Comparison of the scalar dissipation rate peak value and position on the center line.

Auto-ignition spots

As opposed to the DNS simulation, LES simulations bring difficulties to determine what an auto-ignition event is and where it takes place. This comes mainly from the coarser spatial and temporal resolution. Therefore only indirect comparison is carried out.

The auto-ignition spots distribution can be compared from the average heat release as shown in the Figure 4.18. It can be seen that the implementation

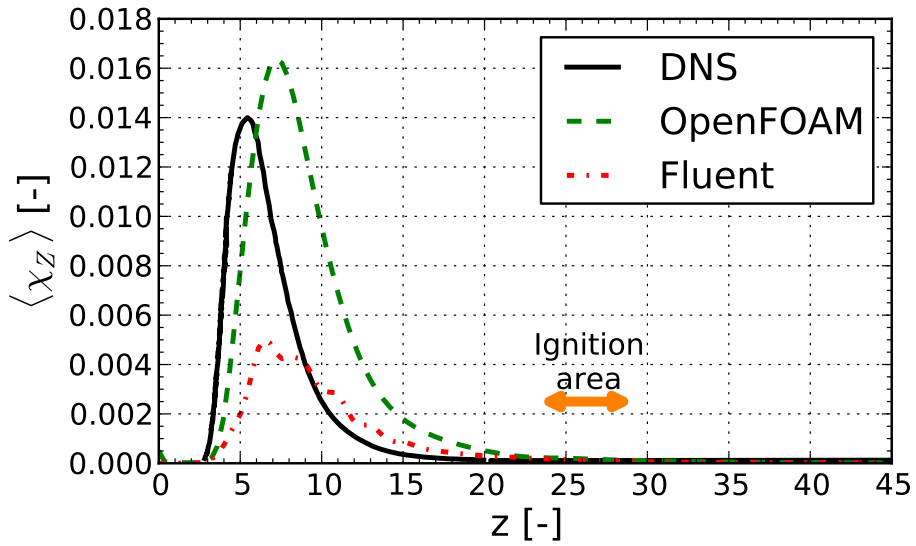

Figure 4.17: Average scalar dissipation rate along the center line in the ETH test case. DNS (solid line); OpenFOAM® (dashed line); Fluent® (dot-dash line)

in OpenFOAM® overestimates the heat release slightly due to the reduced set of species transported in the flow. This is even more pronounced in the lower part of the spots. However the radial spread is similar to the one of the DNS. Fluent® has similar results in the axial direction. But the spread in radial direction is reduced compared to the DNS.

The barycenter of the averaged heat release gives an estimation of the average positions of auto-ignition spots. In the DNS, $\langle r_{AIS} \rangle = 2.05$ and $\langle z_{AIS} \rangle = 26.25$. The barycenter of the heat release is in OpenFOAM® $(\langle r_{AIS} \rangle, \langle z_{AIS} \rangle) = (1.54, 27.24)$ and $(1.47, 28.52)$ in Fluent®.

The minimal auto-ignition length can also be compared. In the DNS, the lowest spot appears at $z = 23$. For the LES simulations, the temperature criterion [110] is used to determine that key length. It defines an auto-ignition event as the position at which the local maximal temperature reached 1% more than the nominal co-flow temperature (here 954.45K). The minimal auto-ignition length is 22.0 in the OpenFOAM® simulation and 22.3 for Fluent®.

According to Kerkemeier et al. [56], a crucial parameter linked to the auto-ignition spots is the conditional scalar dissipation rate on the most reactive mixture fraction, $\langle \chi | Z_{MR} \rangle$. Indeed the auto-ignition spot appear at Z_{MR}

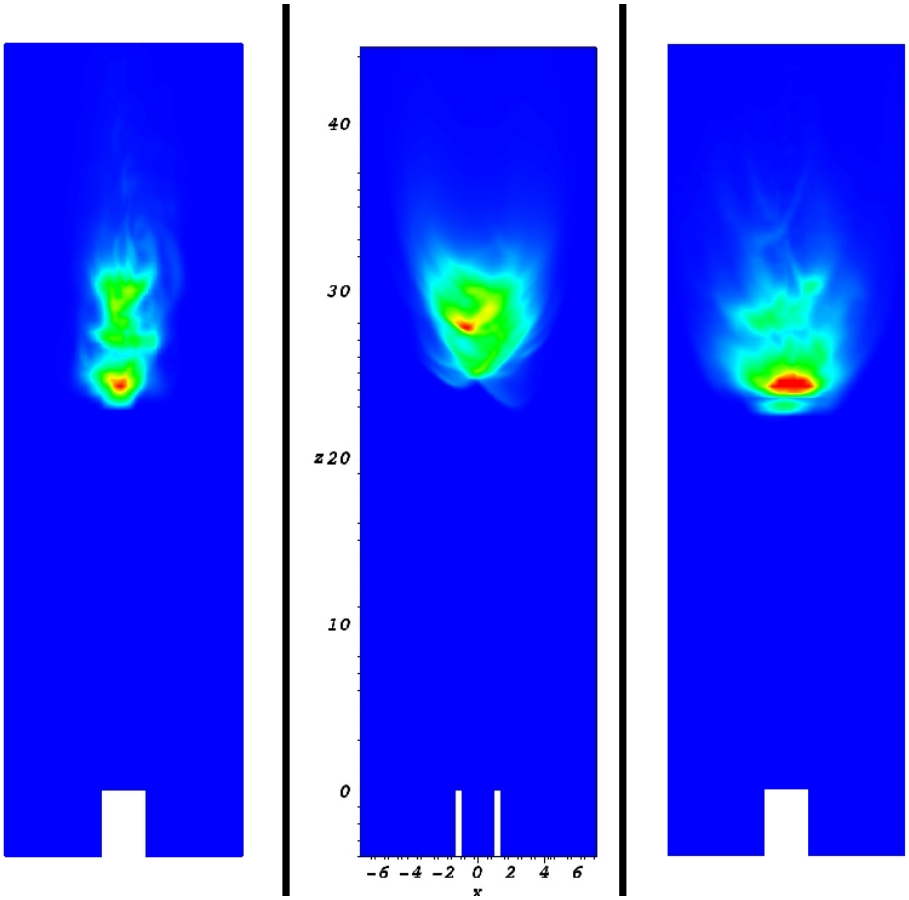

Figure 4.18: X-Z slice of the average heat release in the ETH test case. From left to right, the results are from Fluent®, DNS and OpenFOAM®.

(here equals to 0.04) and for very low value of the scalar dissipation rate. Figure 4.19 depicts the axial evolution of the conditional scalar dissipation rate.

The scalar dissipation rate is generally higher in OpenFOAM® than in Fluent®. This is a consequence of the lower diffusion in OpenFOAM® that sharpens the gradient and consequently increases χ.

The highest spatial resolution of the DNS reduces the error on the position of the iso-surface for which $Z = Z_{MR}$ and on the gradient computation. This is probably the reason for the discrepancy between the LES and the DNS data. But in all cases, the curve follows the same trend: a very quick decrease. The value in the auto-ignition spots area is then similar of the one encountered in the DNS.

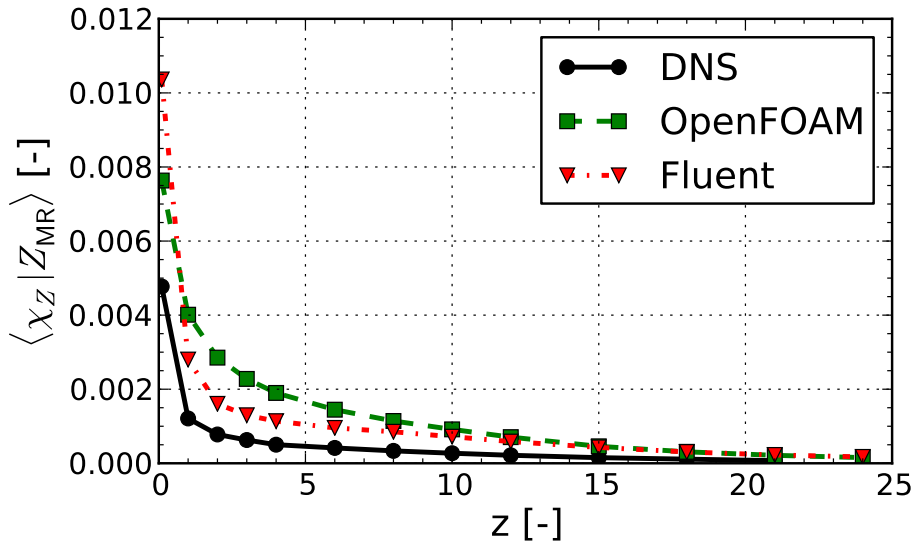

Figure 4.19: Axial evolution of the conditional scalar dissipation rate $\langle \chi | Z_{MR} \rangle$ in the ETH test case. DNS (solid line); OpenFOAM® (dashed line); Fluent® (dot-dash line)

Mixture evolution

The scatter plots in Figure 4.20 compare the distribution of the progress variable at different heights. Directly downstream of the injector, the chemistry is faster on the richer side (the stoichiometric mixture fraction is 0.17). Very quickly, the progression of the reaction is shifted around the most reactive mixture fraction. Further downstream, the peak moves slowly towards richer mixture fractions. And shortly after the minimum auto-ignition length, the progress variable reaches the distribution of post-ignition flamelet: the points are distributed between 0 and the equilibrium curve. Those observations are totally in agreement with the DNS.

From the scatter plots, one might conclude that the chemistry in the Fluent® simulation is a bit slower than in OpenFOAM®. However, this is not the case when looking at the auto-ignition spots positions (see Fig. 4.18). In fact, the scatter plots are always showing points of the same order – OpenFOAM® having only few points with higher values. As the chemistry is accelerating extremely quickly during an auto-ignition event, the spots appear at the same height.

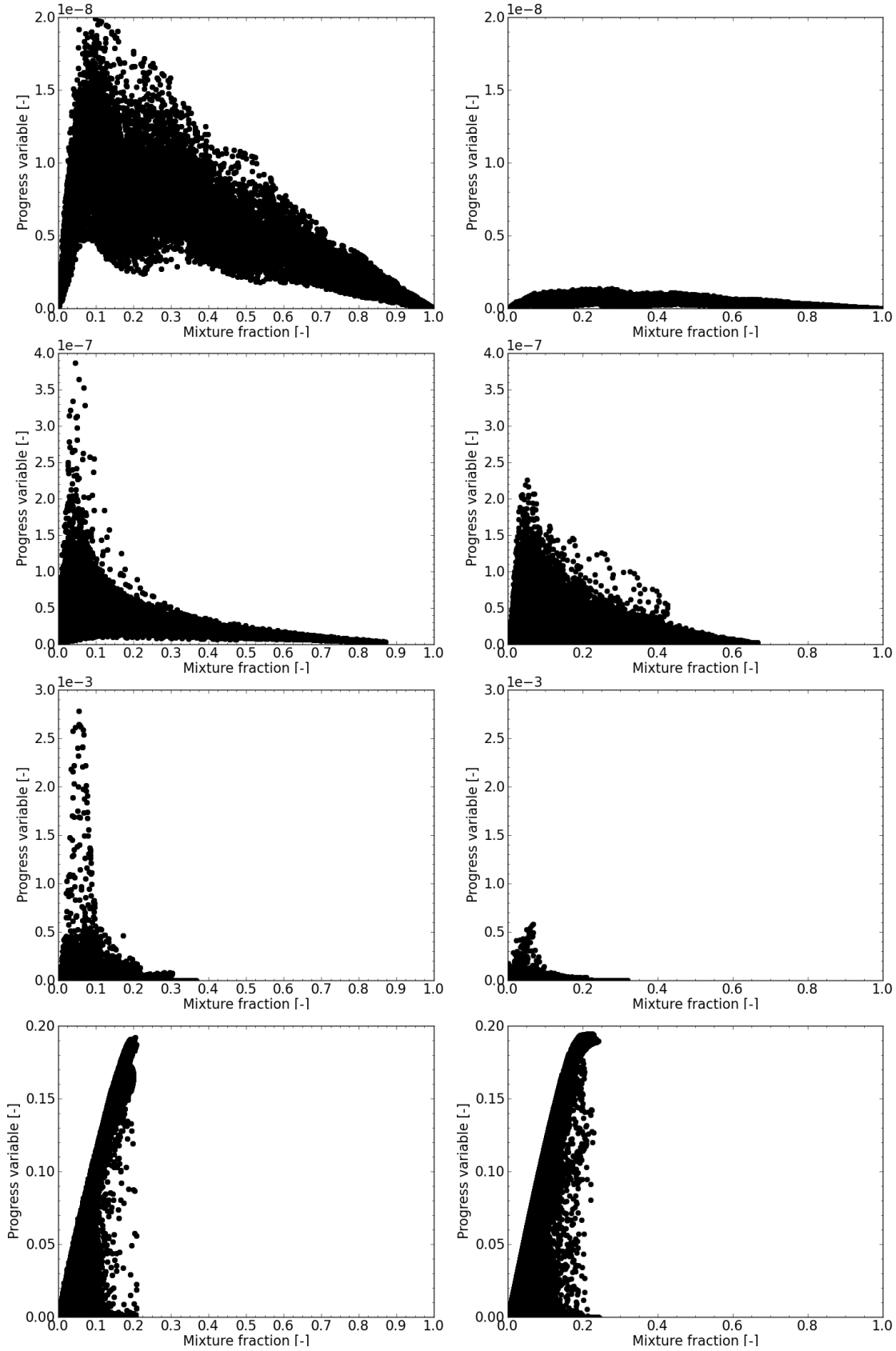

Figure 4.20: Scatter plots of the progress variable at $z = 1$, 10, 22 and 29 (from top to bottom) in the ETH test case. The left column is the results from OpenFOAM® and the right one from Fluent®.

On the effect of the scalar dissipation rate χ_Z

The mixture fraction dissipation rate χ_Z plays a major role in the turbulence-chemistry interaction analysis. In particular, auto-ignition spots are facilitated by low scalar dissipation rate values [82]. And Markides and Mastorakos [75, 77] showed that in their extensive experimental studies the key parameter was the scalar dissipation rate conditioned on the most reactive mixture fraction, $\langle \chi_Z | Z_{\mathrm{MR}} \rangle$. Any settings that will increase it will delay the auto-ignition events.

In the present model, the scalar dissipation rate is not taken explicitly into account in the chemistry. But the configuration being by essence non-premixed, χ_Z takes a wide range of values. Therefore, the importance of χ_Z in this simulation should be assessed. To evaluate the potential impact of the scalar dissipation rate, a possible way to take it into account in the model will be firstly depicted. Then the susceptibility of this simulation to χ_Z will be evaluated.

The unsteady-flamelet configuration is the most used to tabulate chemistry as a function of the mixture fraction, Z, the progress variable, Y_c, and the scalar dissipation rate, χ_Z [39]. However χ_Z being a function of Z (see Eq. (2.38)), each flamelet is more conveniently represented by the scalar dissipation rate at stoichiometric conditions, χ_{st} (unique for each flamelet). It can be easily determined from Eq. (2.39).

In Figure 4.21, the tabulated $\dot{\omega}_{Y_c}$ from unsteady-flamelets using the ETH boundary conditions is plotted. The unsteady-flamelets have been computed for scalar dissipation rate ranging from 0 s^{-1} (equivalent to homogeneous reactors) to 300 s^{-1} (roughly χ_i) using the software FlameMaster of H. Pitsch [92]. Higher values of the scalar dissipation rate won't result in auto-ignition.

The source term of the progress variable is highly variable with the mixture fraction. For the most-reactive mixture fraction, the building of the progress variable is almost insensible to the scalar dissipation rate during the initiation part. Then higher scalar dissipation rate results in higher production terms due to the diffusion of species from higher mixture fraction that speeds up the chemistry. For mixture fraction lower than the most reactive mixture fraction, the very beginning is independent of the scalar dissipation

rate. But very quickly higher scalar dissipation rate induces higher source term. Finally when moving towards stoichiometric conditions the scalar dissipation rate has the known behavior of decreasing the reactivity for a given progress variable value due to the radicals stronger diffusion.

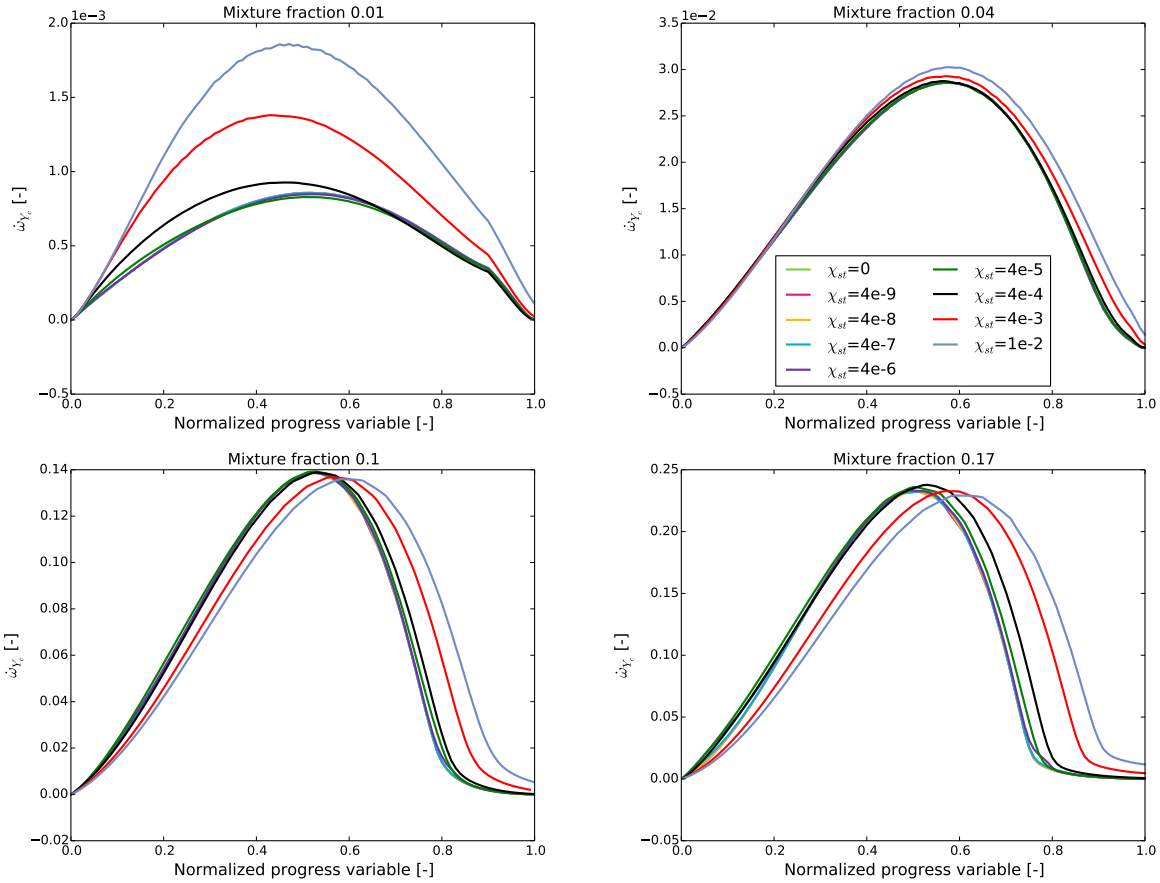

Figure 4.21: Non-dimensional $\dot{\omega}_{Y_c}$ as a function of the normalized progress variable from the tabulated unsteady-flamelets using the ETH boundary conditions for scalar dissipation rate ranging from 0 to 300 1/s at 4 mixture fractions: 0.01 (top left), 0.04 - most reactive (top right), 0.1 (bottom left) and 0.17 - stoichiometric (bottom right). The scalar dissipation rate have been non-dimensionalized using the reference time t_{ref} = 43e-6 s.

In the real simulation only a part of the chemical tables are used. In this case the highest scalar dissipation rates are only encountered close to the injector where the progress variable takes low values. And at those low values, it is not expected that the scalar dissipation rate will influence greatly the chemistry. To get a better idea of the values of the three key parameters (mixture fraction, scalar dissipation rate and progress variable), scatter plots of those parameters are presented in Figure 4.22 at four different heights (z = 1, 10, 22 and 29) corresponding to positions directly after the injector, right after

the highest mixing position, at the auto-ignition spots appearance and right after the auto-ignition appearance area.

The normalized progress variable has very low value up to the auto-ignition area. And as for those low values, the influence of the scalar dissipation rate is very low as seen in Fig. 4.21 for most value of the mixture fraction. It seems reasonable to neglect any direct influence of the scalar dissipation rate on the chemistry.

To verify the assessment that the scalar dissipation rate has a low impact on the chemistry, the scatter plots of $\dot{\omega}_{Y_c}$ in (Z, χ_{st}) space corresponding at the scatter plots of Fig. 4.22 are shown in Figure 4.23. Next to the injector,

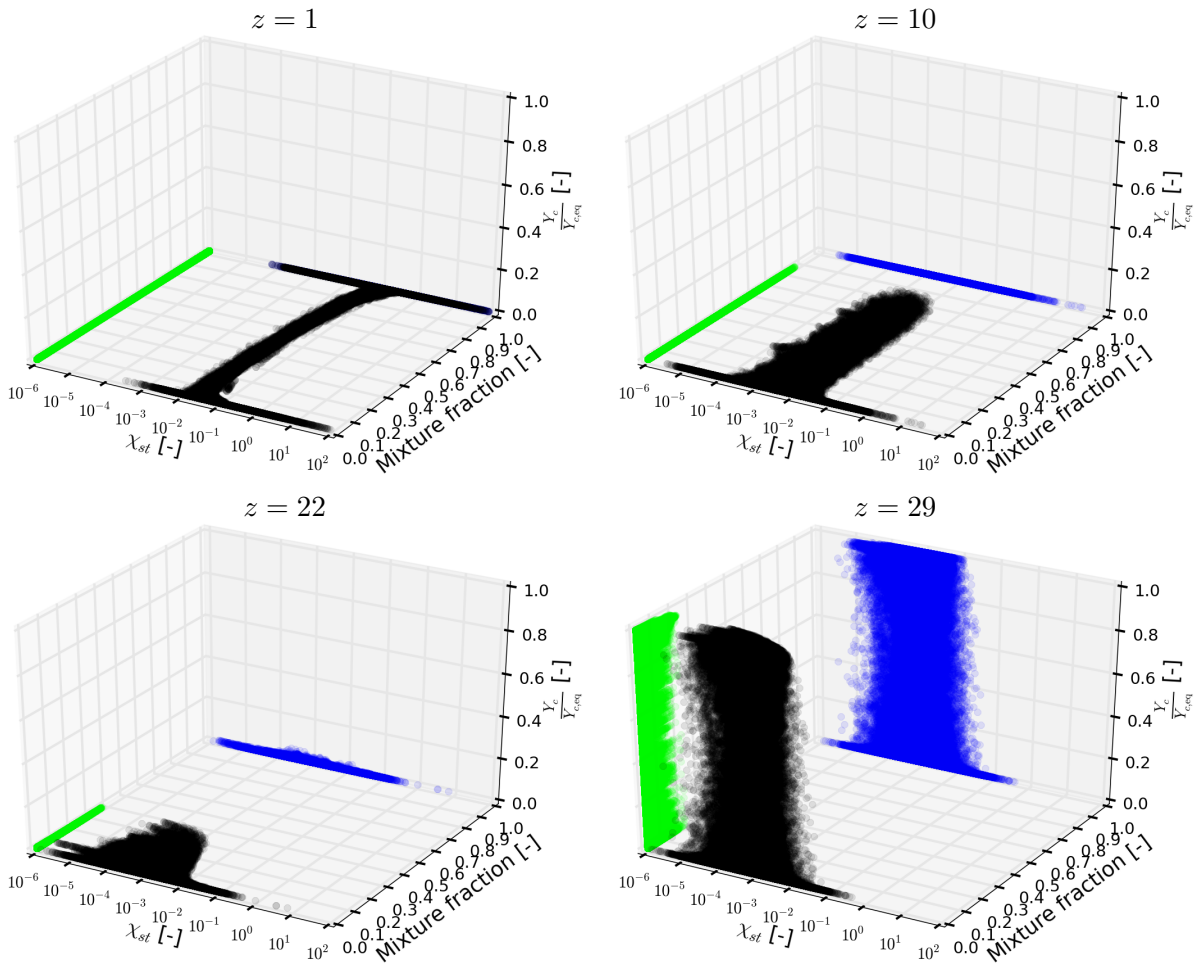

Figure 4.22: Scatter plots of normalized Y_c in (Z, χ_{st}) space at $z = 1$ (top left), 10 (top right), 22 (bottom left) and 29 (bottom right) in the ETH test case from the OpenFOAM® simulation. The black points are normalized Y_c in (Z, χ_{st}) space; the green their projection in the mixture fraction dimension and the blue their projection in the scalar dissipation dimension.

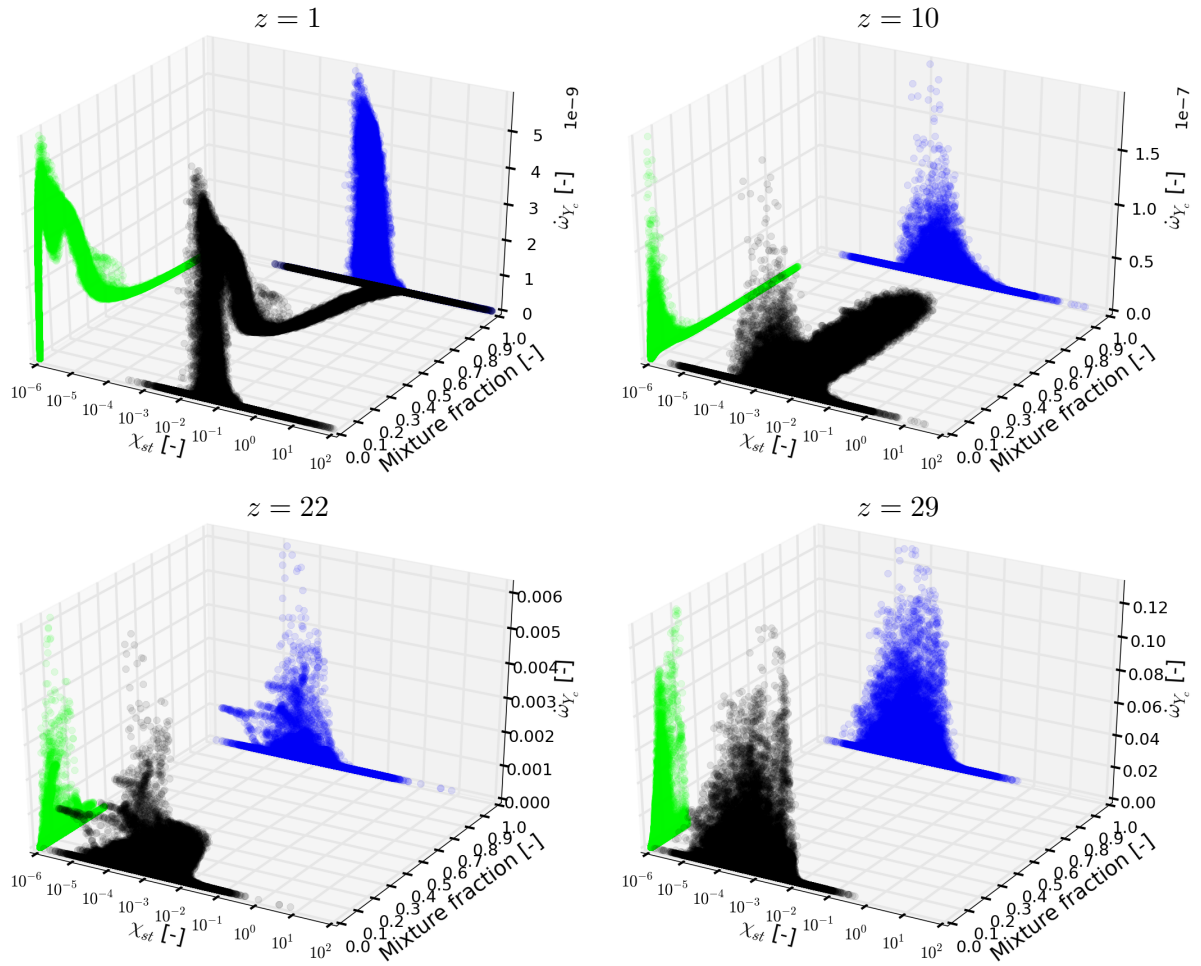

Figure 4.23: Scatter plots of $\dot{\omega}_{Y_c}$ in (Z, χ_{st}) space at $z = 1$ (top left), 10 (top right), 22 (bottom left) and 29 (bottom right) in the ETH test case from the OpenFOAM® simulation. The black points are $\dot{\omega}_{Y_c}$ in (Z, χ_{st}) space; the green their projection in the mixture fraction dimension and the blue their projection in the scalar dissipation dimension.

the scalar dissipation rate takes a value between 0.01 and 0.1 for the points having a non-zero $\dot{\omega}_{Y_c}$. For higher value of the scalar dissipation rate, $\dot{\omega}_{Y_c}$ is zero. The maximum source term being so low that any influence of the scalar dissipation rate will not have great impact on the future state of the particles. Further downstream, the maximum source term shifted to smaller χ_{st} values (around 0.001). The mixture fraction values corresponding to those high source terms are close to the most-reactive mixture fraction at which the scalar dissipation rate has almost no influence (see Fig. 4.21, top right). The points experiencing high scalar dissipation rate (> 0.1) have no active chemistry ($\dot{\omega}_{Y_c} \approx 0$). At $z = 22$, where ignition spots are occurring, for $\chi_{st} < 1e-4$ and $0.05 < Z < 0.22$, $\dot{\omega}_{Y_c}$ takes a great range of values

suggesting a low constraint of the scalar dissipation rate. As the normalized progress variable takes low values at that height (see Fig. 4.22), the look-up tables are nearly independent of the scalar dissipation rate (Fig. 4.21). For points with $\chi_{st} > 5e-2$ the chemistry is inactive. Finally further downstream, $\dot{\omega}_{Y_c}$ distribution seems independent of χ_{st} for $\chi_{st} < 0.01$ as the distribution of $\dot{\omega}_{Y_c}$ is similar for any value of $1e-5 < \chi_{st} < 0.01$.

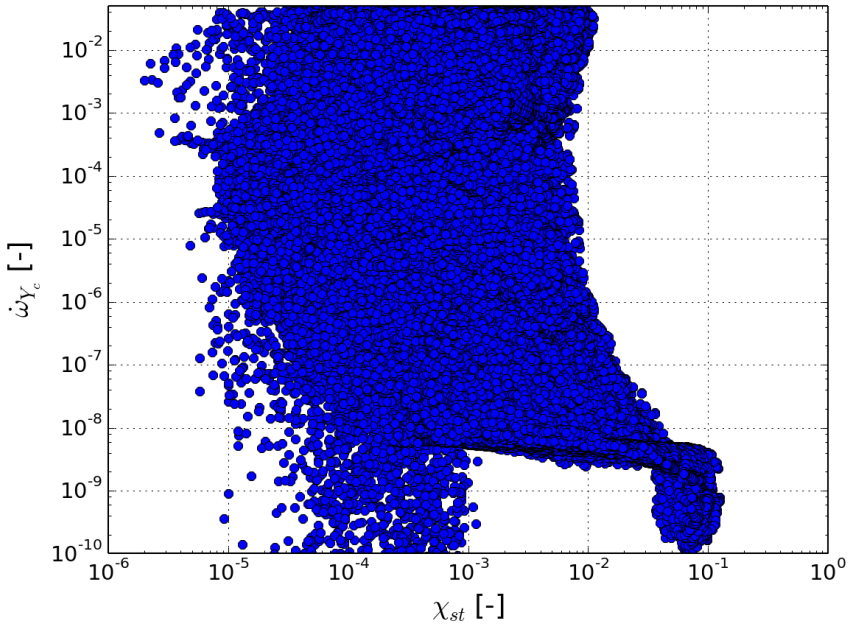

Figure 4.24: Scatter plot of $\dot{\omega}_{Y_c}$ against χ_{st} at $Z = Z_{\mathrm{MR}}$ in the ETH OpenFOAM® simulation.

To summarize the results, the scalar dissipation rate inhibits the chemistry when having a value superior to its quenching value even though the local χ_Z does not directly influence the tabulated chemistry. The points experiencing lower scalar dissipation rate have either low $\dot{\omega}_{Y_c}$ and will not trigger an auto-ignition spot, either a mixture fraction close to the most-reactive one. And for that mixture fraction and low Y_c, $\dot{\omega}_{Y_c}$ is not influenced by the scalar dissipation rate. The latter point is confirmed by Figure 4.24 that shows the distribution of $\dot{\omega}_{Y_c}$ with χ_{st} at $Z = Z_{\mathrm{MR}}$ in the ETH OpenFOAM® simulation. Indeed for $\chi_{st} > 0.03$, $\dot{\omega}_{Y_c} \approx 0$. For $\chi_{st} < 0.01$, $\dot{\omega}_{Y_c}$ takes values independently of χ_{st}. Only the points with $0.01 < \chi_{st} < 0.03$ have $\dot{\omega}_{Y_c}$ bounded with χ_{st}. But anyway, those points are not the most reactive and have few chances to contribute to an auto-ignition event. Therefore it seems fair to assume chemistry taking place in auto-igniting flow is similar to the one taking place in homogeneous reactor, the mixing along the mixture

fraction space (and so the scalar dissipation rate) having no direct strong influence.

Convection-Diffusion-Reaction balance

The scalar dissipation rate plays a important role in flows dominated by diffusion effects. Therefore another methodology to assess the influence of χ_Z in the current simulation is to evaluate the balance between the different terms of the progress variable transport equation Eq. (2.19); namely *convection*, *diffusion* and *reaction* (or in short *CDR*). Their numerical definitions, applied to OpenFOAM® data, are respectively:

$$\begin{aligned} \text{convection} &= -\frac{1}{\Delta V}\sum_{S_k}\bar{\rho}u_i n_i \widetilde{Y_c} S_k, \\ \text{diffusion} &= \frac{1}{\Delta V}\sum_{S_k}\left(\frac{\mu}{\text{Sc}}+\frac{\mu^{\text{sgs}}}{\text{Sc}_t}\right)\left.\frac{\partial \widetilde{Y_c}}{\partial x_i}\right|_{S_k} n_i S_k, \\ \text{reaction} &= \bar{\rho}\widetilde{\dot{\omega}_c}, \end{aligned} \tag{4.6}$$

where ΔV is the volume of the local cell, S_k all the faces of the local cell and n_i is the i-th component of the outwards normal to the S_k surface.

The summations over the cell faces are done using field values evaluated at the face center by linear interpolation from the cells sharing the face.

A general picture of the CDR balance will be first depicted from the time average CDR terms on the center line. But as the history of the fluid particle is presumed to be of primary importance to determine if it will result in an auto-ignition event or not, a particle tracer post-processing of the data will then be done. The evolution of the CDR terms along the tracer particle paths will provide deep insight of the predominant phenomena driving the flow.

The time average CDR balance on the center line is plotted in Figure 4.25. The pattern of the reaction source term being compensated by the convection term with (nearly) no diffusion is typical for auto-ignition case [35, 36]. The position of the reaction peak is coherent with the previous results and corresponds to the average position of auto-ignition spots.

In this particular case, the reaction takes place as soon as the scalar dissipation rate reaches a low value. But this is a mere coincidence of the boundary conditions and the extraction on the center line. Indeed for a axial line passing through the injector but not the center line, the peak in scalar dissipation rate will shift upstream, whereas the reaction peak will

stay at the same position – there is even a slight shift downstream (not shown).

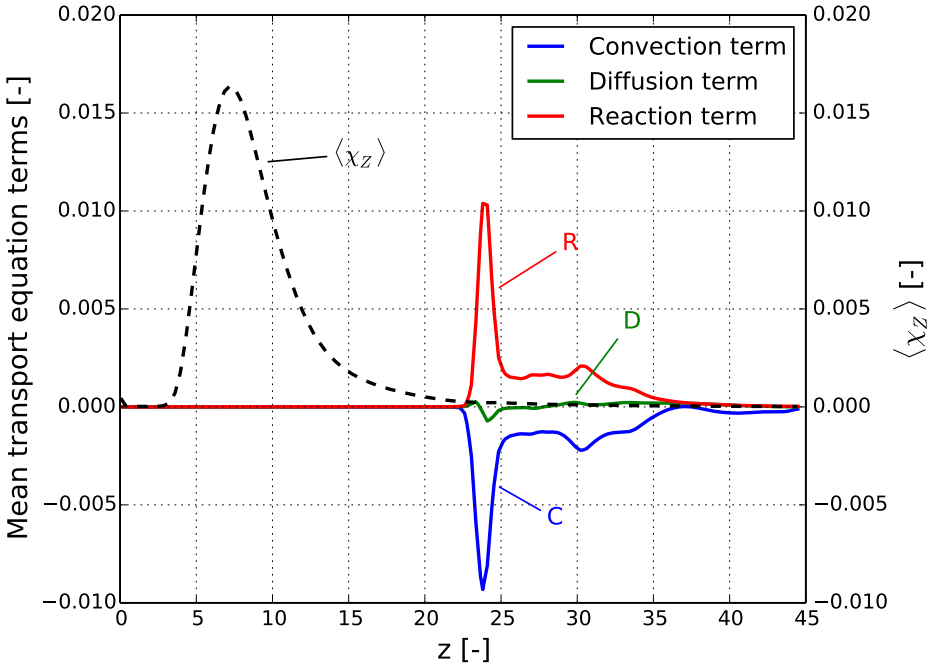

Figure 4.25: Convection (blue) – Diffusion (green) – Reaction (red) balance of the progress variable on the center line in the ETH test case (OpenFOAM® data). The scalar dissipation rate of the mixture fraction (black dashed line) is printed also for interpretation.

The diffusion being almost zero when the reaction takes place confirms the low influence of χ_Z in this simulation.

The auto-ignition spots regime is a highly fluctuating phenomenon. The analysis of instantaneous data and their history are more relevant than the time average fields. Therefore in parallel with the Eulerian solver, tracer particles where injected with the fuel at the rate of 70 particles per time-step resulting statistically in 2 to 20 particles per cell per time-step directly after the injector. The mesh being of high quality, the particles velocity were computed directly from the filtered velocity field without any dispersion model (i.e. subgrid-scale fluctuations have no effect on the particle trajectory).

To discard the particular case of the first AIS, the simulation ran for 3 ms[6] before turning on the injection during 1 ms. The flow being simulated for an additional 3 ms; time at which all particles have left the computational domain.

Those particles can be split in 3 groups:

- The initiating particles: they result in auto-ignition spots (Figures 4.26 and 4.28).
- The sustaining particles: their pattern is similar to the previous group but they reach the critical condition for AIS when being simultaneously absorbed by a flamelet surface (Figure 4.27).
- The propagating particles: the fuel consumption is triggered by the propagation of a flamelet surface (Figure 4.29).

It is worth mentioning that none of the particles left the domain unburnt[7].

The initiating particles encounter first a fast and strong mixing as shown by the variation of χ_Z. The resulting composition is close to $Z_{\mathrm{MR}} = 0.04$ (usually a bit higher 0.06-0.08). At this point the progress variable has barely increased. Then comes the chemistry initiation period during which the mixture fraction drifts up to Z_{MR}. The intermediate radicals build up, the progress variable grows slowly but steadily. Finally the radicals pool reaches a critical concentration. The *explosion* associated with the auto-ignition spots occurs. The steep rise in progress variable is then dissipated by convection and, to lower extent, by diffusion. The major proportion of the diffusion term is due to the radial component and not the axial one. This confirms the auto-ignition character of the combustion [36].

From reactor computation, the minimum auto-ignition time is about 23.5 reference times. This is higher than the time during which there is almost no mixing – i.e. no more influence of χ_Z (about 20 reference times). But it is shorter than the residence time at which the auto-ignition spots occur (about 30 reference times). Therefore the tiny growth of the progress variable during the strong mixing period is non-negligible although this mixing

[6] This is a bit larger than the flow-through time (= 2.1 ms).
[7] A particle was considered as burnt if completing 99% of the combustion.

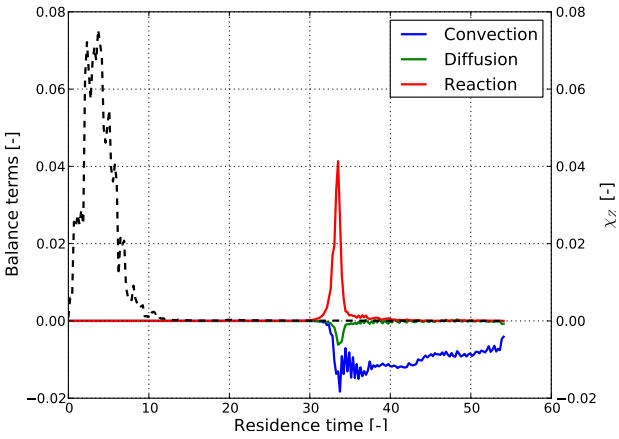

Figure 4.26: History of the CDR balance for a fluid particle resulting in an auto-ignition spots – 1st example.

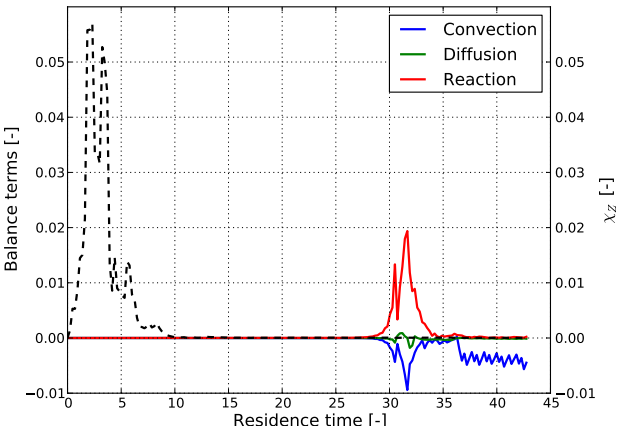

Figure 4.28: History of the CDR balance for a fluid particle resulting in an auto-ignition spots – 2nd example.

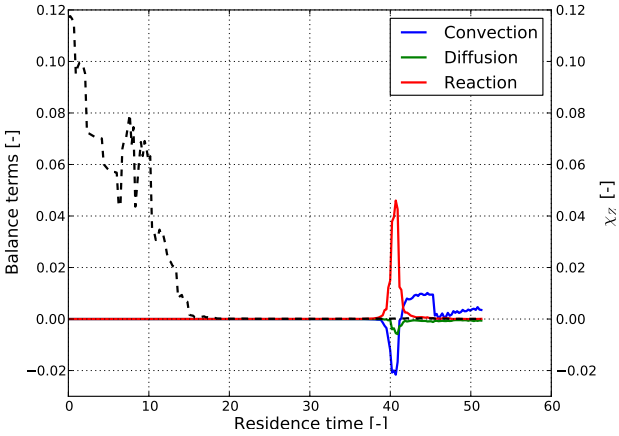

Figure 4.27: History of the CDR balance for a fluid particle sustaining a flamelet.

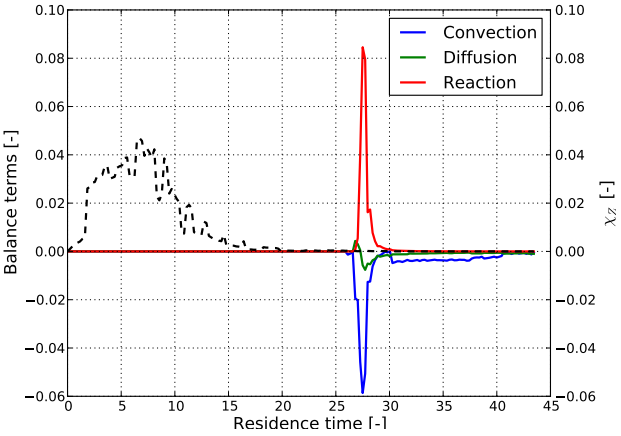

Figure 4.29: History of the CDR balance for a fluid particle starting to react by propagation.

increases the minimal ignition time. In other words, an auto-ignition event is not a sequence of mixing (high χ_Z with $\dot{\omega}_{Y_c} = 0$) followed by reaction (very low χ_Z with $\dot{\omega}_{Y_c} >> 0$). These two effects are on the contrary overlapping and influencing each other.

The sustaining particles have a history similar to the initiating particles (see Fig. 4.27). The main difference is that they are not corresponding to an isolated auto-ignition event. The explosion occurs very close to a flamelet front with which it merges immediately.

The last category of particles does not correspond to an auto-ignition event. Instead the combustion is triggered by a small increase in progress variable

by diffusion. This kind of particles encounters a lighter mixing (the mixture fraction scalar dissipation rate encountered was smaller). That results in a higher mixture fraction at the time the reaction starts, see Fig. 4.29.

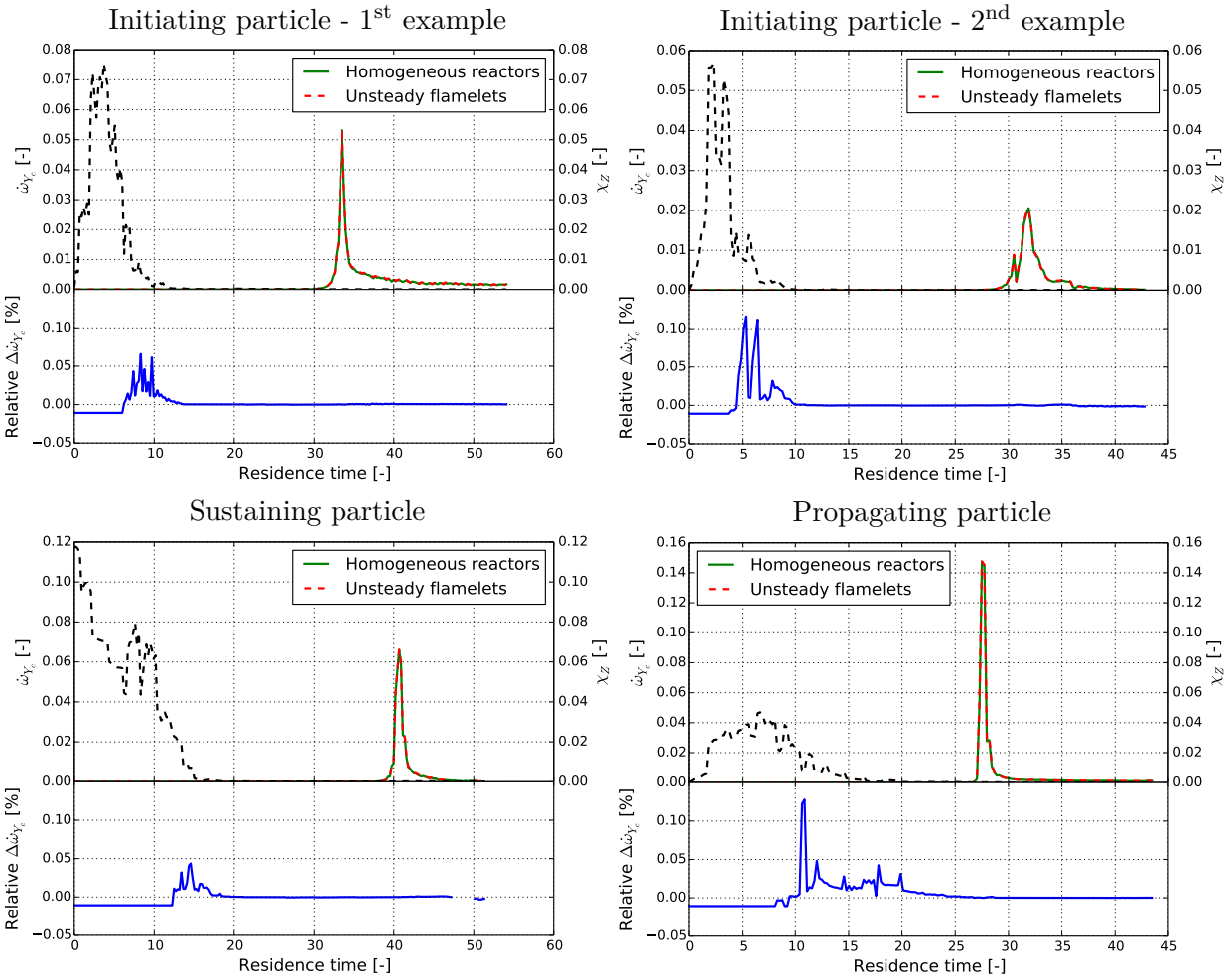

Figure 4.30: Comparison of $\dot{\omega}_{Y_c}$ from tabulated chemistry based on homogeneous reactors and on unsteady-flamelets along particle paths. The dashed black line represents the scalar dissipation rate, the green solid line shows $\dot{\omega}_{Y_c}$ from homogeneous reactors, the red dashed line $\dot{\omega}_{Y_c}$ from unsteady flamelets and the blue solid line highlights the relative error between $\dot{\omega}_{Y_c}$ from homogeneous reactors and $\dot{\omega}_{Y_c}$ from unsteady flamelets.

Fluid particles have a CDR balance similar to the time average results. In particular the diffusion is tiny when the reaction is active. This is another evidence of the low impact of the scalar dissipation rate on this kind of flow. But to further assess this, the progress variable source term, for those 4 particles, interpolated once with a look-up table based on homogeneous reactors and once with one based on unsteady-flamelets, are compared in Figure 4.30. To carry out a fair comparison, the look-up tables were generated with the same software; FlameMaster [92]. In that tool, the progress

variable has a different definition[8]; $Y_c = Y_{H_2} + Y_{H_2O}$. This explains the difference between the values reached in Figures 4.26 to 4.29 and Figure 4.30.

When the scalar dissipation rate reaches a low value, the difference between the look-up tables disappears. In this particular case for initiating and sustaining particles, a large part of the building radical process occurs without influence of χ_Z. However close to the injector some effects are visible. Directly after the injection, the scalar dissipation rate is usually high enough to inhibit the chemistry. But towards the end of the mixing (when reaching low mixture fraction), the scalar dissipation rate has a positive effect on the chemistry compared to look-up tables based on homogeneous reactors. Anyway the error is always very small ($< 0.15\%$). And a noticeable error appears only when the source term has a tiny value. This justifies our hypothesis of neglecting the direct effect of the scalar dissipation rate onto auto-igniting turbulent flow.

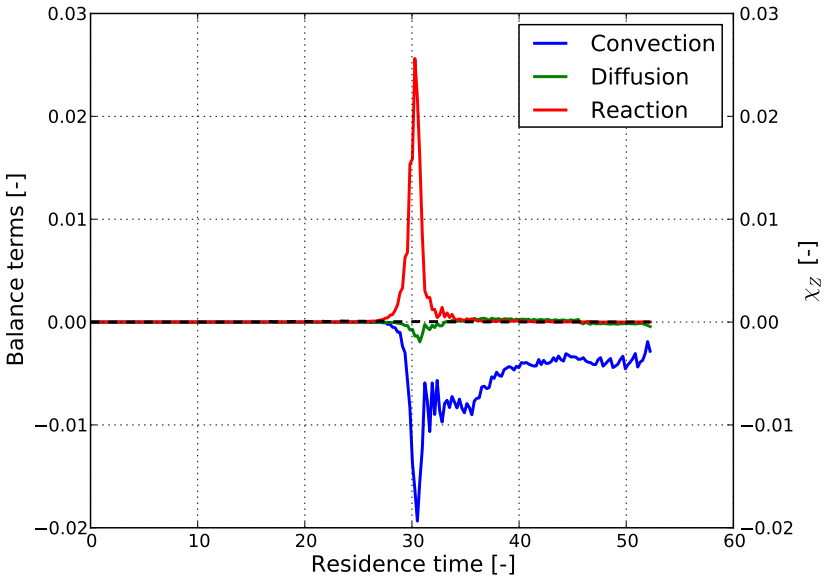

Figure 4.31: History of the CDR balance for a fluid particle resulting in an auto-ignition spots injected in the air co-flow.

A simulation with particles feeding the air co-flow was also performed. An additional group of unburnt particles is obviously found. But the three other groups are present again. The main difference is the absence of a

[8] The definition is hard coded in the code with no way to parametrize it.

strong mixing period (see Figure 4.31 for an example of initiating particle). Instead the mixture fraction rises slowly by diffusion.

This auto-ignition case is certainly close to a flash-back configuration due to the high chemical activity resulting of the high temperature inlets. Therefore the separation between the different groups of particles is not easy – especially between the initiating and sustaining particles. Nevertheless the author believes that the major scenarios of particles history are retrieved in this case.

4.2.3 Markides test cases

After an extensive study on the ETH test case, the model was tested on some of the experiments done by Markides and Mastorakos [75, 77–79]. The important database built for auto-ignition spots regime allow to analyze the sensibility of the solver to the experimental parameters; more specifically, the fuel used, the inlet velocities and the co-flow temperature. All other parameters were kept constant; in particular the turbulent inflow conditions and the turbulent model.

The fuel is injected through a central injector of internal diameter 2.25mm and external diameter 3mm. The fuel is pre-heated by electrical heaters. The co-flow air is also preheated by electrical heaters before passing through a perforated plate with a solidity of 44% and holes of 3mm in diameter. The injection nozzle was placed 63 mm downstream of the perforated plate. The measurement section consists of a quartz tube with inner diameter of 25mm.

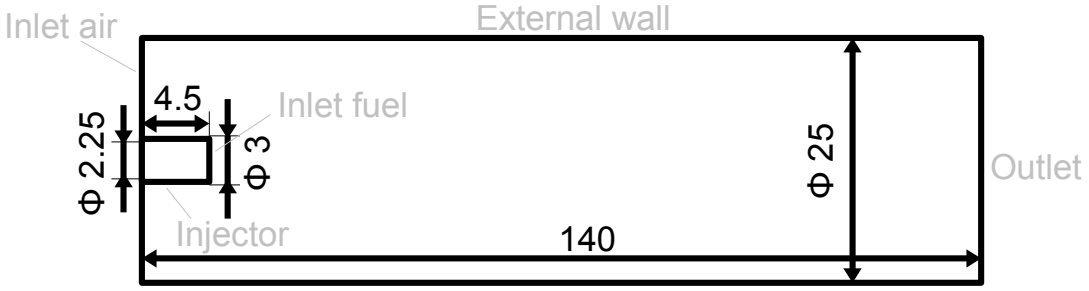

Figure 4.32: Computational domain for the simulation of Markides' experiments. All lengths are mentioned in mm.

The computational domain is defined as mentioned in Figure 4.32. As in the DNS configuration, a small part of the injector was simulated to take into account the injector wall effect on the turbulent structure generated from the vortex generator algorithm at the air inlet. The mesh is an O-grid with 44 cells in azimuthal direction, 47 radially and 148 axially (the total being 305,664 cells) clustered towards the inlets and the center line.

The turbulent inlet flow is mimicked by superimposing to the measurement mean flow a fluctuation using the vortex generator algorithm of Kornev et al. [60] with the turbulent parameters as specified in Table 4.7. The turbulent model chosen is the local dynamic Smagorinsky model. The turbulent Prandtl number was set to 0.4.

The numerical schemes chosen are second order in time and space. Eight stochastic fields are transported to approximate the joint-PDF. Trials with four fields were not able to capture the auto-ignition length properly. And the results with 16 stochastic fields were similar to the one with 8.

	Flow	**Species**	**Temperature**
Air inlet	$\langle u_{\text{air}} \rangle$	$Y_{O_2} = 0.233$	T_{air}
	Turbulence intensity = 13%	$Y_{N_2} = 0.767$	
	Integral length scale $l_t = 4.5$ mm		
Fuel inlet	Parabolic profile with $\langle u_{\text{fuel}} \rangle$	Fuel	T_{fuel}
Injector	Non-slip	No fluxes	No flux
External wall	Slip	No fluxes	No flux
Outlet	Fixed pressure	No fluxes	No flux

Table 4.7: Boundary conditions for the Markides' cases

Table 4.7 summarizes the general boundary conditions. It is worth mentioning that as for the ETH case, the outlet boundary condition for the pressure is set to `waveTransmissive` (with `lInf` equals the tube length and `fieldInf` sets to the atmospheric pressure). The density is also computed from the perfect gas law using a reference pressure instead of the local pressure to increase the stability of the solver.

4.2.3.1 Hydrogen cases

The first set of test cases is using diluted hydrogen as fuel. This test case is interesting as, in addition to the experimental results, data from LES of Jones and Navarro [48] are available. They used the Eulerian stochastic fields approach as well, but with detailed chemistry approach (Yetter mechanism [116]). The tabulated chemistry used in the present work is not computed with the Yetter mechanism, but with the Li mechanism [69]. The latter is known to be superior for low temperature and atmospheric pressure [55, 110].

Table 4.8 summarizes the boundary conditions of the hydrogen test cases. The inlet temperatures are taken to cover the auto-ignition spots regime up to the flash-back limit.

Velocity	$\langle u_{\text{air}} \rangle = \langle u_{\text{fuel}} \rangle = 20$ m/s or 26 m/s
Air temperature, T_{air}	950 - 954 - 959 - 964 - 980 K
Fuel	$Y_{H_2} = 0.14$; $Y_{N_2} = 0.86$; $T_{\text{fuel}} = 750$K

Table 4.8: Inlet conditions for auto-ignition simulations of diluted hydrogen in hot air.

The comparison is carried out on the *mean auto-ignition length*, $\langle L_{\text{ign}} \rangle$, normalized by the injector inner diameter (see Fig. 4.33). Unfortunately the definition of $\langle L_{\text{ign}} \rangle$ is not an easy task. For the experiments, Markides reconstructed a PDF of the OH* chemiluminescence spatial distribution gathering many images. $\langle L_{\text{ign}} \rangle$ is then computed by integrating over the PDF. This procedure overestimates $\langle L_{\text{ign}} \rangle$. Indeed the maximum heat release (corresponding roughly at the maximum of OH* chemiluminescence intensity) occurs after the auto-ignition events, as explained by Markides

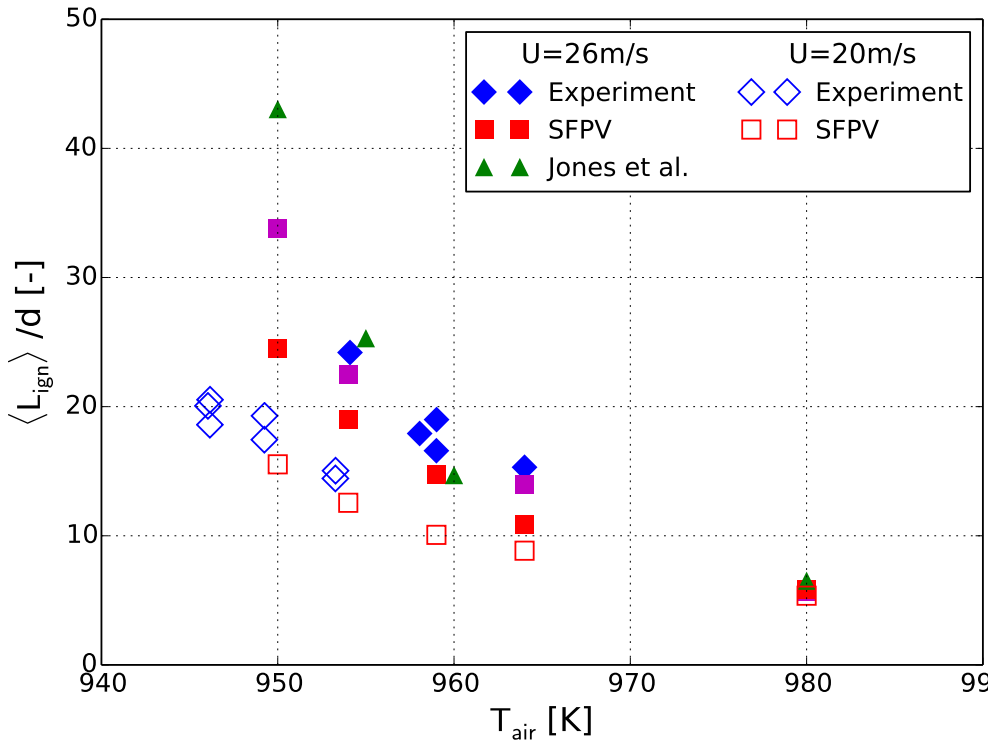

Figure 4.33: Average length of ignition for different conditions of mixing between hydrogen diluted jet and a hot turbulent co-flow of air. The filled symbols correspond to cases with a mean velocity of 26 m/s and the opened symbols to the cases with a mean velocity of 20 m/s. The blue ♦ are the experimental results, the green ▲ the one of Jones and Navarro-Martinez [48] and the red ■ the one using the SFPV model. The magenta squares are the results obtained with the current model but applying the definition of Jones and Navarro (The data are not available at 959K).

et al. [80]. Despite the flaw of that method, a similar method, namely the barycenter of the averaged heat release, was performed to determine $\langle L_{\text{ign}} \rangle$ in our LES simulations. Unfortunately Jones and Navarro-Martinez [48] defines L_{ign} differently. The shortest distance between the injector and the temperature iso-contour at $T = 1.01 T_{\text{air}}$ was considered to estimate L_{ign}. Moreover they do not report the time average of that L_{ign}. Instead they report the first value they got in the simulation although in their simulations L_{ign} decreases towards 0 for all T_{air} except 950 K (see Fig. 5 in [48]). For comparison, the definition of Jones and Navarro has been applied to our simulations (magenta squares in Figure 4.33).

The tabulated chemistry model has a reasonable agreement with the experimental results. The discrepancy with Jones et al. appears to be high. It results from the different chemistry mechanism and computation of L_{ign}.When using their definition, the discrepancy reduces as the first ignition spot occurs always further downstream than the following ones.

More importantly, despite the high sensitivity of those test cases, all trends are recovered; i.e. L_{ign} diminishes when $\langle u_{\text{air}} \rangle$ decreases and when T_{air} increases.

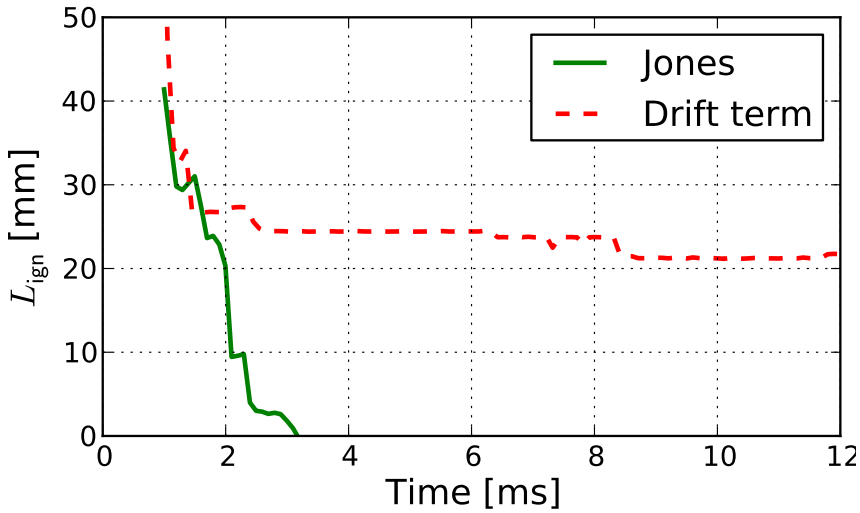

Figure 4.34: Evolution of L_{ign} for the test case $T_{\text{air}} = 950K$ and $\langle u_{\text{air}} \rangle = 26$ m/s using the Jones and the drift term formulation.

The higher sensitivity to flashback seen by Jones et al. is probably due to their deficiency in the stochastic field formulation. Indeed the test described previously on the modeling of D_1 and D_2 is again performed on the test

case $T_{\text{air}} = 950K$ and $\langle u_{\text{air}} \rangle = 26$ m/s. The time evolution of L_{ign} indicates a flash-back for the Jones formulation but a random auto-ignition spots regime with the drift term formulation (see Figure 4.34).

4.2.3.2 N-heptane cases

A second series of test cases was carried out with another fuel: N-heptane. In this case again, the influence of the air velocity and temperature were tested; Table 4.9 summarizes the different test cases. The results were compared to the Markides et al. data [80] from experimental measurements and first-order CMC simulations. The latter simulations were computed using the reduced N-heptane mechanism of Bikas [4]. This mechanism solves 31 species and 27 reactions. The look-up tables were generated using the skeletal mechanism of Zeuch et al. [118] containing 110 species and 1170 reactions. When the former choice is mandatory to limit the chemistry computational cost in the CMC simulation, the choice of an advanced mechanism does not affect much the total simulation time of the present model. Indeed in comparison with the hydrogen test case, the N-heptane test case requires roughly the same amount of computational time. Only the tabulation process is affected by the size of the chemistry mechanism — the N-heptane tabulation takes about 45 minutes when the hydrogen tabulation requires 3 minutes.

Air velocity, $\langle u_{\text{air}} \rangle$	13.8 m/s	17.6 m/s
Fuel velocity, $\langle u_{\text{fuel}} \rangle$	$1.05\langle u_{\text{air}} \rangle$	
Air temperature, T_{air}	1104 - 1109 - 1112 K	1115 - 1126 - 1135 - 1138 K
Fuel	$Y_{C_7H_{16}} = 0.95$; $Y_{N_2} = 0.05$; $T_{\text{fuel}} = T_{\text{air}} - 100$K	

Table 4.9: Inlet conditions for auto-ignition simulations of n-heptane in hot air.

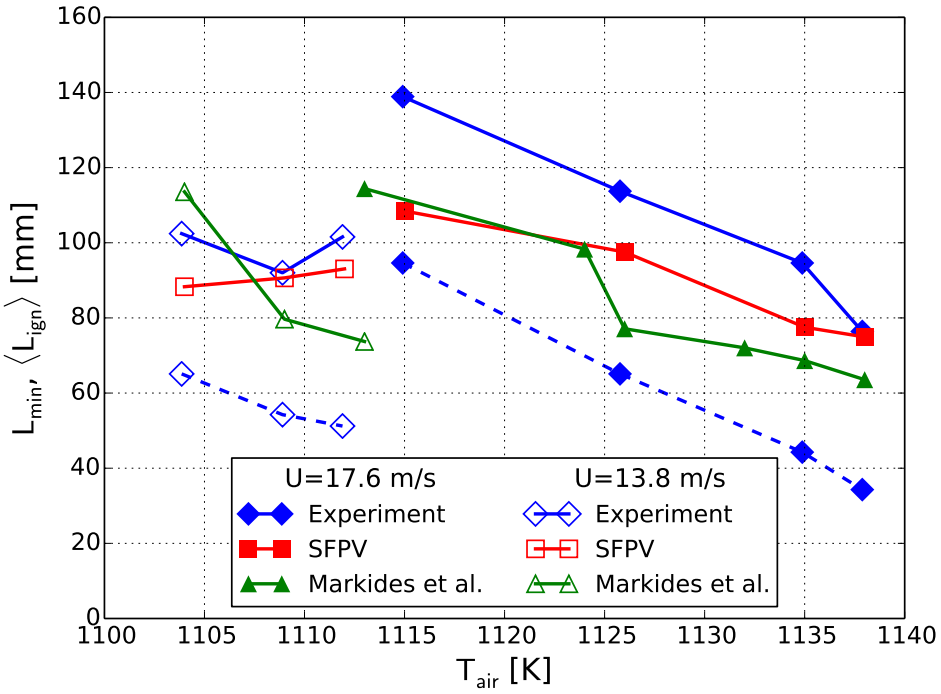

Figure 4.35: Average length of ignition for different conditions of mixing between a N-heptane diluted jet and a hot turbulent co-flow of air. The filled symbols correspond to cases with a mean velocity of 17.6 m/s and the opened symbols to the cases with a mean velocity of 13.8 m/s. The blue ♦ are the experimental results of Markides et al. [80], the green ▲ the CMC [80] and the red ■ the one using the SFPV model. $\langle L_{\text{ign}} \rangle$ is plotted with solid line and L_{min} with dashed line.

Figure 4.35 compares $\langle L_{\text{ign}} \rangle$ for the different test cases. The agreement is again good. This time a minimal auto-ignition length L_{min} was estimated from the experimental OH* chemiluminescence measurements. This length corresponds to 3 % rise in signal from the background relative to the peak intensity.

4.3 Nitrogen oxides prediction

This last section will assess the accuracy and efficiency of the new NO prediction model, see Section 3.2. A first simple validation based on homogeneous reactors will be followed by the simulation of a laminar premixed flame.

4.3.1 Homogeneous reactor

The validation of the NO_x model is first carried out on a zero dimensional reactor at constant pressure as used for the validation of the tabulation chemistry model.

For this test case, the system of equations Eqs. (4.1) has to be solved. The validation is done by comparison of detailed chemistry with tabulated chemistry. For the detailed chemistry data set, the chemical source terms were obtained from the GRI 3.0 mechanism [105]. For the tabulated chemistry model, the source term for the progress variable was determined by linearly interpolating the source term in look-up tables. And for NO, the algorithm described in Section 3.2 was used.

Figure 4.36 shows the results for a reactor composed of methane-air at stoichiometric conditions, atmospheric pressure and an initial temperature of 800K. The dashed red line is the reference data computed using detailed chemistry in Cantera. The blue line shows the reconstruction of Y_{NO} using a look-up table constructed only from the reactor at stoichiometric conditions, while the dot-dashed green line used a look-up table based on two reactors surrounding the stoichiometric conditions. The points mark the switch between the look-up table and the NO_x model. The agreement is good and the equilibrium value is correctly recovered.

Similar tests at other mixture fractions show as well a good agreement between detailed chemistry and look-up tables (+ NO_x model) results.

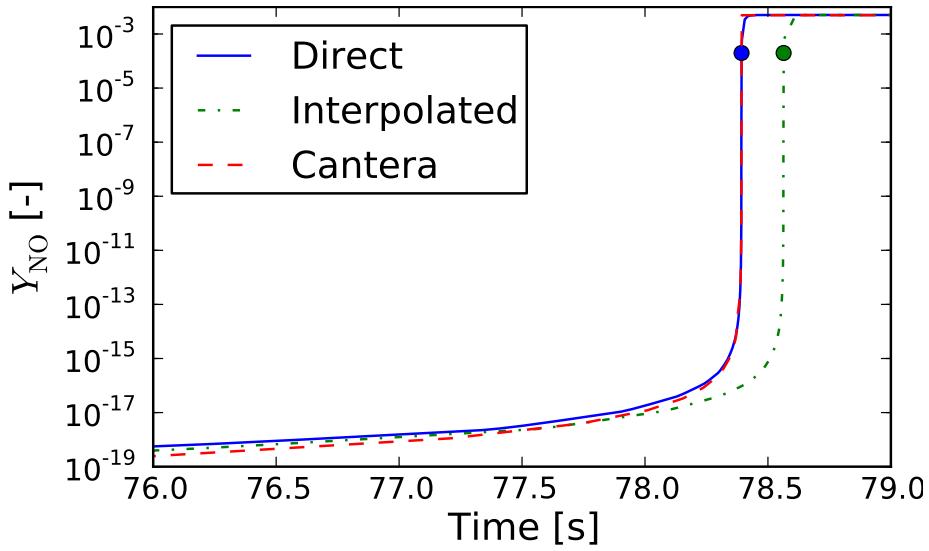

Figure 4.36: Validation on the NO_x model on a 0D reactor at stoichiometric conditions for a mixture of methane-air at atmospheric pressure and with initial temperature of 800K. Red dashed line: Cantera (reference), blue solid line: look-up table constructed from the stoichiometric reactor, green dot-dashed line: look-up table based on two reactors around the stoichiometry. The points indicate the switch between the table and the model.

4.3.2 Laminar premixed flame

The goal of this second test case is to assess the accuracy of the NO_x model based on laminar one-dimensional premixed flame. But prior to that, the tabulated chemistry model implemented in OpenFOAM® needs to be validated on that kind of configuration. Looking at the literature, the test case of van Oijen et al. [112] for validating the tabulated chemistry model, called FGM in that case, was chosen. Indeed van Oijen et al., but also Bradley et al. [7] before them, prove that premixed flames could be simulated accurately with tabulated chemistry. And as the fuel is methane, detailed chemistry of NO formation is available.

In the first part of this section, the simulation of the laminar premixed flame will be described. The tabulation procedure and troubles coming from it will be detailed. Then an evaluation of the new NO_x model will be carried out.

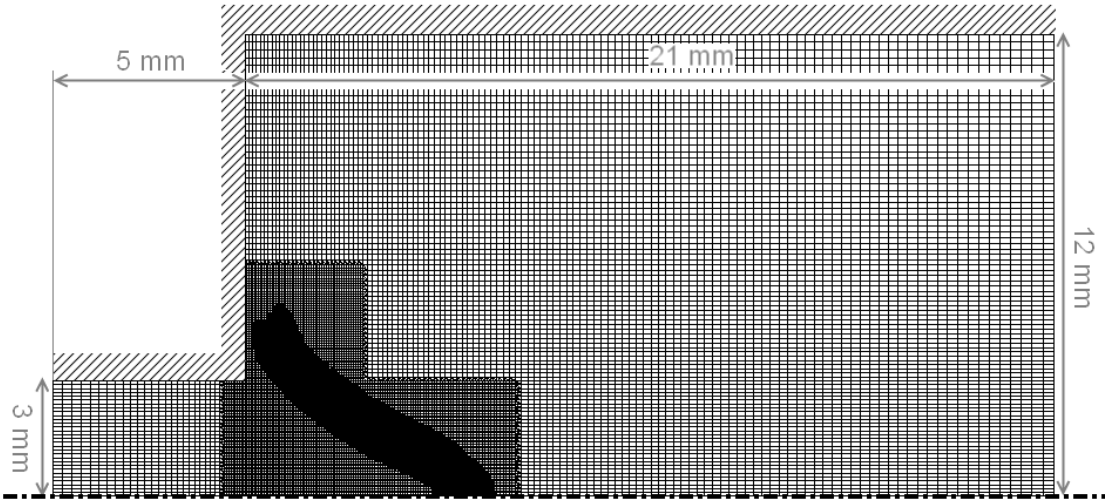

Figure 4.37: Geometry and mesh of the 2D slit burner. The premixed gas is entering by the inlet on the left following a parabolic profile.

4.3.2.1 Tabulation process

The tabulated chemistry scripts were further extended to build look-up tables from 1D laminar premixed flames following the FGM model of van Oijen et al. [112]. The validation test case of van Oijen et al. is a slit burner laminar flame with wall at fixed temperature. Therefore heat losses occur at the wall, especially at the flame basis. This is in fact the stabilization process; without heat losses, the flame will propagate upstream. So in the opposite of the previous test cases, the system is no more adiabatic. Consequently the chemical look-up tables must have an additional parameter representing the heat losses.

In this particular case, the table parameters should capture two phenomena: the combustion progression and the heat losses. Following van Oijen et al., the parameters chosen are the progress variable and the total enthalpy. More precisely the tables are stored in the normalized space (C, β), using the definition of Wang et al. [114] of a heat loss parameter β:

$$\beta = \frac{H_f(Y_1, \ldots, Y_n, T_f) - H_p(Y_1, \ldots, Y_n, T_p)}{H_f(Y_1, \ldots, Y_n, T_f) - H_p(Y_1, \ldots, Y_n, T_f)}, \tag{4.7}$$

where H_f is the enthalpy of the fresh mixture, H_p the one of the burnt products, T_f the fresh mixture temperature and T_p the burnt products temperature after heat losses.

If the system is adiabatic, T_p equals the temperature at equilibrium and β is equal to zero (no heat losses). And if all the heat released by the combustion is lost, β equals 1 as $T_p = T_f$.

The 1D premixed flames are computed for a series of specified β using Cantera [34]. In order to increase β, i.e. to lower the total enthalpy of the fresh mixture, van Oijen et al. [112] suggest reducing the temperature of the mixture. With the drop of temperature, the chemistry slows down, up to the point where no reacting solution can be established. At that point, the enthalpy has to be reduced by another way. van Oijen et al. choose to mix cooled burnt products with the fresh mixture; decreasing their temperature to the inlet fresh mixture temperature.

The first way of diminishing the temperature results in unacceptable temperature values in the look-up tables. In particular temperatures lower than fixed wall temperature appear in the tables. Therefore in our implementation, the temperature is not reduced; only cooled products are mixed to reduce the total enthalpy. But even this procedure does not allow to cover all β values. Indeed at some points the sensible enthalpy will be too low to find a reacting solution. Consequently, flames for β values as high as possible are solved. Then for states with lower total enthalpy, the look-up values are interpolated linearly between the last reacting flame and the burnt products at the fresh mixture temperature (as described in [112]).

Unfortunately another drawback appears when using the script to predict pollutants. Indeed, the recirculated burnt gases are computed from the composition at thermodynamic equilibrium. Therefore species with large chemical time scales were also recirculated in significant amounts. To circumvent the problem, only a subset of the main burnt species were recirculated; e.g. for methane-air mixture CO_2, CO, H_2O, O_2, and N_2.

4.3.2.2 Flow validation

Contrary to the homogeneous reactors, the transport by diffusion is taking place in both codes: in the one dimensional flame and in the CFD solver. Therefore the transport modeling must be identical in both cases. In particular the species diffusion model changes greatly the tabulated values as

shown in Figure 4.38 when comparing differential diffusion ($\mathrm{Le}_k \neq 1$) and identical diffusion coefficients ($\mathrm{Le}_k = 1$).

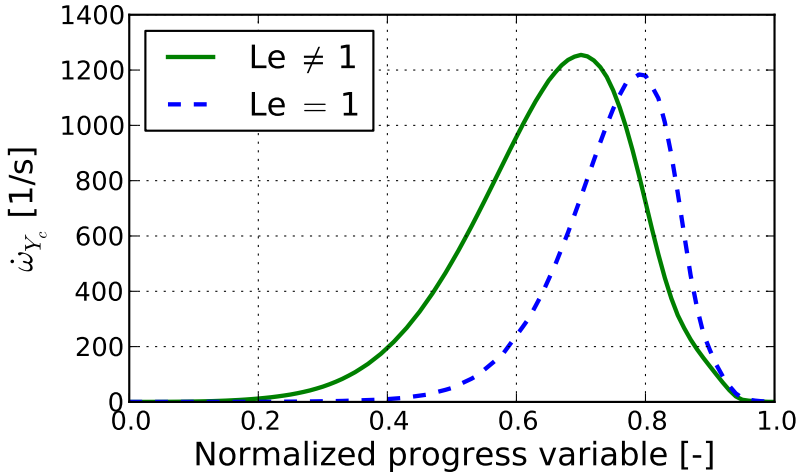

Figure 4.38: Influence of the species diffusion model on the progress variable source terms in 1D laminar premixed flames.

By default OpenFOAM® can simulate multi-species transport only without differential diffusion ($\mathrm{Le}_k = 1$). So the first test case chosen was the slit burner of van Oijen et al. [112] as they made the hypothesis $\mathrm{Le} = 1$. In a second step, the slit burner test case of Somers et al. [107] was selected to assess the capability of tabulated chemistry in laminar premixed flame with differential diffusion effect.

The slit burner of van Oijen et al. [112] was solved once with the DRM22 mechanism [51] and once with the tabulated chemistry model in OpenFOAM®. The boundary conditions are summarized in Table 4.10. And Figure 4.37 shows the geometry and locally-refined mesh.

	Flow	**Species**	**Temperature**
Inlet	Parabolic profile	Methane-Air	300 K
	$u_{\max}$=1 m/s	$\phi = 0.9$	
Walls	Non-slip	No fluxes	300 K
Outlet	Fixed pressure	No fluxes	No fluxes

Table 4.10: Boundary conditions for the laminar slit burner of van Oijen et al. with no differential diffusion effect as given in [112].

The progress variable source term obtained from the detailed and the tabulated chemistry are compared in Figure 4.39. The results are well matching

except at the basis of the flame where the gradient in heat losses is maximal. Those cells are in the region of the tables for which the enthalpy is too low to obtain a reacting solution (even when using the trick of burnt product mixing). And it seems that the linear approximation is overestimating the progress variable source terms for high level of heat losses.

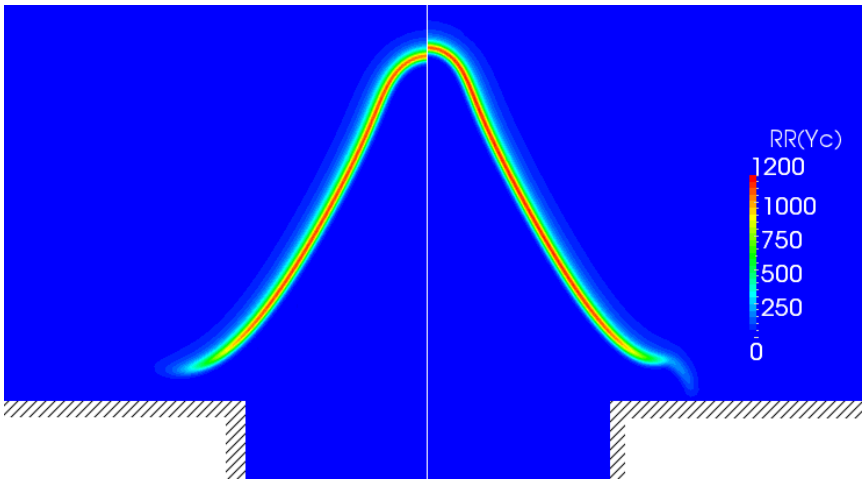

Figure 4.39: Progress variable source term of the slit burner test case of van Oijen et al.; hypothesis Le = 1. Left: detailed chemistry with Le = 1 – Right: look-up tables with Le = 1 in OpenFOAM® and in Cantera.

Figure 4.40 shows the results of the same simulation but with the tabulated chemistry computed with differential diffusion active in Cantera but not in OpenFOAM®. Those results proves the need of coherence for the differential diffusion model in the CFD and in the chemistry codes.

The effect of differential diffusion is complicated to take into account in the tabulated chemistry approach as the species are not transported separately. In particular in this case only the progress variable is transported. Nevertheless, to assess the ability of the tabulated chemistry model, the slit-burner test of Somers et al. [107] was carried out. In this case, the look-up tables were computed using the GRI 3.0 mechanism [105] and activating the differential diffusion model in Cantera. But in OpenFOAM®, differential diffusion being impossible to apply to the single progress variable, a correction was done by tuning the Schmidt number for the progress variable. The geometry is described in Figure 4.41 and the boundary conditions in Table 4.11.

The temperature field of the original paper [107] is compared with the one from the tabulated chemistry in Figure 4.42. The agreement is quite im-

	Flow	Species	Temperature
Inlet	Parabolic profile	Methane-Air	298 K
	u_{max}=1.1 m/s	$\phi = 1$	
Walls	Non-slip	No fluxes	298 K
Outlet	Fixed pressure	No fluxes	No fluxes

Table 4.11: Boundary conditions for the laminar slit burner of Somers et al. as given in [107].

pressive; especially because the chemistry mechanisms used are different (Somers et al. used a so-called skeletal mechanism with 25 reactions and 15 species proposed by Smooke and Giovangigli [106]). So despite neglecting the differential diffusion in the CFD solver, the results taking those effects into account only in the tabulation process can match quite well the reality.

The best agreement between Somers' simulation and the tabulated chemistry calculation was found when using a Schmidt number equals to 0.66 for the progress variable. So the flame shape is influenced by the diffusion coefficient of the progress variable (see Figure 4.43). Unfortunately, the determination of a relation or even the tabulation of the diffusion coefficient, prior to the simulation, is not trivial. For example Lam [67] investigates the effect of chemistry reduction in the frame of the *Computational Singu-*

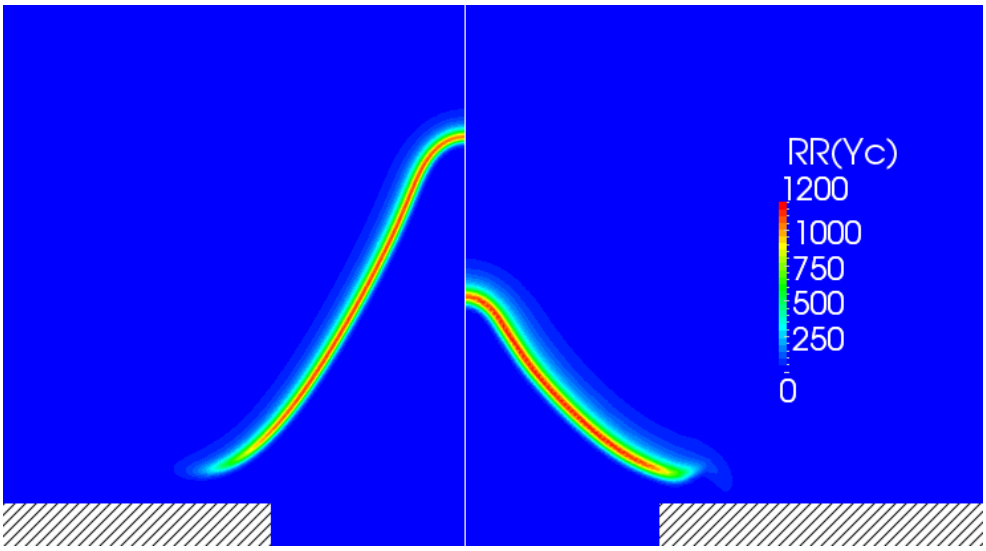

Figure 4.40: Progress variable source term of the slit burner test case of van Oijen et al.; hypothesis Le = 1. Left: detailed chemistry with Le = 1 – Right: look-up tables with Le = 1 in OpenFOAM® but differential diffusion modeling in Cantera.

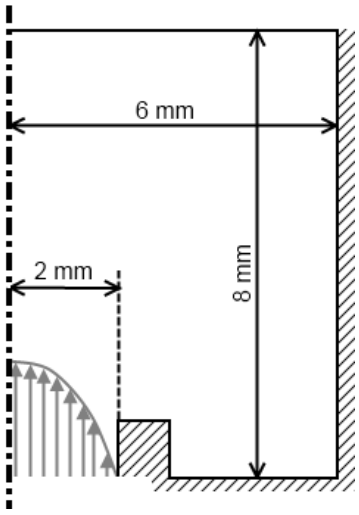

Figure 4.41: Geometry of the 2D slit burner simulated by Somers et al. [107].

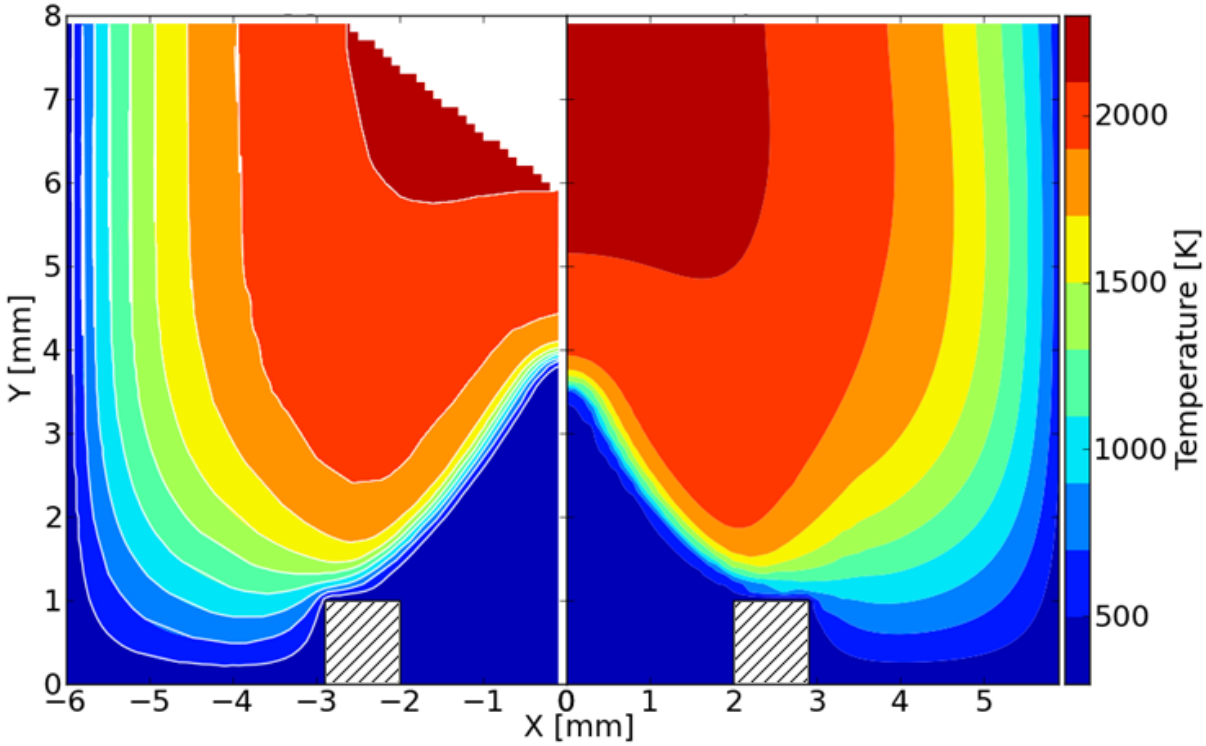

Figure 4.42: Temperature field for a slit burner of methane with differential diffusion model. Left: results from Somers et al. [107], detailed chemistry with differential diffusion model – Right: tabulated chemistry using GRI 3.0 with differential diffusion and Schmidt number modeling for the progress variable.

lar Perturbation (CSP) method on the diffusion coefficients. He shows that the diffusion coefficients resulting from the projection of the diffusion coeffi-

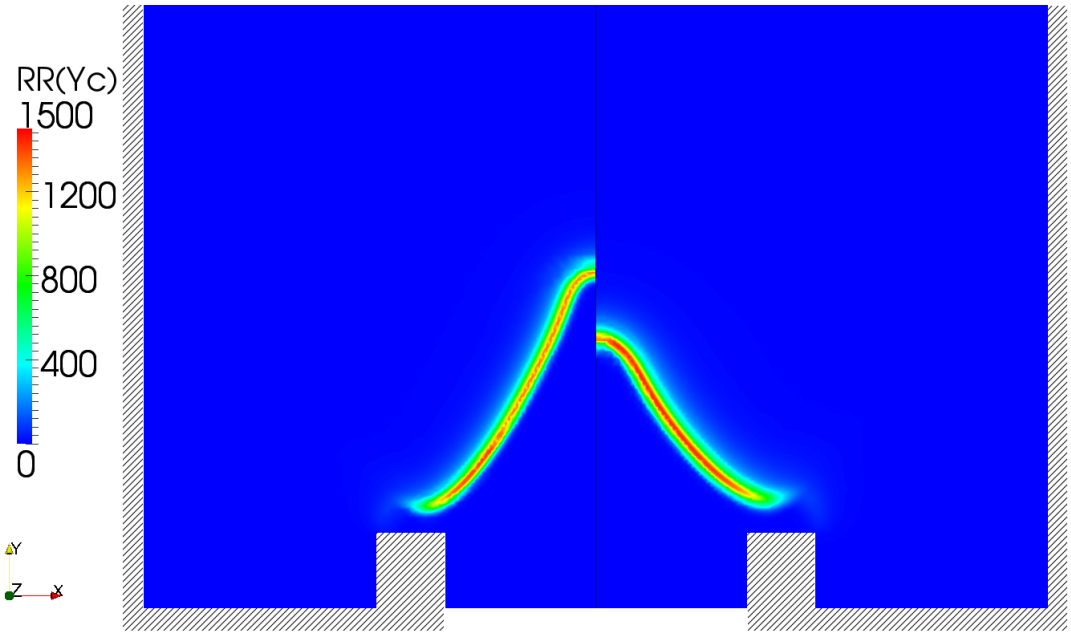

Figure 4.43: Variation of the progress variable source term for a slit burner of methane with the progress variable Schmidt number. Left: Sc = 0.72 – Right: Sc = 0.66.

cients in the slow chemistry subspace combine physical diffusion coefficients with reaction coefficients in non-linear relations.

The progress variable approach is somehow an extreme reduction of a chemical mechanism. Consequently it seems unlikely that its "physically meaningful" diffusion coefficient can be expressed from a simple linear combination of species diffusion coefficients. So the good agreement using the simple Schmidt number approach, proves that the major effect of the differential diffusion is on the chemistry for laminar flows. Introducing it in the look-up tables is an easy way to improve greatly the simulation results at low computational expense.

4.3.3 Nitrogen oxides predictions

The test case of Somers and de Goey [107] is used to validate the NO model for a laminar premixed flame[9]. As OpenFOAM® is by default not able to handle reacting flows with detailed transport of the species, a new solver

[9] The mesh was elongated in the axial direction to have a longer section in which the new model is applied.

called *canteraFoam* was created. This solver relies on Cantera for computing the chemistry and the thermo-physical properties and on OpenFOAM® for solving the conservation equations. The test case of Somers was then solved using GRI 3.0 with a detailed transport model. Those reference results are represented with a black solid line in Figures 4.44.

Four different models are compared to the reference results:

- Y_{NO} table: Y_{NO} is directly interpolated in a look-up table.
- $\dot{\omega}_{\mathrm{NO}}$ table: a transport equation for Y_{NO} is solved with the chemistry source term read in a look-up table.
- Ihme model [40]: a transport equation for Y_{NO} is solved. The chemistry source term is computed from 2 look-up tables: the production source term $\dot{\omega}^{+}_{\mathrm{NO}}$ and the destruction source term $\dot{\omega}^{-}_{\mathrm{NO}}$ normalized by Y_{NO}. Therefore the global source term is given by:

$$\dot{\omega}_{\mathrm{NO}} = \dot{\omega}^{+}_{\mathrm{NO}} + Y^{\mathrm{CFD}}_{\mathrm{NO}} \frac{\dot{\omega}^{-}_{\mathrm{NO}}}{Y^{\mathrm{table}}_{\mathrm{NO}}}. \tag{4.8}$$

- New model: see Section 3.2.2 for its detailed description.

All look-up tables were discretized using 101 grid points for the progress variable dimension and 31 grid points for the normalized total enthalpy dimension from 0 to 0.3. For higher heat losses the linear approximation proposed by van Oijen et al. was adopted.

The left plot in Figure 4.44 compares the reference case to the results obtained with the look-up tables solver, *reactingTableFoam*. The direct interpolation of Y_{NO} in a look-up table is not accurate, especially in the burnt products, due to the lack of sensibility between the progress variable and Y_{NO}. The results of the other models are similar. As only a subset of species are transported without differential diffusion with *reactingTableFoam*, there is a discrepancy in the flame shape compared to the results obtained with *canteraFoam*. Consequently the flow is not exactly identical, as can be seen in Figure 4.45.

Therefore to avoid such a discrepancy of the flows, the NO prediction was solved in a post-process step using the flow from the reference simulation[10].

[10] The progress variable was reconstructed from its definition $Y_c = Y_{\mathrm{CH_2O}} + Y_{\mathrm{CO}} + Y_{\mathrm{CO_2}}$.

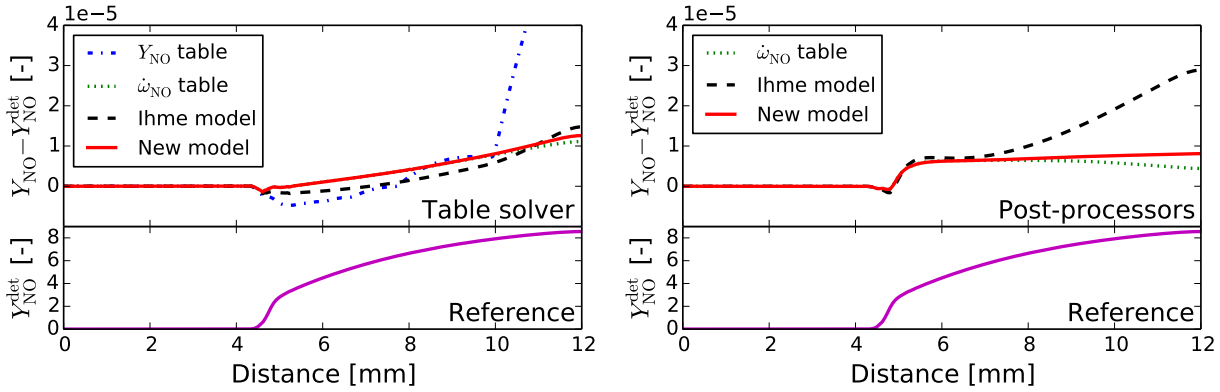

(a) reactingTableFoam VS. canteraFoam (b) canteraFoam with post-processing tool

Figure 4.44: Y_{NO} on the center line of the slit burner configuration of Eggels et al. [21]: detailed chemistry (black line), tabulated Y_{NO} (dot-dashed blue line), tabulated $\dot{\omega}_{NO}$ (green line), Ihme model (magenta dashed line) and the new model (red line).

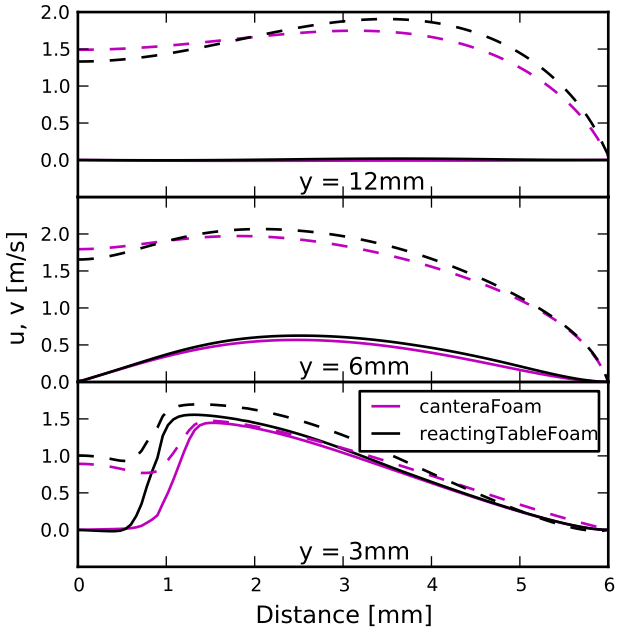

Figure 4.45: Profiles of x (solid) and y (dashed) velocity components along a horizontal line at three different heights. The line at 3 mm cuts the flame in its middle, the one at 6 mm is above the flame and the latest at the exit plane of the domain. Results from *canteraFoam* are in magenta and those from *reactingTableFoam* in black.

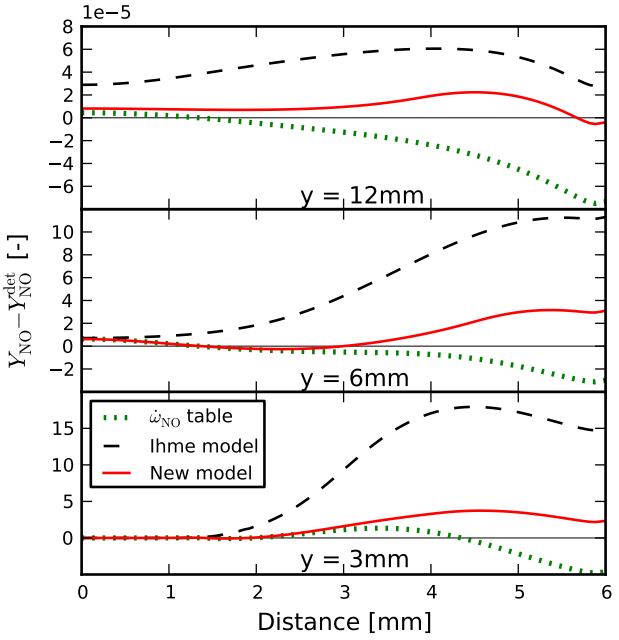

Figure 4.46: Absolute error of Y_{NO} using post-processor calculation at three different heights of the slit burner (3mm, 6mm and 12mm). The models compared are: tabulated $\dot{\omega}_{NO}$ (dotted green line), Ihme model (black dashed line) and the new model (red line).

The right plot in Figure 4.44 displays those results. The Ihme model clearly over-predicts Y_{NO}, showing a steady linear increase. The error with the reference curve is growing with the distance. The discrepancy between the $\dot{\omega}_{\mathrm{NO}}$ look-up table and the new model is small. However, a close look at the end of the curves shows a faster decay of $\dot{\omega}_{\mathrm{NO}}$ for the $\dot{\omega}_{\mathrm{NO}}$ table model. This is coherent with the content of the table (no chemistry for $Y_c = Y_{c,\mathrm{eq}}$). Consequently Y_{NO} falls due to transport effect. The new model is the only one to maintain a correct balance between transport effects and production term in the burnt products. Indeed the error is almost constant far from the flame. So despite an overestimation of Y_{NO} at the end of the combustion (large increase of the error), the new model is the only one to have an evolution similar to the reference case even in the burnt products.

The transverse profiles Y_{NO} in Figure 4.46 confirm those conclusions. The new model present the lowest error especially far downstream of the flame. The Ihme model balances the pure source term with a relaxation term towards $Y_{\mathrm{NO}}^{\mathrm{table}}$. In the burnt products, Y_{NO} tends towards its equilibrium value. But as for Y_{NO} and its source term, the linear interpolation in look-up tables creates a bias resulting in a smaller relaxation time inducing the over-prediction.

4.3.4 Turbulent flame: the Cabra's experiment

Using the new NO_x model for turbulent flow is the next validation step. The validation test case choice was driven by the availability of NO measurement and the type of combustion encounters, namely auto-ignition for which the model has been primarily developed and checked. From those criteria the Cabra's experiment of a lifted methane flame has been chosen. Indeed it has been shown that the stabilization process of that flame was auto-ignition at its basis [20]. And NO measurement are available.

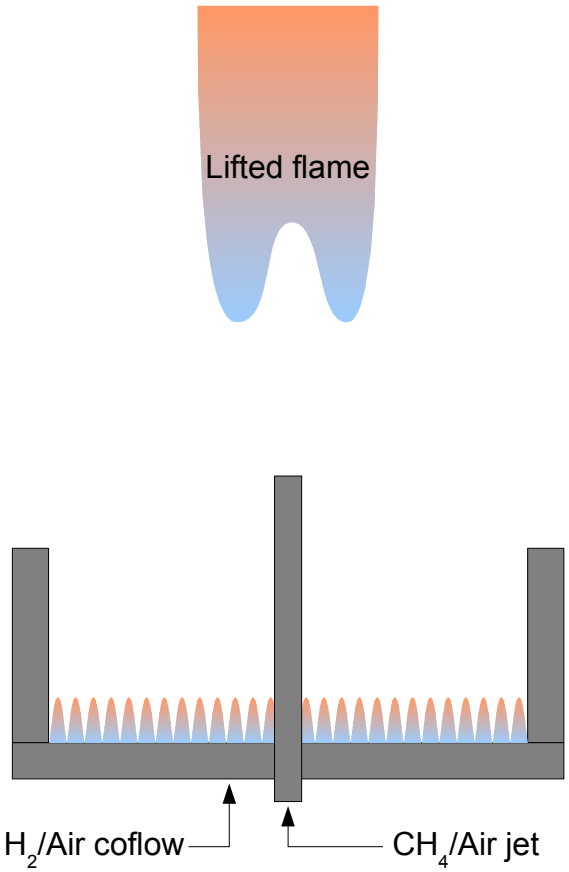

Figure 4.47: Sketch of the methane-air lifted flame experiment.

Figure 4.47 shows a sketch of the lifted methane flame in vitiated co-flow, originally investigated by Cabra et al. [12]. The surrounding burnt gases are generated using a perforated plate (210-mm diameter, 2200 holes of 1.58-mm diameter for a flow blockage of 87 %) as flame holder. The co-flow is composed of a mixture of hydrogen and air at an equivalence ratio of 0.4. An exit collar delays the mixing of the co-flow with the surrounding air. The fuel jet is injected 70 mm downstream of the perforated plate through

a tube of $D_{\text{ref}} = 4.57$ mm (reference diameter) at $U_{\text{ref}} = 100$ m/s (reference velocity). It is composed of methane (37 % in volume) and air (66 % in volume). The resulting stochiometric mixture fraction is 0.177. The flow conditions are summarized in Table 4.12.

	Flow	**Species**	**Temperature**
Co-flow inlet	$\bar{u}_{\text{air}} = 5.4$ m/s	$X_{O_2} = 0.1193$; $X_{N_2} = 0.7285$	1355 K
		$X_{H_2O} = 0.1516$;$X_{CH_4} = 0.0003$	
		$X_{H_2} = 0.0001$;$X_{OH} = 0.0002$	
Jet inlet	$\bar{u}_{\text{fuel}} = 100$ m/s	$X_{O_2} = 0.1452$; $X_{N_2} = 0.5243$	314 K
		$X_{H_2O} = 0.0029$;$X_{CH_4} = 0.3275$	
		$X_{H_2} = 0.0001$	
External wall	Slip	No fluxes	No flux
Outlet	Fixed pressure	No fluxes	No flux

Table 4.12: Boundary conditions for the Berkeley methane lifted flame from measurements [13].

Little information on the velocity fields is available from the experiment. Therefore a non-reacting RANS simulation with a 2D mesh similar to the one of Gordon et al. [36] was carried out. The mean velocity profiles were then extracted at the injection plane and interpolated onto the LES mesh. The turbulent fluctuations in the jet were generated based on the method of Kempf et al. [53], taking 2 % of turbulent intensity and 0.32 mm for the integral turbulent length scale. The subgrid-scale viscosity was evaluated using the dynamic Smagorinsky model. The diffusion coefficients of the species were computed based on a laminar Schmidt number of 0.72 and a turbulent Schmidt number of 0.9.

The computational domain extends over 90 D_{ref} in axial direction and 14 D_{ref} in radial direction. An O-grid mesh with 60x133x265 cells (total 2,113,536 cells) in azimuthal, radial and axial direction was generated, respectively. The cells were stretched toward the core of the cylinder and the inlets. This mesh is similar to the one of Domingo et al. [20].

The time and spatial schemes were second order with limiter for the scalar convection terms. The time-step was 1.75 μs and the averaged values were gathered on 8 τ_{ref} with $\tau_{\text{ref}} = 90 D_{\text{ref}}/U_{\text{ref}}$.

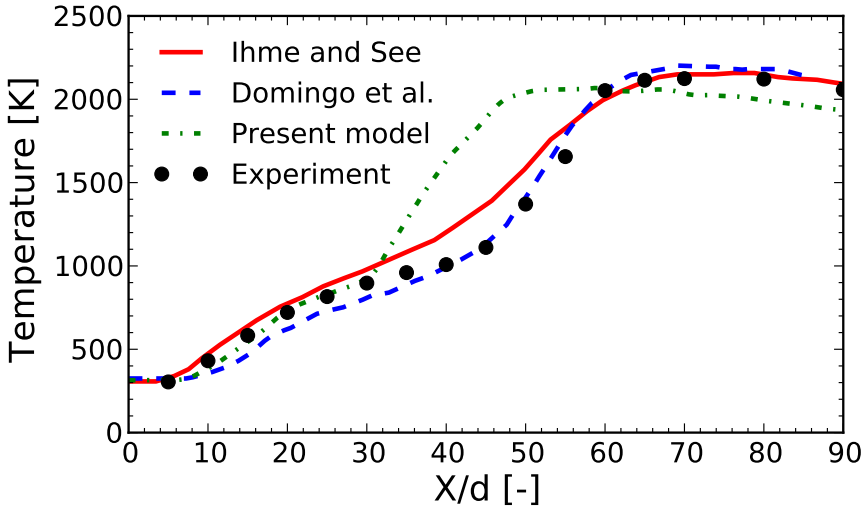

Figure 4.48: Average temperature on the center line of the Cabra methane lifted flame. Different models are compared to the experimental data (•): the double β-PDF based on homogeneous reactor and laminar premixed flames of Domingo et al. [20] (red solid line), the presumed PDF based on unsteady flamelet of Ihme and See [41] (dashed blue line) and the results obtained with the present model (dot-dashed green line).

In Figure 4.48, the time-averaged temperature on the center line is plotted. The points represent the experimental data. Results from three different simulations using tabulated chemistry and transported PDF implementations are also plotted.

- Ihme and See [41] (red solid line): the look-up tables are based on unsteady flamelets computation with 3 parameters – the mixture fraction, the progress variable and the scalar dissipation rate. The joint-PDF has a presumed shape defined as the product of a β-PDF (mixture fraction), statistically most-likely distribution (progress variable), and δ-PDF (scalar dissipation rate).

- Domingo et al. [20] (blue dashed line): the look-up tables are based on the combination of homogeneous reactors and laminar premixed flames (the weighting factor is the progress variable). The joint-PDF is presumed to be the product of two β-PDF; one for the mixture fraction and one for the progress variable.

- The present model (green dot-dashed line): the look-up tables are generated from homogeneous reactors only. The joint-PDF is transported thanks to Eulerian stochastic fields.

The present model starts reacting much earlier than the two other models and the experiment. After data analysis, three elements are identified as possible causes for the discrepancies: the mixture fraction variance, the scalar dissipation rate effect, and the chemical look-up tables.
The statistical error of the stochastic fields method is always greater for the moment $N+1$ in comparison of the moment N. In particular, the variance is less accurately predicted than the mean. So the error on the variance should be evaluated taking as reference the transported variance equation. This is important, as the variance represents the effect of the subgrid-scale fluctuations onto the chemistry.

High scalar dissipation rates are known to influence greatly the chemistry, especially in flames dominated by diffusion process. As the model is not taking this parameter explicitly into account, it could be a reason of the failure of the Cabra's test simulation.

Finally homogeneous reactors are maybe not the best canonical cases to generate the tables. Indeed there are no effects of transport in the mixture fraction space in those tables although the development and stabilization of partially-premixed flames usually depends on the mixing between the oxidant and the fuel. This can be another source of error in the case of lifted flames.

Domingo et al. have obtained a good agreement between the experiment and the simulation with a model not taking into account the scalar dissipation rate neither. The major difference is the computation of the joint-PDF and the table. The later mixes a table based on homogeneous reactor with one based on laminar premixed flames. The introducing of the laminar premixed flames is supposed to add the effect of flame propagation to the stabilization process of the flame in the simulation. In our results the flame is self-stabilized with a table based only on homogeneous reactor. So moving to a table like the one of Domingo et al. would not improve the results; the distance between the injector and the flame tip could even be shortened due to the introduction of propagation effect. So the more-likely source of

discrepancies is the computation of the PDF; and especially the subgrid-scales variance.

Ihme and See used the same transport equation for the variance as Domingo et al.. This reinforces the need of a careful analysis of the error of the stochastic fields method on the estimation of the variance. Indeed in the Markides' experiment presented earlier, the fuel jet and the co-flow have a similar velocity and temperature. Therefore the Reynolds number of the two flows are close; meaning that the level of turbulence, and thus of subgrid-scales variance, was low. But in the Cabra's experiment, the velocity and the temperature are highly different between the fuel jet and the oxidant co-flow. The Reynolds number of the fuel jet is 28000 when the one of the co-flow is 23300. The Reynolds difference will result in a higher level of subgrid-scales structure. Therefore if the stochastic fields method under-estimates the generation of variance, this could explain the lower lifted height observed. A careful analysis of the variance computation with the stochastic fields method will be carried out in the next chapter.

4.4 Summary

Considering all the previous test cases, the combustion model based on the combination of the Eulerian stochastic fields and the tabulated chemistry, SF-PV model, is perfectly adequate for modeling auto-ignition regimes. Nevertheless those configurations are highly sensitive to modeling hypotheses and boundary conditions. Great care should be addressed to the definition of the progress variable. Combining an intermediate species with a major product proves to be the best choice. For the Eulerian stochastic equation, adding a drift term to the micro-mixing model allows to recover the correct transport equation in the limit of highly resolved LES.

From a qualitative point of view, the observations done on auto-ignition spots (apparition on Z_{MR} and for low χ_Z) are coherent with previous DNS.

For auto-igniting turbulent flows such as the ETH or Markides test cases, the scalar dissipation rate has only a weak effect on the chemistry. The assumption of using look-up tables based on homogeneous reactors for such cases is confirmed by the deep analysis of the ETH test case. However the failure to simulate accurately the Cabra's methane lifted flame has highlighted a weakness of the SF-PV model. The next chapter will focus on the possible flaws explaining that failure.

The proposed NO model has been validated for homogeneous reactor at constant pressure and laminar premixed test cases. The obtained results are promising although further testing on turbulent test cases is required to fully assess the improvement brought by the new model.

The failure to simulate the Cabra's lifted flame have blocked that validation. But it shows the possible flaws of the models:

- the look-up table chemistry based on homogeneous reactors may be inadequate with the chemistry occurring in lifted flames,
- the scalar-dissipation rate may have to be taken explicitly into account in the model,
- the variance computed from the stochastic field may be incorrect.

A first comparison between the current model and other models having successfully simulated the Cabra's experiment points to the latest argument as the more-likely cause of discrepancy.

Nevertheless those three factors will be further discussed in the next chapter.

5 Places of improvement

The latest validation test case, the methane lifted flame of Cabra et al. [12, 36], has not been simulated successfully with the present model. Three possible reasons for the discrepancies were identified and will be discussed further: the variance estimation, the role of the scalar dissipation rate and the tabulation process. Some improvement directions will be given based on those elements.

Limitations and possible generalization of the new NO_x model will conclude this chapter.

5.1 Stochastic fields and variance estimation

The Cabra case requires lots of computational resources. Therefore the study of the variance estimation based on Eulerian stochastic fields will be carried out on the validated Markides hydrogen test case with the following conditions: $T_{\text{air}} = 959$ K and $\langle u_{\text{air}} \rangle = \langle u_{\text{fuel}} \rangle = 26$ m/s (see Sec. 4.2.3 for more details).

The variance of a passive scalar is transported according to Equation (5.1) (see Sec. 2.2.2).

$$\frac{\partial \bar{\rho} \widetilde{V_z}}{\partial t} + \frac{\partial \bar{\rho} \widetilde{u_i} \widetilde{V_z}}{\partial x_i} = \frac{\partial}{\partial x_i} \left(\left(D_Z + \frac{\mu^{\text{sgs}}}{\text{Sc}_t} \right) \frac{\partial \widetilde{V_z}}{\partial x_i} \right) + 2 \frac{\mu^{\text{sgs}}}{\text{Sc}_t} \frac{\partial \widetilde{Z}}{\partial x_i} \frac{\partial \widetilde{Z}}{\partial x_i} - 2 \frac{\mu^{\text{sgs}}}{\text{Sc}_t} \frac{\widetilde{V_z}}{\Delta^2}. \quad (5.1)$$

As this was the equation used by Domingo et al. [20] as well as Ihme and See [41], it will be considered as the reference.

Figure 5.1 compares the distribution of the time-averaged mixture fraction variance in time-averaged mixture fraction space from transported fields and computed from stochastic fields (for 8 and 32 fields). The variance from the stochastic fields is lower than the transported one. It seems intrinsic to the Eulerian stochastic fields method as increasing the number of fields does not affect the present results[1]. When looking at the spatial distribution of

the transported variance and the one obtained from the stochastic fields (see Figure 5.3), the differences are even more obvious. It can be seen that the production of variance in the stochastic method is lower than in the transported equation. This results in a lower maximum variance value and faster dissipation (i.e. the volume influenced by mixture fraction variance is smaller).

From a chemical point of view, this means that at the very edge of the injector the higher variance blocks the chemistry, as the peak production for the most reactive mixture fraction is mitigated by the smaller source terms of the surrounding mixture fraction. However, a higher variance further downstream may have a positive impact on the progress variable source term. Indeed, once the radicals are built for mixture fraction close to Z_{MR}, high variance implies transfer of those radicals toward Z_{st} promoting the overall reactivity, since the highest heat release rates occur close to the stoichiometric composition.

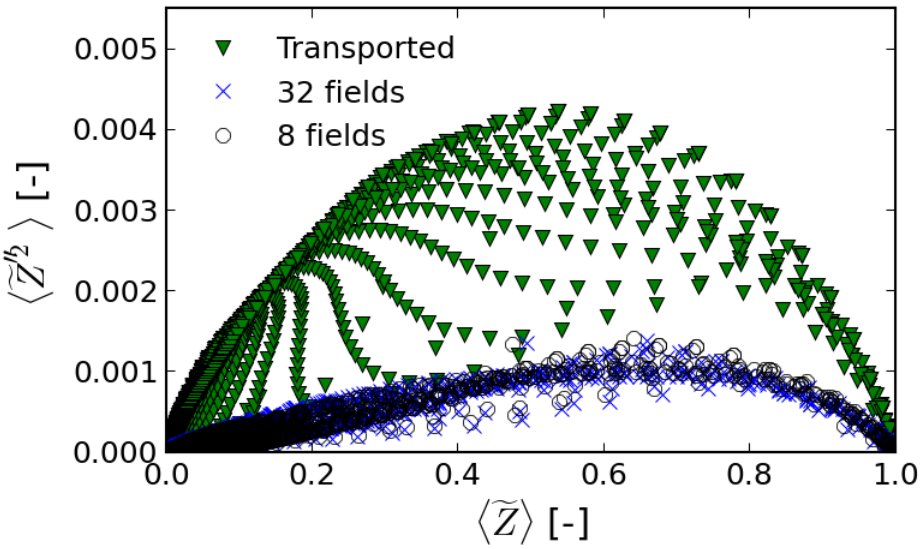

Figure 5.1: Distribution of the time-averaged mixture fraction variance as a function of the time-averaged mixture fraction. Black ○: variance with 8 stochastic fields – blue ×: variance with 32 stochastic fields – green ▼: transported variance.

To figure out the sources of discrepancy, the transported variance equation developed from the stochastic partial differential equation will be derived

[1] Theoretically the statistical error on the second order moment is proportional to $N^{-1/2}$. Therefore 32 fields give about 2 times lower statistical error than 8 fields.

first.
By definition, the variance $\widetilde{V}_{Y_k}$ of a scalar field Y_k is:

$$\widetilde{V}_{Y_k} = E\left[\left(\xi_{n,k} - \widetilde{Y}_k\right)^2\right] = E\left[\xi_{n,k}^2\right] - \widetilde{Y}_k^2. \tag{5.2}$$

The transport equation of $\widetilde{Y}_k$ reconstructed from the stochastic field is given by Equation (4.5). By multiplying it by $2\widetilde{Y}_k$ and applying the chain rule, the transport equation for $\widetilde{Y}_k^2$ is derived:

$$\begin{aligned}\frac{\partial \bar{\rho}\widetilde{Y}_k^2}{\partial t} &= -\frac{\partial \bar{\rho}\widetilde{u_i}\widetilde{Y}_k^2}{\partial x_i} + \frac{\partial}{\partial x_i}\left(\left(D_k + D_k^{\text{sgs}}\right)\frac{\partial \widetilde{Y}_k^2}{\partial x_i}\right) \\ &- 2\left(D_k + D_k^{\text{sgs}}\right)\frac{\partial \widetilde{Y}_k}{\partial x_i}\frac{\partial \widetilde{Y}_k}{\partial x_i} + 2\bar{\rho}\widetilde{Y}_k\tilde{\dot{\omega}}_k.\end{aligned} \tag{5.3}$$

The transport equation of $E\left[\xi_{n,k}^2\right]$ can be derived using Ito's formula [30].

$$df(\xi_{n,k}) = f'(\xi_{n,k})d\xi_{n,k} + 1/2 f''(\xi_{n,k})d\xi_{n,k}^2 + ... \tag{5.4}$$

In this case $f = \xi_{n,k}^2$, so $f' = 2\xi_{n,k}$ and $f'' = 2$. If the development is limited to first order in time dt, as $d\xi_{n,k}$ is given by Eq. (3.1), the only term in $d\xi_{n,k}^2$ to be taken into account is the square of the stochastic term as by definition $E[dW^2] = dt$ [30].

So introducing Eq. (3.1) in Eq. (5.4),

$$\begin{aligned}d\xi_{n,k}^2 &= 2\xi_{n,k}\left(-\tilde{u}_i\frac{\partial \xi_{n,k}}{\partial x_i}dt + \frac{1}{\bar{\rho}}\frac{\partial}{\partial x_i}\left[\left(D_k + D_k^{\text{sgs}}\right)\frac{\partial \xi_{n,k}}{\partial x_i}\right]dt + \dot{\omega}_k dt\right. \\ &- \left.\frac{C_\phi}{2\tau_{\text{sgs}}}(\xi_{n,k} - \widetilde{Y}_k)dt + \sqrt{2\bar{\rho}^{-1}D_k^{sgs}}\frac{\partial \xi_{n,k}}{\partial x_i}dW_i^n\right) \\ &+ \frac{1}{2}\,2\left(\sqrt{2\bar{\rho}^{-1}D_k^{sgs}}\frac{\partial \xi_{n,k}}{\partial x_i}dW_i^n\right)^2.\end{aligned} \tag{5.5}$$

By applying the chain rule, Eq. (5.5) becomes:

$$\begin{aligned}d\xi_{n,k}^2 &= -\tilde{u}_i\frac{\partial \xi_{n,k}^2}{\partial x_i}dt + \frac{1}{\bar{\rho}}\frac{\partial}{\partial x_i}\left[\left(D + D_k^{\text{sgs}}\right)\frac{\partial \xi_{n,k}^2}{\partial x_i}\right]dt \\ &- 2\frac{1}{\bar{\rho}}\left(D_k + D_k^{\text{sgs}}\right)\frac{\partial \xi_{n,k}}{\partial x_i}\frac{\partial \xi_{n,k}}{\partial x_i}dt + 2\xi_{n,k}\dot{\omega}_k dt - \frac{C_\phi}{\tau_{\text{sgs}}}(\xi_{n,k}^2 - \xi_{n,k}\widetilde{Y}_k)dt \\ &+ \sqrt{2\bar{\rho}^{-1}D_k^{sgs}}\frac{\partial \xi_{n,k}^2}{\partial x_i}dW_i^n + 2\frac{1}{\bar{\rho}}D_k^{sgs}\left(\frac{\partial \xi_{n,k}}{\partial x_i}\right)^2(dW_i^n)^2.\end{aligned} \tag{5.6}$$

As the expectation operator is by definition similar to the filter operator, the transported equation of $E\left[\xi_{n,k}^2\right] = \widetilde{Y_k^2}$ is:

$$\begin{aligned} d\widetilde{Y_k^2} &= -\tilde{u}_i \frac{\partial \widetilde{Y_k^2}}{\partial x_i} dt + \frac{1}{\bar{\rho}} \frac{\partial}{\partial x_i} \left[(D_k + D_k^{\text{sgs}}) \frac{\partial \widetilde{Y_k^2}}{\partial x_i} \right] dt - 2 \frac{1}{\bar{\rho}} D_k E \left[\frac{\partial \xi_{n,k}}{\partial x_i} \frac{\partial \xi_{n,k}}{\partial x_i} \right] dt \\ &+ 2E[\xi_{n,k} \dot{\omega}_k] dt - \frac{C_\phi}{\tau_{\text{sgs}}} (\widetilde{Y_k^2} - E[\xi_{n,k} \widetilde{Y_k}]) dt. \end{aligned} \tag{5.7}$$

The Wiener term disappears due to the non-anticipation property; i.e. $\sqrt{2\bar{\rho}^{-1} D_k^{sgs}} \frac{\partial \xi_{n,k}^2}{\partial x_i}$ is independent of dW_i^n and $E\left[\sqrt{2\bar{\rho}^{-1} D_k^{sgs}} \frac{\partial \xi_{n,k}^2}{\partial x_i} dW_i^n\right] = E\left[\sqrt{2\bar{\rho}^{-1} D_k^{sgs}} \frac{\partial \xi_{n,k}^2}{\partial x_i}\right] E\left[dW_i^n\right] = 0$.

Remarking that $E[\xi_{n,k} \widetilde{Y_k}] = E\left[\xi_{n,k} E[\xi_{n,k}]\right] = \widetilde{Y_k}^2$ and applying Eq. (5.2), the variance transport equation can be reconstructed:

$$\begin{aligned} d\widetilde{V_{Y_k}} &= -\tilde{u}_i \frac{\partial \widetilde{V_{Y_k}}}{\partial x_i} dt + \frac{1}{\bar{\rho}} \frac{\partial}{\partial x_i} \left[(D_k + D_k^{\text{sgs}}) \frac{\partial \widetilde{V_{Y_k}}}{\partial x_i} \right] dt \\ &- 2 \frac{1}{\bar{\rho}} \left(D_k E \left[\frac{\partial \xi_{n,k}}{\partial x_i} \frac{\partial \xi_{n,k}}{\partial x_i} \right] - D_k \frac{\partial \widetilde{Y_k}}{\partial x_i} \frac{\partial \widetilde{Y_k}}{\partial x_i} \right) dt \\ &+ 2 \frac{1}{\bar{\rho}} D_k^{sgs} \frac{\partial \widetilde{Y_k}}{\partial x_i} \frac{\partial \widetilde{Y_k}}{\partial x_i} dt - \frac{C_\phi \widetilde{V_{Y_k}}}{\tau_{\text{sgs}}} dt \\ &+ 2 \left(E[\xi_{n,k} \dot{\omega}_k] - \widetilde{Y_k} \tilde{\dot{\omega}}_k \right) dt. \end{aligned} \tag{5.8}$$

The first term is the transport by convection, the second is the transport by molecular diffusion and the subgrid scales, the third term results of the drift term added in the micro-mixing model, the fourth is the production term, the fifth the subgrid-scale scalar dissipation rate and the latest is the chemical source term effect.

The main difference with the transport equation of a scalar variance (see Eq. (5.1)) is the third term resulting from the addition of a drift term in the micro-mixing term[2]. This term represents the unresolved part of the scalar dissipation rate. Therefore the use of the drift term increases the variance dissipation. But as can be seen in Figure 5.2, the distribution of the variance

[2] Remark: without the drift term in the micro-mixing model, the third term disappears as well as the transport by molecular diffusion. And so the conservation equation of a scalar variance won't be recovered neither.

is not drastically changed by the suppression of the drift term; few points are found with a higher variance. Moreover for this test case, the absence of the drift term results in a flashback and not in an autoignition-spots regime[3].

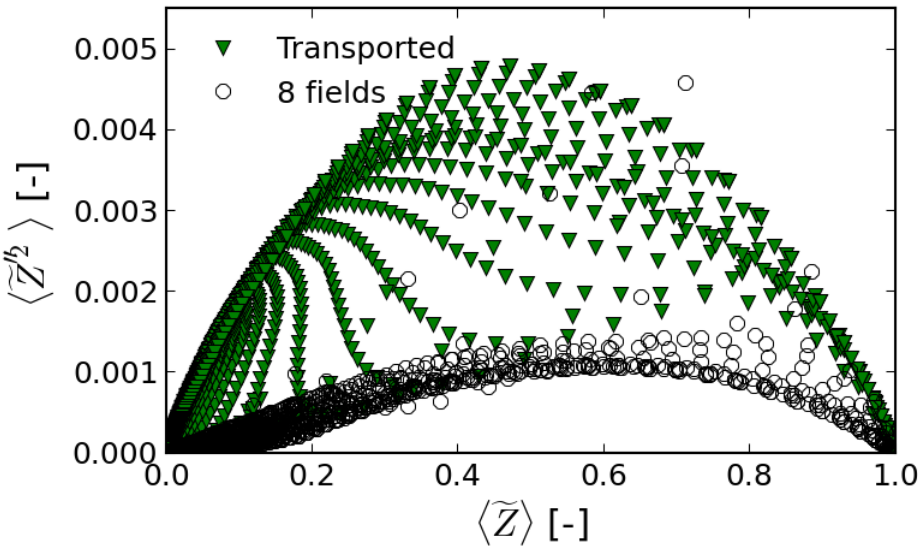

Figure 5.2: Distribution of the time-averaged mixture fraction variance as a function of the time-averaged mixture fraction when using the theoretical expression (see Sec. 4.2.1). black ∘: variance with 8 stochastic fields – green ▼: transported variance.

But this is not the only difference. Indeed there are three additional differences between the transported scalar variance and the Eulerian stochastic field method described in Sec. 3.1.2:

- The definition of τ_{sgs}: in the literature [20, 41, 52] $\tau_{\text{sgs}} = \frac{\Delta^2}{\nu^{\text{sgs}}}$. But the expression of Jones et al. was used; i.e. $\tau_{\text{sgs}} = \frac{\Delta^2}{\nu+\nu^{\text{sgs}}}$.
  On very fine meshes the laminar viscosity becomes non-negligible compared to the turbulent effect. Therefore the expression of Jones et al. implies a stronger variance decay.

- Theoretically a Wiener process has a Gaussian distribution with its mean equal to zero and its variance to dt. The current implementation simplifies the generation by using a dichotomic value $\pm dt^{1/2}$. Therefore the production of high variance may be reduced by absence of higher random values.

[3] To avoid the effect due to the density variation induced by the flashback, the results shown in Fig. 5.2 are computed with the cold flow.

- The latest is the trickiest. Indeed, the scalars have to be bounded between 0 and 1 to have a physical meaning. Therefore all stochastic fields are bounded at the end of the time step to fulfill the physical boundaries. In this process the variance can be artificially reduced for values close to the boundaries. This does not happen when transporting the variance directly.

To study the influence of the previous elements, the reference simulation was done with other micro-mixing models:

1. New definition for $\tau_{\text{sgs}} = \frac{\Delta^2}{\nu^{\text{sgs}}}$.
2. Gaussian noise: the Wiener process is computed from a Gaussian-distributed noise. To enforce the statistic, after generating the random values, their mean and variance are corrected to fit with the definition (mean equal to zero and variance to dt).
3. Gaussian noise + new definition for τ_{sgs}: the combination of the two previous modifications.
4. The Langevin model + new definition for τ_{sgs}: The micro-mixing model is replaced by the combination of a drift term and a Langevin model. Following Sabel'nikov and Gorokhovski [100], the Langevin model is defined as:

$$\begin{cases} -\frac{a}{\tau_{\text{sgs}}}\left(\xi_{n,k} - \widetilde{Y_k}\right) dt + \sqrt{2\frac{b}{\tau_{\text{sgs}}}\xi_{n,k}(1-\xi_{n,k})}dW^n \\ a = 1 + d_0 \frac{E[\xi_{n,k}(1-\xi_{n,k})]}{\widetilde{Y_k}(1-\widetilde{Y_k})} \\ b = d_0 \frac{\widetilde{V}_{Y_k}}{\widetilde{Y_k}(1-\widetilde{Y_k})} \end{cases} \tag{5.9}$$

   d_0 controls the rate of PDF relaxation. Following Soulard et al. [109], a value of 1 was taken.

Table 5.1 summarizes the average AIS height for different micro-mixing model. The averaged heights of the auto-ignition spots are roughly similar.

A deeper analysis will focus on the mixture fraction in order to reduce modeling hypothesis between the transported equations and the stochastic fields. The filtered mixture fraction fields are identical for all tested models (not shown). But differences appear on the second order moment. In Figure 5.3

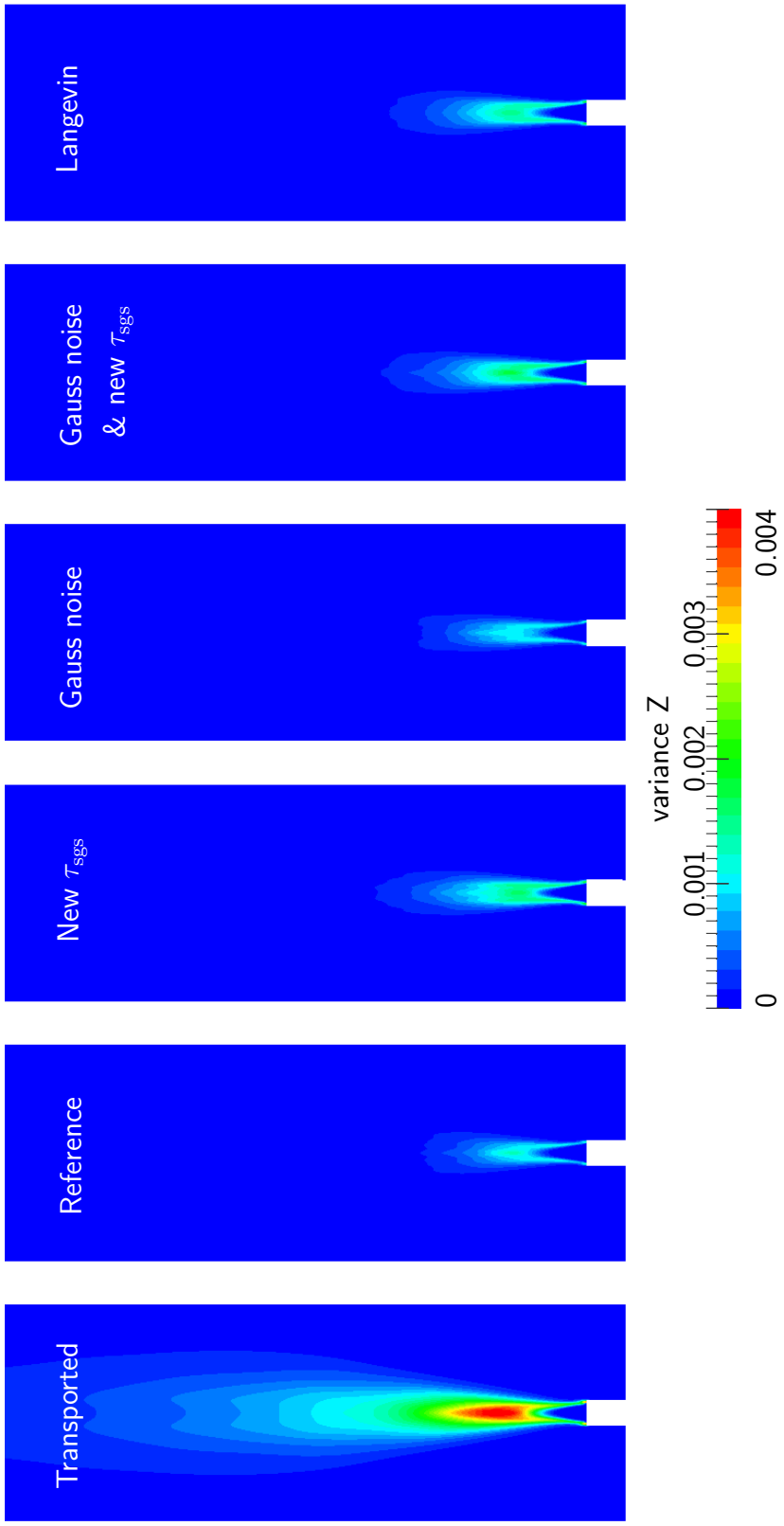

Figure 5.3: Time averaged mixture fraction variance for divers micro-mixing model – from bottom to top: transported equation, reference case (8 fields and $\tau_{\text{sgs}} = \frac{\bar{\rho}\Delta^2}{\mu+\mu^{\text{sgs}}}$), 8 fields and $\tau_{\text{sgs}} = \frac{\bar{\rho}\Delta^2}{\mu^{\text{sgs}}}$, Wiener term based on $N(0,1)$ and old τ_{sgs}, Wiener term based on $N(0,1)$ and new τ_{sgs} and Langevin micro-mixing model.

Micro-mixing model	Average AIS height
Reference case	33.25 mm
New τ_{sgs}	32.9 mm
Gaussian noise with old τ_{sgs}	35.27 mm
Gaussian noise with new τ_{sgs}	32.71 mm
Langevin model	34.8 mm

Table 5.1: Averaged auto-ignition spot height for different micro-mixing models.

the time-averaged variances are drawn. The reference was computed with 8 stochastic fields. The results were identical with 32 fields (see Figure 5.1). The new definition for τ_{sgs} results, as expected, in higher variance and more spatial spread. The Gaussian-distributed random number results in slightly smaller variance, while the Langevin model delivers similar results as the model Gaussian noise + new τ_{sgs}.

Even though the variance is altered by the different micro-mixing models, it is still far from the field obtained when transporting the variance. The parasite term arising from the use of a drift term increases the dissipation of the scalar. But it does not explain totally the fast dissipation of the variance. So a better micro-mixing model should be found. For that some additional research similar to the one of Soulard et al. [109] should be carried out.

The bounding of the stochastic fields could explain the quick dissipation as the Wiener process is centered around the filtered value even when the distribution is far from centered; typically for mixture fractions close to the boundaries. Jones et al. may have got better results by transporting directly the species, since only the lower bound should be enforced.

5.2 The scalar dissipation rate effect

High scalar dissipation rates are delaying auto-ignition events and are related to extinction of flames[4]. Indeed by definition, a high value of the scalar dissipation rate implies an intense diffusion of the species in mixture fraction space. If the diffusion is too strong, radicals, precursors to an auto-ignition event, cannot build up as it will be directly diluted. Therefore the auto-ignition delay is increased. On the other end, a moderate scalar dissipation rate will help the propagation of the flame.

The current model is not taking explicitly into account the impact of the scalar dissipation rate. Nevertheless, where the scalar dissipation rate is large, the variance in mixture fraction should be large. And therefore a similar effect should be seen; i.e. the transport of the species overwhelms the low chemistry source terms. Additionally the previous analysis shows that the variance is underestimated by the Eulerian stochastic fields compared to the transported equation. On the auto-ignition-spots test cases, this was not a problem, as the mixing between the fuel jet and the co-flow was not so intense. But in the case of the Cabra lifted flame, the difference in velocities between the jet and the co-flow implies a scalar dissipation rate close to the injector greater than the extinction scalar dissipation rate. Therefore the source term of the progress variable at that pristine stage is probably overestimated by the model.

The improved mixing for moderate scalar dissipation rate is not taken into account in the tabulation process, as the homogeneous reactors are run separately in mixture fraction space. But the simulation of Ihme and See [41], using unsteady flamelets, agrees very well with the experimental data and flame structure. Therefore the chemistry in this test case seems better captured by unsteady flamelets than by auto-igniting reactors. Moreover the success of 0D-CMC[5] for a broad range of partially-premixed flames tends to support the idea that the scalar dissipation rate is a non-negligible parameter in classical partially premixed flame. It will be therefore interesting to develop the model using unsteady flamelets chemistry. Then it will be possible, based on the results for a test case with high scalar dissipation rate,

[4] A critical value exists above which a flame cannot sustain (see Section 2.2.2).
[5] 0D-CMC is similar to tabulated chemistry based on unsteady flamelets.

to determine if the current failure of the model in such case comes from the inaccurate evaluation of the variance or from the tabulated chemistry.

5.3 Tabulated chemistry modeling

The code developed during this thesis allows to generate tables from homogeneous reactor at constant pressure or laminar premixed flames. The former is adequate for simulating auto-ignition spots regime when the latter can capture premixed flames. However for other type of flames, in particular for diffusion flames, the scalar dissipation rate influences greatly the chemistry and should be taken into account in the tabulation process. The success of Ihme and See [41] for example proves the great potential of tabulated chemistry based on unsteady flamelets for non-premixed and partially premixed flames.

The cost of tabulated chemistry is not on the computation time but on the memory consumption. Section 3.3 has introduced a simple approach to optimize the tabulation process. But others have developed automatic approach for reducing the tables size. For example, the self-similarity behavior of laminar premixed flames have been used extensively by the teams of D. Veynante and L. Vervisch [27, 98, 99, 113, 114]. A more generalized approach based on memory management have also been developed by S. Weise et al. [115].

The current simulations taken into account more and more effects can quickly require tables of high dimensions. Therefore such reduction techniques could be a good addition to the current model implementation to keep the computational cost acceptable.

5.4 NO_x model

The last section will discuss some limits and improvements for the NO_x model.

5.4.1 Limits of the model

Determining the coefficients in Eqs. (3.6) and (3.9) is the key part to ensure accuracy. Although the curve fitting algorithm is easy to apprehend, it comes with some disadvantages:

- If the number of parameters to fit is too large, the fitted algorithm will generate functions with high frequency fluctuations, which increase the error. Indeed in Fig. 3.6, using 2 or 3 time scales results in greater error than 1 time scale. Unfortunately the optimal number of time scales is unknown and differs from one set of conditions to another.

- The accuracy of the fitting depends heavily on the data set used for carrying out the curve fitting. For example if the time evolution is controlled by 4 time scales, but the function to fit has only 3, then the 3 captured time scales will be function of the data set. Indeed, if the data set is short in time, the chance is high that the biggest time scale will not be captured. In the opposite case, if the data set covers a large time, the shortest time scale will most likely be missing.

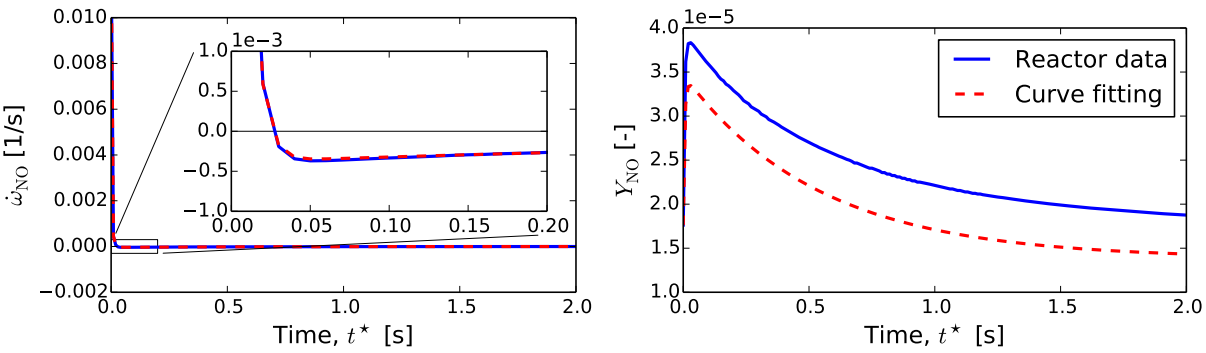

Figure 5.4: Curve fitting for the variation of $\dot{\omega}_{NO}$ (left) and Y_{NO} (right). The boundary conditions are those of the Cabra methane flame with $Z = 0.295$.

The hypothesis on the shape of the function itself can be wrong. Indeed for pathological conditions, the source term of NO is not a series of decreasing exponential. For example in Figure 5.4, $\dot{\omega}_{\mathrm{NO}}$ falls very sharply and becomes negative. Then it relaxes towards zero with a rising exponential. In such a case the algorithm described in Fig. 3.7 does not work anymore. Indeed for a given value of Y_{NO} can correspond two values of $t^{\star}$.

This situation was encountered only at very rich conditions. As, in partially-premixed flames, it rarely occurs to get very rich regions in the burnt products, this limitation does not impact most of industrial flames. But it could bring troubles when investigating diffusion flames .

5.4.2 Generalization

The correlations have been derived for homogeneous reactors and laminar premixed flames. But for other configurations, like unsteady flamelet, algebraic relations cannot be derived so straightforwardly. For such configurations an approach inspired from Zoller et al. [119] could be a solution. The process will be the following: the composition of the table corresponding to $C = 99\%$ will be used to set a homogeneous reactor. Then the curve fitting will be carried out on the time evolution of those reactors. And as the burnt products are found for low values of the scalar dissipation rate, it is probably sufficient to apply the curve fitting only for the set of composition with the lowest scalar dissipation rate.

Another idea to improve of the curve fitting would be to extract the time scales from the method of *Computational Singular Perturbation* (CSP) [67, 68]. This analysis extracts time scales from the eigen-values of the chemical equations. Applying this analysis at the threshold point between the look-up table and the algebraic relations (taken at $C = 99\%$), the required time scales driving the reactions would be identified to the slow time scales with non-zero amplitude.

5.5 Summary

It has been demonstrated that the stochastic differential equation results in the similar equation for the transported variance than the one used by Domingo et al. [20] and Ihme and See [41]. There are only two differences. The drift term introduces in Equation (3.1) creates a new dissipation term in the variance equation derived from it. And the turbulent time-scale hypothesis is reduced because the laminar viscosity is taken into account. Those differences tends to reduce faster the variance with the stochastic fields method. But the results obtained by suppressing those differences are still showing great discrepancies with the result obtained by the direct transport of the variance.

Letting aside the numerical issues, the reason left to explain the error is the bounding process of the stochastic fields. Indeed to maintain physical meaning of the stochastic fields, they are bounded between 0 and 1. This occurs mainly close to the injector where the mixing is taking place between the two pure flows. Unfortunately this is also the place where the variance is produced.

The error between the transported variance and the one resulting of the SF is still low for the test case showed here – the velocities of the fuel and the oxidant being alike. But for case such the Cabra flame, the production of variance is more critical due to the difference in Reynolds number. Consequently the error is expected to be even larger. This prompts the need of a deeper study to improve the estimation of the variance from the stochastic fields.

Although the scalar dissipation rate is not taken explicitly into account in the present model, the success of Domingo et al. [20] with the Cabra flame proves that the flow is chemically controlled as it was shown by Gordon et al. [36]. The roots of the errors produced by the new model should be looked first in the variance prediction. Then the current model could be extended to look-up tables based on unsteady flamelets. This will allow to simulate a broader range of flames; e.g. the Sandia flames D, E and F could be simulated.

Concerning, the new NO_x model, the first improvement to do should be a stricter way of predicting the time scales of NO formation paths in burnt products. The *Computational Singular Perturbation* could bring an elegant solution.

6 Conclusions and Outlook

The computational cost of Large-Eddy Simulations has now reached an acceptable level to be used on a daily basis in an industrial context. This will bring a huge improvement particularly in combustion systems in which the interactions between the turbulence and the chemistry are crucial. But to achieve a good trade-off between modeling hypothesis and computational cost, new combustion models must be designed. The proposed SF-PV model of R. Kulkarni coupling Eulerian stochastic fields' method with tabulated chemistry achieved great success for auto-ignition in turbulent flows.

The canonical test cases carried out during this work refine and validate multiple aspects of that model. Firstly the validation of tabulated chemistry highlights:

- The progress variable definition must combine a radical species with a product species; i.e. for hydrogen, H_2O + HO_2 and for hydrocarbons, CO_2 + CO + CH_2O.
- The relaxation for the species source terms with the respect of atomic budgets is the best implementation of the model.
- For tables based on 1D laminar premixed flames, the coefficients of diffusion model must be identical in the chemistry software and in the CFD one.

The validation on turbulent auto-ignition test cases shows the ability of the model to capture accurately the impact of:

- The temperature of the co-flow,
- The velocity of the flows,
- The fuel composition

on the auto-ignition length and type of flames (no-flame, auto-ignition spots or flash-back).

Moreover the detailed analysis of the ETH test case proves that the physics behind the development and the propagation of auto-ignition spots is correctly captured by the LES model. Indeed spots appear close to the most-reactive mixture fraction. Then comes a spherical growth of the spot. It finally propagates into the rich regions to form a flamelet.

The deep analysis of the auto-ignition spots appearance thanks to tracer particles confirms the weak influence of the scalar dissipation rate in such flows. This allows to speed-up the tabulation process by using only homogeneous reactors.

The final stage of this work was the design of a new nitrogen oxides model. This model is based on the resolution of a transport equation for NO_x with its source term supplied by a look-up table or algebraic relations. Indeed starting from the observation that NO and the progress variable are not (or weakly) coupled in the burnt products, the new model reads the source term in a look-up table up to the reaction completion. Then it switches to algebraic relations approximating by a series of decaying exponentials the evolution of NO source term in the burnt products. The validation of this model in homogeneous reactors and for laminar premixed flames was a success.

Although the model could be partly validated on some test cases, this work found limitations requiring further development.

One issue rose about the differential diffusion modeling. To capture this effect the diffusion coefficient of the progress variable should be modeled more accurately. One solution using element mass fractions was proposed by Gicquel et al. [33]. Unfortunately that solution requires huge look-up tables.

But the biggest limitation left unanswered by this work is the modeling of higher moment orders; especially the variance. Test cases have highlighted a stronger dissipation of the variance in the current model in comparison with a transported variance. Changing the micro-mixing model brought some variations in the results. But the discrepancy remains large. Therefore the main root for this higher dissipation is probably to be found in the bounding process of the stochastic fields. These two points (micro-mixing model and

bounding process) should be the primary concern for further development of the model.

Two interesting extensions of the current model should be taken into account for further developments. First the implementation of look-up tables based on unsteady flamelets would extend the model to a broader range of flames and allows to estimate precisely the influence of the scalar dissipation rate in auto-igniting turbulent flows. Secondly, the model could be extended to compute the chemical source terms in a traditional way (resolution of the chemical ODE system). When using only species, the bounding process of the stochastic fields is applied more rarely; the probability of having $Y_k > 1$ is null. It will then be possible to assess the accuracy of the tabulated chemistry versus standard way of computing the chemistry.

Supervised Theses

Im Rahmen dieser Dissertation entstanden am Lehrstuhl für Thermodynamik in den Jahren 2009 bis 2012 unter wesentlicher wissenschaftlicher, fachlicher und inhaltlicher Anleitung des Autors, die im Folgenden aufgeführten studentischen Arbeiten. In ihnen wurden verschiedene Fragestellungen zur Verbrennungsmodelierung und Selbstzündung untersucht. Ergebnisse aus diesen Arbeiten können in Teilen in das vorliegende Dokument eingeflossen sein. Der Autor dankt hiermit nochmals explizit allen ehemals betreuten Studenten für ihr Engagement bei der Unterstützung dieser wissenschaftlichen Arbeit.

Associated with this Ph.D. thesis are one "student bachelor thesis" and one "student internship" (IAESTE Program) that were supervised by the author of the present work. Those theses were prepared at the Lehrstuhl für Thermodynamik in the years 2009 through 2012 under the close supervision of the present author in its full academical and professional breadth. Various issues were investigated concerning combustion modeling and autoignition problems. Some parts of those supervised theses may have been incorporated into the present thesis. The author would like to express his sincere gratitude to all formerly supervised students for their commitment supporting this research project.

Student	**Thesis**
Robert Mayston	*Numerical Study of Auto-ignition of Turbulent Air in a Cylinder*, IAESTE internship, filed in February 29$^{\text{th}}$, 2012.
Rupert Wildhofer	*Tabulated Chemistry for Premixed Flamelets in Vitiated Air*, Bachelor's thesis, filed in September 29$^{\text{th}}$, 2011.

References

[1] J. Akroyd, A. J. Smith, L. R. McGlashan, and M. Kraft. Numerical investigation of DQMoM-IEM as a turbulent reaction closure. *c4e-Preprint Series*, Preprint 76, 2009. Cambridge.

[2] J. Akroyd, A. J. Smith, L. R. McGlashan, and M. Kraft. Comparison of the stochastic fields method and DQMoM-IEM as turbulent reaction closures. *Chemical Engineering Science*, 65(20):5429 – 5441, 2010. ISSN 0009-2509. doi: 10.1016/j.ces.2010.06.039. URL `http://www.sciencedirect.com/science/article/pii/S0009250910004057`.

[3] S. Ayache and E. Mastorakos. Conditional moment closure/large eddy simulation of the Delft-III natural gas non-premixed jet flame. *Flow, Turbulence and Combustion*, 88:207–231, 2012. ISSN 1386-6184. doi: 10.1007/s10494-011-9368-6. URL `http://dx.doi.org/10.1007/s10494-011-9368-6`.

[4] G. Bikas. *Kinetic mechanisms for hydrocarbon ignition*. PhD thesis, University of Aachen, 2001.

[5] P. Boivin, C. Jiménez, A. L. Sánchez, and F. A. Williams. An explicit reduced mechanism for H-2-air combustion. *Proceedings of the Combustion Institute*, 33(Part 1):517–523, 2011. ISSN 1540-7489. doi: 10.1016/j.proci.2010.05.002.

[6] G. Boudier, L. Y. M. Gicquel, and T. J. Poinsot. Effects of mesh resolution on large eddy simulation of reacting flows in complex geometry combustors. *Combustion and Flame*, 155(1-2):196–214, OCT 2008. ISSN 0010-2180. doi: 10.1016/j.combustflame.2008.04.013.

[7] D. Bradley, L. Kwa, A. Lau, M. Missaghi, and S. Chin. Laminar flamelet modeling of recirculating premixed methane and propane-air combustion. *Combustion and Flame*, 71(2):109 – 122, 1988. ISSN 0010-2180. doi: 10.1016/0010-2180(88)90001-6. URL `http://www.sciencedirect.com/science/article/pii/0010218088900016`.

[8] M. Brandt. *Beschreibung der Selbstzündung in turbulenter Strömung unter Einbeziehung ternärer Mischvorgänge*. PhD thesis, Technische Universität München, 2005.

[9] M. Brandt, W. Polifke, B. Ivancic, P. Flohr, and B. Paikert. Auto-ignition in a gas turbine burner at elevated temperature. ASME, 2003.

[10] M. Brandt, W. Polifke, and P. Flohr. Approximation of joint pdfs by discrete distributions generated with monte carlo methods. *Combustion Theory and Modelling*, 10(4):535–558, 2006. doi: 10.1080/13647830500497815. URL `http://www.tandfonline.com/doi/abs/10.1080/13647830500497815`.

[11] R. Cabra, T. Myhrvold, J.-Y. Chen, R. Dibble, A. Karpetis, and R. Barlow. Simultaneous laser Raman-Rayleigh-LIF measurements and numerical modeling results of a lifted turbulent H2/N2 jet flame in a vitiated coflow. *Proceedings of the Combustion Institute*, 29(2): 1881 – 1888, 2002. ISSN 1540-7489. doi: 10.1016/S1540-7489(02)80228-0. URL `http://www.sciencedirect.com/science/article/pii/S1540748902802280`.

[12] R. Cabra, J.-Y. Chen, R. Dibble, A. Karpetis, and R. Barlow. Lifted methane-air jet flames in a vitiated coflow. *Combustion and Flame*, 143(4):491 – 506, 2005. ISSN 0010-2180. doi: 10.1016/j.combustflame.2005.08.019. URL `http://www.sciencedirect.com/science/article/pii/S0010218005002312`.

[13] R. Cabra. Lifted CH4/Air jet flame in a vitiated coflow, 2002. URL `http://www.me.berkeley.edu/cal/vcb/data/VCMAData.html`.

[14] O. Colin, C. Pera, and S. Jay. Detailed chemistry tabulation based on a FPI approach adapted and applied to 3-D internal combustion engine calculations. In *Third European Combustion Meeting ECM 2007*, 2007.

[15] F. Collonval and W. Polifke. Introduction of differential diffusion effect in methane premixed flame simulations through tabulated chemistry. In *7th OpenFOAM Workshop*, Darmstadt, 2012.

[16] F. Collonval, R. Kulkarni, and W. Polifke. Investigation of progress-variable approach for auto-ignition prediction. 2011. Not published.

[17] F. Collonval, R. Kulkarni, and W. Polifke. Large-eddy simulation of auto-ignition processes for industrial applications. In *Open Source CFD International Conference*, Paris-Chantilly, France, 2011.

[18] F. Collonval and W. Polifke. Modelling the formation of oxides of nitrogen in premix combustion by extending tabulated chemistry with algebraic relations. In *Proceedings of ASME Turbo Expo 2014*, number GT2014-27293, Dusseldorf, Germany, June 16-20 2014.

[19] P. Domingo, L. Vervisch, and D. Veynante. Auto-ignition and flame propagation effects in les of burned gases diluted turbulent combustion. In *Center for Turbulence Research Proceedings of the Summer Program 2006*, 2006.

[20] P. Domingo, L. Vervisch, and D. Veynante. Large-eddy simulation of a lifted methane jet flame in a vitiated coflow. *Combustion and Flame*, 152(3):415 – 432, 2008. ISSN 0010-2180. doi: 10.1016/j.combustflame.2007.09.002. URL `http://www.sciencedirect.com/science/article/pii/S0010218007002519`.

[21] R. Eggels and L. de Goey. Post-processing method for predicting NO formation in one- and two-dimensional premixed methane-air flames. *Combustion and Flame*, 107(1-2):65 – 71, 1996. ISSN 0010-2180. doi: 10.1016/0010-2180(96)00017-X. URL `http://www.sciencedirect.com/science/article/pii/001021809600017X`.

[22] N. Enjalbert, P. Domingo, and L. Vervisch. Mixing time-history effects in large eddy simulation of non-premixed turbulent flames: Flow-controlled chemistry tabulation. *Combustion and Flame*, 159(1):336 – 352, 2012. ISSN 0010-2180. doi: 10.1016/j.combustflame.2011.06.005. URL `http://www.sciencedirect.com/science/article/pii/S0010218011001854`.

[23] U. S. Environmental Protection Agency. Nitrogen dioxide, 2013. URL `http://www.epa.gov/airquality/nitrogenoxides`.

[24] C. Fenimore. Formation of nitric oxide in premixed hydrocarbon flames. In *Symposium (International) on Combustion*, volume 13, pages 373–380. Elsevier, 1971. doi: http://dx.doi.org/10.1016/S0082-0784(71)80040-1. URL `http://www.sciencedirect.`

com/science/article/pii/S0082078471800401. Thirteenth symposium (International) on Combustion.

[25] B. Fiorina, O. Gicquel, L. Vervisch, S. Carpentier, and N. Darabiha. Approximating the chemical structure of partially premixed and diffusion counterflow flames using FPI flamelet tabulation. *Combustion and Flame*, 140(3):147–160, FEB 2005. ISSN 0010-2180. doi: 10.1016/j.combustflame.2004.11.002.

[26] B. Fiorina, O. Gicquel, L. Vervisch, S. Carpentier, and N. Darabiha. Premixed turbulent combustion modeling using tabulated detailed chemistry and PDF. In *Proceedings of the Combustion Institute*, volume 30, pages 867 – 874, 2005. doi: DOI:10.1016/j.proci.2004.08.062. URL http://www.sciencedirect.com/science/article/B7GWS-4DB550N-5/2/dfd30765c76140b5cb793f68f62f0b88.

[27] B. Fiorina, O. Gicquel, and D. Veynante. Turbulent flame simulation taking advantage of tabulated chemistry self-similar properties. *Proceedings of the Combustion Institute*, 32(2):1687 – 1694, 2009. ISSN 1540-7489. doi: 10.1016/j.proci.2008.06.004. URL http://www.sciencedirect.com/science/article/pii/S1540748908000072.

[28] R. Fox. *Computational models for turbulent reacting flows*. Cambridge University Press, 2003.

[29] J. Galpin, A. Naudin, L. Vervisch, C. Angelberger, O. Colin, and P. Domingo. Large-eddy simulation of a fuel-lean premixed turbulent swirl-burner. *Combustion and Flame*, 155(1-2):247 – 266, 2008. ISSN 0010-2180. doi: 10.1016/j.combustflame.2008.04.004. URL http://www.sciencedirect.com/science/article/pii/S0010218008000990.

[30] C. W. Gardiner. *Stochastic methods*, volume 13 of *Springer Series in Synergetics*. Springer, 4th edition edition, 2009.

[31] E. Garnier, N. Adams, and P. Sagaut. *Large eddy simulation for compressible flows*. Scientific computation. Springer London, Limited, 2009. ISBN 9789048128198. URL http://books.google.fr/books?id=_7zowRoPSnoC.

[32] M. Germano, U. Piomelli, P. Moin, and W. Cabot. A dynamic subgrid-scale eddy viscosity model. *Physics of Fluids A: Fluid Dynamics*, 3: 1760, 1991.

[33] O. Gicquel, N. Darabiha, and D. Thévenin. Laminar premixed hydrogen/air counterflow flame simulations using flame prolongation of ILDM with differential diffusion. In *Proceedings of the Combustion Institute*, volume 28, pages 1901 – 1908, 2000. doi: 10.1016/S0082-0784(00)80594-9. URL `http://www.sciencedirect.com/science/article/pii/S0082078400805949`.

[34] D. Goodwin. An open-source, extensible software suite for CVD process simulation. In F. M. M. Allendorf and F. T. editors, editors, *Chemical Vapor Deposition XVI and EUROCVD 14*, ECS Proceedings Volume 2003-08, pages 155–162. The Electrochemical Society, 2003. URL `http://code.google.com/p/cantera`.

[35] R. L. Gordon, A. R. Masri, S. B. Pope, and G. M. Goldin. A numerical study of auto-ignition in turbulent lifted flames issuing into a vitiated co-flow. *Combustion Theory and Modelling*, 11(3):351–376, 2007. doi: 10.1080/13647830600903472. URL `http://www.tandfonline.com/doi/abs/10.1080/13647830600903472`.

[36] R. L. Gordon, A. R. Masri, S. B. Pope, and G. M. Goldin. Transport budgets in turbulent lifted flames of methane autoigniting in a vitiated co-flow. *Combustion and Flame*, 151(3):495 – 511, 2007. ISSN 0010-2180. doi: 10.1016/j.combustflame.2007.07.001. URL `http://www.sciencedirect.com/science/article/pii/S0010218007001721`.

[37] D. Haworth. Progress in probability density function methods for turbulent reacting flows. *Progress in Energy and Combustion Science*, 36(2):168 – 259, 2010. ISSN 0360-1285. doi: 10.1016/j.pecs.2009.09.003. URL `http://www.sciencedirect.com/science/article/pii/S036012850900046X`.

[38] J. D. Hunter. Matplotlib: A 2D graphics environment. *Computing In Science & Engineering*, 9(3):90–95, 2007. URL `http://matplotlib.org`.

[39] M. Ihme and H. Pitsch. Prediction of extinction and reignition in nonpremixed turbulent flames using a flamelet/progress variable

model: 1. A priori study and presumed PDF closure. *Combustion and Flame*, 155(1-2):70 – 89, 2008. ISSN 0010-2180. doi: DOI:10.1016/j.combustflame.2008.04.001. URL http://www.sciencedirect.com/science/article/pii/S0010218008000904.

[40] M. Ihme and H. Pitsch. Modeling of radiation and nitric oxide formation in turbulent nonpremixed flames using a flamelet/progress variable formulation. *Physics of Fluids*, 20(5):055110, 2008. doi: 10.1063/1.2911047. URL http://link.aip.org/link/?PHF/20/055110/1.

[41] M. Ihme and Y. C. See. Prediction of autoignition in a lifted methane/air flame using an unsteady flamelet/progress variable model. *Combustion and Flame*, 157(10):1850 – 1862, 2010. ISSN 0010-2180. doi: DOI:10.1016/j.combustflame.2010.07.015. URL http://www.sciencedirect.com/science/article/pii/S0010218010002038.

[42] J. Jaishree and D. C. Haworth. Comparisons of Lagrangian and Eulerian PDF methods in simulations of non-premixed turbulent jet flames with moderate-to-strong turbulence-chemistry interactions. *Combustion Theory and Modelling*, 16(3):435–463, 2012. doi: 10.1080/13647830.2011.633349. URL http://www.tandfonline.com/doi/abs/10.1080/13647830.2011.633349.

[43] E. Jones, T. Oliphant, P. Peterson, et al. SciPy: Open source scientific tools for Python, 2001–. URL http://www.scipy.org.

[44] W. Jones and S. Navarro-Martinez. Numerical study of n-heptane auto-ignition using LES-PDF methods. *Flow, Turbulence and Combustion*, 83:407–423, 2009. ISSN 1386-6184. URL http://dx.doi.org/10.1007/s10494-009-9228-9. 10.1007/s10494-009-9228-9.

[45] W. Jones and V. Prasad. Large eddy simulation of a piloted methane jet flame with high levels of extinction (Sandia Flame E) using the Eulerian stochastic field method. In *Proceedings of the European Combustion Meeting 2009*, 2009.

[46] W. Jones and R. Lindstedt. Global reaction schemes for hydrocarbon combustion. *Combustion and Flame*, 73(3):233 – 249, 1988. ISSN 0010-2180. doi: 10.1016/0010-2180(88)90021-1. URL http://www.sciencedirect.com/science/article/pii/0010218088900211.

[47] W. Jones and S. Navarro-Martinez. Large eddy simulation of autoignition with a subgrid probability density function method. *Combustion and Flame*, 150(3):170 – 187, 2007. ISSN 0010-2180. doi: 10.1016/j.combustflame.2007.04.003. URL http://www.sciencedirect.com/science/article/pii/S0010218007001022.

[48] W. Jones and S. Navarro-Martinez. Study of hydrogen auto-ignition in a turbulent air co-flow using a large eddy simulation approach. *Computers & Fluids*, 37(7):802 – 808, 2008. ISSN 0045-7930. doi: 10.1016/j.compfluid.2007.02.015. URL http://www.sciencedirect.com/science/article/pii/S0045793007001582.

[49] W. Jones and V. Prasad. Large eddy simulation of the Sandia Flame series (D-F) using the Eulerian stochastic field method. *Combustion and Flame*, 157(9):1621 – 1636, 2010. ISSN 0010-2180. doi: 10.1016/j.combustflame.2010.05.010. URL http://www.sciencedirect.com/science/article/pii/S0010218010001525.

[50] W. Jones, S. Navarro-Martinez, and O. Röhl. Large eddy simulation of hydrogen auto-ignition with a probability density function method. In *Proceedings of the Combustion Institute*, volume 31, pages 1765 – 1771, 2007. doi: 10.1016/j.proci.2006.07.041. URL http://www.sciencedirect.com/science/article/pii/S1540748906000496.

[51] A. Kazakov and M. Frenklach. *Reduced Reaction Sets based on GRI-Mech 1.2*. URL http://www.me.berkeley.edu/drm.

[52] K. A. Kemenov, H. Wang, and S. B. Pope. Modelling effects of subgrid-scale mixture fraction variance in LES of a piloted diffusion flame. *Combustion Theory and Modelling*, 16(4):611–638, 2012. doi: 10.1080/13647830.2011.645881. URL http://www.tandfonline.com/doi/abs/10.1080/13647830.2011.645881.

[53] A. Kempf, M. Klein, and J. Janicka. Efficient generation of initial- and inflow-conditions for transient turbulent flows in arbitrary geometries. *Flow, Turbulence and Combustion*, 74:67–84, 2005. ISSN 1386-6184. doi: 10.1007/s10494-005-3140-8. URL http://dx.doi.org/10.1007/s10494-005-3140-8.

[54] S. Kerkemeier. *Direct Numerical Simulation of Combustion on Petascale Platforms: Application to Turbulent Non-Premixed Hydrogen Autoignition*. PhD thesis, ETH Zürich, 2010.

[55] S. Kerkemeier, C. Frouzakis, A. Tomboulides, E. Mastorakos, and K. Boulouchos. Autoignition of a diluted hydrogen jet in a heated 2-D turbulent air flow. In *Proceedings of the European Combustion Meeting, Vienna, Austria*, 2009.

[56] S. Kerkemeier, C. Frouzakis, K. Boulouchos, and E. Mastorakos. Numerical simulation of autoignition of a diluted hydrogen jet in coflowing turbulent hot air. In *48th AIAA Aerospace Sciences Meeting Including the New Horizons Forum and Aerospace Exposition*, 2010.

[57] M. Klein, A. Sadiki, and J. Janicka. A digital filter based generation of inflow data for spatially developing direct numerical or large eddy simulations. *Journal of Computational Physics*, 186(2): 652 – 665, 2003. ISSN 0021-9991. doi: 10.1016/S0021-9991(03)00090-1. URL `http://www.sciencedirect.com/science/article/pii/S0021999103000901`.

[58] A. Klimenko and R. Bilger. Conditional moment closure for turbulent combustion. *Progress in Energy and Combustion Science*, 25 (6):595 – 687, 1999. ISSN 0360-1285. doi: 10.1016/S0360-1285(99)00006-4. URL `http://www.sciencedirect.com/science/article/pii/S0360128599000064`.

[59] N. Kornev and E. Hassel. Method of random spots for generation of synthetic inhomogeneous turbulent fields with prescribed autocorrelation functions. *Communications in Numerical Methods in Engineering*, 23(1):35–43, 2007. ISSN 1099-0887. doi: 10.1002/cnm.880. URL `http://dx.doi.org/10.1002/cnm.880`.

[60] N. Kornev, E. Shchukin, E. Taranov, H. Kröger, J. Turnow, and E. Hassel. Development and implementation of inflow generator for LES and DNS applications in OpenFOAM. 2009.

[61] N. Kornev and E. Hassel. Synthesis of homogeneous anisotropic divergence-free turbulent fields with prescribed second-order statistics by vortex dipoles. *Physics of Fluids*, 19(6):068101, 2007. doi: 10.1063/1.2738607. URL `http://link.aip.org/link/?PHF/19/068101/1`.

[62] N. Kornev, H. Kröger, and E. Hassel. Synthesis of homogeneous anisotropic turbulent fields with prescribed second-order statistics by the random spots method. *Communications in Numerical Methods in Engineering*, 24(10):875–877, 2008. ISSN 1099-0887. doi: 10.1002/cnm.1009. URL http://dx.doi.org/10.1002/cnm.1009.

[63] R. Kulkarni. *Large Eddy Simulation of Autoignition in Turbulent Flows*. PhD thesis, Technische Universität München, 2013.

[64] R. Kulkarni and W. Polifke. Large eddy simulation of autoignition in a turbulent hydrogen jet flame using a progress variable approach. *Journal of Combustion*, 2012.

[65] R. Kulkarni and W. Polifke. LES of Delft-Jet-in-Hot-Coflow (DJHC) with tabulated chemistry and stochastic fields combustion model. *Fuel Processing Technology*, 107(0):138 – 146, 2013. ISSN 0378-3820. doi: 10.1016/j.fuproc.2012.06.015. URL http://www.sciencedirect.com/science/article/pii/S0378382012002275.

[66] R. Kulkarni, M. Zellhuber, and W. Polifke. Les based investigation of autoignition in turbulent co-flow configurations. *Combustion Theory and Modelling*, 17(2):224–259, 2013. doi: 10.1080/13647830.2012.739711. URL http://www.tandfonline.com/doi/abs/10.1080/13647830.2012.739711.

[67] S. H. Lam. Using CSP to understand complex chemical kinetics. *Combustion Science and Technology*, 89(5-6):375–404, 1993. doi: 10.1080/00102209308924120. URL http://www.tandfonline.com/doi/abs/10.1080/00102209308924120.

[68] S. H. Lam and D. A. Goussis. The CSP method for simplifying kinetics. *International Journal of Chemical Kinetics*, 26(4):461–486, 1994. ISSN 1097-4601. doi: 10.1002/kin.550260408. URL http://dx.doi.org/10.1002/kin.550260408.

[69] J. Li, Z. Zhao, A. Kazakov, and F. L. Dryer. An updated comprehensive kinetic model of hydrogen combustion. *International Journal of Chemical Kinetics*, 36(10):566–575, 2004. ISSN 1097-4601. doi: 10.1002/kin.20026. URL http://dx.doi.org/10.1002/kin.20026.

[70] D. Lilly. A proposed modification of the Germano subgrid-scale closure method. *Physics of Fluids*, 4:633–635, 1992.

[71] T. S. Lund, X. H. Wu, and K. D. Squires. Generation of turbulent inflow data for spatially-developing boundary layer simulations. *Journal of Computational Physics*, 140(2):233–258, Mar 1 1998. ISSN 0021-9991.

[72] A. E. Lutz, R. J. Kee, and J. A. Miller. Senkin: A fortran program for predicting homogeneous gas phase chemical kinetics with sensitivity analysis. Technical Report SAND87-8248, Sandia National Laboratories, Livermore, CA 94551-0969, June 1987. Revised June 1996.

[73] U. Maas and S. B. Pope. Simplifying chemical-kinetics - intrinsic low-dimensional manifolds in composition space. *Combustion and Flame*, 88(3-4):239–264, MAR 1992. ISSN 0010-2180.

[74] P. Malte and D. Pratt. Measurement of atomic oxygen and nitrogen oxides in jet-stirred combustion. *Symposium (International) on Combustion*, 15(1):1061 – 1070, 1975. ISSN 0082-0784. doi: http://dx.doi.org/10.1016/S0082-0784(75)80371-7. URL `http://www.sciencedirect.com/science/article/pii/S0082078475803717`. Fifteenth Symposium (International) on Combustion.

[75] C. Markides and E. Mastorakos. Measurements and simulations of mixing and autoignition of an n-heptane plume in a turbulent flow of heated air. In *MCS 4 Lisbon, October 6-10 2005*, 2005.

[76] C. Markides and E. Mastorakos. Flame propagation following the autoignition of axisymmetric hydrogen, acetylene and normal-heptane plumes in turbulent co-flows of hot air. In *Proceedings of GT2006 ASME Turbo Expo 2006: Power for Land, Sea and Air*, 2006.

[77] C. Markides and E. Mastorakos. Experimental investigation of the effects of turbulence and mixing on autoignition chemistry. *Flow, Turbulence and Combustion*, 86:585–608, 2011. ISSN 1386-6184. URL `http://dx.doi.org/10.1007/s10494-010-9268-1`. 10.1007/s10494-010-9268-1.

[78] C. Markides and E. Mastorakos. An experimental study of hydrogen autoignition in a turbulent co-flow of heated air. In *Proceedings of the Combustion Institute*, volume 30, pages 883 – 891, 2005. doi: 10.1016/j.proci.2004.08.024. URL http://www.sciencedirect.com/science/article/pii/S0082078404000840.

[79] C. Markides and E. Mastorakos. Measurements of scalar dissipation in a turbulent plume with planar laser-induced fluorescence of acetone. *Chemical Engineering Science*, 61(9):2835 – 2842, 2006. ISSN 0009-2509. doi: 10.1016/j.ces.2005.10.040. URL http://www.sciencedirect.com/science/article/pii/S0009250905008110.

[80] C. Markides, G. D. Paola, and E. Mastorakos. Measurements and simulations of mixing and autoignition of an n-heptane plume in a turbulent flow of heated air. *Experimental Thermal and Fluid Science*, 31(5):393 – 401, 2007. ISSN 0894-1777. doi: 10.1016/j.expthermflusci.2006.04.008. URL http://www.sciencedirect.com/science/article/pii/S0894177706000665.

[81] A. R. Masri, R. Cao, S. B. Pope, and G. M. Goldin. PDF calculations of turbulent lifted flames of H2/N2 fuel issuing into a vitiated co-flow. *Combustion Theory and Modelling*, 8(1):1–22, 2003. doi: 10.1088/1364-7830/8/1/001. URL http://www.tandfonline.com/doi/abs/10.1088/1364-7830/8/1/001.

[82] E. Mastorakos. Ignition of turbulent non-premixed flames. *Progress in Energy and Combustion Science*, 35(1):57 – 97, 2009. ISSN 0360-1285. doi: 10.1016/j.pecs.2008.07.002. URL http://www.sciencedirect.com/science/article/pii/S0360128508000415.

[83] R. McDermott and S. Pope. A particle formulation for treating differential diffusion in filtered density function methods. *Journal of Computational Physics*, 226(1):947 – 993, 2007. ISSN 0021-9991. doi: DOI:10.1016/j.jcp.2007.05.006. URL http://www.sciencedirect.com/science/article/pii/S0021999107002173.

[84] D. W. Meyer and P. Jenny. Micromixing models for turbulent flows. *Journal of Computational Physics*, 228(4):1275 – 1293, 2009. ISSN 0021-9991. doi: 10.1016/j.jcp.2008.10.019. URL http://www.sciencedirect.com/science/article/pii/S0021999108005469.

[85] J.-B. Michel, O. Colin, and C. Angelberger. On the formulation of species reaction rates in the context of multi-species CFD codes using complex chemistry tabulation techniques. *Combustion and Flame*, 157(4):701 – 714, 2010. ISSN 0010-2180. doi: 10.1016/j.combustflame.2009.12.014. URL http://www.sciencedirect.com/science/article/pii/S001021800900371X.

[86] A. Naudin. *Simulation des Grandes Échelles de la Combustion Turbulente avec Chimie Detaillée Tabulée*. PhD thesis, INSA Rouen, 2008.

[87] F. Nicoud and F. Ducros. Subgrid-scale stress modelling based on the square of the velocity gradient tensor. *Flow, Turbulence and Combustion*, 62:183–200, 1999. ISSN 1386-6184. doi: 10.1023/A:1009995426001. URL http://dx.doi.org/10.1023/A:1009995426001.

[88] N. Peters. Local quenching due to flame stretch and non-premixed turbulent combustion. *Combustion Science and Technology*, 30(1-6):1–17, 1983. doi: 10.1080/00102208308923608. URL http://www.tandfonline.com/doi/abs/10.1080/00102208308923608.

[89] N. Peters. Laminar diffusion flamelet models in non-premixed turbulent combustion. *Progress in Energy and Combustion Science*, 10(3):319 – 339, 1984. ISSN 0360-1285. doi: http://dx.doi.org/10.1016/0360-1285(84)90114-X. URL http://www.sciencedirect.com/science/article/pii/036012858490114X.

[90] C. D. Pierce. *Progress-Variable Approach for Large-Eddy Simulation of Turbulent Combustion*. PhD thesis, Stanford University, 2001.

[91] C. D. Pierce and P. Moin. Progress-variable approach for large-eddy simulation of non-premixed turbulent combustion. *Journal of Fluid Mechanics*, 504:73–97, 2004. doi: 10.1017/S0022112004008213. URL http://dx.doi.org/10.1017/S0022112004008213.

[92] H. Pitsch. Flamemaster 3.3.10, 2007. URL http://www.itv.rwth-aachen.de/downloads/flamemaster/.

[93] T. J. Poinsot and D. Veynante. *Theoretical and Numerical Combustion*.

[94] W. Polifke, K. Döbbeling, T. Sattelmayer, D. G. Nicol, and P. C. Malte. A NOx prediction scheme for lean-premixed gas turbine combustion based on detailed chemical kinetics. *Journal of Engineering for Gas Turbines and Power*, 118:765–772, 1996.

[95] S. B. Pope. Computationally efficient implementation of combustion chemistry using in situ adaptive tabulation. *Combustion Theory and Modelling*, 1(1):41–63, MAR 1997. ISSN 1364-7830.

[96] S. B. Pope. *Turbulent Flows*. Cambridge University Press, 2000. ISBN 9780521598866. URL `http://books.google.fr/books?id=HZsTw9SMx-0C`.

[97] S. B. Pope. Ten questions concerning the large-eddy simulation of turbulent flows. *New Journal of Physics*, 6, Mar 16 2004. ISSN 1367-2630. doi: 10.1088/1367-2630/6/1/035.

[98] G. Ribert, O. Gicquel, N. Darabiha, and D. Veynante. Tabulation of complex chemistry based on self-similar behavior of laminar premixed flames. *Combustion and Flame*, 146(4):649–664, Sep 2006. ISSN 0010-2180. doi: 10.1016/j.combustflame.2006.07.002.

[99] G. Ribert, K. Wang, and L. Vervisch. A multi-zone self-similar chemistry tabulation with application to auto-ignition including cool-flames effects. *Fuel*, 91(1):87 – 92, 2012. ISSN 0016-2361. doi: 10.1016/j.fuel.2011.07.036. URL `http://www.sciencedirect.com/science/article/pii/S0016236111004339`.

[100] V. Sabel'nikov and M. Gorokhovski. Extended LMSE and Langevin models of the scalar mixing in the turbulent flow. In R. I. of technology (KTH), editor, *Second Internal Symposium on Turbulence and Shear Flow Phenomena*, Stockholm, Sweden, June 27-29 2001.

[101] V. Sabel'nikov and O. Soulard. Rapidly decorrelating velocity-field model as a tool for solving one-point Fokker-Planck equations for probability density functions of turbulent reactive scalars. *Phys. Rev. E*, 72:016301, Jul 2005. doi: 10.1103/PhysRevE.72.016301. URL `http://link.aps.org/doi/10.1103/PhysRevE.72.016301`.

[102] T. Sattelmayer, W. Polifke, D. Winkler, and K. Döbbeling. NOx-abatement potential of lean-premixed GT combustors. *Journal of engineering for gas turbines and power*, 120(1):48–59, 1998.

[103] P. Saxena and F. A. Williams. Testing a small detailed chemical-kinetic mechanism for the combustion of hydrogen and carbon monoxide. *Combustion and Flame*, 145(1â€“2):316 – 323, 2006. ISSN 0010-2180. doi: http://dx.doi.org/10.1016/j.combustflame.2005.10.004. URL http://www.sciencedirect.com/science/article/pii/S0010218005003123.

[104] A. Smirnov, S. Shi, and I. Celik. Random flow generation technique for large eddy simulations and particle-dynamics modeling. *Journal of Fluids Engineering*, 123(2):359–371, 2001. doi: 10.1115/1.1369598. URL http://link.aip.org/link/?JFG/123/359/1.

[105] G. P. Smith, D. M. Golden, M. Frenklach, N. W. Moriarty, B. Eiteneer, M. Goldenberg, C. T. Bowman, R. K. Hanson, S. Song, W. C. Gardiner, V. V. Lissianski, and Z. Qin. *GRI-Mech*, 7 1999. URL http://www.me.berkeley.edu/gri_mech/.

[106] M. D. Smooke and V. Giovangigli. *Reduced Kinetic Mechanisms and Asymptotic Approximations for Methane-Air Flames*. Springer-Verlag, Berlin, formulation of the premixed and non-premixed test problems edition, 1991.

[107] L. M. T. Somers and L. P. H. de Goey. Numerical study of a premixed flame on a slit burner. *Combustion Science and Technology*, 108(1-3):121–&, 1995. ISSN 0010-2202. doi: 10.1080/00102209508960394.

[108] O. Soulard. *Prise en compte d'un spectre d'échelles turbulentes dans la modélisation du micromélange et élaboration d'une méthode de Monte Carlo Eulérienne*. PhD thesis, University of Rouen, 2005.

[109] O. Soulard, V. Sabel'nikov, and M. Gorokhovski. Stochastic scalar mixing models accounting for turbulent frequency multiscale fluctuations. *International Journal of Heat and Fluid Flow*, 25(5):875 – 883, 2004. ISSN 0142-727X. doi: 10.1016/j.ijheatfluidflow.2004.03.008. URL http://www.sciencedirect.com/science/article/pii/S0142727X04000906.

[110] I. Stankovic and B. Merci. Analysis of auto-ignition of heated hydrogen/air mixtures with different detailed reaction mechanisms. *Combustion Theory and Modelling*, 15(3):409–436, 2011. URL http://www.informaworld.com/10.1080/13647830.2010.542830.

[111] L. Valino. A field Monte Carlo formulation for calculating the probability density function of a single scalar in a turbulent flow. *Flow, Turbulence and Combustion*, 60:157–172, 1998. ISSN 1386-6184. doi: 10.1023/A:1009968902446. URL http://dx.doi.org/10.1023/A:1009968902446.

[112] J. van Oijen and L. de Goey. Modelling of premixed laminar flames using flamelet-generated manifolds. *Combustion Science and Technology*, 161(1):113–137, 2000. doi: 10.1080/00102200008935814. URL http://www.tandfonline.com/doi/abs/10.1080/00102200008935814.

[113] D. Veynante, B. Fiorina, P. Domingo, and L. Vervisch. Using self-similar properties of turbulent premixed flames to downsize chemical tables in high-performance numerical simulations. *Combustion Theory and Modelling*, 12(6):1055–1088, 2008. doi: 10.1080/13647830802209710. URL http://www.tandfonline.com/doi/abs/10.1080/13647830802209710.

[114] K. Wang, G. Ribert, P. Domingo, and L. Vervisch. Self-similar behavior and chemistry tabulation of burnt-gas diluted premixed flamelets including heat-loss. *Combustion Theory and Modelling*, 14(4):541–570, 2010. ISSN 1364-7830. doi: 10.1080/13647830.2010.502248.

[115] S. Weise, D. Messig, B. Meyer, and C. Hasse. An abstraction layer for efficient memory management of tabulated chemistry and flamelet solutions. *Combustion Theory and Modelling*, 17(3):411–430, 2013. doi: 10.1080/13647830.2013.770602. URL http://www.tandfonline.com/doi/abs/10.1080/13647830.2013.770602.

[116] R. A. Yetter, F. L. Dryer, and H. Rabitz. Flow reactor studies of carbon monoxide/hydrogen/oxygen kinetics. *Combustion Science and Technology*, 79(1-3):129–140, 1991. doi: 10.1080/00102209108951760. URL http://www.tandfonline.com/doi/abs/10.1080/00102209108951760.

[117] Y. B. Zeldovich. The oxidation of nitrogen in combustion and explosions. *Acta Physicochimica U.R.S.S.*, 21:577–628, 1946.

[118] T. Zeuch, G. Moréac, S. S. Ahmed, and F. Mauss. A comprehensive skeletal mechanism for the oxidation of n-heptane generated by chemistry-guided reduction. *Combustion and Flame*, 155(4):651 – 674, 2008. ISSN 0010-2180. doi: 10.1016/j.combustflame.2008.05.007. URL http://www.sciencedirect.com/science/article/pii/S0010218008001612.

[119] B. Zoller, J. Allegrini, U. Maas, and P. Jenny. PDF model for NO calculations with radiation and consistent NO-NO2 chemistry in non-premixed turbulent flames. *Combustion and Flame*, 158(8):1591 – 1601, 2011. ISSN 0010-2180. doi: 10.1016/j.combustflame.2010.12.026. URL http://www.sciencedirect.com/science/article/pii/S0010218010003809.

A Turbulent inflow generators

Large-Eddy Simulations are known to give a better insight to the phenomena than RANS. Unfortunately this comes with higher requirements. In particular the velocity profiles at the inlets of the computational domain have to contain meaningful temporal and spatial fluctuations. Those fluctuations are especially important when the computational domain is located downstream of a grid or a perforated plate, or to trigger the instabilities occurring at the interface between a fast turbulent jet and a slow co-flow. To generate such variations a so-called turbulent generator will be used.

OpenFOAM® comes with only two generators (random noise and recycling method) that proved to be inadequate for the cases simulated in this work. Therefore a review of some algorithms will be done here.

A.1 White noise

One of the method to introduce fluctuations is to superimpose to a mean value U^{ref} a random white noise scaled by a turbulent intensity I^{turb}. In OpenFOAM®, this model uses additionally a temporal correlation factor α[1]. But as this correlation reduces the RMS fluctuation a correction factor rms_{Corr} is applied. The resulting model is:

$$U_i^{k+1} = (1-\alpha)U_i^k + \alpha\left(U_i^{\text{ref}} + \text{rms}_{\text{Corr}}U([-0.5,0.5])I_i^{\text{turb}}\|\mathbf{U}^{\text{ref}}\|\right), \quad \text{(A.1)}$$

where $U([-0.5,0.5])$ is an uniformly distributed random number in the interval $[-0.5,0.5]$ and $\text{rms}_{\text{Corr}} = \sqrt{12(2\alpha-\alpha^2)}/\alpha$.

This method is usually discarded because it does not contain spatial correlation and all frequencies received the same amount of energy. Consequently the resulting spectra never presents the well known decaying form for high wave numbers. And the high energy of the small scales results in a sharp dissipation of the fluctuations due to a high subgrid-scale viscosity.

[1] The fraction of the new fluctuations being mixed with the previous time step.

A.2 Spectral method

Smirnov et al. [104] developed a random flow generation technique derived from an analytical method of Kraichnan in which the fluctuations are approximated by a series of harmonic functions.

Firstly the velocity correlation tensor $r_{ij} = \widetilde{u_i u_j} - \tilde{u}_i \tilde{u}_j$ is diagonalized in order to find its orthogonal transformation tensor A and its eigenvalues λ_n. The new velocity field can be then computed knowing the normalized fluctuations $v_i'(\mathbf{x}, t)$:

$$\mathbf{U} = \mathbf{U}^{\text{ref}} + A\Lambda V', \tag{A.2}$$

in which v_i' is approximated by a harmonic decomposition:

$$v_i' = \sqrt{\frac{2}{N}} \sum_{n=1}^{N} \left[p_i^{(n)} \cos\left(\tilde{k}_j^{(n)} \tilde{x}_j + \omega^{(n)} \tilde{t} \right) + q_i^{(n)} \sin\left(\tilde{k}_j^{(n)} \tilde{x}_j + \omega^{(n)} \tilde{t} \right) \right]. \tag{A.3}$$

The coefficients $p_i^{(n)}$ and $q_i^{(n)}$ are derived from Gaussian distributed random values. And $k_j^{(n)}$ and $\omega^{(n)}$ are a sample of wave-number vectors and frequencies of the modeled turbulence spectrum:

$$E(k) = 16\sqrt{\frac{2}{\pi}} k^4 \exp(-2k^2). \tag{A.4}$$

A major parameter is the number of samples. In the original publication, Smirnov et al. used 1000 samples. But there are no tests about the dependency of the results on it.

This algorithm should be straightforward to implement. It requires only two parameters: the Reynolds stress tensor and the turbulent time scales. In Smirnov et al., the turbulent length scale is also used. But actually it vanishes in Equation (A.3).

A.3 Precursor simulation

One of the easiest ideas is to simulate an extra domain upstream of the inlet. Then the fluctuations obtained on the precursor can be pasted on the inlet of the actual domain. Unfortunately this technique is computationally very expensive and requires lots of memory to store the intermediate fluctuations.

The so-called *recycling* technique is a variation of that method. In this case, another mesh is not generated. But the mesh is prolongated upstream of the inlet. Then the fluctuations at the new inlet are taken from a cutting plane downstream to it (after some scaling). This method has proven very effective with channel flows or when the turbulence is fully developed like in pipes. Unfortunately, no easy control is available to set the characteristic of the turbulence. Therefore this method is not able to simulate a turbulent flow with an arbitrary spectra; e.g. flow after a perforated plate.

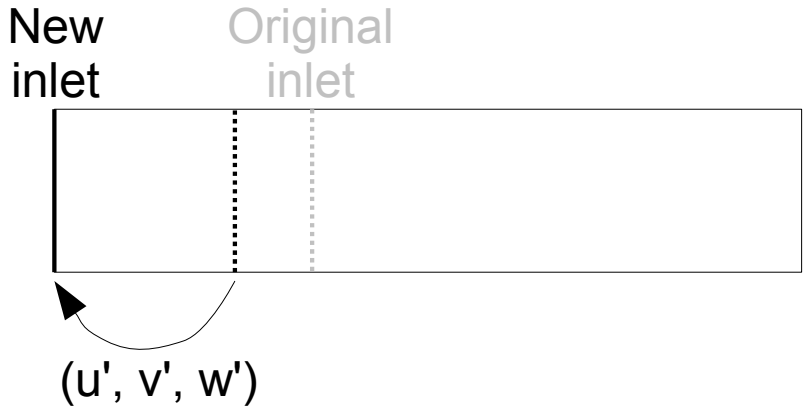

Figure A.1: Turbulent generator: recycling the fluctuations of a downstream plane to set the fluctuations on the inlet.

A.4 Digital filtering

The generation of turbulent fluctuations fulfilling a prescribed spectra, amplitude, and higher moments is a common operation in signal processing. This idea was matured by Klein et al. [57]. Their algorithm filters a 3-dimensional fields of white noise fluctuations to make it fit a give auto-correlation function. The filtered fluctuations are then transformed based on the Lund transformation [71] to get the wanted amplitudes and anisotropy of the turbulent fluctuations.

The time variation is introduced by continuously adding planes filled with a white noise signal upstream of the inlet and convecting them with the mean flow. Then when the plane does not influence the inlet fluctuations it can be discarded.

This method is now well established and was used for example by Jones et al. [48] or by Kerkemeier et al. [56] in both LES and DNS. Therefore, during this project, an implementation of this method was done. Unfortunately, the implementation worked well only for non-parallel simulations. Hence, the simpler version of Kempf et al. [53] was implemented as the equations to solve are easily handled in series and parallel by OpenFOAM®.

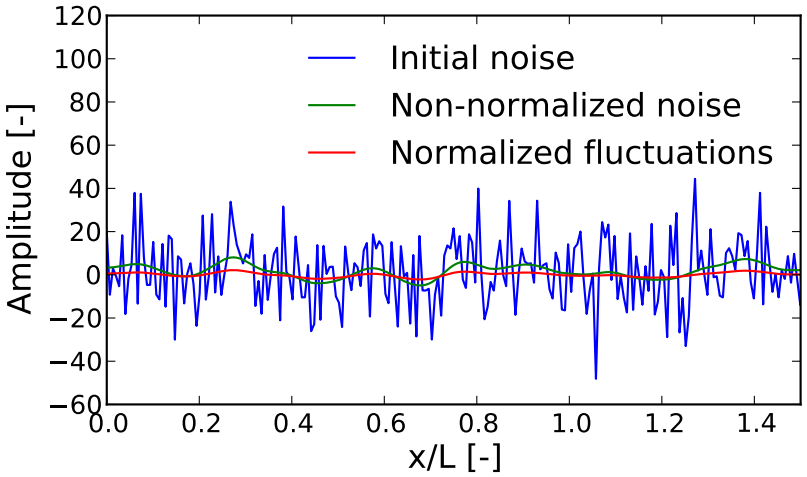

Figure A.2: Application of the Kempf et al. [53] algorithm to a one-dimensional fluctuations with correlation length, L, of 0.6 m.

The algorithm of Klein et al. is complicated to apply to unstructured meshes. Moreover the use of varying turbulent length scale is not easy to implement. To overcome those difficulties, Kempf et al. [53] remark that applying for a certain amount of time a diffusive operator on a white noise results in the same auto-correlation function as the digital filter. Indeed the diffusion operator acts as a Gaussian filter. The auto-correlation function resulting from it has a Gaussian shape as found in homogeneous turbulence in a late stage. Therefore, they propose a new algorithm. After generating a 3-dimensional matrix of white noise, a diffusive operator Eq. (A.5) with a diffusion coefficient function of the turbulent length scale is applied to the white noise. The resulting fluctuations have the proper auto-correlation function. The advantage is that the turbulent length scale can easily be adapted by using an inhomogeneous diffusion coefficient. And the equation to be solved is straightforwardly handled by any CFD code on any kind of mesh. As the Lund transformation should be applied to normally distributed fluctuations (zero in average and unity variance), after applying the

diffusive operator, the signal is normalized as shown in a one-dimensional example in Figure A.2.

$$\frac{\partial U_i}{\partial t} = \frac{\partial}{\partial x_k} D(L_t) \frac{\partial U_i}{\partial x_k} \text{ with i = x, y, z} \tag{A.5}$$

This latter algorithm was implemented in OpenFOAM®. The initial 3D-matrix of fluctuations is generated on a mesh obtained by extrusion of the inlet. On that second mesh, the diffusive operator is applied prior to the main simulation. Then during the simulation, the coherent fluctuations are obtained by evaluating the fluctuations on a cutting plane moving through the second mesh with the mean inlet velocity. Theoretically, the second mesh should be long enough to produce the fluctuations for the entire CFD simulation. But this will imply to store a very large mesh. To reduce the memory requirement, two solutions were developed. If the moving cutting plane reaches the end of the second mesh, its position is reinitialized at the beginning of it. This solution has the drawback of repeating the cycle of fluctuations. Another possibility is to redo the full generation on the second mesh before looping. The flaw in this case will be an inconsistency of the fluctuations. From tests, the second solution was preferred as the inconsistency in fluctuations has a low spatial extension and dissipates very quickly by nature of the turbulence.

A.5 Vortex generator

Kornev et al. [60] took an approach closer to the physical picture of the turbulence: "*(turbulence is) a motion of turbulent spots arising at random positions at random times*" [60]. Each spot/vortex produces a rotational flow with amplitude vanishing exponentially with the distance from the vortex center. The combination of all rotational fields give the amplitude and orientation of the fluctuating part of the velocity.
That method has three advantages:

- Usable on any mesh and with variable time step.
- More easily to understand as it mirrors the physical picture of turbulence.

- Retrieves the analytical solution for homogeneous turbulence.

As the authors of the method gave freely an implementation of the OpenFOAM® code, this method was primary used for all simulations. Unfortunately, this method has a flaw. In case of parallel simulations, the computation of the velocity field at the inlet is carried out entirely by the master processor. Therefore if the number of spots is large (couple of thousands), the computation of the inlet velocity becomes the bottleneck of the simulation. In addition, the actual code allows only the use of inlet with flow normal parallel to the x-axis.

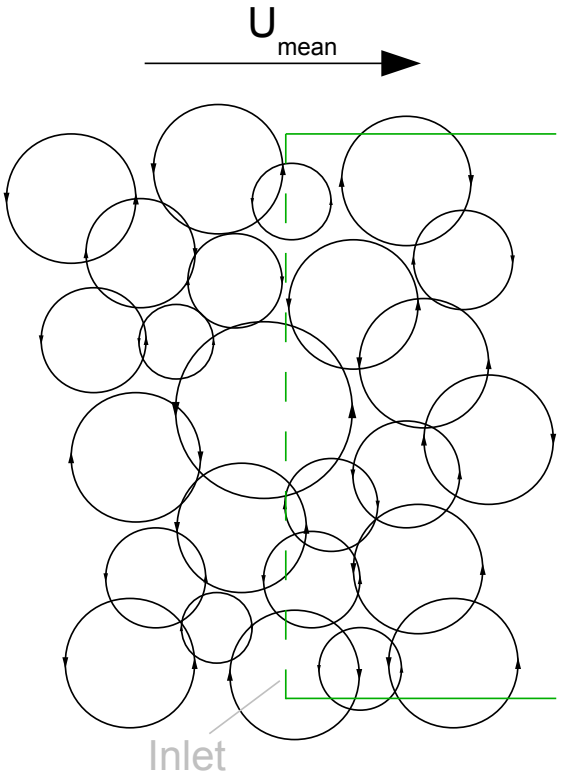

Figure A.3: Representation of the vortex generator idea.

B Derivation of the composition PDF transport equation

In this appendix the formulation of the conservation equation for the one-time one-point composition PDF, $\mathcal{F}_\phi$ will be demonstrated. To do so, first the one-time one-point velocity-composition PDF equation, $F_{u\phi}$, will be derived. Then by integrating over the velocity space, the composition PDF equation will be established. This demonstration is largely inspired by the one given in Appendix A of the Haworth's review on PDF methods for turbulent reacting flows [37].

The starting point is a generic system of Navier-Stokes equations (see Sec. 2.1):

$$\begin{aligned} \frac{\partial \rho}{\partial t} + \frac{\partial u_i}{\partial x_i} &= 0, \\ \frac{Du_j}{Dt} &= -\frac{\partial p}{\partial x_j} + \frac{\partial \tau_{ij}}{\partial x_i} + \rho g_j = \Lambda_j, \\ \frac{D\phi_k}{Dt} &= -\frac{\partial}{\partial x_i}\left(D_k \frac{\partial \phi_k}{\partial x_i}\right) + \rho \dot{\omega}_k = \theta_k \ \text{ for } k = 1...N_s, \end{aligned} \tag{B.1}$$

where $D./Dt = \partial./\partial t + \rho u_i \partial./\partial x_i$ is the material derivative.

Two main demonstrations are known to derive the velocity-composition PDF equation; the "fine-grained" PDF approach and the test-function method. The second method will be used here.

Let us consider an (almost) arbitrary test function $\mathcal{T}(\mathbf{u},\phi)$, the term $\langle\rho\frac{D\mathcal{T}}{Dt}\rangle$ can be derived in two independent expressions. Firstly[1]:

$$\begin{aligned}\left\langle\rho\frac{D\mathcal{T}}{Dt}\right\rangle &= \left\langle\frac{\partial\rho\mathcal{T}}{\partial t}\right\rangle+\left\langle\frac{\partial\rho u_i\mathcal{T}}{\partial x_i}\right\rangle,\\ &= \frac{\partial}{\partial t}\int\int\rho(\psi)\mathcal{T}(\mathbf{V},\psi)F_{u\phi}(\mathbf{V},\psi;\mathbf{x},t)d\mathbf{V}d\psi\\ &\quad+\frac{\partial}{\partial x_i}\int\int\rho(\psi)V_i\mathcal{T}(\mathbf{V},\psi)F_{u\phi}(\mathbf{V},\psi;\mathbf{x},t)d\mathbf{V}d\psi,\\ &= \int\int\mathcal{T}(\mathbf{V},\psi)\left\{\rho(\psi)\frac{\partial F_{u\phi}}{\partial t}+\rho(\psi)V_i\frac{\partial F_{u\phi}}{\partial x_i}\right\}d\mathbf{V}d\psi.\end{aligned}\tag{B.2}$$

The first line comes from the application of the continuity equation. The second is deduced from the definition of the mean. Finally as $\mathbf{V}$ and ψ are independent variables, the third term can be built.

The second expression comes from the derivation of $\mathcal{T}$ on its two explicit variables:

$$\frac{D\mathcal{T}(\mathbf{u},\phi)}{Dt}=\frac{\partial\mathcal{T}}{\partial u_i}\frac{Du_i}{Dt}+\frac{\partial\mathcal{T}}{\partial\phi_k}\frac{D\phi_k}{Dt}=\frac{\partial\mathcal{T}}{\partial u_i}\Lambda_i+\frac{\partial\mathcal{T}}{\partial\phi_k}\theta_k.\tag{B.3}$$

The second term is obtained by substituting Eq. (B.1). Then by multiplying Eq. (B.3) by ρ and taking the mean value:

$$\left\langle\rho\frac{D\mathcal{T}}{Dt}\right\rangle=\left\langle\rho\frac{\partial\mathcal{T}}{\partial u_i}\Lambda_i\right\rangle+\left\langle\rho\frac{\partial\mathcal{T}}{\partial Y_k}\theta_k\right\rangle.\tag{B.4}$$

The mean terms on the right can be expressed in terms of conditional means. For example by integrating by parts, the last term becomes:

$$\begin{aligned}\left\langle\rho\frac{\partial\mathcal{T}}{\partial\phi_k}\theta_k\right\rangle &= \int\int\left\langle\rho\frac{\partial\mathcal{T}(\mathbf{u},\phi)}{\partial\phi_k}\theta_k\middle|\,\mathbf{V},\psi\right\rangle F_{u\phi}d\mathbf{V}d\psi,\\ &= \int\int\rho(\psi)\frac{\partial\mathcal{T}(\mathbf{V},\psi)}{\partial\psi_k}\langle\theta_k|\,\mathbf{V},\psi\rangle F_{u\phi}d\mathbf{V}d\psi,\\ &= \int\int\frac{\partial}{\partial\psi_k}\left[\rho(\psi)\mathcal{T}(\mathbf{V},\psi)\langle\theta_k|\,\mathbf{V},\psi\rangle F_{u\phi}\right]d\mathbf{V}d\psi\\ &\quad-\int\int\mathcal{T}(\mathbf{V},\psi)\frac{\partial}{\partial\psi_k}\left[\rho(\psi)\langle\theta_k|\,\mathbf{V},\psi\rangle F_{u\phi}\right]d\mathbf{V}d\psi.\end{aligned}\tag{B.5}$$

[1] A particular value of the velocity will be noted by $\mathbf{V_i}$ and for the composition ψ will be the annotation.

The integral of the divergence in ψ-space in first term of the last line is identical to a surface integral at the boundary of ψ-space by the Gauss' theorem. For well-behaved functions $\mathcal{T}$ and PDF's $F_{u\phi}$, this integral is equal to zero.

Following the same procedure for $\langle \rho \partial \mathcal{T} / \partial u_i \Lambda_i \rangle$, Equation (B.4) can be rewritten as:

$$\begin{aligned} \left\langle \rho \frac{D\mathcal{T}}{Dt} \right\rangle &= -\int\int \mathcal{T}(\mathbf{V},\psi) \left\{ \frac{\partial}{\partial V_i} \left[\rho(\psi) \langle \Lambda_i | \, \mathbf{V}, \psi \rangle F_{u\phi} \right] \right. \\ &\left. + \frac{\partial}{\partial \psi_k} \left[\rho(\psi) \langle \theta_k | \, \mathbf{V}, \psi \rangle F_{u\phi} \right] \right\} d\mathbf{V} d\psi. \end{aligned} \tag{B.6}$$

Then subtracting Eq. (B.6) from Eq. (B.3),

$$\begin{aligned} \int\int \mathcal{T}(\mathbf{V},\psi) \left\{ \rho(\psi) \frac{\partial F_{u\phi}}{\partial t} \right. &+ \rho(\psi) V_i \frac{\partial F_{u\phi}}{\partial x_i} + \frac{\partial}{\partial V_i} \left[\rho(\psi) \langle \Lambda_i | \, \mathbf{V}, \psi \rangle F_{u\phi} \right] \\ &\left. + \frac{\partial}{\partial \psi_k} \left[\rho(\psi) \langle \theta_k | \, \mathbf{V}, \psi \rangle F_{u\phi} \right] \right\} d\mathbf{V} d\psi = 0. \end{aligned} \tag{B.7}$$

As Eq. (B.7) must be valid for any test function $\mathcal{T}$, the integrand has to be equal do zero:

$$\begin{aligned} \rho(\psi) \frac{\partial F_{u\phi}}{\partial t} + \rho(\psi) V_i \frac{\partial F_{u\phi}}{\partial x_i} &= -\frac{\partial}{\partial V_i} \left[\rho(\psi)) \langle \Lambda_i | \, \mathbf{V}, \psi \rangle F_{u\phi} \right] \\ &\quad - \frac{\partial}{\partial \psi_k} \left[\rho(\psi) \langle \theta_k | \, \mathbf{V}, \psi \rangle F_{u\phi} \right]. \end{aligned} \tag{B.8}$$

The composition PDF is obtained by integrating Eq. (B.8) over the velocity space and developing θ_k according to Eq. (B.1),

$$\begin{aligned} \frac{\partial \bar{\rho} \mathcal{F}_\phi}{\partial t} &+ \frac{\partial \bar{\rho} \tilde{u}_i \mathcal{F}_\phi}{\partial x_i} - \frac{\partial}{\partial x_i} \left(\bar{\rho} \tilde{u}_i - \bar{\rho} \left\langle u_i | \psi \right\rangle_\Delta \right) \mathcal{F}_\phi \\ &= -\frac{\partial}{\partial \psi_k} \left\langle \frac{\partial}{\partial x_i} D_k \frac{\partial \phi_k}{\partial x_i} \middle| \psi \right\rangle_\Delta \mathcal{F}_\phi + \frac{\partial}{\partial \psi_k} \bar{\rho} \dot{\omega}_k \mathcal{F}_\phi. \end{aligned} \tag{B.9}$$

C Example of settings for a test case

The following appendix presents an example of dictionaries needed to set the combustion model described in Chapter 3; namely the Eulerian stochastic fields' method with tabulated chemistry. The parameters shown here are those used to set a simulation of auto-ignition spots of hydrogen in hot turbulent air.

The look-up tables' parameters are specified in the dictionary `$FOAM_CASE\constant\tableProperties`. The ones for the combustion model are given in the dictionary `$FOAM_CASE\constant\combustionProperties`. Finally the model needs a fake chemical mechanism to ensure atomic balances. This is done in two steps. First the file containing the mechanism has to be defined in `$FOAM_CASE\constant\thermophysicalProperties`. Then the fake chemical mechanism file is specified (here an example simply called `reactions` is detailed).

C.1 Tabulated chemistry settings

```
FoamFile // Mandatory header of the dictionary
{
    version     2.0;
    format      ascii;
    class       dictionary;
    location    "constant";
    object      tableProperties;
}

// Keyword to specified the tabulated model
tableSolver     tableFtYc;

// Mixture fraction distribution
ftDistribution
{   // Type of distribution
    distribution        uniform;
    // List of values in the distribution
    values      101( 0 0.01 0.02 ... 0.98 0.99 1 );
    // Parameters needed by the distribution
```

```
    parameters  0();
}

// Progress variable distribution
YcDistribution
{   // Type of distribution
    distribution        loguniform;
    // List of values in the distribution
    values      105( 0 1e-06 1e-05 0.0001 0.001 0.01 0.02
        ... 0.98 0.99 1 );
    // Parameters needed by the distribution
    parameters  2( 4 100 );
}

// Value of the progress variable at equilibrium for
//  each mixture fraction in the distribution
PVeq    101( 0 0.0116 0.0232 ... 0.0052 0.0026 0 );
```

Listing C.1: tableProperties

C.2 Combustion model settings

```
FoamFile // Mandatory header of the dictionary
{
    version     2.0;
    format      ascii;
    class       dictionary;
    location    "constant";
    object      combustionProperties;
}
// Selection of the combustion model
// - ESF with reference thermodynamical pressure, pRef
combustionModel  stochasticIto<rhoCombustionModel,incGasThermoPhysics>;
// - ESF with standard perfect gas law
//combustionModel  stochasticIto<psiCombustionModel,gasThermoPhysics>;
// - delta-pdf with standard perfect gas law
//combustionModel  deltaPDF<psiCombustionModel,gasThermoPhysics>;
// - double-beta-pdf with reference thermodynamical pressure, pRef
//combustionModel  doubleBetaPDF<rhoCombustionModel,incGasThermoPhysics>;

active      yes; //Is the combustion model active?

// ESF parameters
stochasticItoCoeffs
{
    nStochasticFields   8; // Number of stochastic fields
    tables    ( H2O ); // Species to be defined by tables
```

```
    //Sc      0.72; // [optional] laminar Schmidt number
    //Sct     0.85; // [optional] turbulent Schmidt number
    // [optional] Coeff multiplying the relaxation species
    //            source terms
    //cRelax    1.;
    // [optional] if yes relax the species,
    // otherwise read directly the source terms in tables.
    //relaxation yes;
}

deltaPDFModelCoeffs
{
   tables    (CH4 CO CO2 H2O H); //Species to be defined by tables

    //Sc      0.72; // [optional] laminar Schmidt number
    //Sct     0.85; // [optional] turbulent Schmidt number
    // [optional] Coeff multiplying the relaxation species
    //            source terms
    //cRelax    1.;
    // [optional] if yes relax the species,
    // otherwise read directly the source terms in tables.
    //relaxation yes;
}

doubleBetaPDFCoeffs
{
    tables    ( H2O ); // Species to be defined by tables
    // Mixture fraction variance model: transport, algebraic or none
    //varftModel    transport;
    // Square of the progress variable model: transport or none
    //sqrYcModel    transport;

    //Sc      0.72; // [optional] laminar Schmidt number
    //Sct     0.85; // [optional] turbulent Schmidt number
    // [optional] Coeff multiplying the relaxation species
    //            source terms
    //cRelax    1.;
    // [optional] if yes relax the species,
    // otherwise read directly the source terms in tables.
    //relaxation yes;
}
```

Listing C.2: combustionProperties

C.3 Thermophysical properties and element budgets

```
FoamFile // Mandatory header of the dictionary
{
    version         2.0;
    format          ascii;
    location        "constant";
    class           dictionary;
    object          thermophysicalProperties;
}

// thermoType to use rhoReactingTableFoam
thermoType hsRhoMixtureThermo<reactingMixture<incGasThermoPhysics>>;
// thermoType to use reactingTableFoam
//thermoType hsPsiMixtureThermo<reactingMixture<gasThermoPhysics>>;

// Reader type to interpret the chemistry mechanism
chemistryReader          foamChemistryReader;

// Fake chemistry mechanism file
foamChemistryFile        "$FOAM_CASE/constant/reactions";
// Thermophysical properties for all species
foamChemistryThermoFile  "$FOAM_CASE/constant/thermo.foam";

// Inert specie
inertSpecie              N2;
```

Listing C.3: thermophysicalProperties

```
// List of the species to be transported
species    4( H2 O2 H2O N2 );
// List of the chemical reactions
reactions
{   // For hydrogen only one equation ensures atomic budget
    hydrogenReaction
    {
        type        irreversibleArrheniusReaction; // Not used
        reaction    "2H2␣+␣O2␣=␣2H2O";
        A           1.16e+09; // Not used
        beta        1;        // Not used
        Ta          37890.3;  // Not used
    }
}
```

Listing C.4: Reactions file

D Tips and tricks for OpenFOAM®

Sharing is caring.
A.A.

The toolbox OpenFOAM® is still under active development. It has not yet reached the maturity of commercial softwares like Fluent or StarCCM+. The transmission of experience is consequently important to help the new users to enter the code and avoid some mistakes.

D.1 Boundary conditions

For scalars, the boundary conditions are usually straightforward (Dirichlet or Neumann conditions). Unfortunately for the velocity and pressure, this can be more troublesome. Especially in OpenFOAM® those boundary conditions can be independently defined although they are coupled. Moreover, the multiplicity of boundary conditions in the code complicates the choice. The basic rule is: where the velocity is specified, the pressure should be set to zero gradient and vice-versa. Therefore the default parameters should be defined as in Table D.1.

	Velocity	**Pressure**
Inlet	`fixedValue`	`zeroGradient`
Outlet	`fluxCorrectedVelocity`	`fixedValue`
Wall	`fixedValue` or `slip`	`zeroGradient`

Table D.1: Default boundary conditions for the velocity and the pressure.

In case a back flow at the outlet is possible, the pressure boundary condition should be set to `outletInlet`, the velocity to `pressureInletOutletVelocity` and the scalars to `inletOutlet`.

For compressible flow and reacting flows, it is important to let pressure waves exit the computational domain. For this purpose, there is only one

weak solution in OpenFOAM®: the pressure should be set at the outlet as `waveTransmissive`. That boundary condition requires the following parameters:

- `gamma`: Ratio of specific heats
- `fieldInf`: Value of the pressure to relax to – usually atmospheric pressure.
- `lInf`: Wave length of the oscillations to transmit – for channel, put the length of the channel.

An instantaneous pressure and axial velocity fields is shown in Figure D.1 for the ETH test case using reflective boundary conditions at the outlet. Obviously in this case the energy of the wave pressure increased to a point where the results are unphysical. This purely numerical pressure wave disappears when using `waveTransmissive` instead of standard boundary conditions at the outlet.

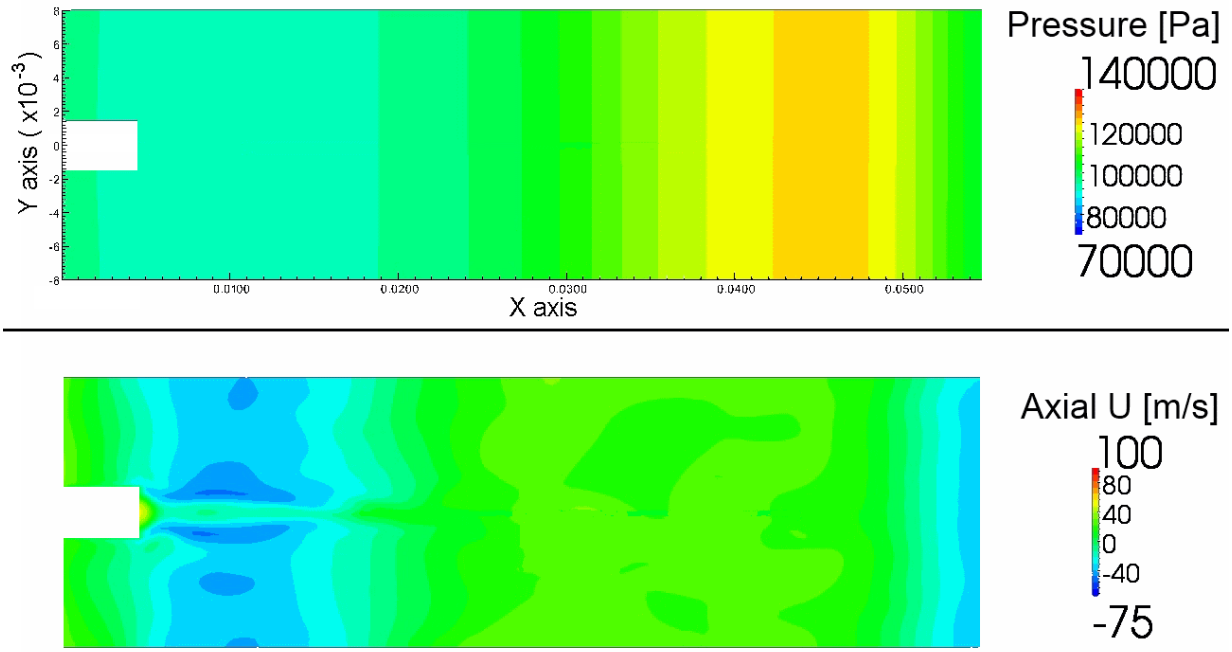

Figure D.1: Possible trouble due to reflective outlet boundary condition.

D.2 The thermodynamic pressure concept

For reacting flows, the compressibility of the flow comes from the high variation of density in the domain. But the pressure is usually almost constant in a combustion chamber. From that remark, some commercial code (like Fluent®) have decoupled the pressure appearing in the momentum equation from the thermodynamic pressure providing the local density. This trick improves drastically the stability of a solver at the expense of a small approximation. Unfortunately this possibility is not implemented in OpenFOAM®. Therefore an implementation was made in which the user should manually specify a reference pressure p_{ref} for all species. The density is then computed from the perfect gas law:

$$\rho = \frac{p_{\text{ref}}}{\frac{R}{M_w}T}, \tag{D.1}$$

where R is the gas constant, M_w the mean molecular weight and T, the temperature. This model is available in the standard release of OpenFOAM® since version 2.2.0 under the name `incompressiblePerfectGas`.

It is important to note that this model uncoupled the pressure and the density. Therefore the thermophysical models based on the density must be used as well as solver using the explicit variation in time of the density (i.e. `rhoReactingFoam` instead of `reactingFoam`).

D.3 Numerical schemes

OpenFOAM® comes with a plethora of numerical schemes. So the choice isn't trivial. In Table D.2, you will find the default schemes used for carrying LES on O-grid and structured meshes in this work.

Category	Scheme	Explanation
Time	`CrankNicholson 1.0`	Implicit, bounded, second-order
Gradient	`cellMDLimited Gauss linear 1.0`	Gradient limited
Convection		
- velocity	`Gauss linearUpwind gradU`	Second/first-order, bounded
- species	`Gauss Gamma01 1.0`	Normalized variable scheme with strict bounds [0.0, 1.0]
- other scalar	`Gauss Gamma 1.0`	Normalized variable scheme
Laplacian	`Gauss linear limited 1.0`	Standard laplacian scheme with limited non-orthogonal correction

Table D.2: Default schemes for LES on structured and O-grid meshes.

For unstructured meshes, it is important to change the gradient scheme from `Gauss linear` to `leastSquares`.